The Role of Phase Transitions for Transmembrane Transportation Processes and Activity

Dissertation

zur Erlangung des akademischen Grades

Dr. rer. nat.

eingereicht an der

Mathematisch-Naturwissenschaftlichen-Technischen Fakultät

der Universität Augsburg

von

Andrej Kamenac

Augsburg, März 2023

Erstgutachter: Prof. Dr. Christoph Westerhausen
Zweitgutachter: Prof. Dr. Matthias Schneider
Tag der mündlichen Prüfung: 16.05.2023

"Ein Abend, an dem sich alle Anwesenden völlig einig sind, ist ein verlorener Abend."

– Albert Einstein

Abstract

The scope of this thesis is to consider phase transitions acting on lipid membranes and the implications on biological processes. To account for the diversity of fields involved, the projects range from transmembrane processes, such as permeabilization - to lateral, in-plane processes, such as enzymatic activity on membranes. The science conducted on these fields study fundamentals to applications and finally achieve the development of a biomedical tool.

Firstly, we studied the membrane phase transition temperature as function of shear flow. Optical measurements of vesicles in microfluidic systems revealed a shift in chain order. The same effect was observed for another lipid type, which is a powerful reference. These results should be considered in the design of therapeutic temperature-sensitive liposomes encapsulating drugs to ensure precise control of the drug release.

Secondly, we studied the nanoparticle uptake of vesicles as function of temperature. The micrographs time series revealed that nanoparticle uptake was a complex function of temperature. Local maxima of the uptake as function of temperature do exist and do correlate with the phase transition. However, - contrary to expectations - the uptake peaks are located around $T = T_{\mathrm{m}} + 3\,\mathrm{K}$. As the uptake is driven by adhesion, we conducted force spectroscopy on the adhesion, which turned out to be a non-linear function of temperature. Adding literature into consideration, we concluded that tension must exhibit a minimum at the nanoparticle uptake maximum. These results might become relevant for the design of porous silica nanoparticles, which are commonly used as a carrier material for drug delivery.

Thirdly, in addition to carrier-centered nanoparticle permeability, we studied general permeability as a function of shear rate and temperature for vesicles. Unexpectedly, we observed all-or-nothing-like permeabilization behavior - entirely different from reports in literature - just by adding shear flow. All-or-nothing behavior is well-known from biology, like in triggering of action potentials. The all-or-nothing-like behavior is triggered at the lipid membrane phase transition temperature. This finding is particularly intriguing, as a macroscopic system acts probabilistic.

Fourthly, after gaining expertise in shearing and permeabilization, we built a novel acoustofluidic permeabilization tool for suspended living cells. Acoustofluidic permeabilization is a vector-free method, where surface acoustic waves couple into the fluid of a microfluidic channel to trap cells in the vortices that are created by the acoustic wave application. The permeabilization is enhanced by more than an order of magnitude for a large spectrum of cargo sizes, ranging from a fluorescent molecule, to sugars and even proteins.

Fifthly, we studied the correlation of permeability and shear forces in a viscosimeter. The cone-plate shearing of suspended cells revealed that the maximum permeability temperature is a linear function of shear rate. However, it was the plate-plate viscosimeter experiments on adherent cells, which brought a real leap forward in terms of robustness, visualization, and spatial information. Thanks to the continuous and linear shear profile, we were able to measure the whole shear dimension at once with only one cell passage. Furthermore, adherent cells allowed for spatial information on the single cell level. Thanks to the spatial information, the results revealed cell de-adhesion to be a non-linear function of shear rate, which is entirely new in literature. On top, we found permeability to be a non-linear function of shear rate - supporting prior findings in the form of fascinating fluorescent micrographs.

Finally, we added biochemistry to the equation and studied membrane phase transition acting on the enzyme activity. The results revealed a correlation of the membrane-associated enzyme activity with the excess heat capacity of the system. In detail, we observed Anti-Arrhenius behavior in a temperature interval above the phase transition temperature - several Kelvin wide. This result resolved a dispute in literature from the 1970's, where non-Arrhenius membrane-associated enzymes could not be accommodated by any theory. However, our results support a thermodynamic theory by Kaufmann. Concerning applications, this result proves the plausibility of the trigger-and-detection principle of the soliton nerve signalling theory.

Contents

List of Figures

List of Tables

1 Introduction

> Throughout history, religions and ideologies did not sanctify life itself. They always sanctified something above or beyond earthly existence, and were consequently quite tolerant of death. [...] Modern science and modern culture have an entirely different take on life and death. They don't think of death as a metaphysical mystery, and they certainly don't view death as the source of life's meaning. Rather, for modern people death is a technical problem that we can and should solve. [...] Humans always die due to a technical glitch. The heart stops pumping blood. The main artery is clogged by fatty deposits. [1]

To most people today, Harari's statement is clear, obvious, and - as scientists enjoy to say - trivial. However, the logical consequence to this statement is that technical glitches are avoidable or repairable. To a possibly unlimited extent.

In this thesis, I do not want to solve mortality. However, I would like to present my small contribution to the advance in the interdisciplinary field of medicine, biology, and physics.

In Harari's quote, he mentions fatty deposits in a negative connotation, being capable of clogging arteries. The commonly used term fat refers to certain molecules, whose chemical structure will be elucidated soon. Fat is an essential part of cells and - besides other molecules - forms membranes. We like to think of fat as of a simple, white, and glibbery material. In fact, fat brings a huge amount of chemistry, biology, and physics with it. And even more important, it brings questions in these disciplines with it, which we are going to address in this thesis.

In the first part, I will present a historic introduction into membranes and their basics. The basics include the chemistry and physics of fats, as well as prominent other components in a membrane.

In the second part, I will present experiments inspired by blood flow in vessels. Therefore, we will expose membranes to flow and study the shift of the membranes thermodynamic properties.

In the third part, the simple flow model will be extended by another medically relevant, real-world substance - nanoparticles - which are abundant in our food and air. We will study the interaction of membranes and the nanoparticles thermodynamically.

In the fourth part, we will approach even further towards real world membranes by using living cells. Based on the results from the prior sections focusing on the interaction of membranes, flow and nanoparticles, we will build a novel - acoustofluidic - drug delivery tool. This novel acoustofluidic drug delivery tool will help testing new potential drugs by forcing them through the cell membrane, which is otherwise not

possible. Furthermore, this acoustofluidic drug delivery tool along with the evaluation could measure the efficiency of the tested drugs. Along the way, fundamental insights on the thermodynamics of the key measure of drug delivery - cell membrane permeability - will be elaborated.

In the last part, we will put thermodynamics in membranes to the test. We will expand the complexity of the system by adding a new biological material to the artificial membranes - enzymes. This study of membrane-enzyme thermodynamic interaction will help draw the boundaries between thermodynamics and biochemistry. On the application side, we will test the membrane-enzyme thermodynamic interaction for the potential of being a trigger-and-detector in an uprising nerve pulse propagation model.

2 Membranes

Practically all living organisms have membranes. Even the ones, where it is not exactly clear if they are actually alive (viruses), have membranes. Membranes are a fundamental tool in biology to satisfy a plethora of requirements for vastly different organisms to function.

To understand the role of membranes in literature, I will provide a historic overview on the discovery of membranes. Based on the latest and most detailed model of membranes, we will study the chemistry of the membranes, especially its most abundant molecules - lipids. Once the chemistry of the lipids is clear, we will continue our bottom-up approach and regard the behavior of lipids in large numbers, which is the thermodynamics of lipids. At this point, we will extend our thermodynamic view of membranes from model membranes purely consisting of solely lipids, to other classes of biological material, especially enzymes.

This uprising ansatz in literature, that membrane thermodynamics govern biochemical processes, like enzymatic catalysis, has various biological applications, two of which this thesis contributes to. The first application is a thermodynamical model of nerve pulse propagation, triggered by membrane-governed enzymatic activity. The second biological application is membrane permeability for drug delivery. At first glance, these two biological applications seem independent, however, we will study the link between these two phenomena, which are lipid phase transitions.

First things first - where does the knowledge about membranes arise from and how were membranes discovered?

2.1 Historic Overview of Membranes

This overview is a concise summary, the interested reader could refer to the original source [2].

The first glimpses into membranes were the discovery of osmotic barriers in plants [3] and were named plasma membrane [4]. Overton then constituted that the membrane must be similar to oil, as permeation through membranes is related to the partition coefficient [5]. This over 120 years old finding is still very relevant as of today to predict membrane permeability, which is a major scope in this thesis.

A refinement of Overton's finding gave Langmuir, when he specified the membrane film must consist of polar headgroups - pointing towards water - and apolar hydrocarbons [6]. Finally, the bilayer structure was revealed by Gorter and Grendel in 1925, showing that the membrane area of the lipids from red blood cells on a Langmuir trough is about twice the surface area of the used red blood cells [7].

Danielli and Davson in 1935 revealed the biochemical diversity of membranes [8]. In particular, they found proteins, from which they constituted, that proteins are adsorbed to the hydrophilic head groups of the membrane. Robertson was the first in 1959 to visualize a membrane with the help of electron microscopy [9]. He also measured the thickness of a membrane bilayer, which he found to be 7.5 nm.

Nicolson and Singer developed the famous Singer-Nicolson model in 1972, which is also called the fluid mosaic model [10]. With the help of x-ray crystallography, they found that membrane proteins have hydrophobic α-helices, that are not only adsorbed to the membrane, but rather span through it. They further constituted that the cell membrane resting phase state is the fluid state, as the diffusion coefficient matches and is two orders of magnitude higher than the gel state. The Singer-Nicolson model is widely used until today.

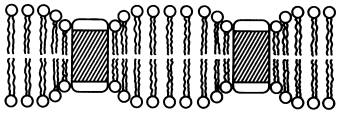

Figure 2: Mouritsen's and Bloom's mattress model. Adapted from [11].

Slight advances to the model had big scientific impact, brought in by Mouritsen and Bloom with their mattress model in 1984 [11], as illustrated in figure 2. They took the distribution of different lipid types into account and stated that the resulting hydrophobic mismatching rather favor some ordering and domain formation. This principle works both ways, e.g. bacteriorhodopsin fluidizes surrounding lipids [12], which we will revisit in later analysis. These effects give a first glimpse into a fundamental field, the lipid-protein interaction. In order to dive into this field, it is essential to understand the structure of lipids and proteins.

2.2 Chemical Structure of Artificial Lipid Membranes

Having understood the history of membrane models and how they matured over time, we will have a close look into the chemical structure of lipids.

The term membrane refers in biology to a mixture of hundreds of different types of lipids, proteins and sugars. Such a cell membrane consists easily of billions of molecules - just counting the lipids in a single cell membrane. Lipids are amphiphatic molecules, which consist of a polar, hydrophilic group - commonly referred to as the head group - and an apolar, hydrophobic hydrocarbon group - commonly referred to as the acyl-chains or tail group.

The acyl-chains interact via van-der-Waals-interactions and are basically characterized by their chain length and their unsaturation degree, which might differ for

the very same lipid molecule. In contrast, head groups interact via their dipoles and hydrogen bonds, as those are mostly zwitterionic or charged.

The head groups consist of commonly two functional chemical groups in a certain order, like choline, phosphate, ethanolamine, glycerol, and serine. An important chemical feature of lipid head groups is the protonation and deprotonation. A quantitative measure for protonation and deprotonation is the pK_a-value, which is generally different for every functional group and which can be determined in titration experiments. A selection of biologically relevant lipids is illustrated in figure 3.

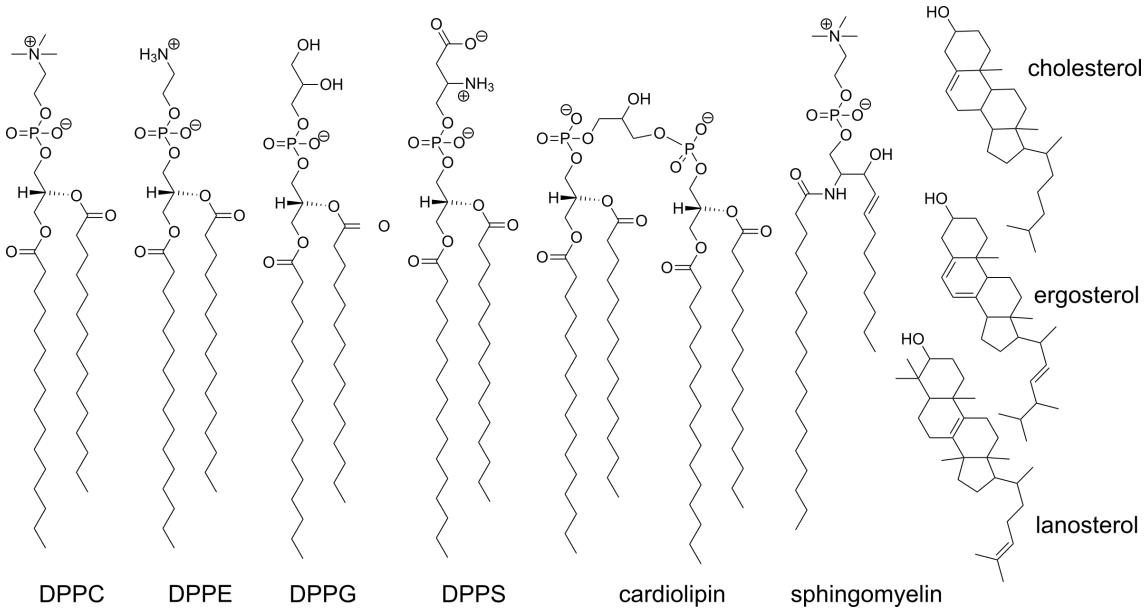

Figure 3: Selection of membrane lipids. Adapted from [2].

Phosphocholine lipids for example display a pK_a of about $pK_a \approx 2-3$ [13]. At this pH value, 50 % of the lipids exist in the charged state ($R-PO_4H-NH_3^+$) and 50 % in the zwitterionic state ($R-PO_4^--NH_3^+$). However, this is dependent on environmental thermodynamic parameters like solvents, ionic strength, pressure, and temperature [2, 14], which is a major subject throughout this study. Note that despite the 50 %-50 % distribution being a steady-state distribution, it is highly non-static in time and each lipid head group will fluctuate between those two states.

In general, the electrostatic nature of the lipid head group has consequences on the whole lipid bilayer. A lipid bilayer structure is an energetic minimum of two opposing forces. On the one hand, head groups repel each other and therefore generate a surface pressure. On the other hand, acyl-chains attract each other and generate a surface tension [15]. As a result, the formation of a bilayer is an interplay of various

parameters, documented in a phase diagram, as visualized in figure 4b. The following biologically relevant categorization results [2]:

- Monomeric Lipids: The lipids are homogeneously dissolved in the aqueous solution. An appropriate approximation of monomeric lipids is an ideal gas, as they do not interact.
- Micells: The lipids are radially arranged, where the acyl chains are on the inner side, so acyl chains avoid contact with water. This is a regime, where the lipids mutually interact and therefore must be described at least by a real gas. Being a real gas is the prerequisite to display phase transitions. Micelle phase transitions have been proven experimentally [16].
- Bilayer: This 2-dimensional double sheet of lipids is a commonly used simplified model of the biological membrane. It displays phase transitions and the following phases:
  - Gel ($L_{\beta'}$) phase: The lipids display a twofold order. The lateral order is a 2-dimensional triangular lattice order. The second order concerns the C-C bonds in the acyl-chains, where the acyl-chains remain in the all-trans configuration. This phase is also referred to as solid ordered (SO).
  - Ripple ($P_{\beta'}$) phase: Here, the lipids have partially melted and therefore display periodic 1-dimensional fluid ripples [17].
  - Fluid (L_{α}) phase: The lipids are laterally disordered, so the 2-dimensional lattice order is lost. Furthermore, the rotational barrier of the hydrocarbon chains is overcome, which enables free rotation. This phase is also referred to as liquid disordered (LD).
  - Liquid ordered (LO) phase: This phase only exists under presence of cholesterol. The liquid ordered phase displays no lateral order, but the C-C bonds remain in all-trans configuration. This phase can be regarded as a gel-like phase with C-C bonds in all-trans configuration, but with no lateral order.

The difference in structure of the membrane phase transition is illustrated in figure 5. Simulations allow for a more detailled illustration of the most important bilayer phase states, which are visualized in figure 4a. Note, that the sheet-like shape of bilayers has a disadvantage at the edges due to exposure to water in the third dimension. However, periodic boundary conditions resolve this dilemma. A lipid bilayer with periodic boundary conditions can be a vesicle.

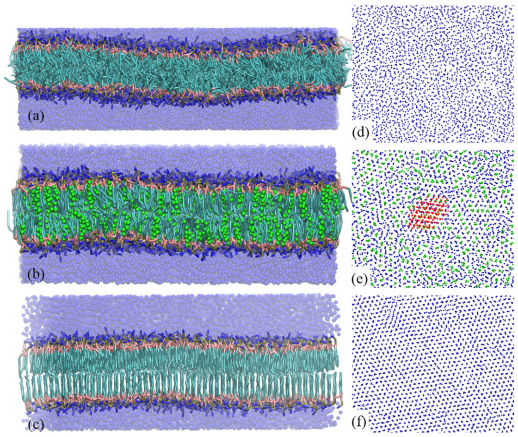

(a) Side and top view simulation of a liquid, liquid-ordered, and gel state.

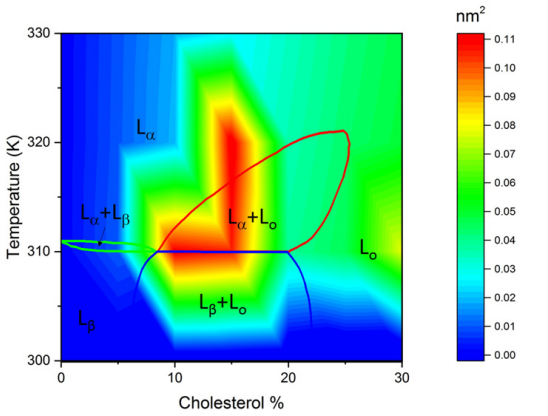

(b) Phase diagram of DPPC and cholesterol. Area color coded.

Figure 4: Phase diagram and molecular visualization of DPPC and cholesterol. Obtained by coarse-grained Molecular Dynamics simulation. Adapted from [18].

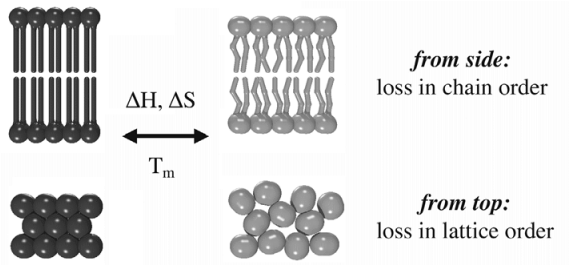

Figure 5: First order transitions in lipids cause loss in the order parameter. Firstly, the lateral lattice order is lost, secondly, the chain order is lost by overcoming the rotational barrier of the carbohydrate units. Adapted from [2].

Vesicles

Vesicles are liquid droplets immersed in a liquid, with an interface that consists of a lipid bilayer. This lipid bilayer is curved, which adds complexity to the system, as will be discussed more thoroughly in section 2.6.6. One vesicular feature of highest interest is the enclosure of an aqueous interior. This enables vesicles as carriers of nanomedicine, most prominently used recently in the COVID-19 mRNA vaccine by BioNTech-Pfizer and Moderna [19]. Further characterization reveals that the vesicle membrane is commonly unilamellar and the shape is mostly spherical, as depicted in figure 6.

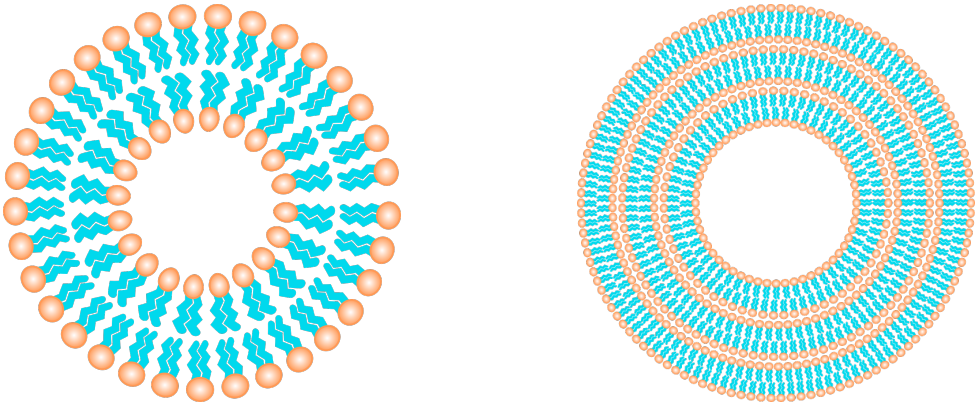

(a) Unilamellar vesicle (b) Multilamellar vesicle

Figure 6: Schematic cross section of lipid vesicles.

Unilamellar vesicles can be anywhere between tens of nanometers and centimeters of diameter. However, as artificial vesicles are a common model for cells, those are called Giant Unilamellar Vesicles (GUV) and will display similar sizes as cells at around 20 µm diameter. To model functional vesicles from organelles, Small Unilamellar Vesicles (SUV) are used and are around $\lesssim 100\,\text{nm}$ in diameter. For vesicles, a small membrane tension exists, which results from the difference of surface tension and surface pressure [20].

Besides vesicles, another model membrane is widely used in literature - the supported lipid membrane.

Supported Lipid Membranes

Supported lipid bilayers commonly consist of a hydrophilic substrate surface, which adheres to the lipid head groups of the membrane. The lipids can form a monolayer, usually achieved by the Langmuir-Blodgett deposition [21]. To achieve a bilayer, Langmuir-Blodgett is also suitable, as well as the vesicle fusion method. It is even possible to deposit an odd number of monolayer leaflets.

Supported lipid bilayers are versatile in their applications. They can be used as biosensors, as it is possible to embedd proteins and other molecules into the membrane. Luckily, many substrate materials are suitable to deposit a bilayer on like glass, mica, or silicon wafers. It is also possible to control the spacing of the lipids on the substrate by adjusting the lateral pressure of the film balance during deposition by Langmuir-Blodgett.

Supported lipid bilayers are convenient to investigate adhesion forces due to their immobility and compatibility with fluorescence and atomic force microscopy. At this point, it is necessary to look in-depth into the physics of lipid membranes.

2.3 Thermodynamics of Lipid Membranes

We continue our bottom-up approach and move from the historic overview of membrane models and the structure of lipids towards the physics of lipids. The physics of lipids starts with a model and continues to the study of the susceptibilities. We will focus on the impact of phase transitions on the observables and how to measure in an biologically relevant environment, which is fluid flow, like in our blood vessels. However, every physical theory needs a model system first.

A very simple but powerful thermodynamic model of a membrane is the two-state Ising model, extensively used in magnetism [22].

Two-State Ising model

In this model, on each lattice point there is a lipid molecule. The lipid molecule can be in one of two states, the gel-like state (A) or the fluid state (B). A possible configuration of a 3x3 lattice is illustrated in figure 7.

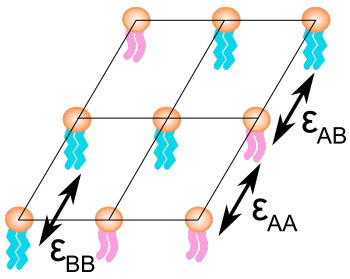

Figure 7: Ising model applied on lipids.

One major quantity in this model is the interaction energy ϵ.

- ϵ_{AA} interaction energy between two lipids, both in the gel-like state (A)
- ϵ_{BB} interaction energy between two lipids, both in the fluid state (B)
- ϵ_{AB} interaction energy between two lipids, each in the respective fluid and gel-like state

The interaction energy ϵ provides information about whether the mixture of these states is homogeneous or phase separated:

$$\epsilon = \frac{1}{2}(\epsilon_{\mathrm{AA}} + \epsilon_{\mathrm{BB}}) - \epsilon_{\mathrm{AB}} \tag{1}$$

For negative ϵ, a homogeneous mixture results. For positive ϵ, phase separation results. Although ϵ is just a simple scalar, it provides information on the whole system. More details can be revealed by a full simulation of the lattice kinetics, as illustrated in 4a and 4b. The interested reader should refer to in-depth literature [2, 23, 24]. Simulations are excellent tools to illustrate the dynamics of phase transitions. However, basic principles are easily studied by classical considerations, like the coupling of heat capacity with the other susceptibilities.

2.3.1 Coupling of Heat Capacity and other Susceptibilities

The simplest thermodynamic model is the ideal gas. Individual ideal gas particles have a mass, but no volume and do not interact. When ideal gases are heated, the gas particles are excited and the energy is stored as translational movement - in detail kinetic energy. No energy is stored in rotation or vibration, due to the lack of volume. The closest approximation for an ideal gas are monoatomic gases, like light noble gases or hydrogen.

The very next more elaborate thermodynamic model than the ideal gases is the real gas. Real gas particles have a mass, do have a volume, and do have an interaction potential. Therefore, when heated, energy can be stored not only in translational, but also in rotational and vibrational modes.

From an experimental point of view, it is interesting to study the susceptibilities of those gases, like heat capacity. Heat capacity is commonly measured using calorimetry. A calormetric measurement of an ideal gas will be constant ($c_p = c_p^0$), in fact, this is a very basic theoretical problem and has a well-known solution ($c_V = \frac{3}{2}R$). However, real gases display a more complicated heat capacity function, because of the interaction potential. In general, the heat capacity can be approximated by $c_p = c_p^0 + \Delta c_p$, where Δc_p is the excess heat capacity, as presented in figure 8.

In general, the function c_p^0 is not trivial for real gases. It is a result of the complexity of the interaction potential. In contrast, the excess heat capacity, Δc_p, for a real gas, is the result of the phase transition. Phase transitions are famously defined by Paul Ehrenfest: A phase transition between phases α and β is of order n, if

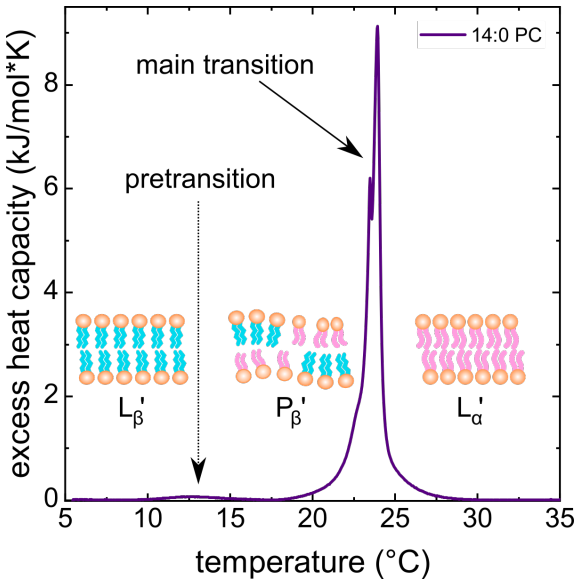

Figure 8: Excess heat capacity of DMPC.

$$\begin{aligned}(\frac{\partial^m G_\alpha}{\partial T^m})_p &= (\frac{\partial^m G_\beta}{\partial T^m})_p,\\ (\frac{\partial^m G_\alpha}{\partial p^m})_T &= (\frac{\partial^m G_\beta}{\partial p^m})_T,\end{aligned} \tag{2}$$

for $m = 1, 2, 3, ..., n-1$ and if

$$\begin{aligned}(\frac{\partial^n G_\alpha}{\partial T^n})_p &\neq (\frac{\partial^n G_\beta}{\partial T^n})_p,\\ (\frac{\partial^n G_\alpha}{\partial p^n})_T &\neq (\frac{\partial^n G_\beta}{\partial p^n})_T.\end{aligned} \tag{3}$$

- G Gibbs free energy
- p pressure
- T temperature

For an experimentalist, the major difference between first order phase transitions and second order phase transitions (and higher order) is the latent heat involved in the first order phase transitions. In second and higher order phase transitions, no latent heat is involved. Formally, the susceptibilities - heat capacity c_p, compressibility κ, and isobar thermal expansion α_p - are also defined as

$$
\begin{aligned}
c_p &= T(\frac{\partial S}{\partial T})_p = -T(\frac{\partial^2 G}{\partial T^2})_p, \\
\kappa_T &= -\frac{1}{V}(\frac{\partial V}{\partial p})_T = -\frac{1}{V}(\frac{\partial^2 G}{\partial p^2})_T, \\
\alpha &= \frac{1}{V}(\frac{\partial V}{\partial T}) = \frac{1}{V}(\frac{\partial^2 G}{\partial T \partial p})_T.
\end{aligned} \tag{4}
$$

Despite a major focus on calorimetry and heat capacity in this thesis, all other susceptibilities suit for analogous experiments as I am going to present. Such other experimental methods studying the other susceptibilities are densiometry and dilatometry.

Nevertheless, for studying heat capacity, the area under the excess heat capacity is of special interest - the enthalpy:

$$
\Delta H = \int_{T_0}^{T_1} \Delta c_p(T) \mathrm{d}T \tag{5}
$$

- T_0: onset temperature of lipid phase transition
- T_1: end temperature of lipid phase transition

While the enthalpy is an experimentally easily accessible quantity, entropy is not. Interestingly, the melting entropy of a phase transition is indeed easily accessible, if an approximation ($\frac{c_p}{T} \approx \frac{c_p}{T_\mathrm{m}}$) is met. This approximation is reasonable for sharp transitions, like in multilamellar vesicles. Therefore, especially in multilamellar vesicles, the melting entropy is

$$
\Delta S = \int_{T_0}^{T_1} \frac{c_p}{T} \mathrm{d}T \approx \frac{\Delta H}{T_\mathrm{m}}. \tag{6}
$$

To get a feeling for the numbers for the entropy of membrane melting, the enthalpy of DPPC is $\Delta H(\mathrm{DPPC}) \approx 38\,\frac{\mathrm{kJ}}{\mathrm{mol}}$, the melting temperature $T_\mathrm{m}(\mathrm{DPPC}) \approx 41\,^\circ\mathrm{C}$, the melting entropy is $\Delta S(\mathrm{DPPC}) \approx 121\,\frac{\mathrm{J}}{\mathrm{molK}}$. Systematic calorimetric studies have revealed, that the head groups contribute to the melting enthalpy, too. In fact, this contribution is negative (phosphocholine head group -51.78$\frac{\mathrm{kJ}}{\mathrm{mol}}$), whereas the contribution of the acyl-chains is positive and about 3.2 $\frac{\mathrm{kJ}}{\mathrm{mol}}$ per carbohydrate unit [2]. As the enthalpy can not become negative, there is a threshold acyl-chain length for a lipid molecule to exhibit a phase transition.

Equation 6 does not only provide an approximation on the melting entropy, but can also be rewritten to stress the dependency on experimental variables:

$$T_\mathrm{m} = \frac{\Delta H}{\Delta S} = \frac{\Delta U + p\Delta V}{\Delta S} \tag{7}$$

If the pressure changes by Δp, the enthalpy changes by $\Delta(\Delta H) = \Delta p \Delta H$, therefore

$$\Delta T_\mathrm{m} = \frac{\Delta(\Delta H)}{\Delta S} = \frac{\Delta V \Delta p T_\mathrm{m}}{\Delta H}. \tag{8}$$

Therefore, a change in pressure results in a shift of the phase transition temperature, according to equation 8. This is well-known from water boiling experiments on mountains. The dependency of the melting temperature on pressure has consequences on the chemical lipid composition of membranes, as membranes adapt to their environment.

Two cases of membrane composition adaptation are remarkable. The first example is from a vastly different community - food microbiology, which includes the study on fermentation, the process of wine making. Interestingly, wine yeast changes its membrane lipid composition as a response to cold stress [25]. The study has cultivated *Saccharomyces* species at low and optimal temperatures and found that in an adaptation process, the species change their lipid composition to improve their fermentation rate at low temperatures. In particular, in terms of adaptation, the most two prominent parameters change. At low temperatures, the degree of unsaturated lipids increase [26] and the acyl-chain length decreases [27]. It would be highly intriguing to spectroscopically measure wine yeast as a function of cultivation temperature using up-to-date optical methods, as will be shortly elaborated on in section 2.3.2.

The second example directly relates the membrane phase transition temperature to pressure. A pressure of $p = 1000 - 2000\,\mathrm{bar}$ shifts the phase transition temperature in biological membranes by about $\Delta T = 1\,\mathrm{K}$ [28]. In this thesis, we will conduct analogous experiments on the shift of the phase transition temperature as function of shear stress. But first, how exactly do we measure phase transitions?

2.3.2 Lipid Phase Transition Measurement Techniques

One of the standard techniques to study a lipid phase transition is via differential scanning calorimetry. It is a quantitative technique with information on the enthalpy and cooperativity. Furthermore, the resolution on the temperature axis is in the milli-Kelvin-regime. Unfortunately, the measured quantity is a scalar and therefore does not provide spatial resolution on the sample.

A good technique to overcome this disadvantage is Atomic Force Microscopy [29, 30], here you have spatial resolution down to the nanoscale. Furthermore it

provides the opportunity to probe the elastic constants of the sample, which are directly linked to the phase transition [24]. The challenge to overcome here is the sample preparation, to the best of my knowledge, the few publications, that exists, study artificial supported lipid bilayers. Though, this might seem as a promising technique - as natural supported lipid bilayers might be produced by osmotically swelling an adhered cell until it bursts and then measuring the immobile leftovers.

Atomic Force Microscopy is a very direct measurement, where the probe comes into contact with the specimen. At contact, the probe material alters the bilayers chemical potential. The chemical potential itself, more exactly the intersection point of the chemical potential of the gel phase and the fluid phase respectively, determines the phase transition along the observable. The direction in which the intersection point is shifted is dependent on the probing material [31]. Therefore, a more non-invasive, non-contact measurement technique is greatly appreciated.

One way to measure phase transitions optically is via fluorescent dyes like Laurdan [32]. This dye is "solvatochromatic" and therefore very sensitive on its coordination by water. The water-to-dye distance is dependent on the phase state of the lipid, as the surrounding water of a gel phase has different dipolar relaxation processes than the fluid phase [24]. The catch of this technique is that a probe molecule has to be inserted into the membrane in the sub-%mol range, which is expected to slighlty alter the phase transition itself towards a smaller and broader, less cooperative peak. This measurement technique is non-contact, but not non-invasive.

To measure non-invasively, the phase transition can be optically measured without inserting a probing dye molecule by infrared spectroscopy [33] or Raman spectroscopy [34]. Other common techniques are electron microscopy [35], where the spatial resolution is high, but cells have to be immobilized.

Langmuir film troughs [36] are used to measure phase transitions in a very versatile manner, as various other variables can be measured in parallel, like capacitance or colorimetric absorption. However, the film trough operates at an air-water interface, which is not a typical biological environment.

Interestingly, lipid phase transitions have been measured extensively in artificial membranes, but fewer in naturally occurring biological membranes. Some examples of the real biological membranes with phase transitions are trout liver [37], Mycoplasma laidlawii [38, 39], red blood cells [40], Escherichia coli [41], algae chara [42], and lung surfactant [43]. The interested reader might refer to literature [2, 44]. In one study, the authors made use of Laurdan to measure lipid chain order *in vitro* cells and vesicles upon shear stress, however, they have not exactly studied phase transitions.

2.3.3 Shear stress upon Cells and Vesicles

In 2013, Yamamoto and Ando published a paper, which measures the chain order in a vesicular model system, as well as *in vitro* cells upon shear stress [45]. Shear stress arises from spatial change in flow velocity of fluids. The most prominent flow of fluids take place in a pipe, which is a cylinder. Here, the velocity profile is parabolic [46]:

$$v(r) = 2\frac{\dot{V}}{R^2\pi}(1 - \frac{r^2}{R^2}) \tag{9}$$

- v velocity
- $\dot{V}$ volume flow
- r radial distance to the tube center
- R tube radius

In a microfluidic channel, the geometry is a quadrangle. In detail, due to technical imperfections, the geometry is possibly even a isosceles trapezoid. However, especially in the middle cross section, the approximation is exact. Further towards the corners, the approximation deviates quantitatively. Nevertheless, equation 9 still holds approximately for a rectangular channel and will be used further. The derivative of equation 9 results in

$$|\dot{\gamma}(r)| = 4\frac{\dot{V}}{R^4\pi}r. \tag{10}$$

where $\dot{\gamma}$ is the shear rate. In contrast to the flow profile in a cylinder, the flow profile in a viscosimeter is inherently different. For all experiments using a viscosimeter in a plate-cone geometry, the shear rate is:

$$\dot{\gamma} = \frac{v}{d} = \frac{2\pi U}{60\tan(\alpha)} \tag{11}$$

- U revolutions per minute
- α cone angle

For a viscosimeter using the plate-plate geometry, the shear rate is proportional to the radius:

$$\dot{\gamma} = \frac{2\pi r U}{60 d} \tag{12}$$

- d plate-plate distance

The shearing of a spherical object, where the interior is incompressible water, like in a vesicle, leads to a deformation D [47]. Deformation results in a elastic response of the membrane, which consequently increases surface tension. The shear profile is:

$$\dot{\gamma} = \frac{4\sigma_0 D}{5a\eta} \exp\left(\frac{64\pi\kappa}{15k_\mathrm{B}T} D^2\right) \tag{13}$$

And the deformation is:

$$D = \frac{L - B}{L + B} \tag{14}$$

- η viscosity
- κ dilatation modulus
- L major axis
- B minor axis

The experimental finding is depicted in figure 9.

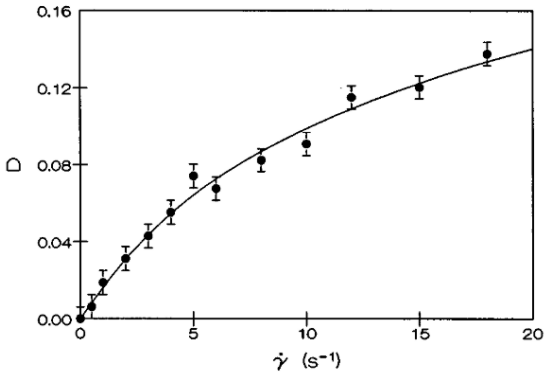

Figure 9: Taylor-Deformation as function of shear rate. Adapted from [47].

The rise in surface tension has been found to be [48]:

$$\frac{\sigma}{\sigma_0} = \exp\left(\frac{\delta A}{A_0} \frac{8\pi\kappa}{k_\mathrm{B}T}\right) \tag{15}$$

And the lateral pressure π is:

$$\pi = \sigma_0 - \sigma \tag{16}$$

- σ surface tension

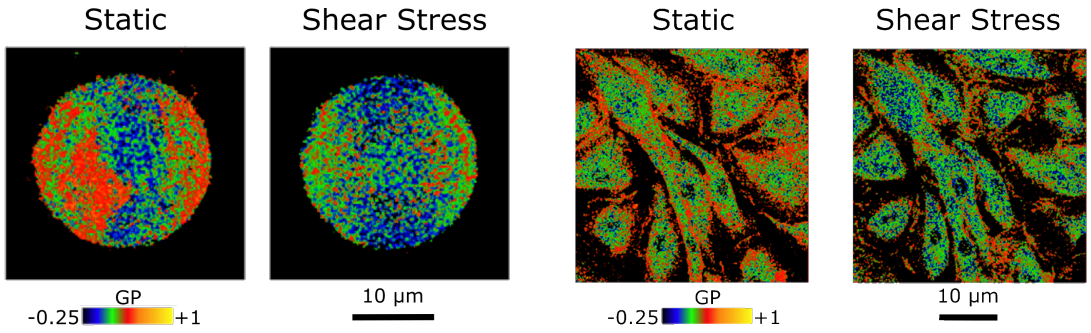

(a) Immobilized giant unilamellar vesicle.

(b) Adherent Human Pulmonary Artery Endothelial Cells (HPAEC).

Figure 10: Generalized Polarization of membranes under static conditions and shear stress. Adapted from [45].

Note, that a change in lateral pressure is tightly related to a change in phase transition temperature [49]. Therefore, the experiments and results of Yamamoto and Ando are intriguing. They use a method able to directly measure phase transitions and are likely aware of literature linking a change in lateral pressure to phase transitions, however the measured system and analysis did not include explicitly phase transitions. In the following, we will dive in-depth into their study. Yamamoto and Ando used endothelial cells stained with Laurdan and measured the chain order as Generalized Polarization (GP) under a confocal microscope. To control the shear forces, a controlled flow was exposed to the adherent cell layer.

Under static conditions, their pseudo color images show various GP values over the membrane. The physical interpretation leads to the coexistence of fluid and gel-like domains at the same time over the whole cell membrane. Accordingly, a phase transition regime at least at phase interfaces must exist, which underlines heterogeneity of the cell membrane including domains and rafts.

In detail, the same micrograph shows a less fluid membrane state at the periphery of the cell. Interestingly, using a staining method, they could identify an accumulation of caveolin in the cell periphery. Caveolin is a protein that forms caveolae, which are typically rich in cholesterol. When cholesterol was extracted chemically (via methyl-β-cyclodextrin, MβCD) or the expression of caveolin was eliminated by siRNA knockdown, high chain-order regions vanished almost completely. Cholesterol increases the chain order, but decreases the lateral lipid order [2].

When shear stress is applied, the whole cell membrane becomes more fluid, as shown in figure 10b. There is a quantitative difference though, the gel-like parts of the membrane become more fluid than the already fluid ones. Time resolved

measurements show that for a certain shear force, the fluidity saturates. However, the time resolved measurements are not long enough for the prior gel-like domains to saturate in fluidity. Also, the authors could not determine a saturation for prior gel-like domains for higher shear rates, as their maximum shear rate is 100 $\frac{\mathrm{mN}}{\mathrm{m}^2}$. These points remain open and intriguing for future studies.

The authors furthermore showed reversibility of the phenomenon. When the shear flow ceased, the fluidity recovered. However the kinetic is not long enough to show full recovery, but recovery does not saturate at the end either. As they repeatedly turn on and off shear forces, they observe fluidification during the shear forces and recovery, when shear forces are turned off. Nevertheless, future studies should revisit the question of complete reversibility.

Reference experiments were conducted by applying a hydrostatic pressure, but no flow. It is clearly visible, that the chain order is insensitive to the applied hydrostatic pressures. This seems in contradiction to previously mentioned literature, finding the phase transition temperature to be a function of hydrostatic pressure [28]. This contradiction resolves, as the total applied pressures varies drastically. In the study of Yamamoto and Ando, the applied pressure is orders of magnitudes smaller, which is legitimate, as they demonstrate the insensitivity of the GP to the present pressure conditions during the experiment. Similar to existing studies, using the setup of Yamamoto and Ando would be highly beneficial to study adaptability of the cells to the shear forces, as well as generally the application of shear forces in the long-term regime.

Other reference experiments were conducted on model membranes, as shown in figure 10a. They immobilized GUV (giant unilamellar vesicles) on the substrate, dyed them with Laurdan and measured the GP. They could observe again a heterogeneous membrane concerning the phase state distribution. This was attributed to the presence of cholesterol in the saturated-unsaturated lipid mixture of DPPC and DOPC, as it invokes phase separation [50].

When shear stress was applied, the GP shifted towards lower values all over the membrane, until the whole membrane became fluid. Surprisingly, the GP value stayed constant at fluid values even after cessation of the shear flow. The GP value did not show any recovery, unlike the cells. The authors did not go into further interpretations on this finding. However, applying basic physical principles, I deduct that no elastic restoring force is acting on the membrane phase state. This means the system was not in equilibrium, nor in an energetic minimum before the shear exposure, during the shear exposure, or after the shear exposure. Consequently, during the trajectory in phase space from the static starting point until the static end point where shear ceased, the free energy must have been approximately constant.

At this point, studying more lipid vesicle mixtures in this setup would be highly desirable to test my interpretation of the results. More precisely, experiments should include a mixture of lipids at certain environmental parameters close to a phase transition. Additionally, in our publication, we observe restoring of the original membrane state, which should be studied extensively and systematically in the future [51].

Nevertheless, in my opinion, the most important difference between the cells and the vesicles is the elastic restoration force of the GP value - representative for the phase state. An obvious difference is that the cells, being a non-equilibrium living system, make use of the elastic restoration force. It might be vital for them. Yet, this does not specify, whether the elastic restoration is purely a passive process, or an active process. In the latter case, the cells might be able to actively sense the membrane phase state and invest energy by a biochemical or biophysical mechanism to restore fluidity. A follow-up study on this topic would be intriguing.

Summarized, the suitability of this giant unilamellar vesicle as a model to the presented cells in figure 10b is questionable. Nevertheless, the authors conclude that the resemblance of the resulting change in fluidity at applied shear forces between the vesicles and the cells is striking. Therefore, this phenomenon does not have the necessity for biochemical reactions or membrane proteins and is purely physical. The authors argue extensively in a physical manner, they suspect effects arising from changes in thermodynamic quantities, like change in membrane composition, change in Ca^{2+} concentration, change in pH, change in temperature, and changes in membrane tension. However, they do not express the thermodynamic nature explicitly.

To dive deeper into the difference between real cells membranes and artificial membranes, we will now take a look into the main extra ingredient in cell membranes - proteins - in detail, enzymes.

2.4 Enzymes

Having layed out the historic overview of membrane models, the chemistry of lipids and the thermodynamics of lipid ensembles, we will continue by introducing a new kind of biological matter - enzymes - into the thermodynamics of membranes. As enzymes are not common in classical physics, we will study the structure of enzymes, their purpose as bio-catalysts and the quantitative measure of it. A very common case of enzymes are membrane-associated enzymes, which deviate in their behavior beyond a quantitative, even to a qualitative extent, which is a major pillar of this thesis. Lastly, this fundamentally different behavior of membrane-associated enzymes

from freely dissolved enzymes will be discussed with regards to the thermodynamics. I will present experiments how the thermodynamics of membranes govern enzyme activity.

It was Wilhelm Kühne in 1878, a German physiologist, who was the first to use the word 'enzyme' [52]. He studied yeast producing alcohol from sugars. Etymologically, the word is derived from the Greek words *en* ('within') and *zume* ('yeast'). However, enzymes reach much deeper into biology than producing alcohol. Enzymes are crucial and central to life. Metabolism in its form would not be possible without them.

A good example are proteins, which we take up in our nutrition. They must be decomposed in our digestive tract to be valuable to us. In theory, this is possible even without enzymes. However, to break just half the peptide bonds, it would take hundreds of years [53]. Enzymes easily accelerate such extremely slow chemical reactions by up to the gigahertz range [54]. The efficiency of enzymes depends strongly on environmental parameters like pH and temperature, which is central to this thesis. But first - what are Enzymes?

2.4.1 Enzyme Structure

Enzymes are a subgroup of proteins. Proteins consist of a sequence of covalently bound amino acids. The sequence can be hundreds of units long and consists of 21 different amino acids. Their exact order is called *primary structure* and is unique for every kind of protein. The peptide backbone is the same for every protein, as the linking unit of all amino acids is an amino (-NH_3^+) and a carboxylate (-CO_2^-) functional group. However, it is the side groups (R_n), that make up the unique properties in the amino acids, as depicted below. The primary structure is encoded into the genome, as it is a one dimensional information.

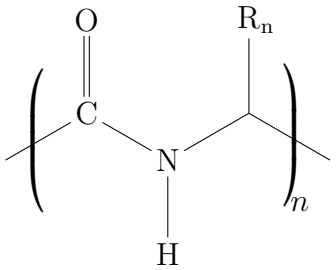

Peptide backbone

The *secondary structure* arises from interaction of side groups. Two major configurations result: the α-helix and the β-sheet. The α-helix is basically a spiral and results in a spring-like geometry, whereas the β-sheet folds like in a folding meter

stick. The boundaries of the meter stick interact and form tube-like geometries. Rarer secondary structures are β-turns and ω-loops.

When multiple *secondary structures* interact, but still share one backbone, a *tertiary structure* forms. Tertiary structures are highly three dimensional and the forming process of this is called protein folding. Protein folding is highly dependent on the environment like salt concentration, temperature, etc. Here, an energetic landscape has to be regarded, as different conformations have different energetic levels.

Equilibration into the energetic minimum levels is not trivial. As proteins are synthesized in ribosomes one amino acid by one, new energetically favorable transition configurations form constantly. Many of these transient transition states are dead ends and prevent a folding into a biologically functional protein. However, to prevent misfolding, folding helper molecules - *chaperones* - are often involved and bridge dead end foldings [55]. But even passive effects, e.g. crowding, influence the folding crucially [56].

For the folding process, interactions between sidegroups are crucial. The interactions can be estimated and categorized by the sidegroup polarity. The polarity ranges from charged to aromatic, as illustrated in figure 11a, depending on the aminoacid residue. Consequently, after folding and relaxation of the total interaction forces, the protein displays polar regions, spatially separated from apolar regions, as illustrated in figure 11b.

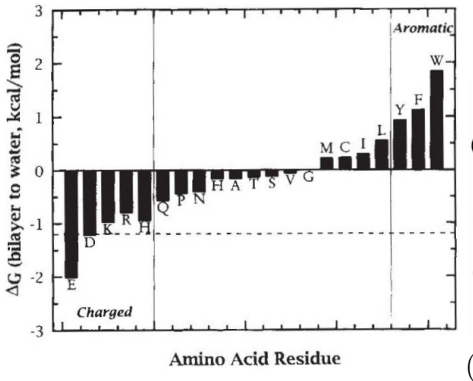

(a) Free energy to transfer a amino acid from an oil phase to an aqueous phase at neutral pH. Adapted from [57].

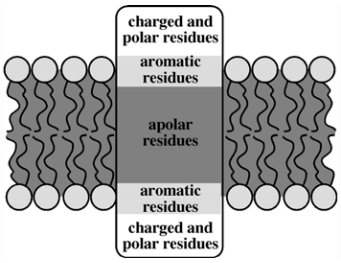

(b) Orientation of aminoacid residues respectively to a membrane. Adapted from [2].

Figure 11: Aminoacid residues sorted for polarity. Side group polarity interactions have a consequence on protein structure.

The resulting forces determine the interaction of the protein with the lipid membrane. Either, the protein adsorbs peripherically to the membrane, which is dominated by electrostatic forces. Or, the protein inserts into the membrane, where their hydrophobic body is in contact with the hydrophobic membrane core and their hydrophilic outerior is exposed to surrounding water. However, as proteins structure is a function of the environment, it is very common for proteins to rearrange in presence of any other substance, e.g. membranes.

There is another possibility, which is highly relevant to this thesis, where the resulting forces are in an equilibrium between different states and transition dynamically from one into the other. For example, this could be from a peripherical adsorption to a transmembrane insertion. Clearly, this kind of membrane proteins are highly sensitive towards any changes (like protonation or thickness) of the membrane. These protein forces can change, e.g. the aminoacid Histidin has a pK_a value around neutral pH and is therefore highly sensitive to the pH value, which changes the electrostatics drastically.

Finally, multiple tertiary structure monomers can interact and form *quarternary structures*.

Enzymes being a subgroup of proteins have a special feature which is fundamentally different from proteins in general. Enzymes are biocatalysts and follow the classical definition of a catalyst. Enzymes take part in a chemical reaction and are released in the end - enzymes are not consumed.

The huge advantage of catalysts in general is the reduction of the activation energy. Without a catalyst, the transition state is energetically very unfavorable. With a catalyst, other - energetically more favorable - transition states form. In detail, the catalyst forms transient bonds with the substrate, resulting in a substrate-enzyme complex.

Once the enzyme-substrate complex separates, the product is released and the original state of the enzyme is restored. This reaction cycle is referred to as *Turnover*. The rate at which the *Turnover* occurs is of special interest.

2.4.2 Enzymatic Activity

The activity of enzymes is a quantitative information on how many molecules are altered per unit time. Therefore, the SI unit is katal and kat = $\frac{\mathrm{mol}}{\mathrm{s}}$. A commonly used unit is U = $10^{-6}\frac{\mathrm{mol}}{\mathrm{s}}$. Enzymatic activity is highly non-constant and a function of environmental parameters: temperature, pH-value, substrate concentration and many other concentrations. For freely dissolved enzymes, the basic dependency of the activity on temperature is exponential until denaturation. In contrast, the

dependency on the pH-value is peak-like with an optimal pH-value. This is also the case for several other concentrations, like certain metal ions for specific enzymes [58]. The dependency on the substrate concentration is more complex.

Substrate Concentration

The activity is generally a function of the relative substrate concentration. This time dependent function is generally categorized into Michaelis-Menten kinetics and non-Michaelis-Menten kinetics. While the latter is dominated by interactive enzymatic reactions, where self-catalytic, allosteric or other kinds of enzymes are involved, the Michaelis-Menten kinetics describes the classic relation, which is the case for this thesis:

$$v = \frac{v_{\max}[S]}{K_{\mathrm{m}} + [S]} \tag{17}$$

- v enzymatic activity
- $v_{\max}$ maximum enzymatic activity
- K_{m} Michaelis-Menten-constant, which marks the substrate concentration, at which $v = \frac{1}{2} v_{\max}$
- $[S]$ substrate concentration

Basically, an analysis of the limits of the Michaelis-Menten-equation results in three regimes of enzymatic activity. The first is at relatively low substrate concentrations, where enzymatic activity is directly proportional to the substrate concentration. In this regime enzymatic activity is low.

The second regime is in excess substrate concentration, where the enzymatic activity is at maximum and constant. This regime is also referred to as the *steady-state*. As keeping the substrate concentration constant is experimentally challenging, all measurements in this thesis are done in the excess substrate regime at constant enzyme concentration.

The third regime is an intermediate regime between the previous two at intermediate substrate concentrations.

Note that the activity is linearly proportional to the enzyme concentration. However, if the substrate concentration is not kept constant and substrate is simply being consumed, the substrate concentration in equation 17 declines faster.

As exponential laws are counter-intuitive, literature uses Arrhenius-plots to linearize the activities.

Arrhenius Plots of Enzyme Activities

A standard procedure for activity measurements is to measure the activity at distinct temperatures. As collision theory models an exponential dependence of the activity as a function of temperature, an Arrhenius plot is a convenient way to present data. In an Arrhenius plot, the logarithm of the activity is plotted against the inverse temperature.

$$k = C \exp\left(- \frac{E_\mathrm{A}}{k_\mathrm{B} T} \right) \tag{18}$$

$$\ln k = \ln C - (\frac{E_\mathrm{A}}{k_\mathrm{B}}) \frac{1}{T} \tag{19}$$

- C collision frequency
- $\ln C$ y-intercept of the Arrhenius plot
- k reaction rate
- E_A empirical activation energy

Note that the activation energy is easily extractable from the slope, which is $\frac{E_\mathrm{A}}{k_\mathrm{B}}$. If the enzyme displays an Arrhenius behavior, a straight line on the Arrhenius plot will appear.

2.4.3 Membrane Associated Enzymes Deviate From Arrhenius Behavior

Certain membrane associated enzymes display kinks in the Arrhenius-plot, often referred to as bi- or ti-phasic Arrhenius plots. The molecular mechanism remains unclear [59]. However, there is a major difference to enzymes in organisms - enzymes are not freely dissolved in bulk liquids, but bound to surfaces and proteins. In fact, this is not the exception, but the rule, as the amount of free water in cells makes up only about 20% [60].

Various molecules have a high potency to bind water, like hyaluronic acid (HA), where $m(\mathrm{HA}) = 1\,\mathrm{g}$ can bind up to $V(\mathrm{H_2O}) = 6\,\mathrm{l}$ of water [61]. This also holds for lipids, where as a rule of thumb, 20-30 water molecules completely hydrate one uncharged lipid [2]. More water has no effect, as a separated, aqueous bulk phase forms. However, especially charged lipids require large quantities of water for hydration. Calorimentric measurements reveal concentrations down to $c = 1\,\mathrm{mM}$ phosphatdylglycerol bind all water in the system.

Therefore, surfaces are of highest importance for in cellulo processes and conditions. This is also true for enzymes: When bound to a cell surface – a membrane – many enzymes change their properties [62]. In the 1970's, many studies have found deviations from a pure Arrhenius-behavior for membrane associated enzymes. More precisely, they found discontinuities and kinks in the Arrhenius plots, indicating deviation from the exponential behavior. A short selection of enzymes, for which discontinuities and kinks were reported: (Na^+-K^+)-ATPase [63, 64, 65, 66, 67], Ca^{2+}-ATPase [68, 69, 70, 71], Cr_{55}-isoprenoid alcohol kinase [15, 59, 72], phospholipase [73, 74, 75, 76], acetylcholinesterase [77, 78, 79], and various other enzymes [80, 81, 82, 83, 84, 85, 86].

The cause of the kinks puzzled the community. Many theories have been proposed, tested, and discarded. One temporarily popular theory proposed a correlation of the enzyme activity and the phase transition of the lipid membrane. However, the data seemed to be inconsistent and more and more individual explanations and exemptions for each case arose.

Interestingly, a very similar course happened recently in fundamental enzymatic studies. However, the enzymes in this case were not membrane-associated, but freely dissolved. Nevertheless, many highly debated studies reported supra Brownian motion diffusion coefficients, going along with increased enzyme activity. This is very surprising, as diffusion limitation is a fundamental thermodynamic concept, putting a natural upper barrier for turnover rates [87]. At first, literature came up with explanations, which were enzyme- and reaction-specific mechanisms like conformation changes [88] or cross-diffusion [89], very similar to what was happening in the 1970's. Finally, in 2020, a careful study by Jee *et al.* has found a simple but powerful underlying general thermodynamic link for supra Brownian motion diffusion [90]. They studied a broad variety of enzymes, covering a large regime in turnover number and Gibb's free energy of the reactions. Their results supported the existence of supra Brownian motion, but only for exothermal reactions. From another point of view, this study finds that substrate availability regulates enzyme motility and therefore activity.

Ambiguities in the 1970's literature on membrane-associated enzymes based on experimental methods made it even harder to interpret the experimental findings. The sensitivity of enzymes to purification techniques is clearly visible by comparing the studies [91] and [92]. Astonishingly, both studies claim to measure the same - the activity of membrane-associated bacteriorhodopsin as function of temperature. The first study finds bacteriorhodopsin to be insensitive to the lipid phase transition - in contrast, the second study indeed finds a sensitivity to the lipid phase transition, labelled contemporary as a biphasic Arrhenius curve. This demonstrates clearly

differences in even qualitative results depending on the method. There is a clear need for more careful interpretation of results in the light of the applied methods.

It already has been reported, that enzymes can respond to different phases in the lipid. In general, it is not trivial that membrane bound enzymes display an activity when dissolved in lipid-free water. Literature reports such lipid 'co-factors', which are necessary for activity of certain enzymes. However, no strict specificity on polar head groups, bilayer structures, or other variables could be determined for enzymes needing lipid co-factors [59]. This finding eliminates the hypothesis, that the biochemical structure is crucial to the enzyme, very much including effects on enzyme conformation. It favors more general, thermodynamic influences on the system, such as the hydration shell of the lipid membrane.

Literature further reports one phenomenon, which is very familiar to the hypothesis of this work. The phenomenon is viscotropic regulation, introduced by Kimelberg and Papahadjopoulos [63, 64]. However, Sandermann reviews this as follows [59]:

> The term 'fluidity' is rather vague and only loosely defined. Associated physical parameters include spectral order parameters, relaxation times, partition coefficients of probe molecules, lateral or rotational diffusion coefficients, T_c values, and so on.

The authors do not identify those parameters as linked with one another due to thermodynamics. Sandermann continues [59]:

> These parameters differ greatly in their physical meanings, yet they have been used to establish a general correlation between lipid motional parameters and the functional properties of reconstituted enzymes.

This statement must be carefully analyzed, as the parameters have been shown to be linked. The first reported breaks in Arrhenius plots have been attributed to melting transitions. Further on, breaks were rather attributed to phase separations, also occurring near melting transitions.

> Discontinuous Arrhenius plots of microsomal and mitochondrial enzyme activities have been attributed to lipid thermal phase transitions [...], even though the Arrhenius 'breaks' were apparently not accompanied by calorimetric phase transitions [...]. [59]

This has to be elucidated further in future studies. Very recent publications observe something similar, appearing inconsistent. On the one hand, optical methods

detect a phase transition, on the other hand, calorimetry does not detect a phase transition [93]. The reason might involve cholesterol, which is well known to suppress structural phase transitions. HeLa membranes contain up to 49% cholesterol [94], this is probably the reason, why the excess heat capacity never exhibited a peak in our experiments. In contrast, endoplasmic reticulum membrane contains only about 5% cholesterol [95]. Nevertheless, publications from the 1970's demanded a change in the dogma.

Some studies, like from Enoch *et al.* [96] and Kumamoto *et al.* [81] aim further towards a new theory of catalysis. Enoch *et al.* start by observing the classic discontinuity in the enzyme activity, where they used 14:0 PC membrane and a certain amount of cytochrome b5. Once they increased the amount of enzyme, the kink disappeared. Consequently, they concluded that lateral diffusion became rate limiting.

However, when they slightly modified the systems components to test the robustness of their conclusion, they found that the discontinuity was caused by a change in the catalytic mechanism, as reviewed by Sanderman [59]. This is supported by Kumamoto *et al.* [81], who conclude that "[a] theory that employs the phase change can adequately accommodate all the data for temperature "breaks" in Arrhenius plots", [81]. Subsequently, they emphasize that the theory needs to be applicable to different membranes and enzymes. The authors state that the theory should be about the general field of catalysis, which is a bold criticism on the existing model.

As Cytochrome b5 is commercially available, I would strongly recommend to measure Cytochrom Reductase b5 in my experimental setup in future studies.

2.4.4 Intrinsic Thermodynamic Quantities Regulate Enzyme Activity

The studies in this field lost momentum and the community turned their attention to other topics. However, this unresolved issue has been picked up by Schneider and coworkers conducting analogous experiments on lipid monolayer associated enzymes. Fichtl investigated the activity of several lipid monolayer associated enzymes [97].

An intriguing example are the experiments on embedded horseradish peroxidase under an isothermal expansion of an 1,2-dipalmitoyl-sn-glycero-3-phospho-(1'-rac-glycerol) (DPPG) monolayer. He found a strikingly similar shape of the enzyme activity and the lipid monolayer compressibility. As elaborated before, compressibility is a susceptibility, as is the heat capacity. All susceptibilities are derivatives of the Gibb's free energy and are mutually coupled [24, 98, 99]. Additionally to his observation of the correlation, the correlation is valid even for variations of the lipid

type (DMPS), just as demanded by Enoch *et al.* The correlation was even conserved for variation of the pH value.

To address the second demand - a variation of the enzyme - Nuschele studied acetylcholinesterase embedded in a lipid monolayer. Even for acetylcholinesterase, very similar results have been found [100]. Summarizing, these results show that the enzyme activity depends on the phase state. This underlines the thermodynamic behavior of membrane associated enzymes and meets further the demands by Enoch *et al.* for an universal explanation of catalysis.

Dynamic Phase Changes Modulate Enzymatic Activity

Fichtl's and Nuschele's experiments beautifully show the independence of enzyme type, distinct pH value, and lipid type. However, they showed that, indeed, there is a dependence on the phase transition, which emphasizes the physical nature and thermodynamic behavior of the membrane associated enzyme activity.

Until now, we have regarded only quasi-static systems in a monolayer. However, these principles hold also for dynamical systems. Dynamical systems are of highest interest for the nerve signaling theory, as the action potential is a propagating pulse phenomenon. Therefore, Fichtl *et al.* applied pH-pulses to DMPS monolayers and measured the activity of embedded acetylcholine esterase to demonstrate the applicability for dynamic changes of the phase state [97]. A propagating pH-pulse can evoke a propagating, local phase transition. When the pulse front is spatially far away from the monolayer associated enzyme, its activity remains indifferent and constant. Once the pulse reaches the enzyme's environment, the activity can be enhanced by more than an order of magnitude.

This study is part of a series of publications establishing a new thermodynamic nerve signalling theory - the soliton model [101] - where the action potential is described by an acoustic-like wave propagating laterally on the membrane. Once the membrane is interrupted by an synaptic cleft, the action potential has to be transformed into a biochemical signal, which heavily involves neurotransmitters and enzymes. The signal transformation requires a trigger- and detector, to which phase state sensitive membrane associated enzymes might be suited for [102]. Ergo, it would be of highest interest if the demonstrated phenomena also hold for bilayer associated enzymes, which I will present experiments on.

Yet - why is an interaction of the membrane associated enzyme activity with the membranes heat capacity expected?

2.4.5 Activity of Membrane Associated Enzymes Becomes a Susceptibility of the Ensemble

The underlying theory has been originally published by Kaufmann [103]. The interested reader might struggle with accessibility of the literature, however, parts have been picked up, elaborated on, and published online elsewhere [2, 104, 105, 106].

In his theory, Kaufmann considers the state of the interface between the enzyme and its surrounding. He then applies Einstein's ansatz to the enzymes interface [107]. When Kaufmann considers the state of the interface, the enzyme is part of the lipid membrane. This is legitimate, as the lipid membrane and the enzyme share one continuous surface of bound water. It is important to realize that the bound surface water is relatively decoupled from the bulk water due to the impedance mismatch [108]. In contrast, the lateral coupling of the bound surface water is strong. This decoupling results in an own thermodynamic potential of the mutual water interface, according to Einstein [109].

The entropy potential can be approximated by a Taylor series to:

$$S(n_i) = S_0 + \Sigma_i \frac{\partial S}{\partial n_i}\delta n_i + \frac{1}{2}\Sigma_i\Sigma_j \frac{\partial^2 S}{\partial n_i \partial n_j}\delta n_i \delta n_j + ... \tag{20}$$

- n_i, n_j thermodynamic variable
- S_0 entropy at equilibrium

The first derivatives $\frac{\partial S}{\partial n_i}$ equal the thermodynamic forces, driving the system back to equilibrium. The second derivatives $\frac{\partial^2 S}{\partial n_i \partial n_j}$ equal the susceptibilities. Fluctuations in the thermodynamic variables are coupled, as elaborated on before [24, 98]. Such fluctuations occur in enthalpy, area per lipid molecule, charge, and also membrane thickness.

At this point, it is important to stress that various microscopic mechanisms exist, which are associated to fluctuations. However, those mechanisms have been found independent from the underlying thermodynamic theory and have been published accordingly. Such mechanisms can very much involve e.g. out of plane membrane fluctuations [110], which, according to the thermodynamic theory, might be one special-case-mechanism, contributing to the total increased activity.

However, the goal of this theory is not to find all specific micromolecular mechanisms, but to set a framework or set of all possible mechanisms contributing. As all those unknown micromolecular mechanisms are included in this statistical approach of an entropy potential of the interface - thus, out of plane membrane fluctuations

[110] are a special case. Nevertheless, out of plane fluctuations are proportional to the heat capacity and other susceptibilities.

The reason why fluctuations are proportional to the fluctuation relies in the *fluctuation theorem*, which is the result of inserting the mean enthalpy results into equation 6:

$$c_{\mathrm{p}} = \frac{\mathrm{d}\langle H\rangle}{\mathrm{d}T} = \frac{\langle H^2\rangle - \langle H\rangle^2}{RT^2} \tag{21}$$

The *fluctuation theorem* is closely related to fluctuation dissipation theorem [111]. Analogously,

$$\kappa_T^V = \frac{-1}{\langle V\rangle}\left(\frac{\mathrm{d}\langle V\rangle}{\mathrm{d}p}\right)_T \tag{22}$$

and

$$\kappa_T^A = \frac{-1}{\langle A\rangle}\left(\frac{\mathrm{d}\langle A\rangle}{\mathrm{d}\Pi}\right)_T \tag{23}$$

$$\kappa_T^A = \frac{\langle A^2\rangle - \langle A\rangle^2}{\langle A\rangle RT^2}. \tag{24}$$

The explicit experimental prediction from this theory is, if the heat capacity of the system exhibits a peak, the membrane associated enzyme activity - being a coupled susceptibility - will as well display a peak during the phase transition [104, 106, 108]. They are related through Maxwell's relations [98]:

$$\Delta c_p \propto \Delta\kappa_{\mathrm{T}} \propto \Delta\alpha_\pi \propto \Delta c_\pi \propto \Delta C_T, \tag{25}$$

where C_T is the isothermal capacitance.

To emphasize, Konrad Kaufmann adds the enzyme activity α into this proportionality [112]. Testing the experimental prediction and therefore this proportionality $\Delta c_p \propto \alpha$ experimentally is one of the major purposes of this thesis.

In the light of this theory, many inconsistencies in experimental findings resolve. For example, some studies suggest that an 'annulus' of 30 surrounding phospholipids determine the activity of the sarcoplasmic Ca^{2+}-ATPase [68]. Newer studies found, that most of the annulus is replaceable by a neutral detergent [113]. Once again, this lessens the importance of exact chemistry and stresses the role of net thermodynamic effect.

Therefore, we designed an experiment to further elucidate the correlation of the membrane associated enzyme activity and the excess heat capacity along the

same lines as summarized above. In major contrast to existing literature, we chose particularly a water-soluble enzyme, which is by its nature not associated in any way to a lipid membrane. The lack of evolutionary bias makes this enzyme an excellent choice to investigate the correlation of membrane phase transitions and enzyme activity.

In particular, I quantify the activity of "a disintegrin and metalloproteinase with a thrombospondin type 1 motif, member 13" (ADAMTS13) in absence and presence of lipid vesicles as a function of temperature. In this temperature range, the lipid vesicles are at different phase states, which I quantify by calorimetric measurements. Additionally, I vary the phase state isothermally by using 13:0 PC, 14:0 PC, and 15:0 PC. For this, I measure the activity of ADAMTS13 in parallel at 24 °C, where 13:0 PC is in the L_α phase, 15:0 PC in the $L_{\beta'}$ phase, and 14:0 PC at the phase transition. Finally, I discuss the observed correlation in the context of Kaufmann's theory of catalysis and describe the contribution to the new model of nerve pulse propagation.

2.5 Nerve Pulse Propagation

After the historic overview of membrane models, as well as the chemistry of lipids, the physics of lipid ensembles, and its impact on membrane-associated enzymes, we will dive into the biological applications. The first biological application is a thermodynamic model on the nerve pulse propagation, a generalization of the model by Hodgkin and Huxley.

In order to sense, a stimulus has to be transmitted from the surface of our body to the brain. The signal can be detected by electrodes - therefore it contains an electrical component and is at least partially a voltage pulse, also called action potential. The action potential propagates along nerve cells, of which the regions relevant to the propagation are called axons and dendrites. Axons and dendrites can be layered in myelin, which enhances the propagation velocity by 2 orders of magnitude.

The Hodgkin-Huxley model claims the action potential to be purely electric. The voltage pulse arises from a temporary and spatially restricted permeability towards ions. The asymmetric ion concentration from the resting state breaks down at this local, transient ion-assisted permeabilization. However, the local, transient ion permeabilization propagates along the axon or dendrite, embodying the action potential. In this model, ion channels cause this local, transient ion permeabilization. Ion channels are switchable and display complicated regulation concerning their openings and closings.

The regulation of the openings and closings is important. Until today, the Hodgkin-Huxley-model has been extended concerning the regulation. Originally, the openings and closings were governed by a threshold voltage. Various specifics have been added ever since, like mechano-sensitive ion channels, temperature-sensitive ion channels [114], cold- and methanol-sensing ion channels [115], acid-sensing (pH) ion channels, lipid-sensing ion channels [116], enzyme-sensing ion channel [117], and so on.

The scientific community of ion channels studies their specificity and molecular mechanisms and even biomimicking them [118, 119]. In this model, it is crucial to assume the membrane being an ideal insulator with a constant capacitance. This allows to come up with an equivalent circuit, which is presented in figure 12.

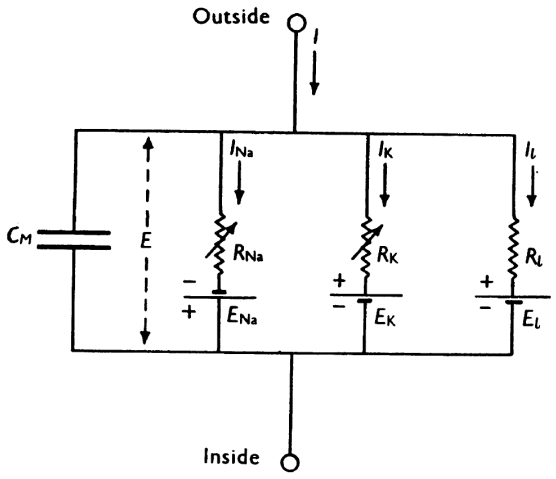

Figure 12: Equivalent circuit of a membrane. Adapted from [120].

Hodgking and Huxley were awarded with the Nobel prize in 1963 for their model. However, many publications raise concerns about major contradictions of this model. In fact, Hodgkin and Huxley were very careful on the wording in their original publication [120]:

> The agreement must not be taken as evidence that our equations are anything more than an empirical description of the time-course of the changes in permeability to sodium and potassium.

Furthermore, if nerves are to be described as electrical cables with an intrinsic resistance, heat dissipation is expected. However, measurement data has found that there is practically no net heat release. To be more precise, heat is indeed firstly released, but reabsorbed in the same quantity. This is possible, because the time to transport heat away is longer than the release and absorption process [121]. A similar

concept has been reported in 2020 from a independent group in an independent scientific field for the diffusivity of enzymes [90].

In this study, the authors report supra Brownian motion diffusion of enzymes. They claim, that during the catalysis event, the released heat induces random thermal reorientation and translocation and thus increases diffusion. However, viscous drag forces from the environment dissipate the motional energy, resulting in a negative feedback.

To be clear, the authors state, that their theory is different from textbook knowledge. Implicitly, they propose two time constants: A long time constant, where the produced heat is scattered into the whole system and the temperature rises globally, which is in agreement with textbook knowledge. However, on a short time constant, the heat is confined locally, consumed by the enzyme and converted into motional energy, which is contrary to textbook knowledge. To the best of my knowledge, this thesis is the first to claim resemblance of those both concepts.

Heat being absorbed via two mechanisms with two time constants is key to the soliton model [101]. In the soliton model, the propagating action potential accompanied by a phase transition of a lipid membrane releases latent heat into the environment. The thermal conductivity of the environment is relatively low, so the heat is at short time scales spatially confined. As the action potential propagates, the phase transition is reversed and the locally confined heat is consumed, resulting in an adiabatic process.

Experimental hints towards the incompleteness of the Hodgkin-Huxley model can be found while studying the energetics of the action potential. A process without any net heat release is an isentropic process. Isentropic processes are reversible. Tasaki also measured mechanic dislocation in the vicinity of a nerve fiber and found it to be in phase with the action potential [122].

However the direct contradiction arises at the capacitance of the equivalent electric circuit. The capacitor plates are the opposing polar head group planes of the bilayer. Capacity is defined as $C = \epsilon\epsilon_0 \frac{A}{d}$ and the distance d is equivalent to the membrane thickness. As Tasaki found a dislocation of d during an action potential, the change in capacitance over time is not zero, as the change in distance over time is not zero $\frac{\mathrm{d}d}{\mathrm{d}t} > 0$ and therefore $\frac{\mathrm{d}C}{\mathrm{d}t} > 0$. This is in direct contradiction to the Hodgkin-Huxley model, where $\frac{\mathrm{d}C}{\mathrm{d}t} = 0$ is assumed. Also, a change in volume, area, and membrane thickness are well known observations for melting transitions. These contradictions have been addressed recently by Kotthaus in 2019, who proposes even another mechanism, a mechatronical mechanism of nerve signaling [123].

Optical measurements including fluorescence anisotropy measurements indicate a phase transition during an action potential. A shift of ambient conditions closer

towards the systems phase transition temperature facilitates triggering an action potential. In contrast, a shift of ambient conditions further away from the systems phase transition temperature, impedes triggering of an action potential [124]. The shift in ambient conditions could be realized by heating or cooling of the system. The interested reader on this subject might refer to literature for a thorough discussion on the inconsistencies of the Hodgkin-Huxley model [2, 97, 101, 102, 108, 125, 126, 127, 128].

To account for these contradiction, a new nerve signaling model has been proposed, the soliton model [101]. This model postulates that a perturbation of the thermodynamic state of the membrane propagates laterally along the membrane. A very good model for demonstration of this concept are lipid monolayers on Langmuir troughs. Many forms of perturbations have been published to propagate along the monolayer and to be accompanied by a local phase transition, such as pH-pulses [102], mechanic pulses [129], and even temperature pulses [124]. Recently, even perturbations on a bilayer have been reported [130].

These models treat the propagation on a single nerve cell. However, the transmission path to the brain generally consists of many nerve cells. Two nerve cells are separated by the synaptic cleft, where the action potential cannot simply translocate into the next nerve cell. Therefore, in the current consensus, the action potential (electrical signal) releases neurotransmitters (chemical signal) at the presynaptic membrane, which diffuse to the postsynaptic membrane, where they trigger a new action potential (electrical signal). The trigger event is mediated by receptor molecules, which form a complex with the neurotransmitters. To free the receptor in order to restore excitability, enzymes hydrolyze the substrate - the neurotransmitters.

However, earlier reports suggested that the hydrolysis products, more precisely the protons, might trigger the new action potential [131]. This is called cholinergic transmission. The interested reader might also consider [132].

2.5.1 Cholinergic Transmission

The major debate concerns the role of acetylcholinesterase in the signal translocation mechanism. In the currently accepted model, acetylcholinesterase frees the receptor, to which acetocholine binds, by hydrolysis. Following a suggestion by Wurzel [131], the acetylcholinesterase hydrolyzes the acetylcholine before reaching any receptor and produces charged choline. According to Wurzel, the charged choline is the cause of excitation and creation of an action potential. According to Kaufmann, the other hydrolysis product - the proton - is the cause of excitation and creation of an action potential [133].

In Kaufmann's model, the protons do not dissociate into the bulk, but get buffered by the negative charges in the membrane, where the acetylcholinesterase is embedded. This proton-buffering significantly changes the electrostatics of the membrane and therefore changes the phase state. One type of molecule, which severely influences the phase state of the membrane, is an anesthetic. The potency of an anesthetic is quantitatively described by the Mayer-Overton rule.

2.5.2 The Mayer-Overton Rule

The potency of anesthetics could be excellently estimated by studying the anesthetics partition coefficient between water and (originally olive) oil:

$$\frac{[C_{\mathrm{H_2O}}]}{[C_{\mathrm{membrane}}]} = P^{-1} \propto \mathrm{ED}_{50} \tag{26}$$

- $[C_{\mathrm{H_2O}}]$ solubility of the substance in water
- $[C_{\mathrm{membrane}}]$ solubility of the substance in oil
- P^{-1} partition coefficient
- ED_{50} median effective dose

The Mayer-Overton-rule is valid for about six orders of magnitude, highly stressing the physical nature of this phenomenon and independence from the molecular chemistry. To be clear, Overtons physical understanding of this proportionality is reduced to the ability of a molecule to dissolve into the membrane of a cell. Any molecule, which dissolves into olive oil, has an anesthetic effect. If the solubility is high enough, the molecule appears to us as an anesthetic. Accordingly, the only reason why different drugs have different ED_{50} is they have a different solubility in oil (partition coefficient). In other words, for the anesthetic effect, it is necessary to exceed a threshold number of molecules inserted into a membrane - per area membrane.

From a thermodynamic point of view, an anesthetic is an impurity. Interestingly, impurities cause a freezing point depression, which is linearly proportional to the molar fraction of the impurity x.

$$\Delta T_{\mathrm{m}} = (\frac{RT_{\mathrm{m}}^2}{\Delta H})x \tag{27}$$

But not only anesthetics have an effect on the phase transition temperature. It is well-known that proteins change the shape of the heat capacity profile, as the interaction energy ϵ_{PA} & ϵ_{PB} (between a protein and the lipid in the respective phase

state A or B, where A is favorable at small temperatures) is generally different. Qualitatively, it holds:

- $\epsilon_{\mathrm{PA}} = \epsilon_{\mathrm{PB}}$ broadening of the peak [23]
- $\epsilon_{\mathrm{PA}} = \epsilon_{\mathrm{PB}} \ll \epsilon_{\mathrm{lipids}}$ small broadening of the peak [23]
- $\epsilon_{\mathrm{PA}} < \epsilon_{\mathrm{PB}}$ heat capacity peak is shifted towards lower temperatures, higher protein miscibility in the fluid phase [134]
- $\epsilon_{\mathrm{PA}} > \epsilon_{\mathrm{PB}}$ heat capacity peak is shifted towards higher temperatures, higher protein miscibility in the gel-like phase [135]

Quantitatively, the shift in membrane phase transition temperature has been calculated [136]. The authors found that an anesthetic concentration of ED_{50} lowers the melting temperature by $\Delta T_{\mathrm{m}} = 0.5\,\mathrm{K}$. This value should be kept in mind for the experimental results of the permeability studies.

2.6 Membrane Permeability

Until now, the first biological applications is the thermodynamic nerve pulse propagation theory, which relies on a phase transition propagating along the membrane. The next biological application relies on phase transitions as well. During phase transitions, the permeability of a membrane spikes. To understand this phenomenon, we will study the membrane permeabilization mechanism, existing permeabilization techniques, and the ansatz in this thesis for a new permeabilization technique using acoustofluidics. We will use acoustofluidic permeabilization to develop a drug delivery tool for living cells. Finally, we will gear up to nanoparticle-mediated permeability on lipid membranes. As a start, I would like to provide an introduction to the paradigm of cell membrane permeability.

2.6.1 Membrane Permeability Based on Born's Continuum Model

A biological membrane has various functions. One obvious function is being a passive barrier for internals of the organism, ranging from cell organelles, to DNA, RNA, and ions like Na^+. In contrast, the cell membrane has to be permeable to various kinds of nutrients. These requirements seem to contradict at first, but is reality for biology. However, the textbook view on this topic is represented best by a quote from the lecture notes of a Spring School I visited in 2018 [137]:

> "The impermeability of the lipid bilayer for charged molecules makes it a perfect electrical insulator."

The authors argued with Born's continuum model [138] and found:

$$W = \frac{Q^2}{8\pi\epsilon_0 r}\left(\frac{1}{\epsilon_{\text{Lipid}}} - \frac{1}{\epsilon_{\text{Water}}}\right) = 174\,\frac{\text{kJ}}{\text{mol}} \tag{28}$$

- Q charge
- ϵ_{Water} permittivity water $\epsilon_{\text{Water}} \approx 80$
- ϵ_{Lipid} permittivity lipid acyl chains $\epsilon_{\text{Lipid}} \approx 2$
- ϵ_0 permittivity vacuum

Which was a too high energetic barrier to be biologically reasonable, as the lipid bilayer became permeable at $V_{\text{mem}} = 2\,\text{V}$.

Summarized, the textbook view represents the membrane as an insulator, a passive barrier, which has biochemical mechanisms to allow for selective transmembrane

transport. In this textbook view, proteins like aquaporins permit water to permeate the membrane by forming pores in the cell membrane. Electrostatic forces inside the pore enable the selectivity for water. This concept is analogous for ion channels and pumps, which are ATP-driven.

2.6.2 Membrane Permeability Mechanisms

The following permeation mechanisms are known:

- Transmembrane diffusion
- Pores
- Pore-forming proteins
- Endocytosis

The first mechanism, transmembrane diffusion, is largely neglected for ions based on Born's continuum model. This model might be appropriate - in cases where the assumptions are fulfilled and no phase transition is involved.

The first findings of the importance of phase transitions in permeability have been done in 1973 [139]. The authors find a peculiarity, which can easily be missed. Exemplary, for artificial DPPC membranes, ^{22}Na permeation peaks at the phase transition temperature [2]. Therefore, variation of phase state must be a control measurement when studying permeability, as suggested by Schneider [108].

A quantitative model has been established later on [140], connecting permeability and lateral compressibility κ_T^A. This model regards how much tension it takes to induce a defect, similarly to pumping a balloon, until it pops:

$$P = C_0 + C_1 \kappa_T^A \tag{29}$$

- P permeability
- C_0 $C_{0,1,...}$ constants

As susceptibilities are coupled [98, 99], κ_T^A is [141]:

$$\kappa_T^A = \kappa_{T,0}^A + \frac{\gamma_A^2 T}{A_0} \Delta c_p \tag{30}$$

This can be used in equation 30, resulting in [140]

$$P = C_2 + C_3 \Delta c_p. \tag{31}$$

This model indeed predicts a maximum permeation at the melting transition. Pure diffusion through the membrane as a permeation mechanism is insufficient to explain a peak in permeation at the phase transition. Meanwhile, plenty of studies have been conducted on energetics of membrane pores [142, 143]. On the single pore level, Blicher *et al.* [141] and Wunderlich *et al.* [125] have calculated the amount of work needed to form a pore:

$$\Delta W(a) = \frac{1}{2\kappa_T^A}(\frac{a}{A_0})^2 A_0 \tag{32}$$

In this equation, the pore forming energy is inversely proportional to the isothermal compressibility. Therefore, once the isothermal compressibility peaks at the melting transition, the pore forming energy breaks down. Consequently, also on the single pore level in a simple model system, the pore forming energy breaks down at the phase transition. This simple model system only requires one type of lipids, therefore, the resulting concept of spontaneous pore formation is very fundamental. However, this does not yet take effects into account, which arise from more complex systems, like accumulation of proteins.

To elaborate on pores, further microscopic and theoretical studies characterize pores into two categories, hydrophobic pores and hydrophilic pores. The difference is at the rim. Acyl-chains of hydrophobic pores are in contact with water at the rim, whereas in hydrophilic pores lipids rearrange such that the acyl chains are protected from water, as presented in figure 13a.

Hydrophobic pores are energetically unfavorable and collapse fast. Once the pore overcomes a critical radius of about $r \approx 0.5\,\text{nm}$, hydrophilic pores are meta-stable at $r \approx 0.8\,\text{nm}$ under certain conditions. Any type of disturbance, like mechanical stress or electrical fields, change the pore energy landscape, as presented in figure 13b. For moderate disturbances, this might very well facilitate forming pores. However, for extremer conditions, pore-forming leads to a burst of the cell or vesicle, just like in the pumping-the-balloon comparison.

Another mechanism to form pores is by protein-mediation. Proteins are known to form pores in membranes. Examples are alamethicin, melittin, and margainin. The pore sizes can be up to the magnitude of 100 nm. Oliynyk *et al.* visualized this via atomic force microscopy in the tapping mode, revealing a high softness in the vicinity of the pore rim, where the peptide is located [144]. This finding is very interesting, as softness is equivalent to a high compressibility, which in turn represents the membrane state. To be clear, a high compressibility is associated with a phase transition.

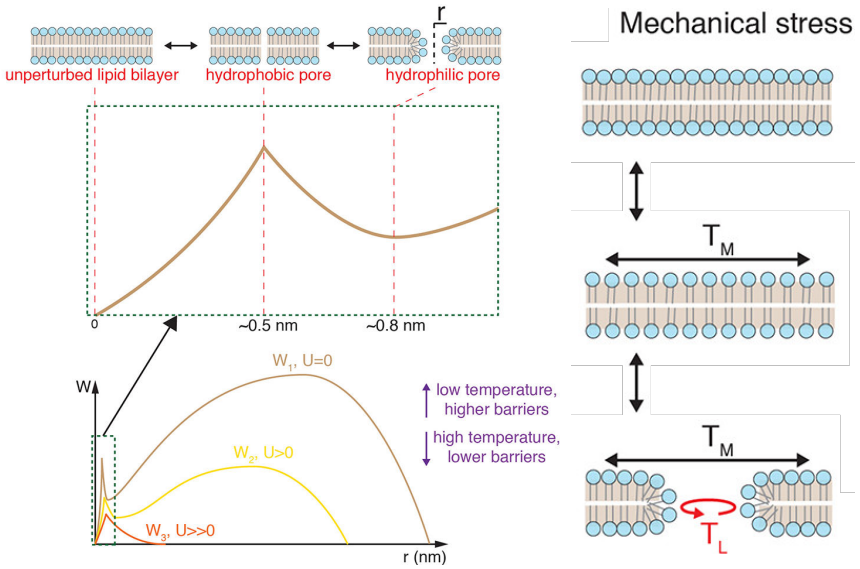

(a) Pore formation as function of radius. (b) Various forces achieve Permeabilization.

Figure 13: The energy landscape of pore formation is highly dependent on thermodynamic quantities, like temperature. Adapted from [95].

The formations of pores can be mediated by many techniques. In the following, we will take a in-depth look into permeabilization techniques.

2.6.3 Permeabilization Techniques

Intracellular delivery is a major mutual challenge for various applications, like cell-based therapies, gene editing, induction of pluripotent stem cells, intracellular probing, and many more. An excellent and extensive review has been done by Stewart *et al.* [95]. The following paragraphs provide a brief summary.

The two main strategies of drug intracellular loading are either membrane non-disruptive or membrane disruptive. Membrane non-disruptive techniques tend to be of biochemical nature and include vectors, vehicles, nanocarriers, detergents, and other delivery particles. These methods are rather elaborate and require detailed knowledge about the molecular targets. Therefore, they do not offer a general solution for cell-based screening of agent libraries. Membrane disruptive techniques tend to be of physical nature and include electroporation, optoporation, micro-injection, and shear mediated permeabilization, presented in figure 14. Physical concepts are mostly carrier-free.

An interesting feature of the novel permeabilization techniques presented in this thesis is that it is a combination of several techniques in their pure form. Firstly,

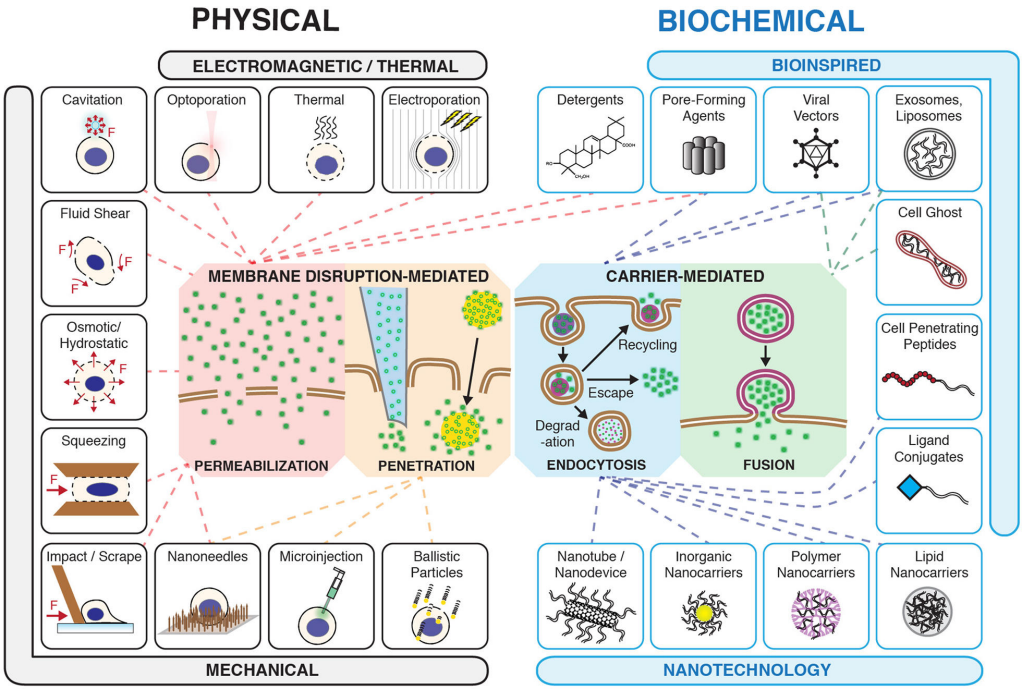

Figure 14: Detailed overview of the permeabilization techniques. Adapted from [95].

a common permeabilization technique is Electroporation [145]. The electrical field induces a transmembrane potential, which exerts electrostatic forces on ions. These might create defects, which facilitates a transient pore formation [146]. A major challenge of electroporation is the post-treatment cell death.

Secondly, a very intuitive method for permeabilization is the ultrasonic treatment. For example, sonoporation methods expose the cells to ultrasound in the range of $f = 20\,\text{kHz} - 10\,\text{MHz}$. Various applications utilize sonoporation, like for clot lysis in blood vessels, stimulation of bone fracture healing, and tumor treatment [147]. In the context of drug delivery, sonoporation facilitates pores in the plasma membrane by microfluidic cavitation and implosion [148]. However, cavitations are usually scarce in fluids, therefore the efficiency is low. To overcome this, ultrasonic contrast agents can be added, for example microbubbles [149, 150]. Promising, new contrast-agent-free sonoporation methods even achieve a high throughput at a high cell viability [151].

Thirdly, a treatment involving microfluidics is fluid-mechanical treatment. These techniques utilize flow-induced shear forces to form pores. In detail, flow can cause buckling instabilities in the lipid bilayer and facilitate pore-opening [152]. Microfluidic channels offer a classic parabolic velocity profile and therefore a linear shear profile. In contrast, an even simpler shear profile - a constant shear rate - is commonly realized in shearing disc viscosimeters using the plate-cone-geometry. This technique

is used in this thesis as well, along with the plate-plate geometry. A viscosimeter offers the most defined shear profile and is known to enhance cell permeabilization [153]. All these fluid-mechanical approaches come with low Reynolds numbers, which indicate a highly laminar flow.

Outside of the highly laminar regime, further fluid-mechanical techniques exist. Interestingly, one technique presented by Ramesan *et al.* [154, 155] originates from solid state physics and RF-engineering. The authors use surface acoustic waves (SAW) to generate oscillating acoustic pressure on the cells. In their setup, the adherent cells are not directly exposed to surface acoustic waves. In between is a couplant fluid and a well plate with glass bottom. A major drawback of this method is the strong cell number limitation, due to the geometric limitations of the interdigital transducer and the leakiness of surface acoustic waves in liquid environments. Ramesan *et al.* did not report acoustofluidic streaming in the experiments, although using parameters, which are known to induce acoustic streaming, especially at these high powers [156, 157, 158].

In the approach presented in [159], we combine laminar flow in a microfluidic channel with chaotic advection employing SAW. Chaotic advection traps suspended cells within a continuous fluid stream in the microchannel to overcome the drawbacks of the previous concepts. Major advantages of this method are precise spatial and temporal control of the applied SAW in the microfluidic framework. The exact setup is presented in section 9.4. This permeabilization strategy was inspired by the mixing concept reported earlier [157, 160, 161].

2.6.4 Permeabilization Procedure

Taking a look in the typical experimentalist's workflow, the workflow consists of four steps, as illustrated in figure 15. At the first step, the drug and the cell suspension merge as a homogeneous fluid. This is not trivial, as mixing quality determines the dye concentration exposure distribution. As our acoustofluidic approach originates from mixing, for our permeabilization method, this challenge is resolved automatically. Nevertheless, at this point, the drug has not been inserted into the cells yet.

At the second step, the permeabilization technique is applied and ideally, the cell membrane has been permeabilized. Once a cell membrane has been permeabilized, the drug can start to diffuse inside the cell. The exact or relative time where a cell membrane has been permeabilized might vary for all cells of the experiment. Here, experimental details matter, the exact permeabilization time evolution governs the uptake distribution. Furthermore, the whole permeabilization time interval of an

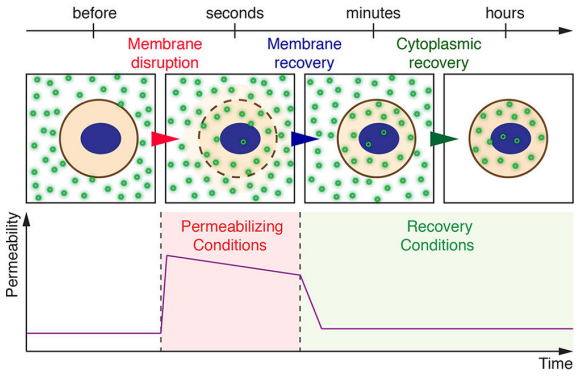

Figure 15: Typical permeabilization procedure. Adapted from [95].

experiment is critical, too. It should be as long as necessary for the desired uptake, but as short as possible to avoid excessive cell stress.

At the third step, cell membrane permeabilization has ended, leading to a rehealing of the membrane. Once again, time matters, the shorter the rehealing process between end of treatment applied and cell membrane has healed, the narrower the uptake distribution. Now, the cell membrane has become impermeable, again. At this point, the drug is inside the cell, as well as outside the cell. Ideally, the concentration is similar. However, this is unrealistic due to many surfaces and barriers inside the cell, which impede diffusion. It might be possible, that the drug has an affinity towards the cell interior, e.g. because of the drug chemistry. Experimentally, due to the low contrast between the cell exterior and interior, classical analysis methods, like fluorescence microscopy, are not feasible.

In the last step, the contrast is restored by eliminating the fluorescent dye from the extracellular medium. This is commonly referred to as washing. The improved contrast allows for a differentiation of permeabilized cells, as they appear bright. At this point, it becomes obvious, that a closer look to the cell membrane is beneficial to study permeabilization.

2.6.5 Cell Membrane

In contrast to artificial membranes, cellular membranes consist of more than pure lipids. Other molecules are mainly proteins and sugars, as illustrated in figure 16.

Real membranes differ for organelle types and are not necessarily symmetric, as specified in table 1. According to the table, phosphocholines are commonly the most abundant lipids, followed by phosphoethanolamines, and cholesterol. Note, that saturated lipids commonly outnumber the unsaturated lipids, which is presented in

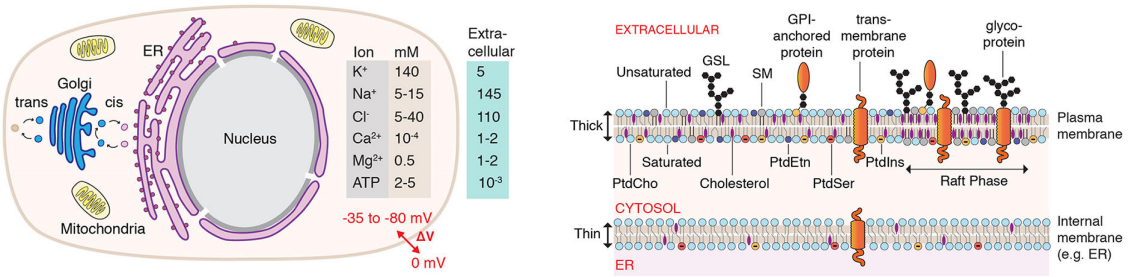

(a) Membranes and conditions in a typical animal cell. Note that besides the goal of overcoming the plasma membrane, additionally overcoming the nuclear membrane is of special interest for transfection purposes.

(b) Diversity in proteins, sugars, and lipids for different membranes. Note the difference between the plasmamembrane and the organelle membrane and the membrane asymmetry.

Figure 16: Key cell structure and properties. Adapted from [95].

table 2. Although lipids in general outnumber the other molecules by far, proteins make up about 50 wt.% of biological membranes.

Besides the numbers of lipids, the cell structure is important. The cell structure of a typical animal cells is presented in figure 16, in addition to quantitative information on intra- and extracellular ion concentrations and membrane potential. Furthermore, the figure shows more details on the membrane compositions and the underlying actin cortex linked to the plasma membrane.

When treatment is applied to a cell for permeabilization purposes, many events and event paths are possible, as illustrated in figure 17. On the one hand, if plasma membrane repair fails, then the cell dies. Dead cells do not have an intact cell membrane, leading to spontaneous permeabilization, which has to be considered in the experiments.

On the other hand, if the plasma membrane repair succeeds, then the cell survives. In this case, cell stress has to be considered, as it follows a permeabilization treatment and might have left damage.

Even if the cell survives, the cell can still initiate apoptosis and die. Electroporation [145] is a method, which is successful in permeabilizing the cell membrane, however, the ionic composition of the cytoplasm is disturbed, which can lead to apoptosis [163, 164]. In some scenarios, like direct tumor treatment, this can be a highly desired effect [165, 166]. In the best case scenario, the cell regenerates to its pre-treatment state.

Permeabilization of the cell membrane for the purpose of forcing water-soluble material into the cell is the interesting scenario for *in vitro* therapeutic research

Table 1: Membrane head group composition for various cells and organelles. Phosphatidylcholines (PC), phosphatidylethanolamines (PE), phosphatidylserines (PS), phosphatidylinositols (PI), sphingomyelin (SM), cardiolipin (CL), cholesterol (chol). Adapted from [162].

Membrane	PC	PE	PS	PI	SM	CL	Glycolipid	Chol	Others
Erythrocyte (human)	20	18	7	3	18	–	3	20	11
Plasma (rat liver)	18	12	7	3	12	–	8	19	21
ER	48	19	4	8	5	–	tr	6	10
Golgi	25	9	3	5	7	–	0	8	43
Lysosome	23	13	–	6	23	≈ 5	–	14	16
Nuclear membrane	44	17	4	6	3	1	tr	10	15
Mitochondria	38	29	0	3	0	14	tr	3	13
Neurons	48	21	5	7	4	–	3	11	1
Myelin	11	17	9	1	8	–	20	28	6

Table 2: Distribution of acyl chains of erythrocyte (in wt%). Adapted from [162].

Lipid head group	16:0	18:0	18:1	18:2	20:3	20:4	22:0	22:4	22:5	22:6	24:0	24:1
PC	31	12	19	22	2	7	–	–	2	–	–	–
PE	13	12	18	7	2	24	2	8	4	8	–	–
PS+PI	3	37	8	–	3	24	3	4	3.5	10	–	–
SM	24	6	–	3	–	1.4	9.5	–	–	–	23	24
Total	20	17	13	9	1.5	13	2	3	2	4	5	4

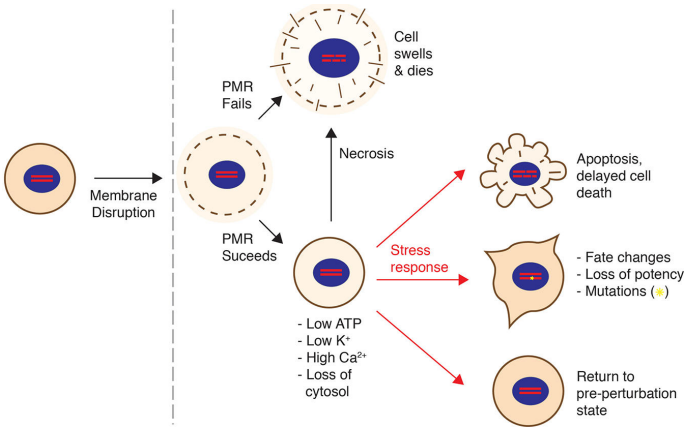

Figure 17: Event tree for the possible cell responses to permeabilization treatment. Adapted from [95].

and development. However, hard particles behave differently in terms of uptake. An important group of hard particles are nanoparticles, which are abundant in our environment.

2.6.6 Membrane Nanoparticle Permeability

The term nanoparticles categorizes particles with a common size in the nanometer range. Even larger particles in the micrometer range are called microparticles and are commonly visible under a light microscope. In contrast, nanoparticles, require electron microscopy for visualization. Particles below $\approx 1\,\text{nm}$ approach the atomic scale.

Nanoparticles promise big advances for potential medical applications. Studies have been conducted on implant materials [167, 168, 169], carrier materials for drug delivery [170, 171, 172, 173], clinical trials to image tumors [174], antibacterial agents [175], and nanomedicine [176, 177, 178]. However, nanoparticles have potential medical downsides, too. Many studies have documented potential harms, which are widely present in human environments. Such nanoparticles can be found in cosmetics, paints, and printer toners [179, 180, 181], like titan dioxide (E 171), silver (E 174), and silicon dioxide (E 551). Known undesirable effects are such as toxic and coagulatory effects [182] and pregnancy complications [183]. However, these findings are not easily transferable to humans, as they have been conducted using certain model systems.

Nanoparticle Models

Studies on nanoparticles are manifold. On the one hand, applied studies have been done on *in vivo* models to conduct direct measurements on mammals, such as mice [184]. To obtain a macroscopic picture, studies measure quantities such as LD50 values [185], or quantify the bio-distribution of nanoparticles [186]. On the other hand, *in vitro* studies focus on a microscopic picture. Such experiments show a temperature difference in nanoparticle uptake, such as no nanoparticle uptake at 4 °C- in contrast to significant uptake at 37 °C [187, 188, 189]. Besides experimental studies, *in silico* studies supplement literature with e.g. metadata analysis. One study found that the main toxicity is connected to material chemistry [190]. Another crucial dimension are studies at an even more fundamental level, which use artificial models. Artificial lipid models allow for insight into the nanoparticle-cell interaction [31, 191, 192], which is a major interest of this thesis.

In detail, artificial model systems can serve as a model for internalization pathways. Internalization pathways have a broad diversity, as medical applications span a broad diversity of substances. These substances reach from molecules to proteins and even beyond, which can be accommodated by nanoparticle models, as size and surface chemistry is tuneable.

Lots of very concrete nanoparticle associated applications are already well established, even elaborate ones like opto-triggered nanoparticle systems for cancer therapy [193]. However, not even the passive nanoparticle uptake has been fundamentally understood, yet. The passive mechanism carries crucial biological relevance, as it is omnipresent and takes place spontaneously. Here, environmental sensitivity, like temperature dependency of the nanoparticle uptake, is well known from *in vitro* experiments, which exhibits a nonlinear relation [189].

To understand such macroscopic effects, microscopic models are crucial. Therefore, Deserno published a physical model of nanoparticle engulfment based on three major energetic contributions: The adhesion energy (E_{adh}) as the driving force, the bending energy (κ) and the tension energy (σ) as the opposing forces [194]. Based on the interplay of these forces, three regimes of nanoparticle-membrane interaction were identified: Repulsion, partial engulfment, and full engulfment. Repulsion appears below an adhesion energy threshold, which depends on the bending modulus of the membrane and the particle radius. The partial engulfment regime appears above this adhesion energy lower limit until the upper limit $r_{(c,\sigma)} = 2\frac{\kappa}{E_{\mathrm{adh}}-\sigma}$. Above this upper limit, nanoparticles are fully engulfed.

At the end of the full engulfment, there is a catch. The fully wrapped particle forms a membrane neck. A fission event separates the once continuous membrane into two

separate membranes. One membrane is wrapped around the nanoparticle, just like a vesicle, but with a solid interior instead of aqueous medium. The other membrane is still the original one, but with a membrane defect, a *pore*, which heals after its characteristic lifetime. Typical lifetimes are $\tau \approx 100\,\mathrm{ms}$ [125], but can be largely increased to the order of seconds by applying tension via micropipette aspiration [195].

However, while the pore exists, the physical situation changes drastically. The closed system is now an open system, allowing the exchange of mass, in particular fluid flow, which additionally reduces membrane tension. Mind the reduced membrane tension has a feedback on the next nanoparticle uptake process. To estimate the dominant opposing force, the relation $\lambda = \frac{2\kappa}{\sigma}$ is useful, where either bending is dominant if $\lambda > 1$, or tension if $\lambda < 1$ [196].

Bending Modulus

A closer elaboration on the three parameters reveals further insights. The first key parameter, the bending modulus, is according to Helfrich [197]:

$$e_{\mathrm{bend}} = \frac{1}{2}\kappa\big(c_1 + c_2 - c_0\big)^2 + \bar{\kappa} c_1 c_2 \tag{33}$$

- e_{bend} bending energy per unit area
- c_0 spontaneous curvature
- $c_{1,2}$ local principal curvatures of the two-dimensional membrane surface
- $\kappa, \bar{\kappa}$ elastic moduli

Quantitatively, typical values for e_{bend} are about $e_{\mathrm{bend}} \approx 10^{-19}\,\mathrm{J}$ for a fluid membrane (DOPC, room temperature) [198]. An elegant geometrical consideration from Heimburg [2] approximates the bending modulus to

$$K_{\mathrm{B}} = \frac{D^2}{16\kappa_T^A}. \tag{34}$$

- D membrane thickness

Note, that the bending modulus is inversely proportional to the isothermal compressibility. As the isotherm is a highly non-linear function at the phase transition, so is the bending modulus. The bending modulus has been simulated as function of temperature, which revealed a minimum at the melting transition [24].

Only few experimental studies exist to complement this simulation. Two studies use DMPC and DPPC GUV and measure the bending modulus in the melting regime and above, but not at lower temperatures [199, 200]. In contrast to Heimburg, they measure an anomaly within $T_\mathrm{m} \leq T \leq T_\mathrm{m} + 6\,\mathrm{K}$. Within $T_\mathrm{m} \leq T \leq T_\mathrm{m} + 3\,\mathrm{K}$, the bending modulus first rises to a maximum, until it decreases for $T_\mathrm{m} + 3\,\mathrm{K} \leq T \leq T_\mathrm{m} + 6\,\mathrm{K}$ to a limit for both DMPC and DPPC [199]. Interestingly, cholesterol - well known to suppress first order lipid phase transitions - increases the bending modulus and diminishes the maximum [200].

Newer measurements close the gap in literature and span the whole relevant temperature axis - even below T_m, as can be seen in figure 18. The study finds a bending modulus for DPPC giant unilamellar vesicles that is one order of magnitude higher in the gel phase compared to the fluid phase [201]. In the fluid phase, the bending modulus is constant and $K_\mathrm{B} \approx 10^{-18}\,\mathrm{J}$, whereas deep in the gel phase, the bending modulus is about constant and $K_\mathrm{B} \approx 10^{-19}\,\mathrm{J}$.

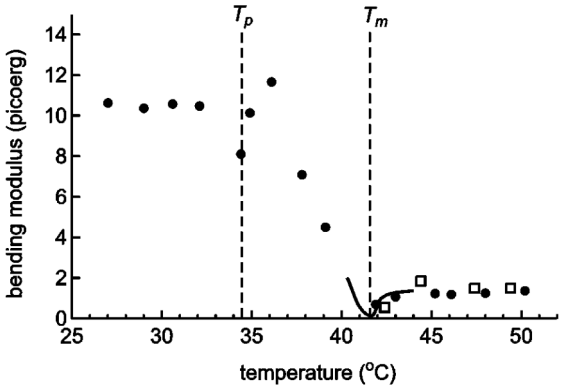

Figure 18: Bending modulus as a function of temperature. Adapted from [201].

However, at both phase transitions, K_B exhibits a minimum, as calculated three years prior by Heimburg. Between the transitions - in the ripple phase - K_B rises linearly from $K_\mathrm{B} \approx 10^{-19}$ J to $K_\mathrm{B} \approx 10^{-18}\,\mathrm{J}$.

A quantitative study on the bending modulus confirms the good comparability of red blood cells and artificial vesicles, although the membrane composition is different [202]. This could indicate also a good comparability to cells. However, this might not be true for every kind of cell, as phase transitions have a huge diversity in broadness. Some studies find broad phase transitions for biological membranes [93], others sharp and narrow phase transitions [203].

Nevertheless, the bending modulus is governed by the hydrophobic part of the lipid bilayer [204]. Quantitatively, the bending modulus is a power law of the packing parameters [205]. Therefore, an effect on the bending modulus is obvious, as a

melting transition consists of structural changes, which effectively results in a change in area and volume per lipid molecule [206].

Tension

The second key parameter, membrane tension, is characterized by two regimes. For the low-tension regime, the tension rises exponentially with increasing area dilation. With rising tension thermal fluctuations become restricted. In contrast, for the high-tension regime, tension rises linearly as function of area dilation. The linearity originates from the direct expansion of the area-per-molecule [207]. Membrane tension has been experimentally observed, e.g. in red blood cells [202]. Drastic change in membrane tension happens when the diameter of a blood vessels changes, like in capillaries. Or, as will be shown in this thesis, during the adhesion process of any type of molecule or nanoparticles.

Older studies have shown subtle impact of tension on vesicle phase transitions. However, a newer study reveals drastic impact on the fluid-solid phase transition [208]. The authors observe

> [...] differently shaped solid domains (striped or irregular hexagons), [a] shift [in] fluid–solid transition temperatures, [...] a triple-point–like intersection [...]. [208]

Tension might be a

> [...] potential switch of microstructure in responsive engineered materials; it is an important morphology-determining variable in confined systems, and, in biological membranes, it may provide a means to regulate dynamic structure. [208]

This is yet another possibility to apply physical specificity to biology without the need for a biochemical cascade reaction.

Adhesion

The third key parameter, the adhesion energy, is a collective term and includes the following forces: van-der-Waals, hydration, hydrophobic, double-layer forces, protrusion forces, and thermal undulation [209]. The largest contributors in the case of bilayers and substrates are the van-der-Waals forces and the electrostatic forces.

Van-der-Waals forces can be expressed as [210]:

$$F_{\mathrm{vdW}} = -\frac{A_{123}}{6\pi}\left(\frac{1}{D^3} - \frac{2}{(D+T)^3} + \frac{1}{(D+2T)^3}\right) \tag{35}$$

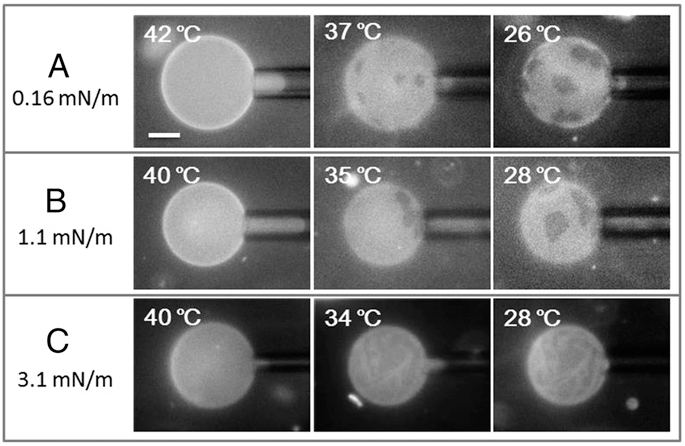

Figure 19: Cooling of a DOPC/DPPC vesicle under tension. Interestingly, the tension governs which solid phase forms. Also, a shift in melting temperature - for different tensions - is clearly visible. Adapted from [208].

- A_{123} Hamaker constant $A_{123} \approx (3-4) * 10^{-21}$ J
- D distance bilayer-silica surface
- T bilayer thickness

At small distances, this equation simplifies to

$$F_{\mathrm{vdW}} = -\frac{A_{123}}{6\pi D^3} \tag{36}$$

and

$$E_{\mathrm{vdW}} = -\frac{A_{123}}{12\pi D^2}. \tag{37}$$

However, this does not sufficiently describe the adhesion energy quantitatively. The double-layer interaction in an electrolyte is approximated by the Fogg-Healy-Fürstenau equation [211]:

$$W_{\mathrm{dl}} = \frac{\epsilon\epsilon_0\kappa(2\psi_1\psi_2 - (\psi_1^2\psi_2^2)\exp(-\kappa D)}{\exp(\kappa D) - \exp(-\kappa D)} \tag{38}$$

- ϵ dielectric constant of water
- ϵ_0 dielectric constant
- ψ_1 bilayer surface potential

- ψ_2 silica surface potential
- D bilayer surface - silica surface distance
- κ Debye constant

As phosphocholine is zwitterionic $\psi_{1,2} = 0$. Therefore, the equation is simplified to:

$$W_{\mathrm{dl}} = \frac{-\epsilon\epsilon_0\kappa\psi_0}{\exp(\kappa D) - \exp(-\kappa D)}, \tag{39}$$

which further simplifies at small and large distances to:

$$W_{\mathrm{dl}} = -\epsilon\epsilon_0\kappa\psi_0^2 \exp(-2\kappa D) \tag{40}$$

$$W_{\mathrm{dl}} = -\epsilon\epsilon_0\kappa\psi_0^2 \exp((-2\kappa D)/2D) \tag{41}$$

However, adhesion also strongly depends on the material of the nanoparticle. Here, we use silica, which is highly relevant to our human environment. Silica nanoparticles are universally used as an additive to food under the terms E 551, E 558 Silicon dioxide and Silicate™. Furthermore, silica nanoparticles are highly popular as drug delivery vehicles.

The adhesion energy between silica and lipid membranes has been studied extensively. Anderson *et al.* conducted a fundamental study both experimental and theoretical. In this study, they measured force-distance curves between silica and phospholipid membranes in two different environments [209]: Repulsion in ultra-pure water and attraction in buffered physiological salt concentrations, as charges are shielded by the ions. Quantitatively, the adhesion energy of silica to DMPC in the fluid phase is $E_{\mathrm{adh}} = (0.5 - 1)\ \frac{\mathrm{mJ}}{\mathrm{m}^2}$. However, adhesion energies can range from $E_{\mathrm{adh}} = (10^{-5} - 1)\ \frac{\mathrm{mJ}}{\mathrm{m}^2}$ for different conditions [209, 212].

Interestingly, the numbers are slightly misleading for the microscopic picture at the interface of the lipid bilayer and the silica. The interaction is not trivial. When the membrane adheres to silica, two equilibrium distances exist [213]: In the first case, the membrane is separated by $d_1 = 2.5\,\mathrm{nm}$ from the silica substrate, with a water layer in between. In the other case, no water layer separates the membrane from the silica, therefore $d_2 = 0\,\mathrm{nm}$. This results in a highly distorted bilayer governed by the substrate roughness. No other equilibrium distances exist, as they are unstable due to hydration forces, where distorting the orientation of water molecules is energetically unfavorable.

Threshold Ion Concentration and Saturation for Nanoparticle Uptake

A deeper look into adhesion reveals several dependencies. In the study by Wittmann, Kamenac *et al.*, we focused on the ion concentration switching on and off the adhesion energy [214]. We found a salt dependent threshold value for attraction. The threshold is at about $c_{\text{crit}} \geq 15\,\text{mM}$ NaCl for a supported lipid bilayer in the fluid phase (DOPC) and a micrometer sized silica bead.

The adhesion energy rises for higher salt concentrations, until it saturates at about $E_{\text{adh}} = 60\,\frac{\mu\text{J}}{\text{m}^2}$. Note that these quantitative values deviate from Anderson *et al.* [101], which might arise from methodological differences. However, the peculiarity is the threshold in ion concentration. This result should be severely implemented in future studies on adhesion energy between silica and lipid membranes and should be systematically studied for other substrates.

Indeed, the ion concentration threshold behavior has been confirmed for uptake experiments. In the study conducted by Strobl *et al.*, they went one step further and added nanoparticle size as another parameter. Their finding is striking: The lower threshold for nanoparticle uptake is $c_{\text{crit}} \geq 15\,\text{mM}$ NaCl for 60 nm particles and DOPC GUV [192]. This suggests an all-or-nothing behavior and another possibility for a specificity mechanism without the need of direct biochemical cascade reactions. At this point I would like to mention, that to the best of my knowledge, the adhesion energy has so far not been measured quantitatively in the gel state at non-zero salt conditions.

Shift in Phase Transition Temperature

Finally, a direct shift of the phase transition temperature of the nanoparticle-wrapped membrane has been reported [31]. A follow-up study took this result into account on direct nanoparticle uptake measurements and expanded the theoretical model by adding a thermodynamic point of view [191]. Surprisingly, on top of an effect on nanoparticle-membrane interactions, membrane-membrane adhesion forces change, too.

Membrane-membrane adhesion forces consist of undulation forces, which are tension dependent. On the one hand, tension rises for nanoparticle uptake, as nanoparticles consume membrane area. This is only possible,as water inside the GUV is nearly incompressible, which keeps the volume constant. On the other hand, tension drops when pores allow fluid to escape the vesicle interior. The trade-off of these two processes highly depends on the pore lifetime. In turn, pore lifetime is a function on the membrane state. Pore lifetime is enhanced close to the main phase transition of phospholipid membranes [125, 141].

Furthermore, simulation results reveal an additional regime, where nearly unlimited nanoparticle uptake appears [192]. Experimental results also gave a first glimpse experimentally into nanoparticle uptake of gel state vesicles and observed qualitative differences for different nanoparticle sizes [191]. However, there is a lack of systematic experimental studies on nanoparticle uptake as function of the phase state. This will be addressed in the section 4.3.

3 Optical Detection of Structural Phase Transitions in Vesicles and Living Cells

This section presents results relying on a bachelors thesis project by Jacob Brunner [215] and a masters thesis project by Nicolas Färber [216], which were both supervised by me. The objectives of this work are the following. Firstly, measure the membrane phase transition optically. Secondly, study the relationship of structural phase transition and shear flow and the quantitative measure of it. Thirdly, test whether a structural phase transition is detectable for *in vitro* cells.

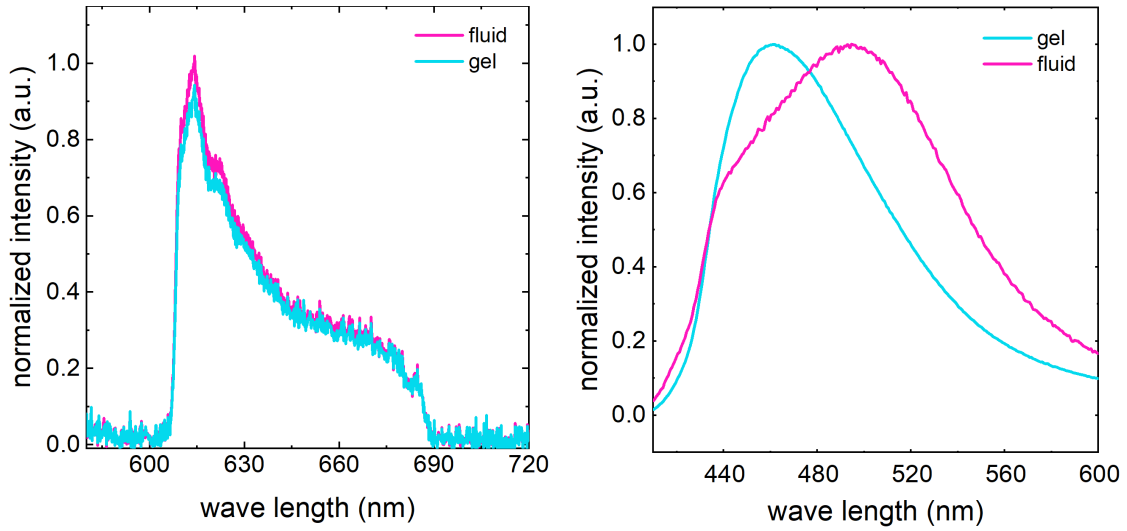

(a) Fluorescence emission spectrum of Texas Red™ DHPE-labelled vesicles for two different phase states. The vesicles consist of the fluorescent dye and 15:0 PC. Clearly, no significant shift is visible and therefore the dye is optically insensitive to changes in the phase state and unsuitable for the optical measurement of the membrane phase state.

(b) Fluorescence emission spectrum of Laurdan-labelled vesicles for two different phase states. The vesicles consist of the fluorescent dye and 15:0 PC. Clearly, the spectral position of the maximum is sensitive to changes in phase state and is perfectly suitable for the optical measurement of the membrane phase state.

Figure 20: Emission spectrum of multilamellar vesicles stained with different fluorescent dyes.

To choose the right fluorescent dye for optical measurements of the membrane phase state, literature offers a plethora of options [217]. The main purpose of fluorescent dyes is imaging. Therefore, ideally, the dye has a high specificity for a peculiarity of the cell, like organelles.

Our goal is different, as we seek for a dye, which is sensitive to the structural phase transition. A dye, which is not sensitive to the phase transition of membranes, is presented in figure 20a. In contrast, another dye, which indeed is sensitive to a structural phase transition, is presented in figure 20b. In detail, 6-Dodecanoyl-*N,N*-dimethyl-2-naphthylamin (Laurdan) is indirectly sensitive to the structural phase transition. Its spectral emission is sensitive to the dipolar relaxation of the lipid-surrounding water the first place. As the dipolar relaxation of the surrounding water is a function of the membrane phase state, Laurdan is sensitive to phase transitions.

Summarized, Laurdan might not be a commonly used dye in literature, as the large majority of literature is interested in imaging, however, it is perfect for our purposes and can be easily combined with microfluidics.

3.1 Spectral Shift of Membrane Dye Emission in Multilamellar Vesicles under Shear Force

We combine the optical measurement of the Laurdan-stained membranes with microfluidics, to generate well-defined shear forces. In contrast to figure 20b, the following experiments are quantitative in terms of temperature, shear rate, and shift in wavelength. Firstly, I present the fluorescence emission maximum as function of temperature for two different lipids at static conditions. Secondly, I elaborate on one of the lipids - 14:0 PC - in the form of multilamellar vesicles. Here, the wavelength of the fluorescence emission maximum is a function of temperature at a high shear rate. To refine these results, I present a new set of experiments, where the shift in fluorescence emission maximum is function of temperature and shear - at a finer resolution. Thirdly, I present analogous experiments using another type of lipid - 15:0 PC - to fully exclude system-specific effects from the setup.

The fluorescence emission maximum as function of temperature for 14:0 PC at static conditions ($\dot{\gamma} = 0$) in figure 21a shows the achievement of the first objective - to measure the phase transition optically. The same is true for 15:0 PC at static conditions ($\dot{\gamma} = 0$) in figure 21b. For both lipids, the phase transition temperature is well-known and measured calorimetrically. The results T_m(14:0 PC) = 24 °C and T_m(15:0 PC) = 33 °C agree with literature [2]. Optical measurements show a steep jump (at highlighted data points) in fluorescence emission maximum at both T_m for the respective lipid. Also, the temperature range was chosen appropriately to include the other lipids T_m on the measured temperature range. To be clear, figure 21a shows no jump in fluorescence emission maximum at T_m of 15:0 PC and *vice versa* for figure 21b.

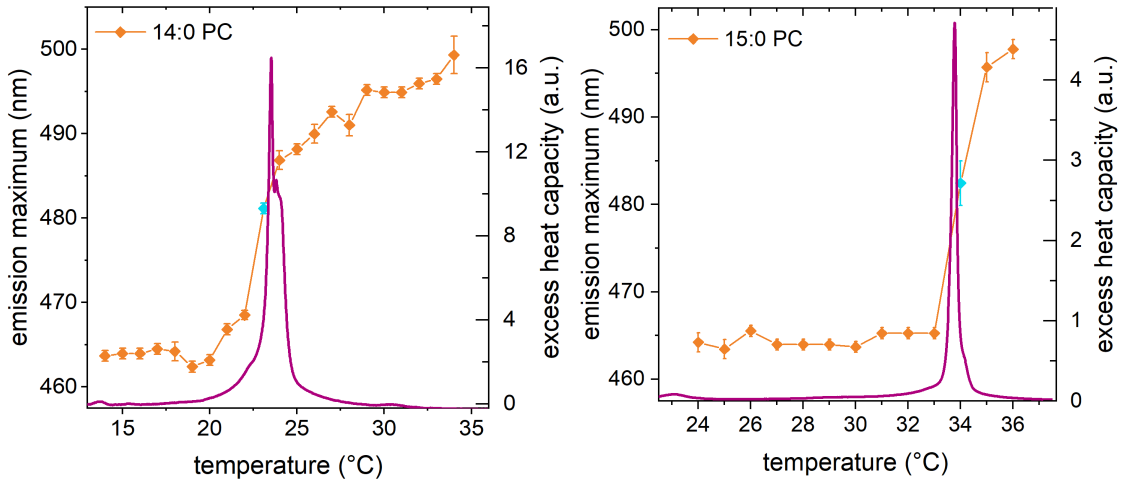

(a) 14:0 PC Multilamellar vesicles

(b) 15:0 PC multilamellar vesicles

Figure 21: Reference measurement - Correlation of excess heat capacity and fluorescence emission maximum as function of temperature. The highlighted data points mark the inflection points, which indicate the phase transition optically.

In contrast, to static conditions, the results for 14:0 PC at a high shear ($\dot{\gamma} = 8000\,\frac{1}{\mathrm{s}}$) rate are presented in figure 22. Clearly, there is a shift in fluorescence emission maximum $\Delta\lambda \approx -3.9\,\mathrm{nm}$, which corresponds to a shift on the temperature axis of about $\Delta T_\mathrm{m} = -0.17\,\mathrm{K}$. This results in a linear trend with a slope of about $\frac{-0.17\,\mathrm{K}}{8000\,\frac{1}{\mathrm{s}}}$. Note, that the discrepancy at the inflection data points exceeds the error bars.

Therefore, the membrane phase state was successfully changed by shear flow, measured optically. In principle, Yamamoto and Ando have done something very similar, as elaborated in section 2.3.3 [45]. However, the results of their study and this thesis contradict. In their study, the vesicle chain order decreases under shear, here, the chain order increases under shear. This contradiction could not be resolved to the last. However, there might be some critical differences in the studies.

In their setup, they use unilamellar, immobilized vesicles, consisting of 3 lipid types. In contrast, we here use single-lipid multilamellar vesicles flowing through the illumination zone. Based on these differences, the comparability of the results is limited as follows.

While Yamamoto and Ando have single-vesicle information, we have statistical information on many vesicles flowing in and out of the detection area. In the worst-case, in their study, the volatility might be higher due to the lack of statistical information. However, I do not expect any qualitative discrepancy to arise from this difference.

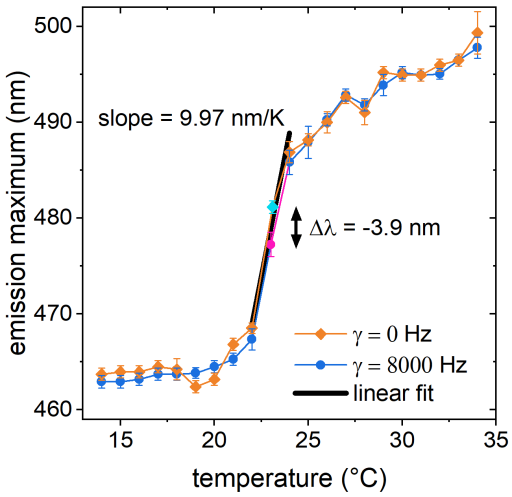

Figure 22: Fluorescence emission maximum of 15:0 PC as function of temperature for two different shear rates. The maximum shifts under shear flow towards lower wavelengths, indicating an increase in chain order for increasing shear rates.

This is also true for the difference in mobility. In the worst-case, the technical implementation of the immobilization mechanism using poly(L-lysine) might slightly alter the phase state. However, as the study provides spatial resolution, no such effect is visible to the naked eye.

For the difference in lamellarity, it remains unclear, whether qualitative discrepancies might arise. This is supported in the following statement by Heimburg:

> This finding leads to the notion that unilamellar lipid membrane transitions are close to the critical point but most likely in the continuous regime (not first order). [2]

Here, he describes the qualitative difference between phase transitions in multilamellar vesicles (first order) and unilamellar vesicles (not first order). However, in the following sentence, he states that the debate on this hypothesis is still unresolved.

Another major difference are the used lipid types. Additionally, Yamamoto and Ando did not determine the phase state of the vesicles calorimetrically. This lack of absolute determination of the location in the phase space impedes comparability. On top of that, the use of cholesterol complicates the phase diagram drastically - as a new phase - the solid disordered phase, is introduced and the first-order properties of the phase transition are suppressed. Additionally, shear might changes the phase diagram and cause further effects in phase separation. This could also alter the lipid composition, along with the chain order.

To increase data quality of figure 22 and challenge the contradiction, a I present a new set of experiments. The experimental setup remains unchanged, however, more shear rates enable a finer resolution on the shear rate axis. The results are presented in figure 23.

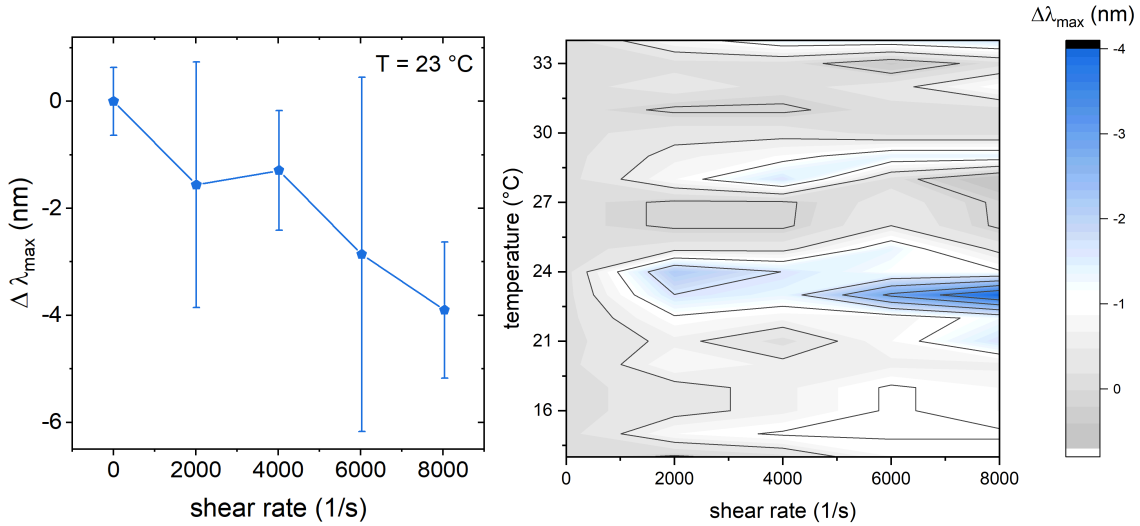

(a) Shift in fluorescence emission maximum as function of shear rate at isothermal conditions ($T = 23\,°C$).

(b) Emission maximum shift color-coded as function of shear rate and temperature.

Figure 23: Spectroscopic measurements as function of shear rate and temperature for 14:0 PC multilamellar vesicles.

Figure 23a shows the shift in fluorescence emission maximum as function of shear rate at $T = 23\,°C$. The resulting shift of $\Delta\lambda \approx -3.9\,nm$ supports the results in figure 22 to a quantitative extent. Therefore, the contradiction persists.

To obtain figure 23b, graphs like in figure 23a were obtained for various isothermal measurements. Figure 23b presents the results as a heat plot. It becomes very clear, that this shift is not caused by a flow artifact. Indeed, it is caused by a change in phase state, as the amplitude in wave length shift is specific to a set of temperature **and** shear rate. Furthermore, after relieving the flow, the emission maximum shifted back, strongly supporting reversibility (data not shown), which has also been reported by Färber, Reitler, and Kamenac *et al.* [51]. This observation crucially differs from the observation by Yamamoto and Ando. Therefore, I highly encourage further experiments on shear stress at various phase states, at various lipid compositions, measured optically.

To challenge the hypothesis even further to exclude any system specific effects, we conduct the equivalent experiments using 15:0 PC. This lipid is practically identical

to 14:0 PC, but the acyl chains are one hydrocarbon unit longer. The longer acyl-chains shift the phase transition temperature to $T_m = 33\,°C$ - a significantly higher temperature.

The results are presented in figure 24, which is the 15:0 PC analog to figure 22. It shows a shift in the fluorescence emission maximum for 15:0 PC at a high shear rate ($\dot{\gamma} = 8000\,\frac{1}{s}$) compared to static conditions. The shift in fluorescence emission maximum is $\Delta\lambda \approx -8.5\,nm$, which corresponds to a shift on the temperature axis of about $\Delta T_m = -0.5\,K$. This results in a linear trend with a slope of about $\frac{-0.5\,K}{8000\,\frac{1}{s}}$. Therefore, the qualitative results agree well. However, the shift in emission maximum for 15:0 PC is larger than for 14:0 PC, which could be caused by the higher thickness or by an asymmetric free energy.

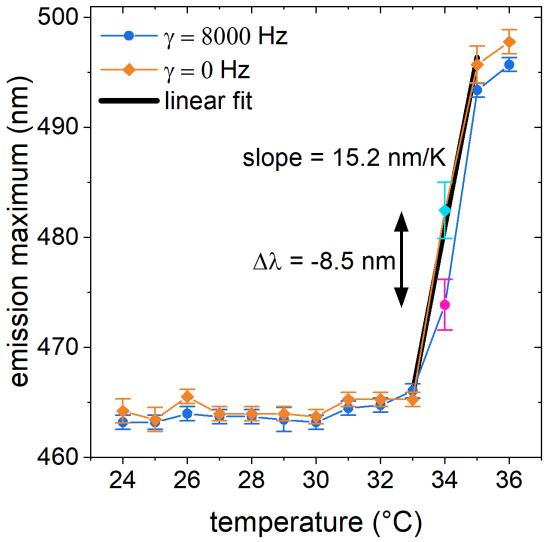

Figure 24: Fluorescence emission maximum of 15:0 PC as function of temperature for two different shear rates. Similar to figure 22, the chain order increases for an increasing shear rate.

Analogously to figure 23, we conduct a new set of experiment using 15:0 PC to refine the resolution on the shear axis. The results are presented in figure 25.

In contrast to figure 23a, in figure 25a, the shift in emission maximum appears to saturate quickly at about $2000\,\frac{1}{s}$. As a result, the slope has to be corrected to about $\frac{-0.5\,K}{2000\,\frac{1}{s}}$. Consequently, the calculated threshold shift of $\Delta T = 0.5\,K$ from anesthetics - elaborated on in section 2.5.2 - is reached within the present experimental conditions - and therefore in many biological systems like blood vessels or bone fluids.

To obtain the analogous to figure 23b, graphs like in figure 25a are obtained for various isothermal measurements. Figure 25b presents the results as a heat

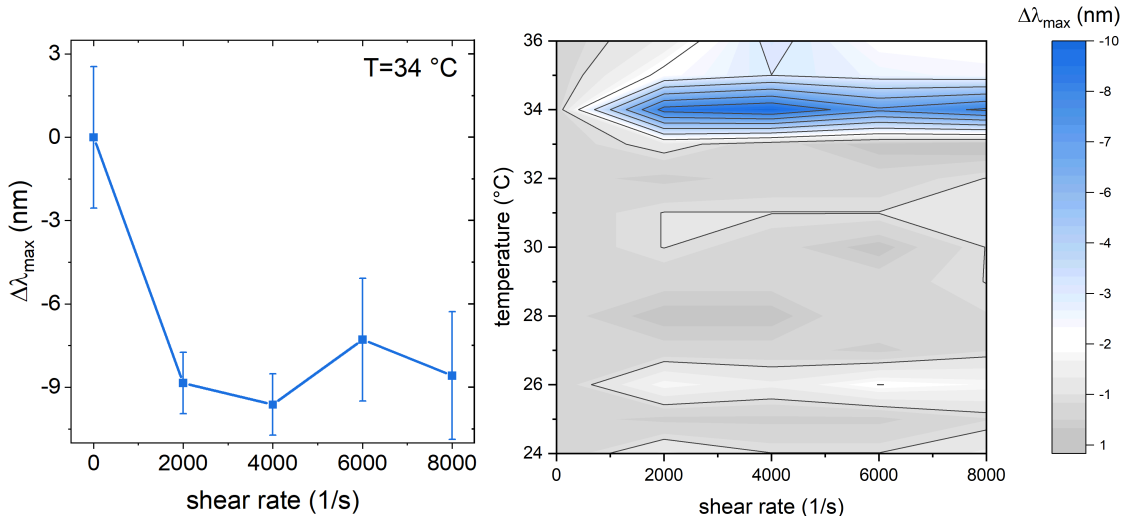

(a) Isothermal measurement of the emission maximum as function of shear rate.

(b) Contour plot of the emission maximum spectral position as function of temperature and shear rate.

Figure 25: Spectroscopic measurements as function of shear rate and temperature for 15:0 PC multilamellar vesicles.

plot. Once again, the highest amplitude in emission maximum shift appears at the phase transition temperature for higher shear rates. This fingerprint-like behavior excludes system-specific effects to cause the shift in emission maximum for both lipids. Furthermore, note, that the temperature range spans for all measurement sets over both transition temperatures, being another powerful reference feature.

Having studied a homogeneous lipid system, it would be intriguing to study a lipid mixture. By using e.g. an equal mixture of 14:0 PC/15:0 PC lipids, a heterogeneous membrane forms, displaying a stable phase boundary over a broad temperature range. I expect a greater sensitivity of the generalized polarization on the shear rate, as nucleation sites are not scarce.

Although having tried to disprove the hypothesis, by using 15:0 PC multilamellar vesicles, the data presented in figure 25b and 23b do not falsify the hypothesis. Rather, the results support the hypothesis. Accordingly, the second objective has been accomplished, as we have found a shear rate dependence of the phase state of the multilamellar vesicles. These results are highly interesting for therapeutic liposomes used as vehicles for drugs [218]. Such temperature-sensitive liposomes have to be carefully designed in terms of their lipid composition to be close to a phase transition. However, as the liposomes are transported through the blood flow to their destination, they are exposed to shear forces. Here, the quantitative shift of

the phase transition temperature should be accounted for a precise control of the drug release.

Naturally, the question is - and third objective - is this applicable to *in vitro* cells and how can this be valuable and useful to cells?

3.2 Optical Phase State Measurement of Living Cells

Blicher *et al.* showed that artificial membranes are most permeable at the phase transition [141]. Therefore, we tried to find a possible phase transition in *in vitro* cell membranes, to make use of it for permeabilization purposes. The characterization of lipid membranes phase state is classically measured by calorimetry. While this is routine work using artificial lipid membranes - and has been conducted in this thesis various times figure 21a 21b - it is not trivial for *in vitro* and *in vivo* cells. An extensive review on this can be found in section 2.3.2.

An alternative to calorimetric measurements are optical measurements, which are summarized in section 2.3.1 and offer various advantages. Recent publications have achieved measuring phase transitions in cells using other dyes [51, 203]. However, prior to these publications, we have used the FRET (Förster-Resonance-Energy-Transfer) mechanism to measure the phase state of *in vitro* cells to a partially successful extent, which will be described in the following.

The cells are stained using non-fluorescent Calcein-AM (acetoxymethyl), which spontaneously diffuses through the membrane into the cell. Once inside the cell, the acetoxymethyl groups are removed by esterases, which results in fluorescent Calcein. This chemical is commonly used as part of an assay to detect living cells. Additionally to the Calcein-AM, DPH (1,6-Diphenyl-1,3,5-hexatriene) is added to the cells, which spontaneously integrates into the cell membrane. Having two dyes with an overlapping emission and excitation spectrum, the distance-sensitive FRET signal makes use of the binary-like area and thickness values of the fluid and gel-like state. The results are presented in figure 26.

Figure 26 shows the FRET-signal as function of temperature. The signal being relatively linear, we are not being able to detect a phase transition. In some publications, phase transitions were successfully measured calorimetrically such as in *e. coli* [44]. In detail, according to the predictions, the phase transition was supposed to be somewhere near the cultivation temperature, so the cells could make use of being near the phase transition. Hence, the temperature range in figure 26 does span from $T = 28\,^{\circ}\mathrm{C} < T < T = 41\,^{\circ}\mathrm{C}$. However, this measurement was the beginning of further endeavour and a series of publications to quantifying the phase state of a cell as function of temperature and therefore phase state.

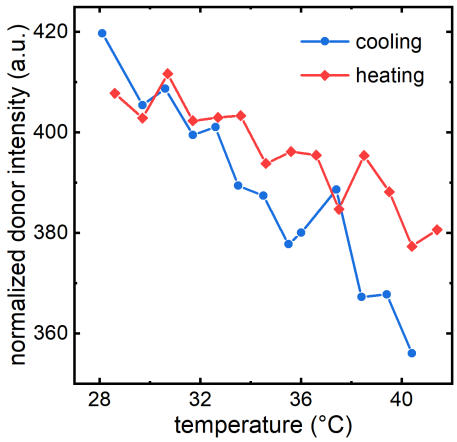

Figure 26: FRET efficiency as function of temperature. The cell membrane fluidizes for increasing temperature.

Later, a peak-like behavior was indeed found, but at lower temperatures, than predicted [51, 219]. For HeLa cells, the studies found different T_m for adherent and suspended cells. For adherent cells, they found $T_m \approx 15\,°C$ and for suspended cells, they found $T_m \approx 28\,°C$. The phase transition is very broad for HeLa cells (FWHM $\approx 40\,K$), which disabled us to identify the data point at $T = 28\,°C$ as T_m, as the trend appears linear on this small scale. Therefore, figure 26 is in excellent qualitative agreement with literature [51] - and it did give the same trend as published later, which is a decrease in chain order as function of temperature.

After the short excursion to cell membrane phase transition detection, we continue with phase transitions in artificial membranes. As indicated before, phase transitions in artificial membranes are known to permeabilize membranes. In the following, we will study the permeability - or uptake - of silica nanoparticles in giant unilamellar vesicles as function of temperature and therefore phase state.

4 Phase-state dependent Silica Nanoparticle Uptake of Giant Unilamellar Vesicles

A large part of the results in this section is in the process of publishing [220].

Permeabilization has various mechanisms, as elaborated in section 2.6, we here focus on endocytosis-like permeabilization. This type of internalization could be relevant to bacteria, as the cytoskeleton is not involved [221]. As a model system, we use giant unilamellar vesicles and silica nanoparticles. We measure the nanoparticle uptake by the vesicles as function of temperature and therefore phase state. The precise setup is described in section 9.2. Figure 27b shows the nanoparticles using scanning electron microscopy. In contrast, giant unilamellar vesicles are larger in diameter by three orders of magnitude, as presented in figure 27a. The nanoparticle uptake experiment is illustrated in figure 28a.

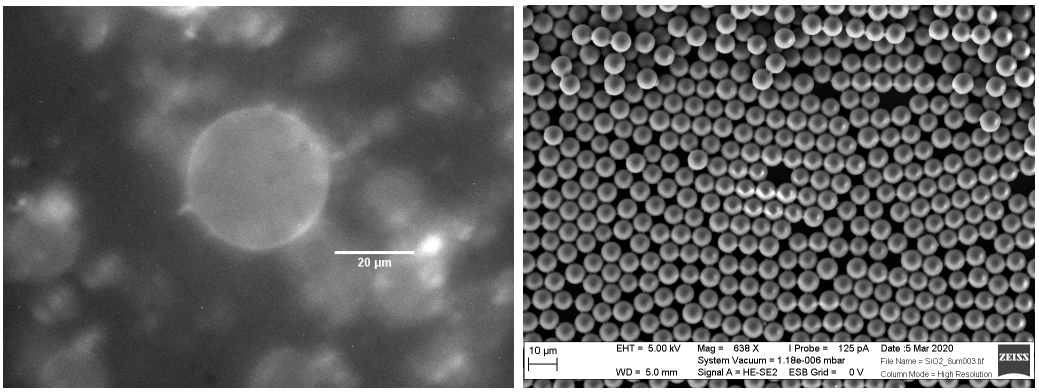

(a) Giant unilamellar vesicle imaged by fluorescence microscopy.

(b) Scanning electron microscopy of mono- and doublelayers of silica nanoparticles.

Figure 27: Imaging the two key components of the model system.

To study the nanoparticle uptake as function of phase state, giant unilamellar vesicles are suspended in aqueous salted buffer. The phase state is carefully adjusted by precise temperature control using a peltier element are on top of the container and a thermocouple. After temperature equilibration, nanoparticles are exposed to the vesicles and recorded via fluorescence micrographs. The fluorescent micrographs are presented in figure 28c. Here, the shrinkage of a giant unilamellar vesicle is visualized as a time series. As an image contains only 2D data, the quantity *surface area shrinkage* is accessed by assuming a spherical shape of the vesicle and associated basic geometrical calculations. A resulting characteristic shrinkage time series is presented in figure 28b.

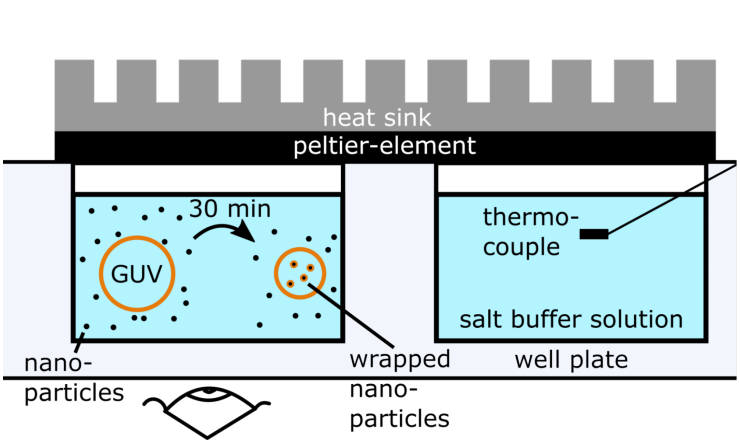

(a) Experimental setup

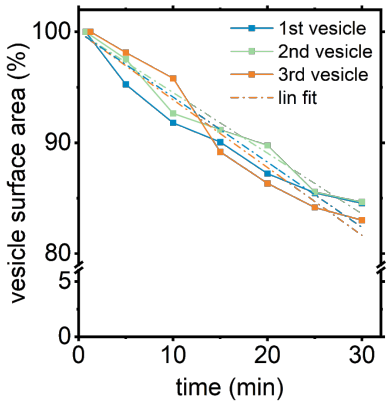

(b) Characteristic shrinkage kinetic

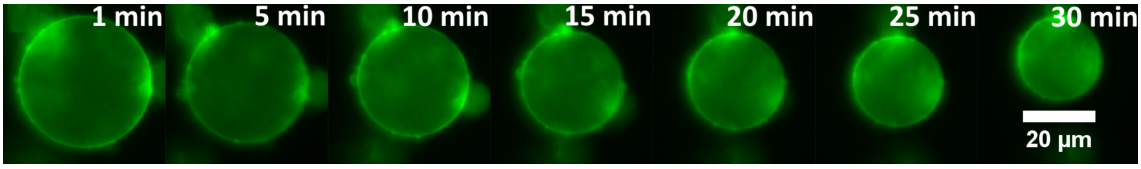

(c) Giant unilamellar vesicles fluorescent micrographs

Figure 28: Nanoparticle uptake experiment

Calorimetry on Vesicles

The comparison of nanoparticle uptake rates and the membrane state requires a calorimetric measurement of the excess heat capacity of the system to identify the main phase transition region. On the one hand, the excess heat capacity $\Delta c_p(T)$ of giant unilamellar vesicles is presented in figure 29, as well as the excess heat capacity of multilamellar vesicles. The excess heat capacity of giant unilamellar vesicles show the characteristic pretransition T_p = 21 °C and the main transition at T_m = 34 °C. The transition peaks display a FWHM of $\mathrm{FWHM_p}$ = 1 K and $\mathrm{FWHM_m}$ = 1.5 K. In contrast, multilamellar vesicles display characteristic temperatures at T_p = 21.8 °C and T_m = 33.9 °C, with their main transition being much sharper at $\mathrm{FWHM_p}$ = 2.3 K and $\mathrm{FWHM_m}$ = 0.3 K. This is a well-known effect arising from the strong cooperativity of multilamellar vesicles, which has been reported before and is in accordance with literature [31].

4.1 Shrinkage Rate as Function of Time and Shrinkage

On the other hand, nanoparticle uptake is a complex function of phase state. Comparison of uptake rates is challenging because the rate is not constant as function of

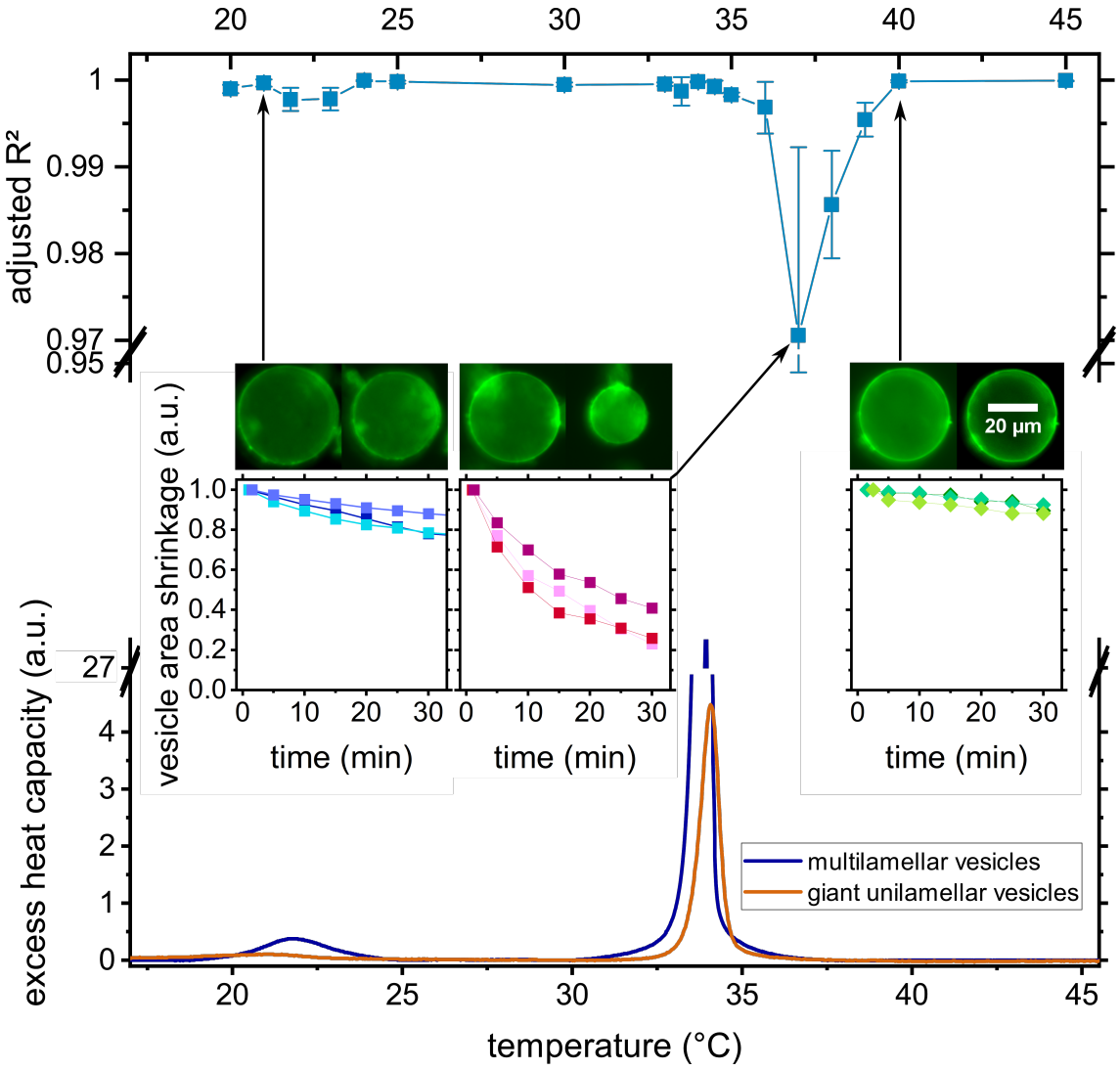

Figure 29: R^2 as a function of temperature and therefore phase state. A measure for the phase state is the excess heat capacity. The two peaks indicate two phase transitions, a pretransition at T_p = 21 °C and a major transition at T_p = 34 °C for 15:0 PC. The fluorescent micrographs visualize the start and end sizes originating from the nanoparticle uptake (∅ = 60 nm). Quantitative data about the kinetic is respectively presented below the micrographs, which is the reduction in vesicle surface area as function of time.

time. To account for this and to visualize it, figure 29 presents the adjusted R^2 value of the linear fits. On the one hand, by far most data points are close to 1, implying a good accuracy for the linear fit. The linear trend suggests further shrinkage for

longer observation time, which is in accordance with postulated unlimited regimes. On the other hand, few adjusted R^2 values deviate from 1 in figure 29, implying a worse accuracy of a linear fit. The inset kinetics in figure 29 show a distinct curvature indicating an asymptotic, saturating trend. To achieve better fitting quality, these data points were fitted using exponential functions. However, the additional fitting parameters of the exponential function make the comparison obsolete. Note, that the non-linear uptake rates are in proximity of the phase transition regions, indicating a correlation of phase transition and NP uptake.

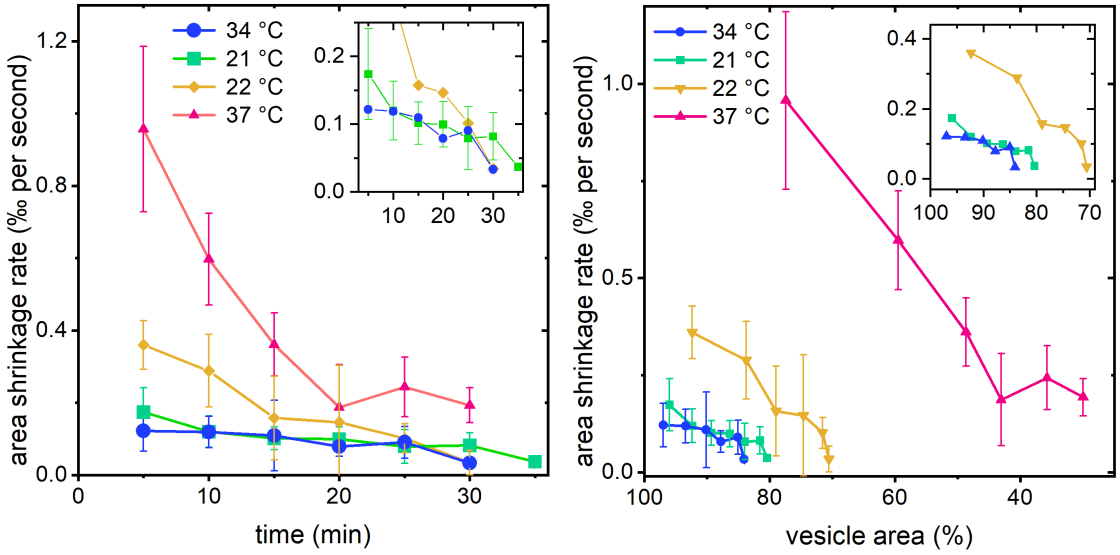

(a) ...time. (b) ...vesicle area.

Figure 30: Vesicle surface area shrinkage rate as function of...

To dive deeper into the data, we analyze the time evolution of the vesicle area shrinkage rate for four temperatures of interest. The results are presented in figure 30a. Note that all curves are steadily declining and are clearly not constant. This is somewhat surprising, as the presented linear fits expect constant rates. In contrast to all other trends, the shrinkage rate evolution at $T = 37\,°C$ is the only temperature, at which shrinkage has notably reached a saturation at around 0.2 ‰ per second. All the other curves continuously decline, while $T = 37\,°C$ is rather constant over a time span of $t = 10\,\text{min}$, until the observations ends.

Figure 30a contradicts the conclusion from the paragraph discussing the R^2 data from figure 29. It was concluded, that if $R^2 = 1$, this suggests unlimited uptake at this temperature. However, as figure 30a provides quantitative information on the shrinkage rate as function of time, the conclusion has to be revisited. The monotonic decrease of shrinkage rate of the presented temperatures $T = \{21\,°C; 22\,°C; 34\,°C\}$

suggests a limited uptake - unless the approach is asymptotic. This is not true for $T = 37\,°C$, as the shrinkage rate is constant over a time span of $t = 10\,\text{min}$.

Figure 30b supports this conclusion. Here, the same data is plotted against the vesicle relative area. All shrinkage rates decline monotonically and seem to approach 0, especially $T = 22\,°C$, which declines even faster than the others. Once again, this is not true for the vesicles at $T = 37\,°C$. At this temperature, the vesicles show a saturation at moderate shrinkage rates, suggesting unlimited uptake.

The shrinkage rate limits are interesting to study and were not in the center of attention at the time these measurements were conducted. Interesting questions arising are what exactly causes this shape of shrinkage rate time evolution. This could be studied by using Laurdan as a dye instead of Hydroxyethanesulfonate (DiOC-14). Laurdan could be used to monitor the chain order during the nanoparticle uptake. However, the experimental setup should be reconsidered, as it is not exactly advantageous for continuous measurements, nor in the collapsing region of the vesicle at small diameters.

The following paragraphs focus on the beginning of the kinetic, where the physics are more defined. In this region, the nanoparticles are freshly exposed to the vesicles, resulting in maximal shrinkage rates - depending on the starting conditions, which is precisely our interest. Therefore, in the following, we simplify the shrinkage rate to a constant value, which is a good approximation for the beginning of the time series. The results are presented in figure 31a.

4.2 Shrinkage Rate as Function of Temperature and Phase State

Figure 31a presents the shrinkage rate as function of temperature and therefore phase state. The value range is between 0‰ and 1 ‰ per second. More importantly, the shape of the function is qualitatively similar to the shape of the excess heat capacity, as the shrinkage rates exhibit peaks in proximity of both phase transitions. However, a systematic shift exists towards slightly higher temperatures.

The relative position of the shrinkage rate peak is observed at $T_{\text{p}'} = T_{\text{p}} + 1\,\text{K}$ for the pretransition and at $T_{\text{m}'} = T_{\text{m}} + 3\,\text{K}$ for the main transition. Interestingly, the amplitudes of the peaks are not proportional to neither the shrinkage rate curve, nor the excess heat capacity. As the vesicle area shrinkage rate is not proportional to the excess heat capacity and therefore the enthalpic characteristics of the phase transition, the sensitivity might be rather to the structural changes. Structural changes are e.g. membrane thickness, lateral order or spatial distribution of ripples.

In this context, non-enthalpic differences between the phases have been studied by De Haas *et al.* [222]. In this study, they conclude that in the fluid phase, the

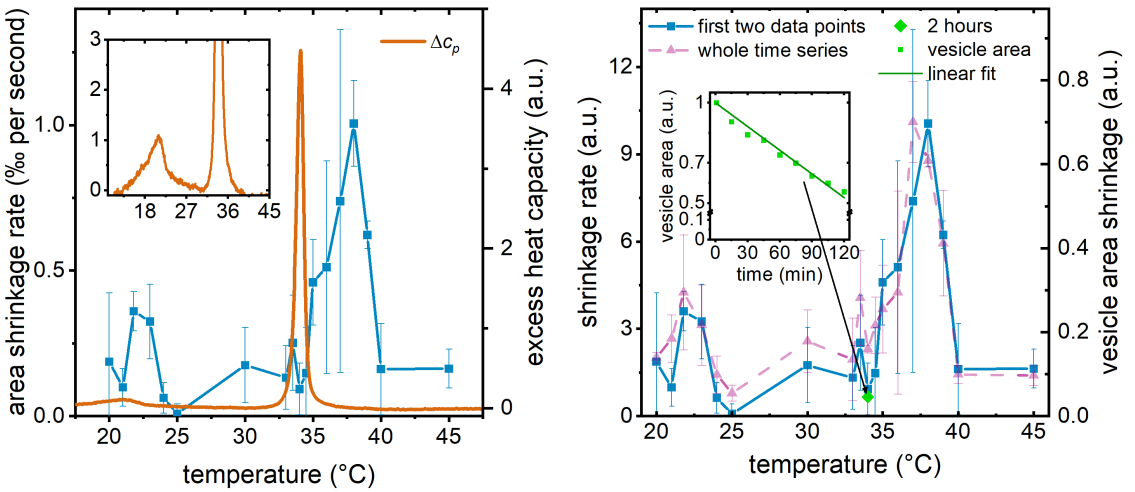

(a) ... relative to the excess heat capacity.

(b) ... evaluated using the first two data points vs. using a linear fit over the whole time series - normalized for comparability.

Figure 31: Vesicle area shrinkage rate as function of temperature for 15:0 PC giant unilamellar vesicles and silica nanoparticles ($\varnothing = 60\,\mathrm{nm}$, $c = 1\frac{\mathrm{m}^2}{\mathrm{l}}$)...

entropic repulsive force due to thermal undulations is larger than the van der Waals attraction. In contrast, for the gel state, both quantities are comparable. Therefore, at the phase transition, there is a change of the vesicle interaction from a weak attraction below the main phase transition temperature to a repulsion above.

However, in *in vitro* cell experiments on nanoparticle uptake at $T = 37\,^{\circ}\mathrm{C}$ and $T = 4\,^{\circ}\mathrm{C}$, opposite results have been found [189]. At low temperatures, nanoparticle uptake halts, whereas at high temperatures, nanoparticle uptake thrives. Although the exact T_m has not been reported for the human adenocarcinomic alveolar basal epithelial A549 cells (A549 cells), if we assume a similar $T_\mathrm{m} \approx 15\,^{\circ}\mathrm{C}$ as HeLa cells, the experimental temperature has been chosen low enough to reach the gel phase [219]. In conclusion, the findings of De Haas *et al.* might not be the dominant mechanism for impeded nanoparticle uptake at low temperatures in A549 cells.

Nevertheless, in the study of Lesniak *et al.*, the temperature resolution consists of just 2 data points. Further investigation improving resolution on the temperature axis would be interesting. Particularly because nanoparticle uptake seems not to be very sensitive on the quantitative enthalpic change, as concluded from figure 31a. In contrast, the conclusion suggests a stronger sensitivity of the uptake rates on the structural effects. To investigate such structural effects further, we focus on the silica-phosphocholine surface interaction in the following.

4.3 Silica-Phosphocholine Adhesion as Function of Temperature

To revisit figure 31a, the vesicle area shrinkage rate maximum is shifted relatively to the phase transition temperature by $\Delta T = +3\,\mathrm{K}$. At first, this shift on the temperature axis seemed like an artifact and we suspected an experimental flaw. However, to my surprise, peculiarities at $\Delta T = +3\,\mathrm{K}$ had been observed before to a quantitative extent. The studies elucidated the bending energy as function of temperature and they found the same relative peak temperature shift $T' = T_\mathrm{m} + 3\,\mathrm{K}$ [199, 201]. However, as a higher bending modulus would impede nanoparticle uptake, this would contradict our data. Therefore, the bending energy maximum is not the cause of the vesicle area shrinkage maximum. Note, that the bending modulus exhibits dips at the phase transition temperatures [201].

The contradiction can only be resolved by a thorough examination of changes of the physical situation, which is the nanoparticle-membrane interaction. When membrane adheres to nanoparticles, the chemical potential of the lipids changes when in contact with silica. This stabilizes the fluid phase of the membrane, quantitatively to $T'_\mathrm{m} = T_\mathrm{m} - 2.5\,\mathrm{K}$ for 60 nm nanoparticles [31, 223]. However, this does not resolve the contradiction yet, as this is the opposite direction on the temperature axis.

To resolve this contradiction, we study the adhesion energy as function of temperature and therefore phase state. To access this quantity, we conduct atomic force spectroscopy of a silica bead glued onto a tip-less cantilever and approach a supported lipid bilayer as function of temperature, as illustrated in figure 32a and described in detail in section 9.2. Note, that in the following experiments, 14:0 PC is used instead of 15:0 PC, due to experimental convenience. This mainly concerned higher evaporation rates of the buffer solution for 15:0 PC, as operating temperatures are $T_\mathrm{m} \pm 10\,\mathrm{K}$ and therefore up to $T = 45\,^\circ\mathrm{C}$. However, I do expect full comparability of the qualitative results. The results are presented in figure 32b.

Figure 32b shows a typical force distance curve with the characteristic adhesion jump on the retraction. However, the figure shows another retraction without an adhesion. Many efforts were taken to account for a thorough examination if this was an artifact or not. The frequency of these non-adhesive retraction peaks around the phase transition temperature $T_\mathrm{m} = 24\,^\circ\mathrm{C}$. The quantitative results of the non-adhesive frequency as function of temperature is presented in figure 32c as a heat map. Clearly, in the far fluid state, almost all retractions contain adhesive retractions. However, in the proximity of the phase transition temperature, adhesive retractions collapse, both in frequency and in absolute counts. To be clear, this is not a result of a lack of trials and measurements.

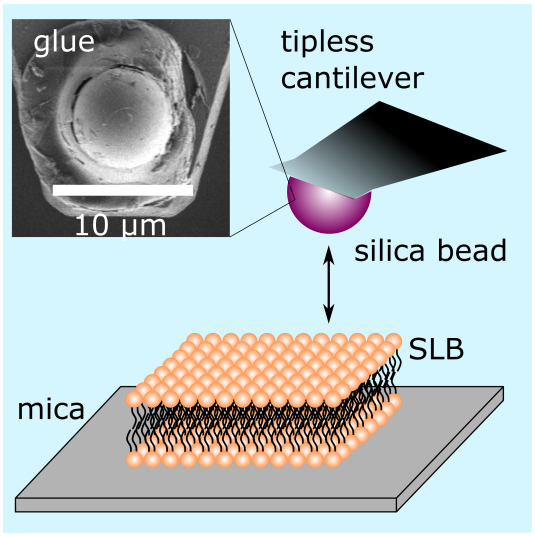

(a) Illustration of the experiment.

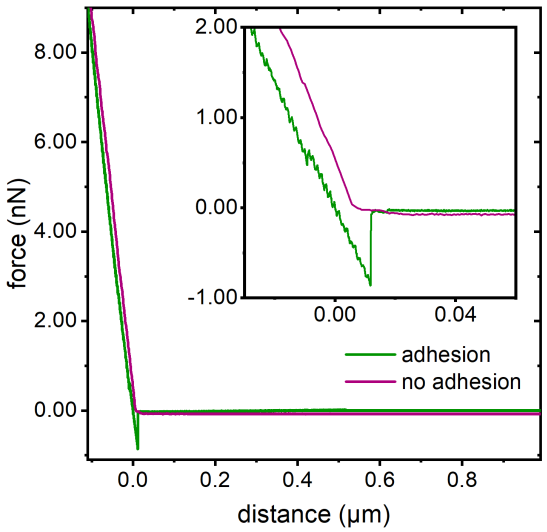

(b) Force distance curves of a silica bead on a DMPC supported lipid bilayer. Both curves display retractions.

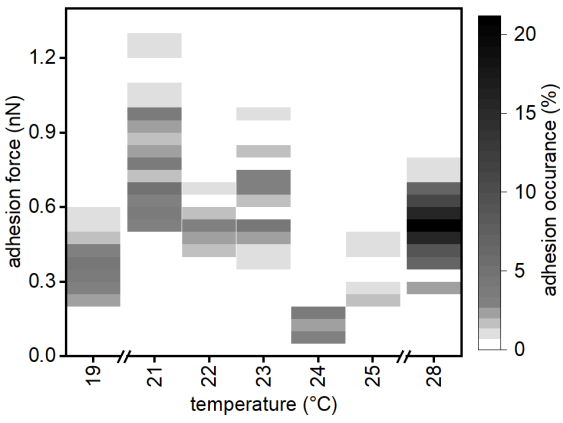

(c) Heat map of the adhesion force as function of temperature.

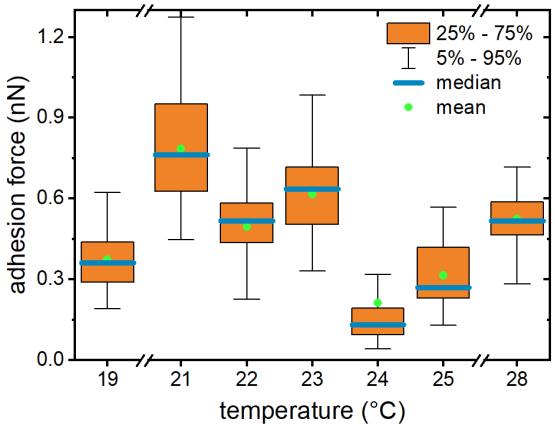

(d) Box plot of the adhesion force and occurrence frequency as function of temperature.

Figure 32: Atomic force spectroscopy of a silica bead on a supported lipid bilayer as function of temperature ([NaCl] = 75 mM).

The paradox is, that to evaluate an adhesion energy, it is crucial to identify an adhesion peak. However, if the adhesion energy collapses close to 0, the data will be filtered out and treated as an artifact. Only non-zero adhesion events will contribute to the data presented, which is a form of bias. Therefore, using this method, it is not possible to discriminate real zero-adhesion-energy and artifacts. However, for close-to-zero-adhesion-energy and above, this method is accurate and beneficial.

Furthermore, the very lack of adhesion events does contain information, as well. Therefore, figure 32c is the best evidence of the collapse in adhesion energy close to the phase transition.

To be certain on this result, we checked for reproducibility: First, we measured a significant adhesion occurrence frequency at $T = 28\,^{\circ}\mathrm{C}$. Secondly, using the very same setup, we immediately changed the temperature to $T = 24\,^{\circ}\mathrm{C}$ and measured hardly any adhesion events. Thirdly, still using the very same setup, we changed back to $T = 28\,^{\circ}\mathrm{C}$ and measured restored adhesion occurrence frequency. Thus, we can conclude that the adhesion energy is a function of the phase state and the adhesion energy collapses at the phase transition temperature.

This result is not solely supported by the frequency of adhesion occurrence, but by the measured quantitative adhesion force, as presented in figure 32d. While the adhesion force of $F_{\mathrm{adh}} = 0.5\,\mathrm{nN}$ is equivalent to the adhesion energy of about $E_{\mathrm{adh}}(28\,^{\circ}\mathrm{C}) = 0.5\,\frac{\mathrm{mJ}}{\mathrm{m}^2}$, our results match well with one of our previous studies [214]. However, around the phase transition temperature, the adhesion energy is about $E_{\mathrm{adh}}(24\,^{\circ}\mathrm{C}) = 0.1\,\frac{\mathrm{mJ}}{\mathrm{m}^2}$, strongly suggesting a collapse. Due to the methodological bias at zero-adhesion-energy, we can not tell if $E_{\mathrm{adh}}(24\,^{\circ}\mathrm{C}) = 0$.

Future experiments could further elaborate on these findings. To somewhat avoid the bias by potentially discarding zero-adhesion-retractions, I propose the following setup. Bring the silica bead and the supported lipid bilayer into contact and exert a constant retraction force on the cantilever, which is smaller than F_{adh}. At this point, vary the temperature and check if the silica bead is still in contact or retracting. If the adhesion energy collapses at the phase transition temperature, the cantilever will retract even at low forces. The system will behave like a switch in terms of adhesion - also known as all-or-nothing-like behavior in biology.

To be clear, cells could tune the adhesion of various substances by tuning their lipid composition, which in turn changes T_{m}. Another way to change T_{m} is by an altered protein expression, as well as direct protein mediated binding, which in turn mediating membrane state and thus adhesion. Most likely, a combination of all mechanisms are involved. A sinusoidal modulation on the retraction force, instead of being constant, will bring further insights on the sharpness of the transition. Additionally, further investigation on adhesion at the pretransition T_{p} is an interesting task for future work.

Summarizing, membrane nanoparticle uptake is strongly a function of phase state. Phase state governs the undulation forces and therefore the adhesion energy. This has been experimentally verified by measuring shrinkage rates being a function of temperature and even shrinkage. Quantifying shrinkage rates as function of time further enables us to identify limited uptake regions, as well as unlimited

ones. Furthermore, force spectroscopy of silica beads on membranes allows for quantification of the adhesion as function of phase state. Interestingly, adhesion energy collapses at the phase transition temperature, being in accordance to the reported shift in undulation forces reported in literature.

It would be intriguing to conduct analog experiments closer to biological reality. This could be achieved by using cell membranes, as well as a defined protein corona on the silica bead, e.g. by dipping it in bovine serum albumin (BSA) prior to experiments. Also, a study on various substrate materials would be insightful, as studies have shown different excess heat capacity shapes, where the leaflets melt either independently and decoupled on SiO_2, or cooperatively on gold [224].

Having gained fundamental insight into the nanoparticle uptake as function of phase state, we will go one step further. From the very specific system of endocytosis-like nanoparticles, we will go towards more general permeabilization mechanism, which is pore-mediated. We will use the pore-mediated mechanism to build a tool for small and large molecules *in vitro* cell permeabilization.

5 Permeabilization of Living Cells and Vesicles

The precise control of permeabilization is vital for cells. In this section, I present the results of the work published by Kamenac *et al.* [159], Färber, Reitler, and Kamenac *et al.* [51], and from three masters thesis projects by Katharina Biechele [225], Felix Schilberth [226], and Nicolas Färber [216], which were all supervised by me. In the publication and the master thesis projects, the focus is on designing, building, and optimizing measurement setups for suspended and adherent *in vitro* cell permeabilization - as well as quantifying the permeabilization and putting it into perspective to existing methods and literature.

5.1 Permeability of Vesicles as Function of Temperature and Shear Rate

As elaborated on in the previous sections, phase transitions alter membrane properties drastically. In this context, Blicher *et al.* has reported phase-transition-induced permeabilization. At this point, we pick up this result and take it further by applying it on *in vitro* cellular model systems. However, first things first - we start by reproducing these results.

5.1.1 Permeability as Function of Temperature in Artificial Membranes

Blicher *et al.* showed that artificial membranes are most permeable at the phase transition [141]. Permeability has no inherent direction, the term refers to cargo going from the exterior to the interior and *vice versa*. We make use of this *vice versa* principle to build a simplified setup, where giant unilamellar vesicles are filled with Calcein from the beginning and lose their cargo when permeabilized.

Once the giant unilamellar vesicles are transferred to a dye-less solution, the dye escapes the vesicle interior through transient pores. This dye escape is proportional to the loss in intensity on a micrograph. Figure 33a shows a micrograph of such a pore-mediated depletion of Calcein from a giant unilamellar vesicle into the exterior.

To reproduce Blicher *et al.* quantitatively, intensity loss time series are measured at several distinct temperatures. Figure 33b presents the dye depletion as function of time for 14:0 PC giant unilamellar vesicles, which has a $T_\mathrm{m} = 24\,^\circ\mathrm{C}$. Clearly, the depletion kinetics show low permeability for the gel state at $T = 17\,^\circ\mathrm{C}$, slightly higher permeability at $T = 31\,^\circ\mathrm{C}$, and highest permeability for $T = T_\mathrm{m}$. Concluding, we qualitatively reproduced the study by Blicher *et al.*

Having extensively studied the effect of shear rate on membrane phase transition temperature in section 3.1, we combine this with permeability studies in the following.

Surprisingly, an unexpected behavior arose - all-or-nothing-like permeabilization of vesicles.

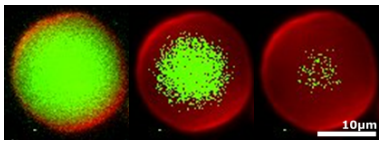

(a) Micrographs of GUV Calcein depletion as function of time from left to right.

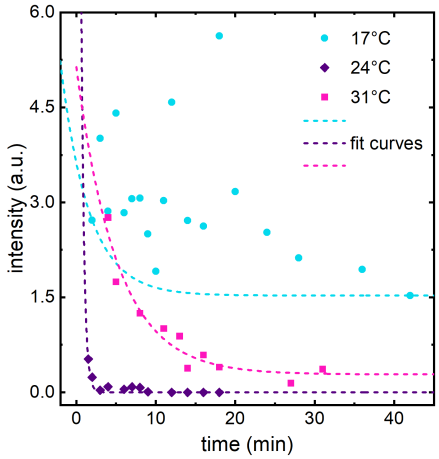

(b) Quantitative Calcein depletion kinetics of GUV at various phase states.

Figure 33: Calcein depletion of 15:0 PC GUV as function of temperature and time ([FITC – Dextran] = 5 µM). Simplified and visualized reproduction of Blicher *et al.* [141].

5.1.2 All-Or-Nothing-like Permeabilization of Vesicles

We study the permeability as function of shear forces by pumping vesicles through microfluidic tubings and compare micrographs before and after the shear treatment. Therefore, we fill giant unilamellar vesicles with FITC-Dextran already at the fabrication stage. The vesicle flow is carefully adjusted with the help of a syringe pump. Most important, the temperature is precisely controlled by placing the tubings into a heat bath. The results are published [51] and presented in figure 34.

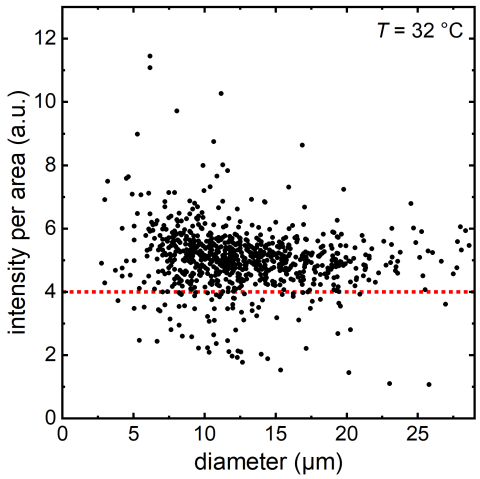

(a) Fluorescence intensity scatter plot of dye content of giant unilamellar vesicles after shear flow at $T = 32\,°\mathrm{C}$.

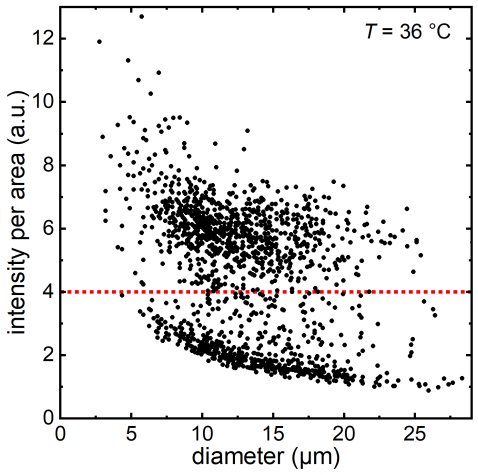

(b) Fluorescence intensity scatter plot of dye content of giant unilamellar vesicles after shear flow at $T = 36\,°\mathrm{C}$.

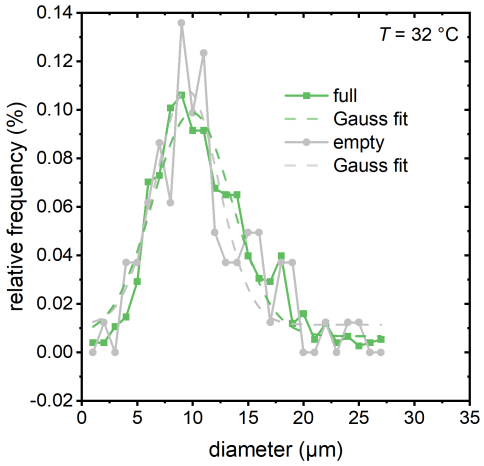

(c) Histogram of figure 34a.

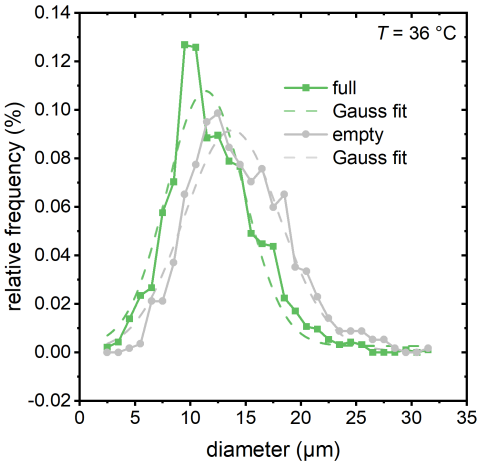

(d) Histogram of figure 34b.

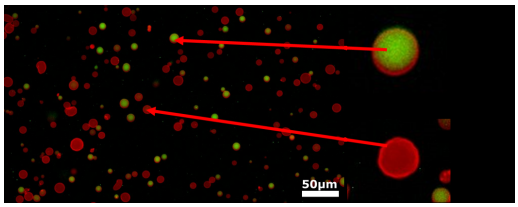

(e) All-or-nothing-like behavior of vesicle depletion after shear flow treatment at T_m. Adapted from [51].

Figure 34: 15:0 PC giant unilamellar vesicles were filled with FITC-Dextran and shear flow treated at $\dot{\gamma} = 500\,\frac{1}{\mathrm{s}}$. The discrimination between "full" and "empty" utilizes the highlighted intensity threshold value at $I = 4$. The vesicles were filled with [Glucose] = 100 mM and suspended in equimolar Sucrose solution.

The scatter plots in figures 34a and 34b show the raw data of the micrographs - mean intensities per area for a flow rate of $\dot{Q} = 2\ \frac{\mathrm{ml}}{\mathrm{h}}$. The temperatures were adjusted to be in the deep fluid phase and in the deep gel-like phase. For the gel-like phase, a single population is visible with few statistical outliers in all directions. However, for the fluid phase, suddenly two populations arise.

To be clear, this result was unexpected to us. We expected a single population for all temperatures, just like in figure 34a. According to our expectations, the system would be sensitive the phase transition and therefore the population would gradually shift far away from T_m and sharply at T_m. However, by looking at the micrographs from the shear flow treated samples, the dual-population-behavior is elegantly visualized in figure 34e. In this micrograph, "full" and "empty" vesicles are visible to the naked eye.

Consequently, we started searching for biases in our experimental setup. One idea was the possibility for a size bias, where the flow in the tubings could possibly burst larger vesicles or filter smaller vesicles out, which respectively could be contributing disproportionately to the fluorescence intensity. However, this is ruled out by analyzing histograms of the vesicles sizes before and after shear treatment. They show no significant differences, as presented in figures 34c and 34d. The interested reader might refer to the original publication, which contains further reference measurements [51].

I would like to emphasize, that this finding is qualitatively different from Blicher *et al.* [141]. Experimentally, the only significant difference is the flow. Therefore, shear flow has to be involved in the interpretation of the results in the following.

As a parabolic flow profile is present in the tube, the according shear profile is linear (see section 2.3.3). Therefore, the vesicles experience a shear force range between $0 < \dot{\gamma} < \dot{\gamma}_\mathrm{max}$, where the maximum shear force acts at the channel wall. The exact shear force acting on a vesicle depends on its diameter d, as the shear rate is defined as $\dot{\gamma} = \frac{v}{d}$. However, there is a special case for at the region of the center axis of the tube. Here, some vesicle cross the center axis, which causes the crossed part of the vesicle to be sheared in the other direction. Therefore the maximum shearing ranges from the part of the vesicle in the very center to the farthest part from there. As a result, the lowest shear rate achievable is $\dot{\gamma}_\mathrm{min} = \frac{v}{\frac{d}{2}}$.

However, it is questionable, how frequently vesicles are exactly centered to the middle of the tube or within a vesicle radius distance. The assumption to be normally distributed over the tube cross-section is justified - but is only exactly true at the beginning of the tubings. The non-inertial lift force draws the vesicle towards the tube center, which distorts the normal distribution [227]. Yet, the non-inertial lift force decreases for increasing convergence to the center axis. Nevertheless, if the

vesicle permeabilization displays a threshold behavior, above which the vesicles deplete, the shear rate has to be in that range.

There is a study in literature, which reports threshold behavior of vesicles at the phase transitions as function of shear rate [222]. They found phase transitions at critical shear rates in the order of $\mathcal{O}(1\,\frac{1}{\mathrm{s}})$. However, this value is a nonlinear function of temperature, as the critical shear rate vanishes above the phase transition temperature. The $Q = 2\,\frac{\mathrm{ml}}{\mathrm{h}}$ used in this experiment result in a shear profile ranging in $\dot{\gamma}_{\mathrm{min}} \approx 0\frac{1}{\mathrm{s}} \leq \dot{\gamma} \leq \dot{\gamma}_{\mathrm{max}} = 100\,\frac{1}{\mathrm{s}}$, covering the critical shear rate range. However, the comparison should be handled with care, as the lipid system differs, e.g. in lamellarity.

Summarized, a shear-induced phase transition, as reported in De Haas *et al.* [222], combined with a continuous range of shear forces acting on the vesicles, could be the reason for the separation into two populations. However, further investigations on this topic would be intriguing, as a seemingly highly mechanistic system acts probabilistic.

5.1.3 Quantitative Permeabilization of Vesicles as Function of Distinct Shear Rate and Temperature

To engage into the all-or-nothing-like permeabilization behavior quantitatively, further experiments have been conducted. In the scatter plot from figure 34b, we apply the threshold in intensity to discriminate between "full" and "empty" vesicles. This discrimination allows to display the fraction of empty vesicles as function of temperature for various shear rates. The results are presented in figure 35.

The pre- and post-transition level of the step-function show peculiarities. For the two low shear rates, $500\,\frac{1}{\mathrm{s}}$ and $100\,\frac{1}{\mathrm{s}}$, the pre-transition level is similar and low. In this regime almost all vesicles do not permeabilize and do not lose cargo. Once the phase transition temperature regime is reached and exceeded, a significant portion of vesicles are permeabilized and lose their cargo.

By a carefully analysis of the experimental procedure, we could identify a bias for the step-like behavior. To conduct the experiment, the vesicles are taken out of the fridge ($T_{\mathrm{fridge}} \lesssim 8\ ^{\circ}\mathrm{C}$) and heated to the equilibrium temperature of the experiment. If the temperature of the experiment is higher than the phase transition temperature, the vesicles have to cross the phase transition temperature. Therefore, it is not possible to conduct experiments at higher temperatures than the phase transition temperature, without the bias from crossing the phase transition temperature. The bias induced by crossing the phase transition will be elucidated in the following.

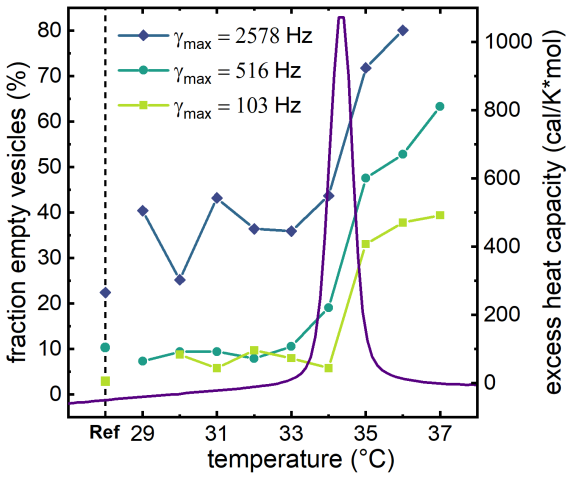

Figure 35: GUV permeability as function of temperature and shear rate. Permeability was measured by the fraction of full and empty vesicles. Permeability is a step-like function of shear rate and displays a all-or-nothing behavior. Additionally, shear forces shift the phase state of the vesicles towards lower temperatures. Adapted from our publication [51].

The major cause of depletion of FITC-Dextran from the vesicles is by formation of spontaneous pores [141]. Accordingly, the amount of work required to form a pore is proportional to the compressibility [141], which is known to collapse at the phase transition [201]. Consequently, the number of pores formed for the low shear rates on the low-temperature-side of the step-function is negligible. Once the phase transition is reached, a significant number of pores are introduced into the system, enabling depletion.

Many studies report a stabilization of pores and widening by orders of magnitudes by an external force [195]. Therefore in combination with softening at the phase transition, we strongly assume stabilization of vesicle pores by shear forces and the phase state. This could also be the reason, why depletion in the post-transition regime is enhanced, as the phase transition regime was crossed and the formed pores were still present due to stabilization.

At first glance, the measurements at the high shear rate of $\dot{\gamma} = 2500\,\frac{1}{\mathrm{s}}$ breaks the argument, as the level of the low-temperature-side of the step-function is significantly increased. The total curve still shows a sigmoidal behavior, as the vesicles permeabilization rises further in the transition regime and in the post-transition regime. However, firstly, the data should be considered in perspective to the already elevated reference value at static conditions. Secondly, this could be the consequence of overcoming a mechanical threshold to induce pore formation.

To challenge the interpretation of the sigmoidal function being caused by the bias, it is be necessary to rerun the experiment using vesicles resting in the fluid phase at room temperature, e.g. 14:0 PC or 13:0 PC. The results reveal the analog behavior [51]. This supports the experimental bias in crossing the phase transition temperature for experiments at $T > T_m$ and *vice versa* for experiments with lower T_m.

Summarized, vesicles are more permeable at higher shear rates, as well as at their respective phase transition temperature. This can not be explained due to spontaneous dye loss, as spontaneous pores are of size $r \lessapprox 1\,\text{nm}$ and the dye size is about $d = 2.3\,\text{nm}$. Furthermore, analog static experiments reveal no all-or-nothing-like behavior. Therefore, the all-or-nothing-like behavior must arise from applying shear flow to the system. In detail, the all-or-nothing-like behavior is a non-linear response of the pore formation to mechanical shear forces. The increased permeability for higher shear rates is likely to originate from mechanically induced shear-stabilized pores. Naturally, the next step is to study permeability on *in vitro* cells under shear flow.

5.2 Permeability of HeLa Cells as Function of Temperature and Shear Rate

Permeabilization studies of *in vitro* cells carry high expectations in the field of *Drug Delivery*, due to their potential therapeutic application. Before presenting the novel and published acoustofluidic permeabilization method, we focus on the dependence of drug uptake as function of shear force to finally draw quantitative conclusions on the enhanced model drug uptake.

5.2.1 Shear Flow Induced Permeabilization of Suspended Living Cells

The novel, acoustofluidic method, is a combination of various contributions, as elucidated in section 2.6.3. The acoustofluidic setup is described extensively in section 9.4. One by one, we will quantify the individual contributing mechanisms. The first permeabilization mechanism is pure shear flow, as reported earlier [228].

The exact setup of the pure shear flow is presented in figure 36a. In this setup, a cell suspension flows through a microfluidic channel and comes into contact with a model drug - a fluorescent dye. The results of the permeabilization by pure shear flow is presented in figure 36b and 36c.

In detail, the cells are exposed to shear stress within the microchannel without bulk contact to the dye, as illustrated in figure 36a. However, two mechanisms drive

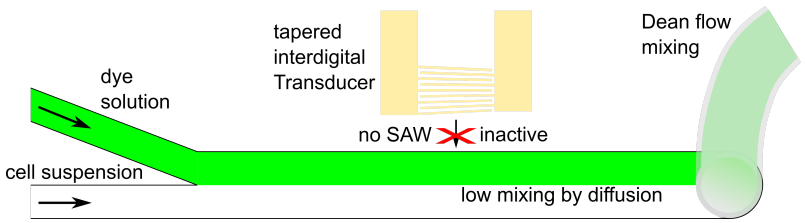

(a) Illustration of the experimental setup - at deactivated SAW.

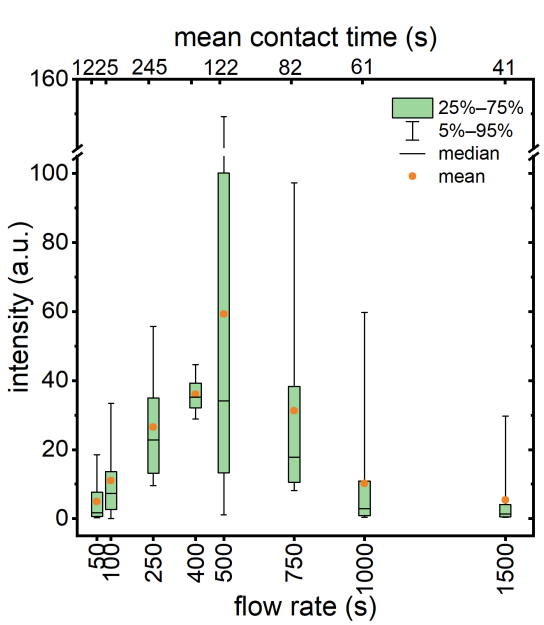

(b) Cell permeabilization as function of shear flow.

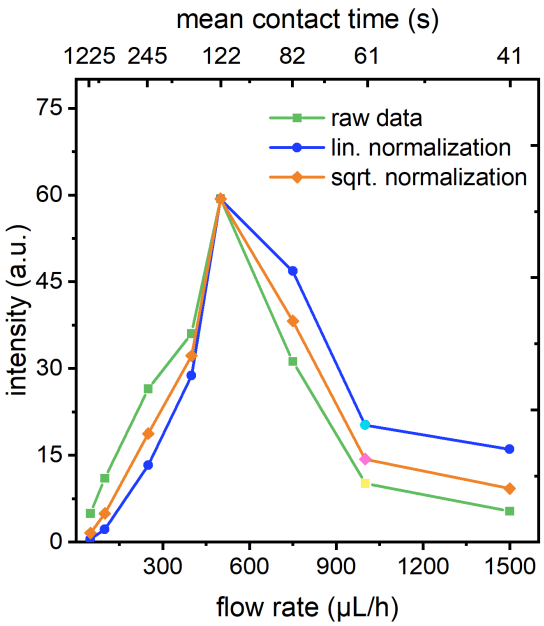

(c) Cell permeabilization as function of shear flow with a contact time correction factor.

Figure 36: Calcein uptake as function of temperature and shear rate. Adapted from [159].

mixing of the cell suspension and the dye solution. Firstly, diffusion is predominant at the interface of the cells suspension and the dye solution, along the microchannel. Secondly, Dean flow [229] finally fully mixes due to the high curvature at the outlet, which consists of the microchannel-tubing intersection. However, due to the low efficiency and short time span, diffusion-driven mixing is negligible.

For low flow rates $0\,\frac{\mu L}{h} \leq Q \leq 500\,\frac{\mu L}{h}$, the uptake increases linearly. For further increasing flow rates $Q \geq 500\,\frac{\mu L}{h}$, the uptake decreases. Interestingly, at $Q = 1500\,\frac{\mu L}{h}$, the uptake is comparable to quasi-static conditions at $Q = 50\,\frac{\mu L}{h}$. Reports from 2008 claim that permeabilization is a linear function of shear stress for cells [153]. However, our experiments show a clearly non-linear relationship. Interestingly, the error bar is large at the maximum permeabilization flow rate. This is in good agreement with

the peak-like, non-linear relationship, as small deviations on the x-axis - flow rate - result in a large variation on the y-axis - permeabilization.

At first glance, there seems to be a trivial solution for this finding. The constant length of the outlet tube limits the exposure time of the cells to the dye and thus quantified uptake. However, we account for the variation of exposure time as function of flow rate Q in figure 36c. Here, the original values are rescaled with a contact time dependent factor. In the end, the non-linearity persists and the finding of a pronounced maximum is conserved.

Additionally to the calculation, we test this hypothesis experimentally for robustness. As an additional reference experiment at a fixed flow rate of $Q = 1000\,\frac{\mu L}{h}$ and an outlet tube length of $l = 20\,\text{cm}$, we vary the exposure time by varying the length of the outlet tube. The results are presented in figure 37.

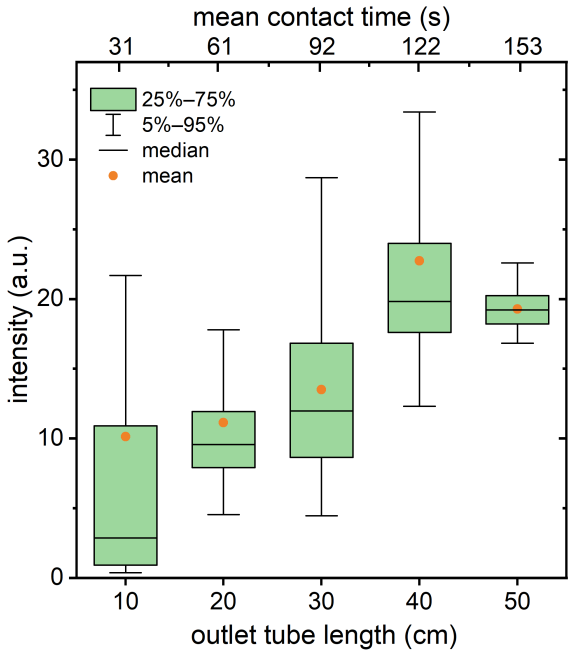

Figure 37: Cell permeabilization as function of outlet tube length and therefore contact time. Adapted from [159].

In accordance, cell permeabilization increases for increasing the outlet tube length at this flow rate. Interestingly, the increase is not greater than the factor of two, being consistent with the theoretical estimations in figure 36c. Taking these findings into account, the uptake mechanism is diffusive, as expected for a pore-mediated mechanism [230].

Sharei *et al.* found a saturation degree, where 70 % - 90 % of the total uptake happens in the first minute after treatment. This agrees well to our results for an

outlet tube length of $l = 40 - 50\,\text{cm}$. At this outlet tube length, the dye uptake saturates presumably due to pore resealing [230]. Strikingly, for a calculation with the mean flow velocity and an outlet tube length of $l = 40\,\text{cm}$, the mean cell-dye exposure time is $t = 122\,\text{s}$ in our setup, which differs from the literature value by a factor of 2. However, taking into account, that the major part of the cells travels close to the center (non-inertial lift forces, see [227]), the discrepancy of the mean velocity to the velocity at the center is a factor of 2. This eliminates the discrepancy to literature precisely.

Having quantitatively confirmed the findings by Sharei *et al.* [230], we have identified the permeabilization mechanism to be pore-mediated. However, pores are intrinsically transient and reversible, which has not convincingly been covered in literature, yet. This gap will be closed by the following experiments.

5.2.2 Reversibility of the Pore-Forming Mechanism

To test reversibility of this method, we add a pre-treatment to the experiment from figure 36b, as illustrated in figure 38. The pre-treatment consists of pumping the cell suspension at a high flow rate - $Q = 4000\,\frac{\mu\text{L}}{\text{h}}$ - through the same microchannel in order to activate the pore forming. Subsequently, we use the very same cells for an experiment in the style of figure 37. The results are presented in figure 39.

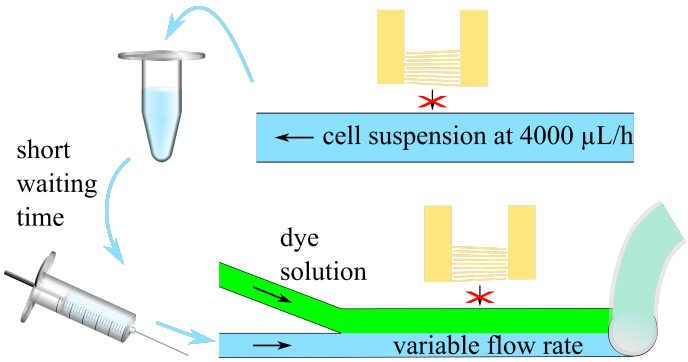

Figure 38: Illustration of the pre-treatment setup. After a shear treatment at $\dot{\gamma} = 4000\,\frac{1}{\text{s}}$, a $t = 10\,\text{min}$ waiting time is followed by additional experiments to quantify the uptake as function of shear rate. Adapted from [159].

Analogously to figure 36b, a distinct maximum appears in figure 39 for a flow rate of $Q = 500\,\frac{\mu\text{L}}{\text{h}}$. Therefore, the results of the experiment could be reproduced with an additional pre-treatment of the cells. A difference in the technical details of illumination diminishes the quantitative dye uptake.

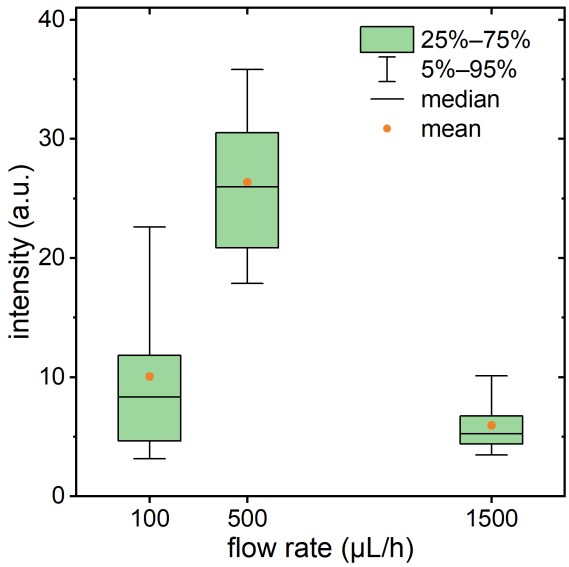

Figure 39: Reproduction of the results from figure 36b after pre-treatment from figure 38. Adapted from [159].

At this point, conclusions from the former experiments can be applied here. Firstly, formation of pores is a function of the compressibility [141], which is a function of the thermodynamic membrane state. Interestingly, a study has shown, that suspended HeLa cells are very close to the phase transition temperature at ambient conditions [219]. However, the same study has measured a shift of phase transition temperature as function of shear rates of the order of $\Delta T \approx 1\,\mathrm{K}$. Therefore, the shift in phase state is likely to be not predominant in the permeabilization by pure shear flow.

Secondly, we have proposed pore forming by mechanical stimulation [51]. In this study, the conclusion is not definitive and questions the pore formation by pure mechanical stimulation. Additionally, figures 36b and 39 show that permeabilization is a non-linear function of shear rate.

Summarizing, adding a high-shear-pre-treatment reproduces the results from the original experiment, which shows reproducibility and strongly suggesting a reversible pore-forming-mechanism.

We have thoroughly studied the permeabilization by shear forces of *in vitro* cells and found it to be reversible, pore-mediated, and a function of shear rate. These results are crucial for the fundamental experiments later in this section and crucial for the applied acoustofluidic permeabilization tool, which will be discussed next.

5.2.3 Acoustofluidic Trapping of Suspended Cells

As the contribution to permeabilization by pure shear flow has been quantified, we upgrade the complexity of mechanical stimulation employing surface acoustic waves. The surface acoustic waves in the microfluidic channel create trapping vortices and the corresponding pressure fluctuations. Note that by employing surface acoustic waves, the permeabilization and exposure to high dye concentrations happens at the same location and time. The setup is illustrated in figure 40.

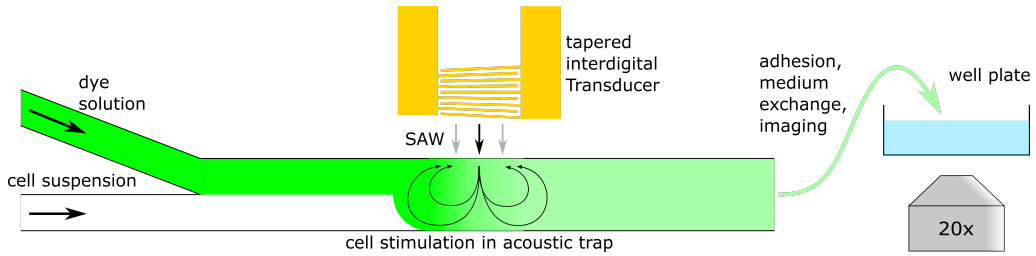

Figure 40: Illustration of the acoustofluidic permeabilization setup. Adapted from [159].

Surface acoustic waves couple into the microchannel and create vortices, which trap suspended cells, while a steady stream of dye solution flows by. This setup comes with three adjustment parameters, the surface acoustic wave input power level P, the flow rate Q, and the surface acoustic wave cycle duration t_{SAW}. Firstly, we vary and study P and Q, before we then focus on the surface acoustic wave cycle duration t_{SAW}. The results are presented in figure 41.

For these experiments, we keep the flow rate constant at $Q = 100\,\frac{\mu\mathrm{L}}{\mathrm{h}}$. No significantly enhanced uptake takes place for power levels up to $P = 28\,\mathrm{dBm}$. At $P = 29\,\mathrm{dBm}$, the cells are greatly permeabilized compared to the pure flow reference (see figure 36b, $Q = 50\,\frac{\mu\mathrm{L}}{\mathrm{h}}$, no SAW). The permeabilization is enhanced by a factor of 18 for the mean value. On the one hand, the large error shows that even significantly higher permeabilization is possible. On the other hand, this large distribution presumably can not be narrowed down due to the chaotic nature of the method. Various factors cannot be controlled, such as the dwelling time of the cells in the trap, or the exact occupied streamline in the vortex and thus shear stress.

The permeabilization decreases again at $P = 30\,\mathrm{dBm}$. At this power, cell death is promoted. Promoted cell death causes a decrease in mean cell density by an order of magnitude compared to $P = 29\,\mathrm{dBm}$.

Another explanation for the decrease in permeabilization efficiency is the intertwinement of the power level and the flow rate [160]. In this study, the authors found a requirement for good miscibility. Good miscibility requires a quantitatively similar

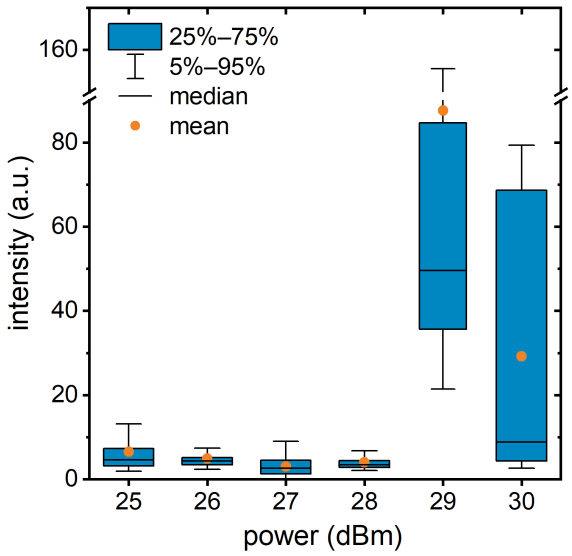

Figure 41: Permeabilization as function of surface acoustic wave power ($Q = 100\,\frac{\mu L}{h}$, $t_{SAW} = 1\,\text{min}$). Adapted from [159].

flow rate between the perpendicular flow generated from the surface acoustic waves and the flow along the channel. Therefore, a higher power level requires higher flow rates for an efficient trapping. We will test the applicability of this study in the following.

5.2.4 Mismatch of Flow Rates Diminishes Permeabilization

To test the hypothesis from the prior paragraph, we vary the flow rate at a purposely non-optimal constant power level of $P = 28\,\text{dBm}$, according to figure 41. The results are presented in figure 42.

As anticipated, permeabilization diminishes at reduced cell trapping efficiency for relatively high flow rates of $Q = 100\,\frac{\mu L}{h}$. However, at relatively lower flow rates of $Q \lesssim 80\,\frac{\mu L}{h}$, permeabilization is high. Quantitatively, at lower flow rates, the permeabilization is 8 times higher than at slightly higher flow rates, which demonstrates the volatility of the flow-matching-criteria. Interestingly, the enhancement factor quantitatively matches the enhancement factor from figure 42, exhibiting quantitative consistency.

Summarized, surface acoustic waves enhance permeabilization exceeding pure-flow-mediated permeabilization. Surface acoustic waves introduce a dual stimulation - an oscillating electrical field, as well as additional flow and therefore additional shear

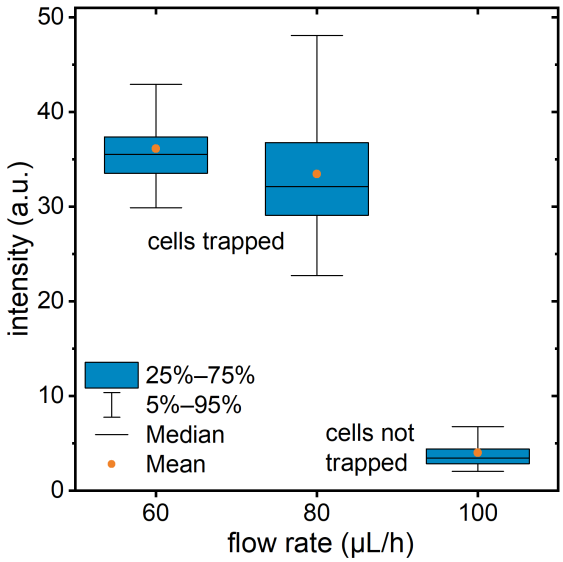

Figure 42: Permeabilization as function of flow rate. The sharp decline in permeabilization arises from the transition of trapped cells to untrapped cells. Adapted from [159].

forces. Conveniently, flow and shear forces are experimentally measurable, which will be studied in the following.

5.2.5 Quantification of the Flow Profile

Besides the approximated shear profile by calculation, we quantify the velocity and shear profile via particle image velocimetry - the interested reader might refer to Thielicke and Stamhuis [231]. The flow fields are visualized in figure 43 as a heat map. To draw a comparison, both flow profiles are needed - without and with SAW application.

The measurements reveal, that pure shear flow results in a maximal shear rate of about $\dot{\gamma} = 30\,\frac{1}{s}$. This is in accordance with the calculations assuming a parabolic flow profile. In contrast, surface acoustic waves increase the maximum shear rate by a factor of more than two.

The surface acoustic waves are visible as two vortices in the particle image velocimetry image. At those vortices, the shear rate is maximal. The cells being trapped in these vortices perceive continuous stimulation by these higher shear forces, which leads to an enhanced permeabilization.

It is not trivial to compare the surface acoustic wave experiment to a pure flow experiment at double the flow rate. At the first glance, a doubled flow rate

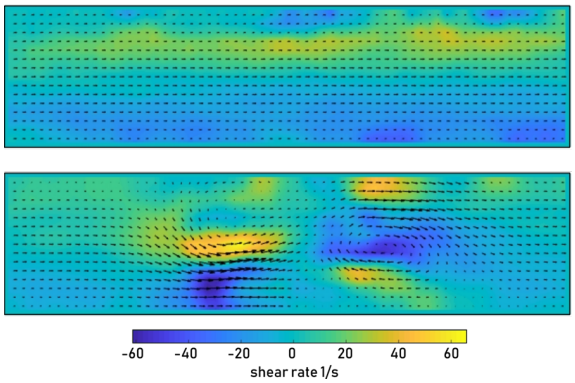

Figure 43: Particle image velocimetry to quantify the shear rate profile of the flow without (top) and with (bottom) surface acoustic waves. Adapted from [159].

would compensate the doubling in shear rate in the surface acoustic wave experiment. However, firstly, the factor of two is a conservative approximation, as the z-component is neglected by the projection onto the x-y-axis. Secondly, treatment times are not comparable, as cells are trapped in the vortices. Pure flow experiments entirely lack of this feature. Nevertheless, the increased permeability by surface acoustic waves indeed is partly explained by the increased shear rate.

To elaborate on the feature of trapping - especially in terms of time - we focus in the following on the surface acoustic wave cycle duration.

5.2.6 Optimal SAW Cycle Duration

The SAW cycle duration t_{SAW} marks the time the vortices need to sweep through the three frequencies. As at the end of this time, the cycle repeats, the vortices jump back spatially from the last position to the first position. This results in a release of all cells trapped in the vortices. Therefore, t_{SAW} is at the same time the maximum dwell time $t_{\mathrm{d,max}}$ and double the mean dwell time $t_{\mathrm{d,mean}}$. On the one hand, future experiments could improve the setup and equalize both times to achieve a narrow dwell time distribution. On the other hand, this setup realizes a broader spectrum of treatment, which could be of desirable.

To quantify the optimal SAW cycle duration, we vary this parameter at a given flow rate and power level ($Q = 80\,\frac{\mu\mathrm{L}}{\mathrm{h}}$, $P = 28\,\mathrm{dBm}$). The results are presented in figure 44. Permeabilization increases linearly as function of SAW cycle duration, until it reaches a maximum at $t_{\mathrm{SAW}} = 2\,\mathrm{min}$. Short t_{SAW} are similar in permeabilization to the quasi-static reference ($Q = 50\,\frac{\mu\mathrm{L}}{\mathrm{h}}$, no SAW, see figure 36b). The permeabilization enhancement factor is ≈ 13.

For $t_{SAW} > 2\,\text{min}$, the permeabilization decreases. This originates from the induction of increased cell death (mean cell density at $t_{SAW} = 6\,\text{min}$ is decreased by a factor of 4 compared to $t_{SAW} = 2\,\text{min}$). Keep in mind, that the evaluation method is conservative, as the cells are not evaluated immediately, but only consider those surviving even after a 2 hour incubation period. In total, the results suggest a trade-off between increasing permeabilization for higher trapping times and promoted cell death for even higher trapping times.

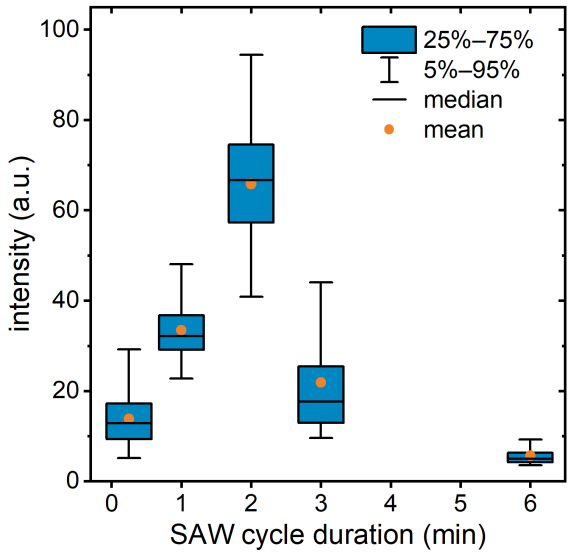

Figure 44: Permeabilization as function of SAW cycle duration. Adapted from [159].

As described previously, $t_{SAW} = 2\,\text{min}$ is equivalent to a mean dwell time $t_d = 1\,\text{min}$, which in turn agrees well with the saturation behavior from figure 36b and literature [230].

After a thorough measurement on the effect of potential of cell membrane permeabilization, it is worth taking a step back and exploring the mechanisms this is achieved with. Firstly, as the substrate is piezoelectric, an oscillating electrical field is part of the wave. The field strength is as high as $E = 10^4\,\frac{\text{V}}{\text{m}}$. Interestingly, this has been claimed in literature to be a major permeabilization mechanism [154]. However, we estimate this contribution to be negligible here, as the penetration depth (Debye length) is at the order of $\lambda_D = 1\,\text{nm}$ at the present salt concentration of $c(\text{ion concentration}) = 310\,\text{mM}$ [232].

Secondly, as discussed for figure 43, the trapping feature prolongs the exposure time to high shear rates. The prolongation by the vortices is the mean dwell time $t_d = 60\,\text{s}$ (for a SAW cycle time of 2 min), additionally to the travel time through the microfluidic channel $t \approx 6.9\,\text{s}$. Therefore, the exposure time to high shear rates differ

by an order of magnitude. This enables a higher energetic input into the membrane, which we expect to result in more transient pores [233].

Thirdly, the dye availability significantly improved. In contrast to pure shear flow, employing surface acoustic waves comes with a constant background mixing feature. The mixing ensures a homogeneous dye concentration *everywhere, all the time.*

To be clear, while permeabilization, the dye diffuses from the close surrounding of the cell into it. Once dye has diffused into the cell, the dye concentration diminishes in the cell proximity. Consequently, a depletion zone develops over time. This depletion zone is countered in pure shear flow only by diffusion driven mixing, as low Reynolds numbers are present. Diffusion driven mixing is negligible compared to the mixing feature of surface acoustic waves.

Finally, it might even be possible, that due to the vortex mixing, the dye is actively flushed into the cell, instead of relying on a diffusive mechanism. We confirmed the diffusive dye-uptake earlier only for the pure shear flow case. Modelling flushing-assisted dye uptake could be done by the artificially increased diffusion coefficient. The diffusion coefficient has to be anisotropical. The anisotropy must firstly account for the high shear rate zones of vortices. Secondly, it has to account for the cell trajectory and cell orientation, to account for the direction dependence of the flushing effect.

Any further discrimination in space and time is beyond the technical capabilities of the setup. However, it is possible to increase the value of this novel permeabilization method by studying the spectrum of uptake cargo.

Cargo Size Limits

To assess the efficacy of our novel permeabilization method over various differently sized cargo, we test various sizes of model compounds. The molecular weight spans about two orders of magnitude: Calcein (m_U = 0.6 kDa), FITC-Dextran (m_U = 10 kDa), and eGFP (m_U = 27 kDa). One technical peculiarity between these different fluorescent dyes is the varying amount of excitable fluorophores per dye molecule and thus molecular weight. To account for this, we measure the intensity of a constant mass concentration ($c = 0.2\,\frac{\mathrm{mg}}{\mathrm{ml}}$). The results are presented in table 3.

To test the limits of the cargo size to cross the pores, we conduct experiments with surface acoustic waves, analog to figure 41, as well as static control experiments. The results are presented in figure 45.

Table 3: Normalized dye brightnesses.

Fluorescent Species	Brightness	Dye Concentration	Molecular Weight
Calcein	1	0.2 $\frac{\text{mg}}{\text{ml}}$	0.6 kDa
FITC-Dextran	0.12	0.2 $\frac{\text{mg}}{\text{ml}}$	10 kDa
eGFP	0.46	0.2 $\frac{\text{mg}}{\text{ml}}$	26.9 kDa

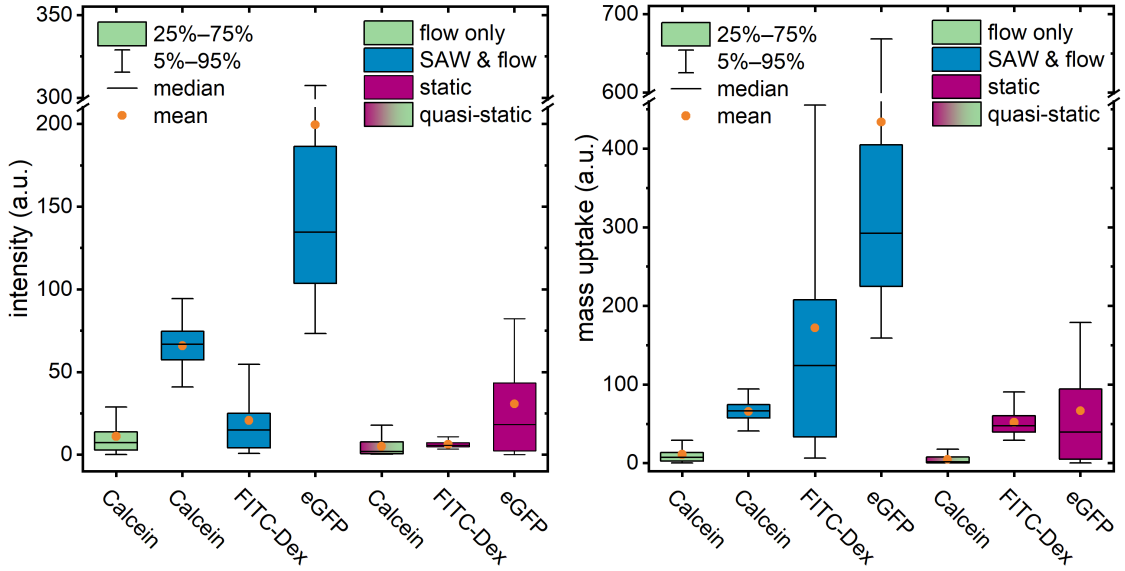

(a) Raw data of incorporated dye intensity. (b) Normalized to mass brightness according to table 3.

Figure 45: Permeabilization as function of cell treatment and dye (Q = 80 $\frac{\mu\text{L}}{\text{h}}$, P = 28 dBm, t_{SAW} = 1 min). Adapted from [159].

In this set of experiments, the permeabilization for acoustically trapped cells is enhanced about 6-fold for Calcein, which is in good agreement with the enhancement factor ≈ 8 of figure 42. In contrast, the enhancement factor for optimal conditions is 18, as shown in figure 41. The major contribution to the discrepancy of these enhancement factors arises from the gentler treatment (in figure 41: Q = 100 $\frac{\mu\text{L}}{\text{h}}$, P = 29 dBm, and t_{SAW} = 1 min; in figure 42: Q = 80 $\frac{\mu\text{L}}{\text{h}}$, P = 28 dBm, and t_{SAW} = 2 min). Interestingly, as the optimal SAW cycle duration has been identified to be t_{SAW} = 2 min from figure 44 and as the trend is linear, I would expect a doubling of the permeabilization for figure 41 from an enhancement factor of 18 to 36. Also, a uniform dwell time of t = 2 min by controlling the cell inflow to the vortex site would further enhance the factor.

Uptake FITC-Dextran is 3-fold compared to the static reference, whereas eGFP is 6-7-fold higher. This result at first glance is somewhat unexpected, as *a priori*, a bigger molecule is less likely to cross the same pore for two reasons.

First, sterical blocking of the pore edge and the cargo impede uptake. Second, the diffusion coefficient is a function of molecular weight, according to the Chapman–Enskog theory.

However, the first argument is not exactly valid, as molecular weight is not identical to size. The geometric body of Calcein is point-like compared to the size of the other molecules $d_{\mathrm{Calcein}}(m_{\mathrm{U}} = 0.6\,\mathrm{kDa}) = 0.7\,\mathrm{nm}$ [234]. eGFP is rather globular, therefore the size scales to the third root of its mass $d_{\mathrm{GFP}}(m_{\mathrm{U}} = 26.9\,\mathrm{kDa}) = 2.8\,\mathrm{nm}$ [235]. In contrast, the shape of FITC-Dextran is rod-like, causing a linear scaling of its length to its mass $d_{\mathrm{FITC-Dextran}}(m_{\mathrm{U}} = 10\,\mathrm{kDa}) = 2.3\,\mathrm{nm}$ (according to supplier).

For the second argument, it is the easiest to calculate the diffusion coefficients D using the Stokes-Einstein-equation [234]:

$$\begin{aligned} D(\mathrm{Calcein}) &= 3.3 * 10^{-10}\,\frac{\mathrm{m}^2}{\mathrm{s}} \\ D(\mathrm{FITC-Dextran}) &= 1.1 * 10^{-10}\,\frac{\mathrm{m}^2}{\mathrm{s}} \\ D(\mathrm{eGFP}) &= 1.0 * 10^{-10}\,\frac{\mathrm{m}^2}{\mathrm{s}} \end{aligned} \tag{42}$$

According to Fick's law, diffusion is a linear function of D, therefore, neglecting all other contributions, the permeabilization factors of the dyes should be

$$3 * c_{\mathrm{FITC-Dextran}} \approx c_{\mathrm{Calcein}} \approx 3 * c_{\mathrm{eGFP}}.$$

However, they are

$$c_{\mathrm{eGFP}} \approx c_{\mathrm{Calcein}} \approx 2 * c_{\mathrm{FITC-Dextran}}.$$

As a result, using acoustofluidic trapping, FITC-Dextran is half as permeable as Calcein, however, it is more permeable than expected based on the diffusion coefficients. In contrast, eGFP is as permeable as Calcein, although expected to be less permeable by a factor of 3.

Summarized, the novel permeabilization method presented here and published in literature [159] facilitates permeabilization by acoustofluidic trapping. This method still holds for significantly larger molecules (almost 2 orders of magnitude), such as sugars and proteins. A priori, we expected a limit at the protein level, however, it is perfectly applicable. Future work might test for larger molecules, like plasmids.

As a an outlook on the acoustofluidic permeabilization tool, I would like to present results and remarks regarding certain claims in literature.

5.2.7 Plausibility of Nanoaberrations without Acoustofluidic Treatment

In Ramesan *et al.* [154], the authors claim they found a new permeabilization mechanism employing surface acoustic waves on adherent cells. In this publication, they claim having found a new mechanism - explicitly not to be pore-related - but mediated by what they call indentations and nanoaberrations. They back this claim by scanning electron micrographs of the permeabilized cells, which they took by "freezing" (immobilizing procedure) the cells during or right after the treatment.

On these micrographs, they find holes in the membrane with a diameter of about $d = 500\,\text{nm}$, which is supposed to be smaller than pore sizes from literature ($d = 1 - 10\,\mu\text{m}$). However, it has been extensively reviewed in section 2.6.2, that standard meta-stable pores exist from $d \geq 0.8\,\text{nm}$ on. On top of the size-difference, they support their claim by comparing lifetimes of this new internalization mechanism. They claim shorter lifetimes of presumably few seconds or less, whereas pore resealing requires minutes.

However, I doubt the finding of a new internalization mechanism, as claimed in the study. Firstly, the authors line of argumentation is as follows: *Because* no pores were observed, there *were no* pores. I find this misleading, as they did not show in the first place, that this method is consistently able to image pores. If they would have used another permeabilization method - which is known to be pore-mediated - and they would have imaged these pores using their protocol, only then would their line of argument be convincing.

Secondly, the difference in size to known pore sizes is a factor of 2, which is relatively low. At best, they might have extended the known size spectrum of these pores down to 500 nm in regard to the literature they cited.

Thirdly - and most importantly - I could reproduce their results by accident. I prepared samples using a similar protocol based their study. Surprisingly - we imaged small holes of the size of less than $d \lessapprox 100\,\text{nm}$ on the cell membrane, as presented in figure 46c. To be clear, the cells did not receive any permeabilization treatment besides the immobilization protocol in section 9.3.

The diameters in figure 46c are even smaller than in their study. An appropriate comparison is impossible at this point. In their study, they neither provide a comparable magnification factor, nor high quality images. Nevertheless, having applied no permeabilization treatment at all and being able to observe even smaller "nanoaberrations" questions their results significantly. In my opinion, at best, their

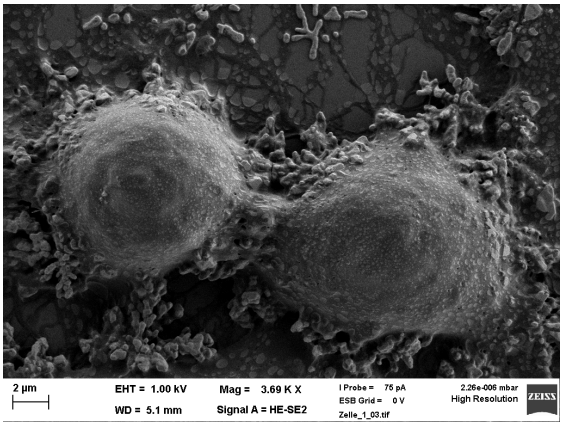

(a) Two neighboring HeLa cells are visible, both exhibit small holes abundantly.

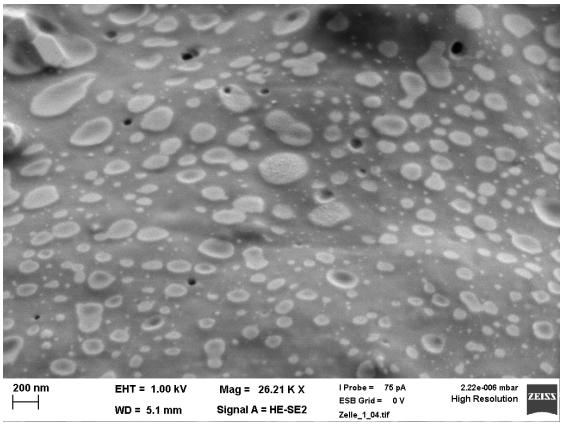

(b) Magnification of the right cell in figure 46a has been magnified.

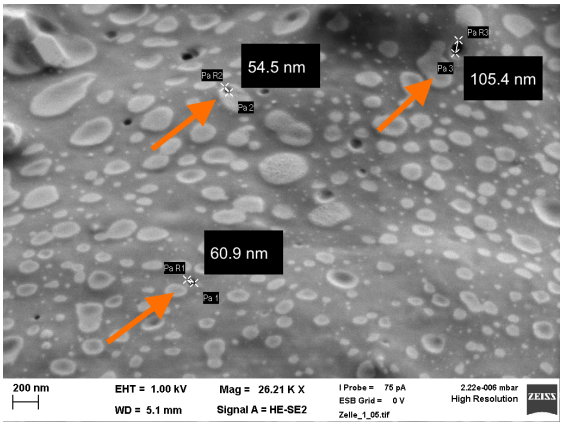

(c) The holes exhibit diameters of 50 nm-100 nm.

Figure 46: Scanning electron microscopy of immobilized HeLa cells.

SAW treatment enlarged the sizes of holes like in figure 46c. The enlargement could have the holes visible to them in the limited technical capabilities of their scanning electron microscope, which in turn led to a bias in their evaluation. The fact that they found these holes even in their control questions these results further. It would be intriguing to have insight into this rebuttal process for future studies.

After this novel tool for acoustofluidic cell permeabilization, we continue our fundamental research and add temperature as another dimension, to be able to measure a temperature-shear-rate-permeabilization landscape.

5.2.8 Permeabilization Landscape - Intensity as Function of Temperature and Shear Rates of Suspended Cells

To obtain a landscape diagram, we conduct temperature-controlled shear exposure to suspended HeLa cells in a viscosimeter using a cone-plate geometry, as discussed in section 2.3.3 and similar to literature [153]. The use of a commercial viscosimeter allows for high-quality shear rate control.

Figure 47a shows the internalized dye intensity as function of temperature at static conditions ($\dot{\gamma} = 0$). It shows a distinct maximum at $T = 38\,°\mathrm{C}$ (squares), which has been highlighted in the figure. Dye uptake at supraphysiological temperatures rises due to protein denaturation and membrane blebbing [236] and is not of interest to this thesis.

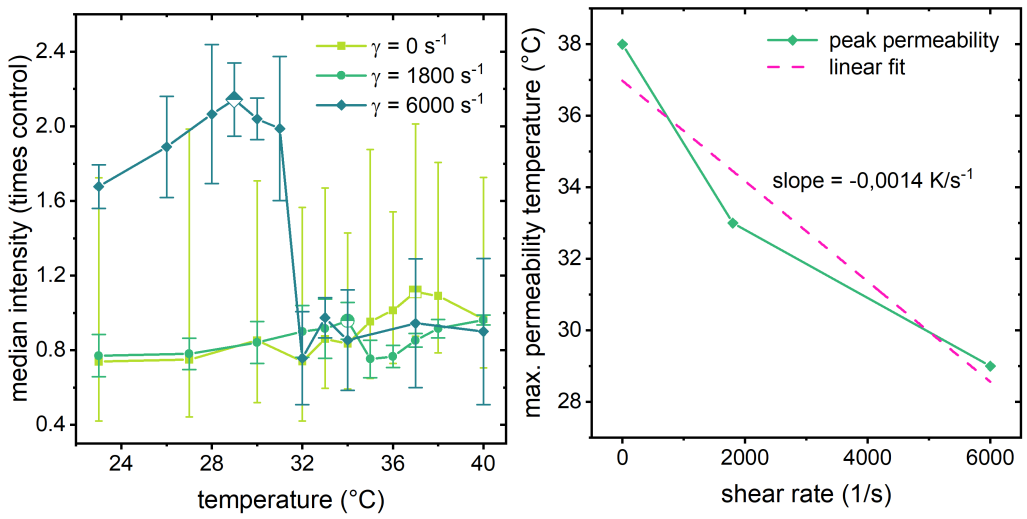

(a) Permeabilization as function of temperature at three shear rates. The highlighted data points mark the maximum uptake temperatures.

(b) Maximum Permeabilization temperature as function of shear rate. The slope of the linear trend indicates a shift in the maximum permeabilization temperature of $1.4\frac{\mathrm{K}}{1000\,\frac{1}{\mathrm{s}}}$.

Figure 47: Permeabilization of suspended HeLa cells as function of temperature and shear rate.

Figure 47a shows further the permeabilization as function of temperature and shear rate. The data is qualitatively and quantitatively reproducible and the number of evaluated cells at each temperature is at least 1000. The shape of the curve for $\dot{\gamma} = 6000\,\frac{1}{\mathrm{s}}$ could be interpreted either as a two-level behavior, or as a slight peak at $T = 29\,°\mathrm{C}$ (diamonds), followed by a sharp decline. We further evaluated the peak

position of $\dot{\gamma} = 1800\,\frac{1}{\mathrm{s}}$ (circles) and plotted all peak temperatures as function of shear rate in figure 47b.

Figure 47b shows a linear trend of the permeability peak position as function of shear rate, which is an important result. Quantitatively, this peak shifts about -1,4 K per $1000\,\frac{1}{\mathrm{s}}$, stabilizing the fluid phase. The shear rate $\dot{\gamma} = 1000\,\frac{1}{\mathrm{s}}$ corresponds to a shear stress of $\tau = \eta\dot{\gamma} = 1\,\mathrm{Pa}$, as the dynamic viscosity of water is $\eta = 1\,\mathrm{mPa*s}$. Shear stress of this magnitude can be found throughout the human body - in blood flow [237, 238], bone fluid flow [239], urinary tract [240] or air flow [241]. Shear stress is well-known to be crucial for e.g. stem cell differentiation [242].

Another, independent set of experiments, conducted in another project finds similar results. The results are presented in figure 48 and reveal a shift of the maximum permeabilization temperature at -0.6 K per 1000 $\frac{1}{s}$.

Two arguments support the robustness of the results. Firstly, these experiments have been conducted independently and over an even broader range of shear rates, ranging up to $\dot{\gamma} = 18{,}000\,\frac{1}{\mathrm{s}}$. Secondly, the use of two different fluorescent dyes, which differ in molecular weight ($m_{\mathrm{U}}(\mathrm{Calcein}) = 0.6\,\mathrm{kDa}$ and $m_{\mathrm{U}}(\mathrm{FITC-Dextran}) = 10\,\mathrm{kDa}$) and size, still follow the same linear trend.

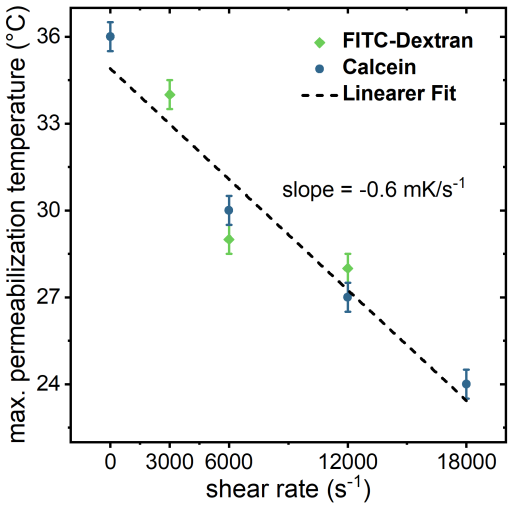

Figure 48: Maximum permeabilization temperature as function of shear rate for suspended cells in a custom-built viscosimeter.

To dive deeper into the data and to get a glimpse on the permeabilization landscape, we will focus on the distribution of the permeabilization as function of temperature and shear rate. To be clear, similar experiments to figure 47a will be conducted, but with a smaller temperature mesh and more importantly another dimension displaying the intensity distribution. The results are presented in figure 49a and 49b.

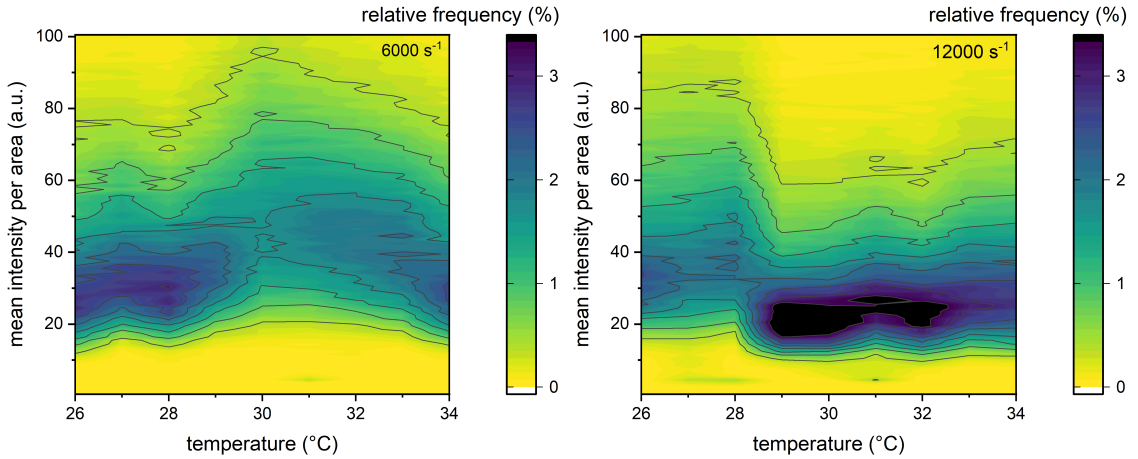

(a) $\dot{\gamma}$= 6000 $\frac{1}{\mathrm{s}}$ (b) $\dot{\gamma}$= 12000 $\frac{1}{\mathrm{s}}$

Figure 49: Permeabilization landscape - Intensity distribution as function of temperature and shear rate of suspended HeLa cells. Treatment time t = 1 min on a plate-cone viscosimeter geometry. The experiments were conducted in a 1:1 mixture of dye solution (c = 1 $\frac{\mathrm{mg}}{\mathrm{ml}}$) and cell medium with c = 11 vol.% Optiprep™ to prevent sedimentation.

Figure 49a shows the shear rate of $\dot{\gamma}$ = 6000 $\frac{1}{\mathrm{s}}$, where the permeabilization landscape is presented. In detail, the dye uptake is now color coded, in contrast to figure 47a, where the information on distribution is hidden in the error bars. Interestingly, two maxima evolve around T = 27 °C and T = 34 °C, as can be seen by the dark regions. However, these maxima quickly decline for higher intensities, as the high mean intensities are of light green color. At T = 30 °C, the tail of the Gauss distribution reaches the farthest into high intensities, which is indicated by the contour line. Consequently, at T = 30 °C, the permeabilization here is the highest.

In contrast, employing a shear rate of $\dot{\gamma}$ = 12000 $\frac{1}{\mathrm{s}}$ shows a significantly different permeabilization landscape, as presented in figure 49b. Here, the temperature, at which the permeabilization is highest, is at T = 27 °C. Consequently, the $\dot{\gamma}$ = 6000 $\frac{1}{\mathrm{s}}$ higher shear rate shifted the maximum 3 K towards lower temperatures, resulting in a shift of $\frac{-0.5\,\mathrm{K}}{1000\frac{1}{\mathrm{s}}}$. This is in excellent agreement to the results obtained before.

At this point, I would like to add our publication [51] to the comparison. In the study, we report a shift in phase transition temperature of $\Delta T_\mathrm{m} \approx 0.6\,\frac{\mathrm{K}}{1000\frac{1}{\mathrm{s}}}$. The numbers agree excellently. However, I would like to point out, that not exactly the same quantities were measured. In the data presented here, suspended HeLa cells display a maximum permeabilization temperature, which shifts linearly by $\approx \frac{-1.4\,\mathrm{K}}{1000\frac{1}{\mathrm{s}}}$ to $\approx \frac{-0.5\,\mathrm{K}}{1000\frac{1}{\mathrm{s}}}$. In the publication, the phase transition temperature of giant

unilamellar vesicles shifts upon shear stress $\Delta T_{\mathrm{m}} \approx 0.6 \frac{\mathrm{K}}{1000 \frac{1}{\mathrm{s}}}$. The quantitative agreement strongly suggests a correlation and good comparability of respective artificial and real membranes.

Although the figures 47b and 48 show robust results, the experimental design has an imperfection - the shear dimension can only be measured discretely. Discrete measurements are labor-intensive and comparability is impeded, as experiments are conducted on several days with changing cell passage numbers. Therefore, I designed an experimental setup, which draws the line in the sand as clear as it can be. For that, I chose the setup to be a plate-plate viscosimeter with adherent HeLa cells to conduct permeability experiments as above. The advantages are elaborated on in the next section.

5.2.9 Permeabilization as Continuous Function of Shear Rate and Discrete Function of Temperature on Adherent Cells

To extend our findings to adherent cells, we use a viscosimeter with plate-plate geometry to have a continuous, linear shear treatment for permeabilization. The advantages of this setup are tremendous. Firstly, using a viscosimeter is essential. Viscosimeters are designed for shear studies. In a viscosimeter, the shear profile is experimentally as defined as it can be.

Secondly, the setup has a radial symmetry. Radial symmetry makes any kind of non-linearity immediately visible to the naked eye. In contrast, local imperfections or artifacts are not radially symmetric and are therefore easily distinguishable.

Thirdly, the plate-plate geometry allows for a continuous, linear shear profile. Consequently the applied shear rate ranges between $0 \leq \dot{\gamma} \leq \dot{\gamma}_{\max}(r_{\max})$. To be clear, one experiment in the plate-plate geometry contains more information than a whole set of experiments in the plate-cone geometry.

Finally, adherent cells are crucial, as they are immobile on the experimental time scale. This allows for unlimited observation and continuous, spatial information on the single cell level. In contrast, in an commercial viscosimeter, it is impossible to take micrographs during the ongoing experiment, as the bottom plate is not transparent.

A fluorescent micrograph is presented in figure 50. To access the spatial information and make use of the single cell information, it is convenient to use two kinds of fluorescent markers with different colors. The first marker (NucBlue™) stains the cell nucleus in blue and is used to identify the cell position. The other marker (Calcein-AM) stains the cell cytosol in green and is used to quantify cell permeabilization. Calcein-AM is originally used to mark alive cells, as only a functioning

metabolism will trigger fluorescence intensity in the dye. Therefore, to quantify permeabilization, the loss in intensity is attributed to loss in dye from the cell interior due to permeabilization.

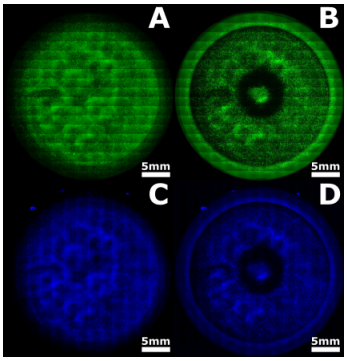

Figure 50: Two-channel fluorescent micrographs of adherent HeLa cells before and after shear treatment. A) Calcein-AM in the cytosol in green before the shear treatment. B) Cell nucleus in blue before the shear treatment. C) Remaining Calcein after the shear treatment. D) Remaining cells on the substrate.
Treatment time $t = 1\,\mathrm{min}$ on a plate-plate viscosimeter geometry. The experiments were conducted at $T = 30\,^{\circ}\mathrm{C}$ in a 1:1 mixture of dye solution ($c = 1\,\frac{\mathrm{mg}}{\mathrm{ml}}$) and cell medium. The rotational frequency of $U = 1000\,\mathrm{rpm}$ generated a linear increase in shear rates of up to $\dot{\gamma} = 10\,\mathrm{k}\,\frac{1}{\mathrm{s}}$.

At the first glance of figure 50, artifacts - like cell density irregularities - are immediately visible in the *a priori* picture. Fortunately, we can identify those as artifacts due their asymmetric pattern. Furthermore, they do not disturb the analysis, as firstly, the cell density averages out over the ring and secondly, the data is analyzed on the single-cell level, where cell density is irrelevant.

At the second glance of figure 50, characteristics exhibiting radial symmetry come to attention, which are indeed caused by shearing. The *a posteriori* micrograph in the FITC-channel indeed exhibits a dark ring. Consequently, this indicates a specific increase in permeability at this (narrow) particular shear rate (range). However, as the DAPI-channel exhibits the same dark ring, it simply follows that the cells detach at this particular (narrow) shear rate (range).

As permeabilization is the focus of this work, this side result was at first irritating and it was treated as an artifact to get rid of. However, a closer examination revealed that the origin of this de-adhesion is intriguing.

Various literature exists, which does not observe this shear rate specific peak in detachment [153, 243]. After a thorough examination, I realized that this setup

is a different realization of a study from earlier by our group [243]. However, I would argue, that viscosimeter design is much more suitable and reliable to study de-adhesion as function of shear rate. The well-defined linear shear profile is inherent to the viscosimeter - in contrast to the asymmetric acoustic streaming from figure 51c. On top of being asymmetric, the continuous shear profile of the jet has been binned to four discrete values.

Their finding is a linear de-adhesion rate as function of shear rate. In contrast, we find a highly non-linear cell de-adhesion as function of the shear rate. These results contradict each other, although their comparability is good: Firstly, the shear rate ranges are similar. Secondly, the force distribution is continuous and areal. This is not true for AFM studies, where the cantilever applies a point-like force.

Nevertheless, the existence of a dark ring in the DAPI-channel is directly linked to de-adhesion at a particular (narrow) shear rate (range). Therefore, cell ce-adhesion is a non-linear response function by the cell-adhesion-apparatus to the shear rate. To the best of my knowledge, this result is the first of its kind and is about to be published soon. However, at this point, we refocus on the permeability as function of shear rate.

In figure 51a and figure 51b, the analysis accounts for the de-adhesion, by analyzing permeabilization on the remaining adherent cells. Certainly, there is some kind of bias in this study, as we have unwillingly filtered de-adhered cells from the analysis. However, within the limits of this setup, it is not possible to account for these cells. One easy possibility to access these cells would be to analyze the supernatant of the sample, where those cells are suspended in. The information would lack the exact information on shear rate, as its trajectory in the sheared liquid volume is untraceable *a posteriori*.

Despite having accounted for the detached cells, the FITC-intensity loss - which is the measure for permeability - displays a peak. In detail, the cells are permeabilized for a (narrow) particular shear rate (range), which - at this point - strongly supports that permeability is a non-linear function of phase state. To secure these results, we put great effort in reproducibility.

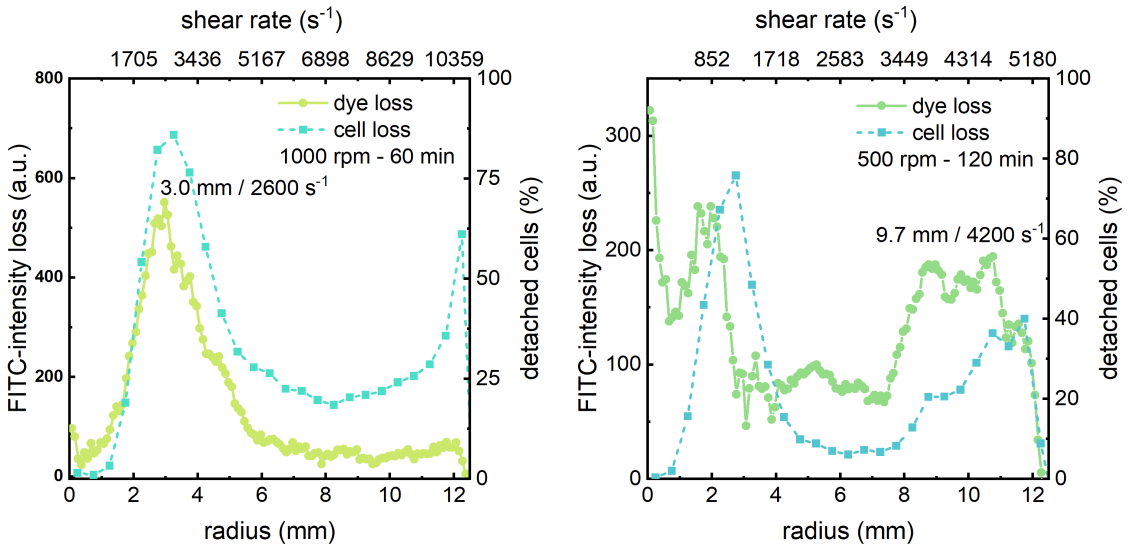

(a) In the first part of the experiment, the cells are exposed to U_1 = 1000 rpm between $0 < t < 60$ min.

(b) In the second part of the experiment, the very same cells are exposed to U_2 = 500 rpm between 60 min $< t <$ 120 min.

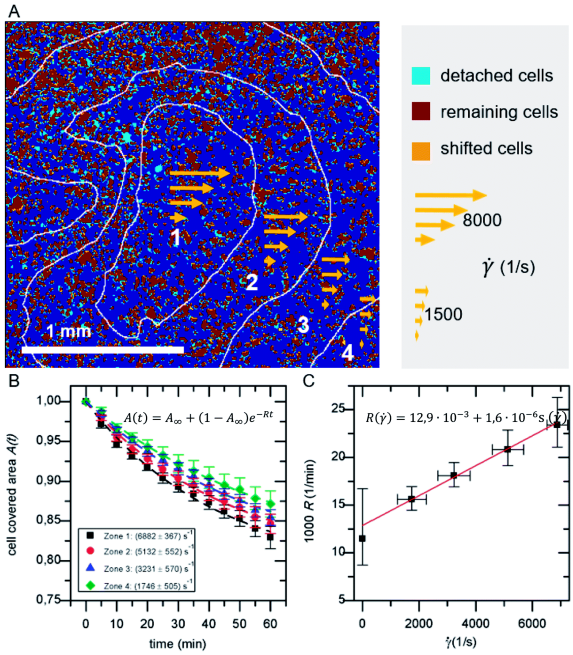

(c) Cell de-adhesion as function of shear rate. Adapted from [243].

Figure 51: Permeabilization and de-adhesion as function of shear rate and radius.

Reproducibility

We have reproduced the experiment many times where we have observed de-adhesion and permeabilization rings. However, those rings appeared at slightly varying radii and therefore shear rates. This variation was unexpected and puzzling. After careful consideration, this could originate from several biological and technical errors.

Firstly, cell passaging at a different time point in their cell cycle might lead to variations in the membrane due to variations in cell maturity. Secondly, the custom-built viscosimeter is a powerful achievement on its own, however, it comes with technical imperfections. The major technical imperfections are: limited quality of ball-bearings and higher tolerances. These imperfections lead to different effective shear rates in every experiment, although plate-plate distance was presumably adjusted. Before having put lots of effort to improve the technical quality of the setup, we present another experiment, which was supposed to keep all technical imperfections constant. The results are presented in figure 51b.

The experiment of figure 51b immediately succeeds the experiment of figure 51a. Therefore, the biological error arising from varying cell passages is eliminated by using the very same cells. However, obviously, the cells in the second part of the experiment have already been stressed from the first part of the experiment.

The technical error is tackled by applying half the rotational speed of the viscosimeter from figure 51a. Therefore, the technical error is (presumably) eliminated, as no hard adjustments requiring a reassembly are necessary, just turning a knob. Quantitatively, using this procedure, ball bearing tolerances might not allow to *a priori* predict precisely the exact shear profile if the system. However, this procedure should be able to provide the exact relative variation of the shear profile.

The formation of a permeability peak in figure 51a has already been discussed. Indeed, in the consequent experiment of figure 51b, a second permeability peak forms - as expected. However, I would have expected the radius to be at double the value from figure 51a, as the rotational speed was half. In contrast, the first radius was at $d_1 \approx 3.0\,\mathrm{mm}$, the second radius is at $d_2 \approx 9.7\,\mathrm{mm}$.

At this point, another technical error was spotted: The glass substrate itself bends to the outwards as function of shear rate. Therefore, a thicker glass substrate increases the technical sophistication of the experimental setup. The results using the thicker glass substrate are presented in figure 52.

Figure 52a clearly shows the formation of a permeabilization peak at the radius $r_1 = 3.8\,\mathrm{mm}$ after $t = 39\,\mathrm{min}$. Subsequently, after $t = 39\,\mathrm{min}$, the rotational speed is halved and the shear treatment continues until $t = 165\,\mathrm{min}$. The results are presented in figure 52b. To be clear, the data from figure 52a is not included explicitly in

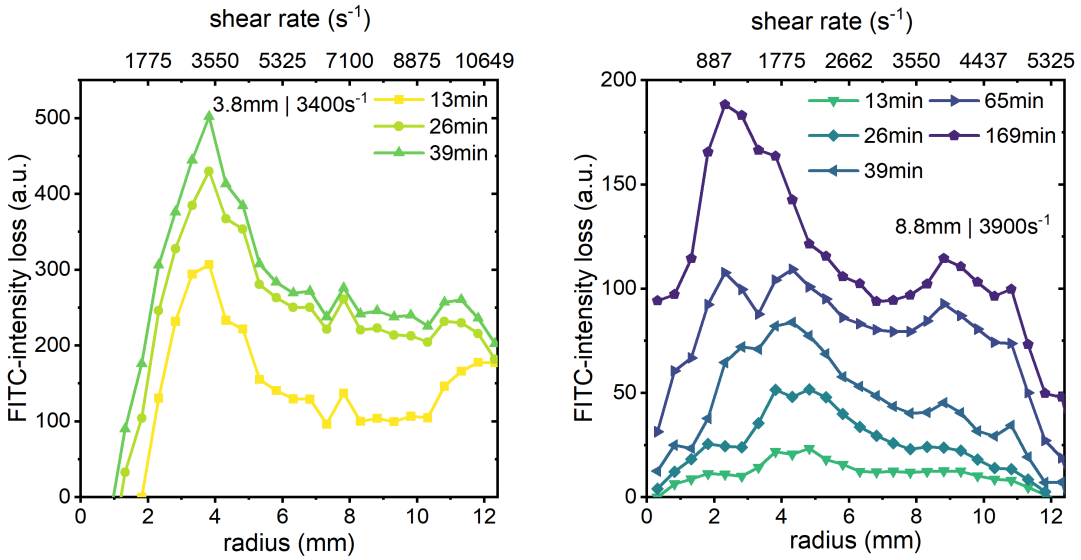

(a) In the first part of the experiment, the cells are exposed to $U_1 = 1000\,\text{rpm}$. The times indications are relative to the cell intensities at the very beginning, before any shear treatment.

(b) In the second part of the experiment, the cells are exposed to $U_2 = 500\,\text{rpm}$. The time indications are relative to the beginning of shear treatment at $U = 500\,\text{rpm}$ and *after* the shear treatment at $U = 1000\,\text{rpm}$.

Figure 52: Permeabilization as function of radius and shear rate. The experimental setup is analog to figure 51, but has been technically improved.

figure 52b. However, it is implicitly included, as the outcome from the prior shear treatment provides the initial conditions for figure 52b.

Consequently, after $t = 39\,\text{min}$ of starting the second part of the experiment, a second peak emerges at $r_2 = 8.8\,\text{mm}$. However, the prediction for the peak was at $r_2 = 2 * r_1 = 7.6\,\text{mm}$. Once again, it does not exactly match the prediction.

At this point, we suspect further technical errors as the root of cause. In detail, the plate-plate distance is a function of shear rate, as the thrust force from the rotation acts on the plate in z-direction. Unfortunately, the mounting of the plate behaves like a spring to a certain extent.

Summarized, taking into account that the shearing device is custom-built, I consider this to be fantastic results, proving the permeability and de-adhesion to be a non-linear function of shear rate. Many successor experiments with improved technical setups, protocols and more applications, have been and are being conducted to this project.

5.2.10 Comparison Permeabilization of Suspended and Adhered HeLa Cells

Comparing the Permeabilization of HeLa cells in suspension and in adhesion, suspended HeLa cells showed a permeabilization maximum at $T = 30\,^{\circ}\mathrm{C}$ at $\dot{\gamma} = 6000\,\frac{1}{\mathrm{s}}$. However, adherent HeLa cells showed a permeabilization maximum around $\dot{\gamma} = 3000\,\frac{1}{\mathrm{s}}$. Although there are minor differences in the experimental setup, like the fluorescent dyes and viscosimeter geometry, these differences should be negligible. Therefore, the difference in maximum permeabilization shear rate has to originate from the difference between being adhered or suspended.

As follow-up study has recently been published, which elaborates on permeabilization as function of chain order [219]. They found a difference in chain order for suspended and adhered cells. For suspended cells, the membrane is less fluid than for adherent cells at any constant temperature. Furthermore, they measured permeability and chain order simultaneously as function of temperature. Their finding revealed maximum permeability at $GP \approx 0$ and therefore a correlation of permeability and phase transition, as supported by our results.

Finally, after studying phase transitions in the fields of fundamental biophysics, applied biophysics, and biomedical engineering - biochemistry remains as a major player in the field of biological sciences.

6 Enzyme Activity at Melting Membranes

Until now, we have studied, what happens in the membrane and through the membrane when we apply shear forces and change temperature. At this point, we will focus on what happens *at* a membrane and how phase transitions influence this. Historically, this field is associated to biochemistry, as it heavily involves enzymes.

6.1 Acetylcholinesterase Activity as Function of Temperature

As elaborated beforehand in section 2.4, there is a major dissent in literature about the correlation of membrane associated enzyme activity and heat capacity. In this thesis, we overcome the flaws in past literature and carefully design a lipid system bridging experimental imperfection in literature. In detail, I use large unilamellar vesicles, which display a broader excess heat capacity to not be missed in 1 K temperature steps, but still sharp enough to display a detectable effect. Furthermore, I use acetylcholinesterase to ensure high biological relevance, as acetylcholinesterase hydrolyzes the neurotransmitter acetylcholine, which is of crucial to nerve signalling theory.

The experimental setup is described in section 9.5. Briefly, I measure the acetylcholinesterase activity as function of temperature. The measurements are conducted colorimetrically, as illustrated in figure 53.

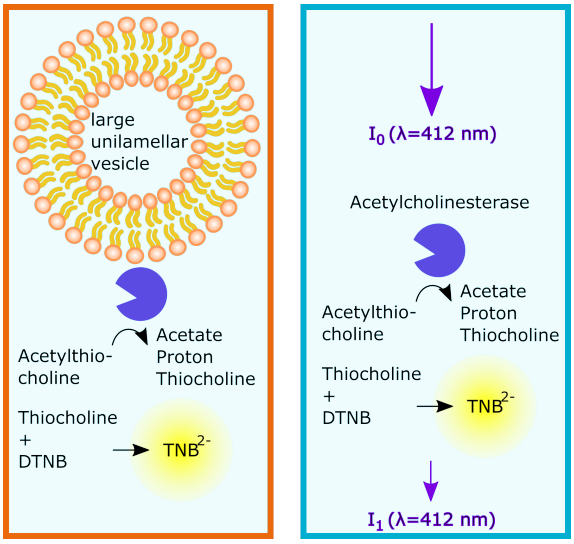

Figure 53: Illustration of the experimental design. The activity is colorimetrically measured for enzymes attached to vesicles (left) and for freely dissolved enzymes (right).

Colorimetric assays relate the absorption of light directly to the enzymatic conversion of substrate by the Lambert-Beer law. However, the direct product of the enzymatic conversion is thiocholine, which is optically inactive. By adding a colorimetric marker to the solution, we gain optical activity. In detail, Ellmann's reagent (DTNB) reacts with thiocholine to TNB^{2-} and can be spectroscopically analyzed at $\lambda = 412\,\text{nm}$ [244]. The difference in concentration of TNB^{2-} at the start and the end of the reaction is directly proportional to the enzyme activity.

The colorimetric endpoint kinetics are performed simultaneously and quasi continuous on the temperature axis. In detail, two activities (DMPC+AChE and free AChE) are measured at the same position on the spatial temperature gradient, resulting in two measurements at constant temperature. In the first of the two samples, the enzyme is attached to the vesicles, in the other, the enzyme is freely dissolved, serving as a reference. The results are presented in figure 54.

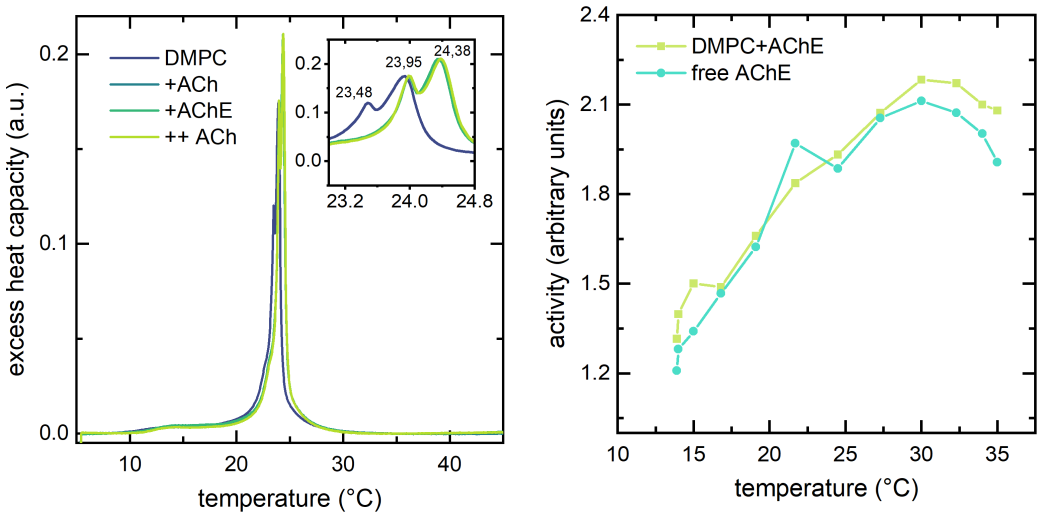

(a) Excess heat capacity of: DMPC; DMPC and acetocholine (+ACh); DMPC, acetocholine, and acetylcholinesterase (+AChE, all substrate cleaved); DMPC, acetylcholinesterase, and acetocholine at a higher concentration (++ACh).

(b) Acetylcholinesterase activity as function of temperature.

Figure 54: 14:0 PC membrane associated acetylcholinesterase activity as function of temperature and phase state.

The excess heat capacity of the system is presented figure 54a. For all measurements, the main phase transition is clearly visible as a peak. Interestingly, the double-peak

characteristic of DMPC could be resolved in the measurement. The pretransition is hardly visible at $T_\mathrm{p} \approx 14\,^\circ\mathrm{C}$. To address one major experimental flaw in literature, I firstly measure the excess heat capacity of pure DMPC vesicles, which display the main transition temperature at $T_\mathrm{m} = 23.95\,^\circ\mathrm{C}$. Secondly, I add acetylthiocholine (+ACh) to the vesicles at the final concentration of the experiments. The addition of acetylthiocholine shifts the main transition temperature notably to $T'_\mathrm{m} = 24.38\,^\circ\mathrm{C}$. The addition of acetylcholinesterase (+AChE) and the subsequent conversion of acetylthiocholine does not shift the main transition temperature further. Neither does further addition of acetylthiocholine (++ACh) to five times the original final concentration. Nevertheless, according to Kaufmann's theory, we expect an activity peak at $T_\mathrm{m} = 24.38\,^\circ\mathrm{C}$- to be exact - as this is representative of the experimental setup. However, as the experimental temperature steps are $\Delta T = 1\,\mathrm{K}$, in the following, we assume T_m(14:0 PC + ACh + AChE) = T_m(14:0 PC + ACh) = T_m(14:0 PC) $\approx$ $24\,^\circ\mathrm{C}$.

Figure 54b presents the results of the activity of acetylcholinesterase bound to DMPC vesicles, as well as freely dissolved acetylcholinesterase. The activity rises to a maximum and then decreases for increasing temperature. While this is qualitatively the predicted behavior, the maximum activity temperature $T_\mathrm{max} = 30\,^\circ\mathrm{C}$ does not match T_m(14:0 PC) $\approx 24\,^\circ\mathrm{C}$. Furthermore, the freely dissolved enzyme displays the same behavior to a quantitative extent. Therefore, these experiments do not support the predictions.

To further elucidate on this, I exchange the lipid from DMPC to 1,2-dilauroyl-sn-glycero-3-phospho-L-serine (sodium salt) (12:0 PS). This yields in fundamentally different results, presented in figure 54b.

In figure 55a, the freely dissolved acetylcholinesterase activity increases steadily. In contrast, the membrane associated acetylcholinesterase increases first, but then decreases after a maximum. However, acetylcholinesterase associated to 12:0 PS large unilamellar vesicles shows a rather small and broad peak. In contrast to 14:0 PC, acetylcholinesterase activity at 12:0 PS membranes is qualitatively a function of membrane phase state, as the theory predicts.

A thorough analysis of the experiment reveals a slight decrease in activity for the very last data point of freely dissolved acetylcholinesterase. In principle, the technical hardware provides a temperature gradient of $T \pm 10\,\mathrm{K}$, which is sufficient to test for predictions according to Kaufmann. However, as this decrease is reproducible, we measure a higher, overlapping temperature interval. The results are presented in figure 55b and reveal a decrease in activity for the membrane attached acetylcholinesterase, as well as for the freely dissolved acetylcholinesterase. While this is expected for the membrane associated enzyme, as a broad, but small peak is present, the freely

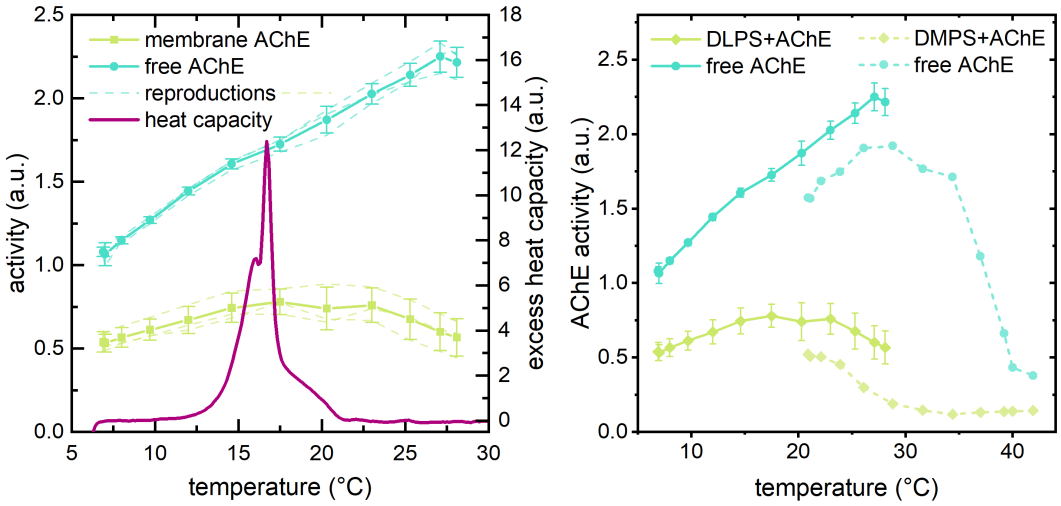

(a) The temperature range is $\Delta T \approx 20\,\mathrm{K}$. (b) The temperature range is $\Delta T \approx 35\,\mathrm{K}$.

Figure 55: Membrane associated acetylcholinesterase activity as function of temperature. The membrane are 12:0 PS large unilamellar vesicles.

dissolved enzyme activity decreases as well. Denaturation can be excluded, which starts around $T \gtrapprox 40\,^{\circ}\mathrm{C}$, not at $T \gtrapprox 30\,^{\circ}\mathrm{C}$. Figure 55b includes the data from figure 55a and both data sets match quantitatively well, despite a minor decrease in activity for the newer data, probably due to aging effects on the enzyme. The decrease in activity starting at $T \gtrapprox 30\,^{\circ}\mathrm{C}$ might arise from a heat block [108].

Summarizing, acetylcholinesterase is partly sensitive to the membrane phase transition. For DMPC, the activity of the freely dissolved enzyme is equivalent to the membrane associated enzyme. For 12:0 PS, a relatively small and broad peak is visible for the membrane associated acetylcholinesterase. However, a heat block might interfere with the temperature range of the experiment. Therefore, I exchange the enzyme to a "neutral" enzyme, ADAMTS13, which is not evolutionary associated with lipid membranes to exclude membrane-enzyme interaction effects possibly developed by evolution.

6.2 ADAMTS13 Activity as Function of Temperature

The enzyme ADAMTS13 is extensively introduced in section 2.4.5. The work presented in this section relies to a large extent on a publication by Kamenac *et al.* and partly from the masters thesis project [128, 245].

6.2.1 ADATMTS13 Kinetic

The experimental setup is thoroughly described in section 9.5. Briefly, figure 56a illustrates the usage of large unilamellar vesicles, displaying an excess heat capacity peak with intermediate sharpness.

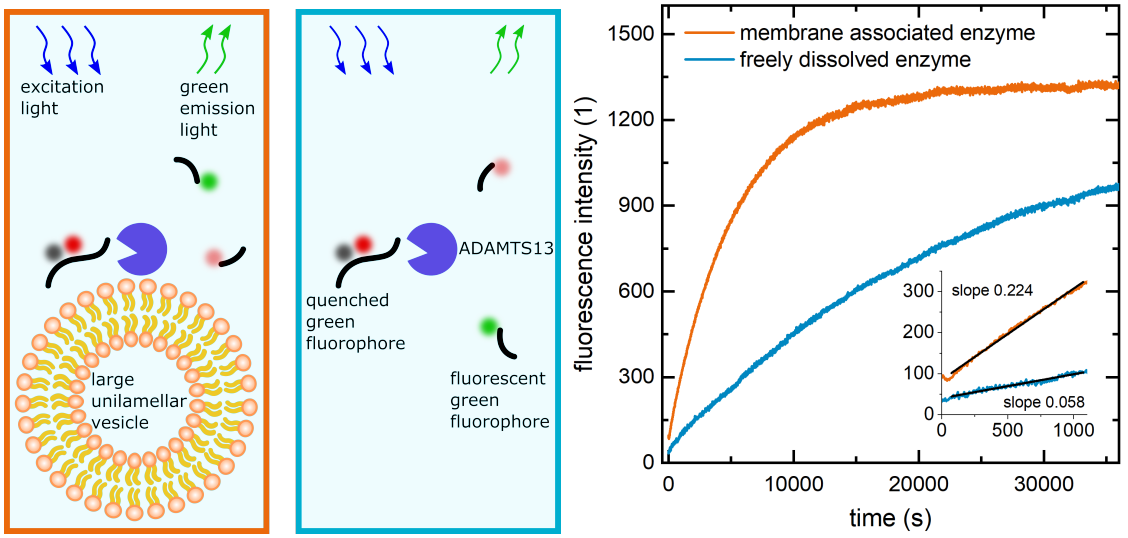

(a) Illustration of the experimental design. The activity is fluorometrically measured for enzymes attached to vesicles (left) and for freely dissolved enzymes (right).

(b) Typical kinetic measurement ($T = 26\,^{\circ}\mathrm{C}$) of freely dissolved enzyme (blue) and membrane (14:0 PC) associated enzyme (orange).

Figure 56: Enzyme activity as function of time at constant temperature. Adapted from [128].

Besides the lipid carrier system, we use a commercially available assay to measure the enzyme activity. As depicted in figure 56a, the enzyme is attached to the lipid membrane and converts a minimal version of the original substrate von Willebrand factor, which is called VWF86 [246, 247]. The peculiarity of the VWF86 is being a fluorescence-resonance-energy-transfer-based (FRET) fluorescent label, which is quenched in the uncleaved state and emits green in the cleaved and unquenched state.

To distinguish the change in activity contributed by the presence of the vesicles, I conducted reference measurements on two levels. On the first level, the reference to the membrane-associated enzyme is a freely dissolved enzyme, just like for the acetylcholinesterase experiments in section 6. To be clear, vesicle solution is substituted with buffer. On the second level, the background fluorescence signal is quantified by substituting the enzyme with buffer.

This setup allows to measure enzyme kinetics fluorometrically. A typical pre-analyzed measurement over a 10 hours time span is presented in figure 56b. Whereas the vesicle-containing sample reaches saturation rather quickly, the vesicle-free reference has not yet saturated within the 10 hours time span.

In the inset of figure 56b, a typical evaluation of the activity is presented. This is in contrast to the acetylcholinesterase experiments, where endpoint kinetics lack continuous temporal data and do not allow for in-detail temporal analysis. After a short warm-up time, the kinetic is linearly fitted from t_1 = 100 s to t_2 = 1100 s. A linear fit has two main characteristics, the slope and the y-intercept. While the y-intercept is ideally 0, as the thermal cleavage has been corrected prior by the second level references, in reality it is slightly positive. This fluorescence originates from the short time span between starting the chemical reaction - by adding and mixing the enzymes to the substrate - and starting the measurement. However, as excess substrate is available and the activity is proportional to the slope, the slightly positive y-intercept is irrelevant.

6.2.2 ADAMTS13 as Function of Temperature Attached to 14:0 PC and 15:0 PC Vesicles

Figure 57 shows the activity and the excess heat capacity as function of temperature for two different lipids. The main phase transition temperature is in accordance with literature [31]. The width of these large unilamellar vesicles excess heat capacity curves is higher compared to MLV, because of reduced cooperativity [23].

Moreover, Figure 57a shows the steady state activity of ADAMTS13 as a function of temperature in a freely dissolved state and associated to 15:0 PC LUV (orange squares). The activity of the freely dissolved enzyme increases with increasing temperature (blue circles) in accordance with an Arrhenius behavior, as reported earlier in literature [58]. In contrast, ADAMTS13 associated to 15:0 PC membranes shows an overall higher activity and a pronounced maximum at T_{max} = 34 °C. This activity maximum temperature matches the excess heat capacity maximum temperature. The control measurement presented in figure 57d reveals the substrate fluorescence intensity is not a function of temperature.

It is important to emphasize, that this is an inherent qualitative difference to the freely dissolved enzyme. In particular, between T = 33 °C and T = 38 °C, the activity decreases with increasing temperature, which is an anti-Arrhenius behavior. It is intriguing, that the 15:0 PC associated ADAMTS13 activity is overall elevated in comparison to in its freely dissolved state. At the peak activity, the 15:0 PC

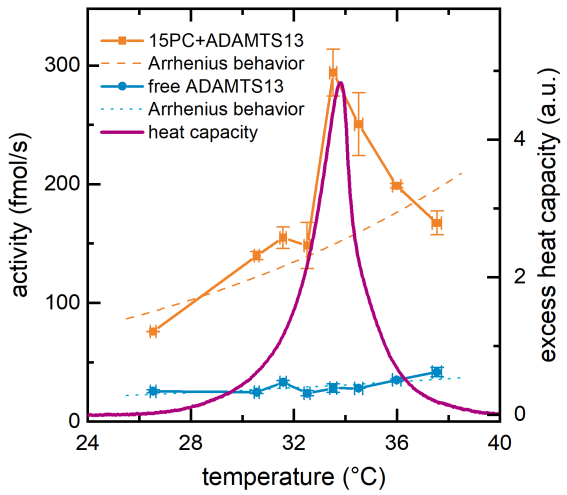

(a) Continuous kinetics of freely dissolved ADAMTS13 and associated to 15:0 PC large unilamellar vesicles.

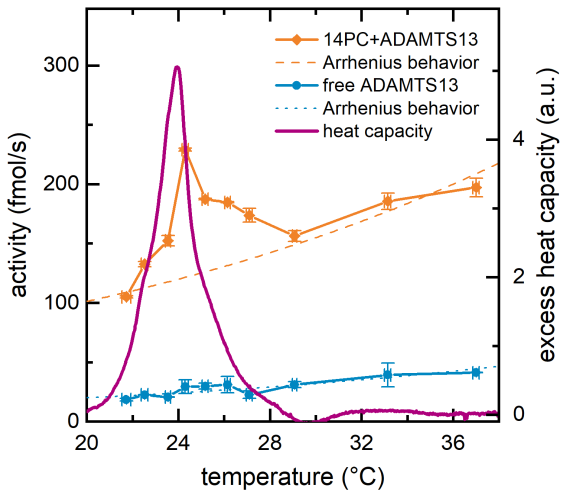

(b) Continuous kinetics of freely dissolved ADAMTS13 and associated to 14:0 PC large unilamellar vesicles.

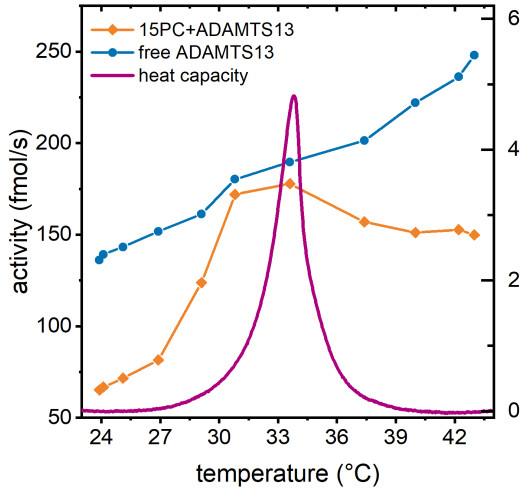

(c) Endpoint kinetics of freely dissolved ADAMTS13 and associated to 15:0 PC large unilamellar vesicles. All measurements were conducted simultaneously.

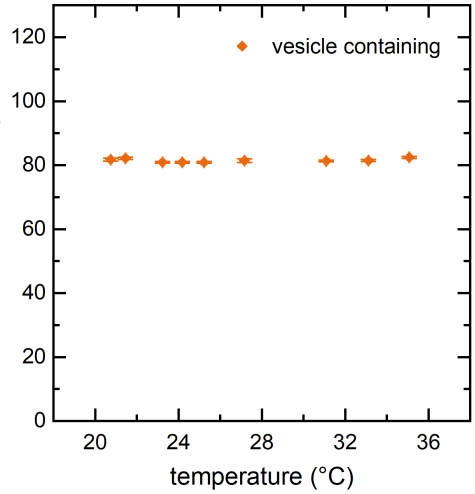

(d) Cleaved substrate fluorescence is not a function of temperature.

Figure 57: Correlation of excess heat capacity and ADAMTS13 activity as a function of temperature and therefore membrane state. Adapted from [128].

membrane associated ADAMTS13 is increased by a factor of about 10 compared to the reference.

We want to make sure this correlation is not a product of system specific coincidence. Such a system specific coincidence could be an eventual evolutionary bias in terms of temperature optimization. However, we can disprove this potential evolutionary bias twofold. Firstly, this potential evolutionary bias has been observed to not exist in literature [58]. Secondly, we conduct reference experiments to exclude the possibility experimentally.

To do so, we exchange the membrane lipids from 15:0 PC to 14:0 PC. This is crucial, as the head groups are identical, so there is no change in chemistry. However, the acyl-chain is one unit shorter. This slightly decreases the thickness of the membrane, but we do not expect any influence on the enzyme, as ADAMTS13 is bound peripherically. More importantly, the use of 14:0 PC substantially shifts the phase transition temperature of the system from $T_\mathrm{m} = 33\,^\circ\mathrm{C}$ to $T_\mathrm{m} = 24\,^\circ\mathrm{C}$.

The results are presented in figure 57b and reveal, that the shift in excess heat capacity to $T_\mathrm{m} = 24\,^\circ\mathrm{C}$ is accompanied by a shift in the activity peak to $T_\mathrm{max} = 24\,^\circ\mathrm{C}$. Once again, the peak activity temperature matches with the maximum excess heat capacity temperature, just as in figure 57a. The peaks characteristics are similar, as the FWHM is identical for both excess heat capacities and for both activities respectively.

Furthermore, we conduct endpoint kinetics on ADAMTS13 as well, analog to the acetylcholinesterase experiments. Endpoint kinetics on a temperature gradient are conducted simultaneously, which excludes any error by one-time-pipetting-contamination and enzyme aging. The results are presented in figure 57c. Qualitatively, it is identical to figure 57a and fully supports the hypothesis. Even more so quantitatively, as the simultaneous measurements result in a smooth curve exhibiting a peak. We would like to emphasize, that in comparison to the literature and as elaborated on in 2.4, this does not result in a kink in the Arrhenius plot.

The illustration in figure 58 visualizes the results of figure 57, where the activity is enhanced at the phase transition temperature of membrane associated ADAMTS13. In fact, this illustration - as explicit and concise as it can be - serves as an inspiration for a real experiment. This new experimental setup improves comparability and excludes any eventual artifacts arising from the presence of a soft interface. For example, an artifact could be the influence of lateral diffusion of substrate along the membrane, which is not possible for freely dissolved enzymes as there is no surface. In detail, we measure the activity of ADAMTS13 associated to 13:0 PC, 15:0 PC, and 14:0 PC large unilamellar vesicles simultaneously and *isothermally* at $T = 24\,^\circ\mathrm{C}$.

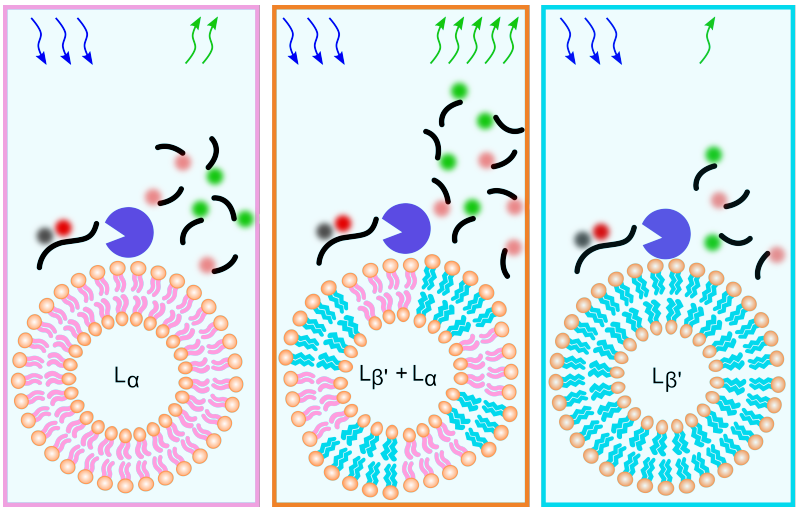

Figure 58: Illustration of the results and microscopic picture from figure 57: ADAMTS13 (purple circle segment) is attached to membranes at three different membrane states: fluid, phase transition, and gel-like (indicated by their acyl-chain shape and color). Uncleaved FRET-substrate (black with colored dots in gray and red) from the left side gets converted to product (right side, colored now green and red as FRET is eliminated). Excitation is indicated by the blue arrows, whereas exmission is indicated by green arrows. The quantity of product and green emission arrows indicate the increased activity in the form of an endpont kinetic at any point in time before saturation. Adapted from [128].

The simultaneous measurement excludes any doubts related to enzyme aging or day-to-day experimental ambiguities. The results are presented in figure 59.

6.2.3 ADAMTS13 Activity as Function of Acyl-Chain Length

Figure 59b shows the excess heat capacity as function of temperature. Most importantly, at $T = 24\,°C$, Δc_p(13:0 PC) ≈ 0, Δc_p(15:0 PC) ≈ 0, and Δc_p(14:0 PC) $>> 0$. As a consequence, 13:0 PC is in its fluid state, 15:0 PC is in its gel-like state, and 14:0 PC is at its phase transition. This is the thermodynamical situation at the activity measurement presented in figure 59a. ADAMTS13 associated to 14:0 PC clearly shows the highest slope and therefore activity, which is presented in a bar chart in figure 59c. Both other enzyme-lipid systems exhibit significantly less activity. The asymmetric activities could result from the underlying Arrhenius behavior or from an asymmetrical entropy potential.

In principle, the information from figure 59a could have been obtained from figure 57 for 14:0 PC and 15:0 PC. However, the advantage of this experimental design is clearly the exclusion of errors, as described above. Nevertheless, these results are in perfect qualitative agreement with figure 57. The quantitative activities slightly vary, which might originate from enzyme aging. The combination of the consecutive and simultaneous measurements convincingly demonstrates the correlation of the membrane associated enzyme activity and the excess heat capacity of the lipid membranes. This is in good agreement with the prior findings on permeability correlating with the excess heat capacity, which is also a two-dimensional membrane property.

To put these results into perspective to literature, the common Arrhenius plot is convenient and presented in figure 60. The Arrhenius plot does not show kinks or discontinuities. In contrast, it shows peaks at the phase transition temperature for the membrane associated enzyme for both lipid systems and a straight line for the freely dissolved enzyme.

Interestingly, this shape has been reported before by Lehto and Sharom [76] for the activity of Phospholipase C at DMPC membranes. However, their interpretation was vastly different. They interpreted it in the context of biphasic curves as a triphasic curve. They concluded the non-Arrhenius behavior arises from a change in collision frequency with increasing temperature due to ΔS at the phase transition. Another interpretation, popular later on in the 70's, was the assumption for these results to be caused by phase separation. Accordingly, the lipid domain phase separation would occur at the transition temperature and would act as a solubilizing agent for the substrate. This would have caused enhanced accessibility of the substrate.

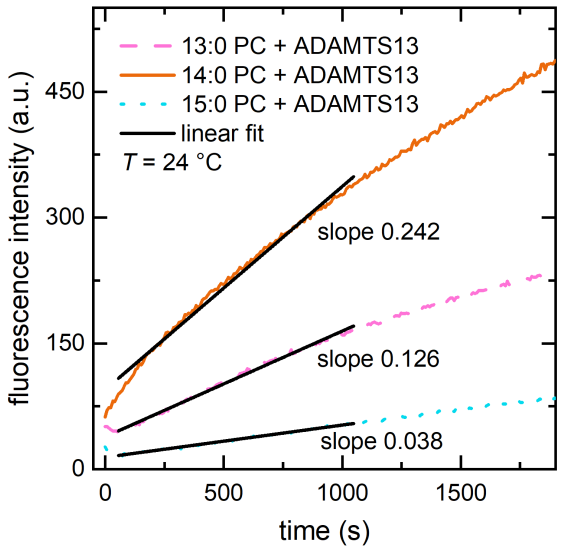

(a) Activity measurement at $T = 24\,°C$ for 13:0 PC, 14:0 PC, and 15:0 PC associated ADAMTS13.

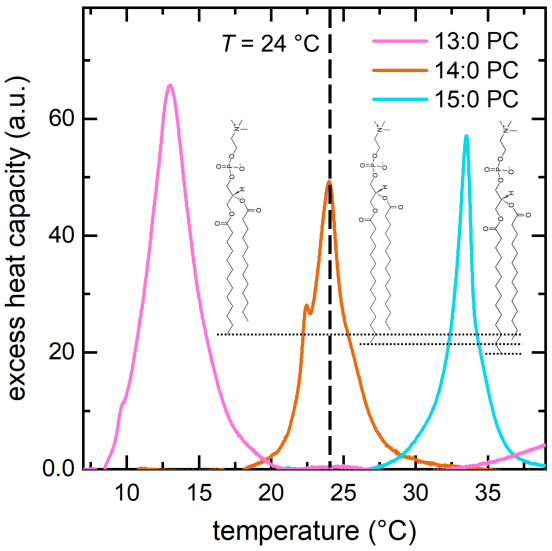

(b) Excess heat capacity of large unilamellar vesicles of 13:0 PC, 14:0 PC, and 15:0 PC ($T = 24\,°C$).

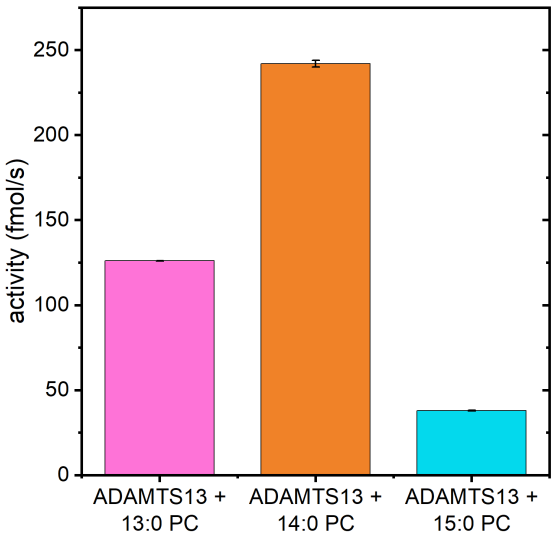

(c) ADAMTS13 activity determined from the kinetics shown in figure 59a. The slope has been evaluated using the time window $t = [100\,s; 1100\,s]$. This evaluation has been labelled 'original' in figure 59d.

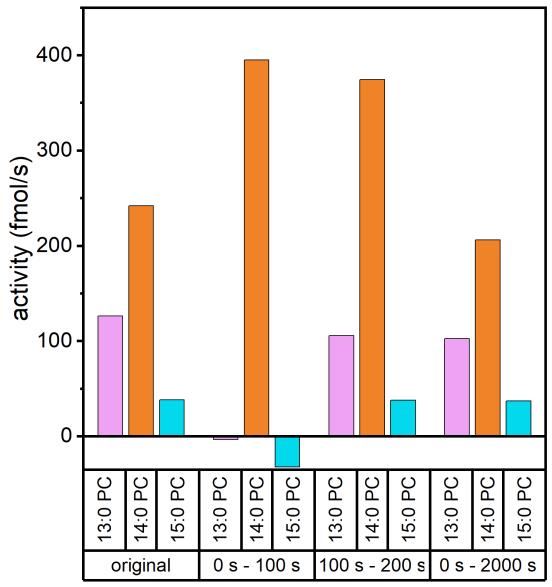

(d) ADAMTS13 activity for different evaluations of the data from figure 59a. The 'original' evaluation from figure 59c is the most conservative evaluation. All other evaluations use different time windows result in an even more severe differences in activity of ADAMTS13 at different membrane phase states.

Figure 59: Control experiments using ADAMTS13 associated to 13:0 PC, 14:0 PC, and 15:0 PC vesicles. Adapted from [128].

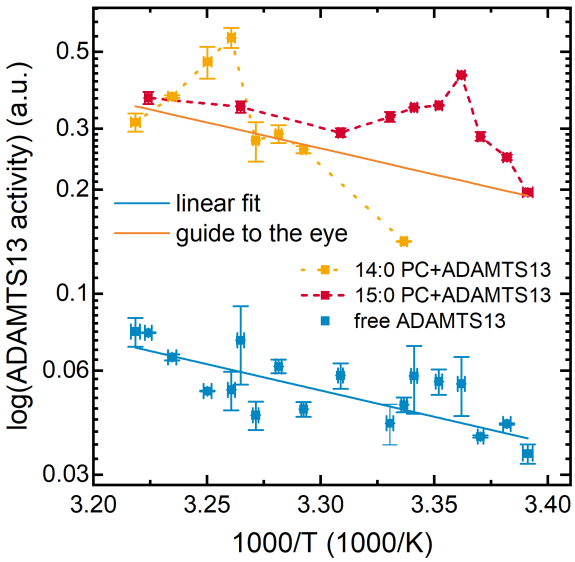

Figure 60: Arrhenius plots of the data shown in figure 57. Note, that the plot does not show kinks or discontinuities. In contrast, it shows peaks at the phase transition temperature for the membrane associated enzyme and a straight line for the freely dissolved enzyme. Adapted from [128].

Kimelberg and Papahadjopoulos [64] report inconsistent results regarding the position of the kinks on the temperature axis with respect to the phase transition temperature. They find the kinks to occur at the beginning of the main phase transition and at the end for various lipids. For others, the temperatures vary even further. However, they note that slight variations of the aqueous environment, e.g. a 3 mM Mg^{2+}, shifts the heat capacity profile of DPPG liposomes by $\Delta T = 10\,\mathrm{K}$. It is important to add, that this is also the case for proteins [23]. Paradoxically, they measured pure phospholipid vesicles calorimetrically, instead of measuring the whole system including the proteins.

Nevertheless, for the first time, an intriguing idea arose at this point in the publication - as their results revealed that membrane fluidity influences enzyme activity, they speculated, that the *vice versa* might be possible:

> The fluidity of the membrane lipids can be controlled by cholesterol, fatty acyl chain length, and unsaturation, and it in turn can be a means of controlling the activity of membrane-bound enzymes. Thus, by affecting the activity of key membrane enzymes, lipid fluidity could have a controlling influence on the general metabolism of the cell. It is quite possible that changes in membrane lipid fluidity could be involved both in physiological controls as well as pathological situations. [64]

This prediction is perfectly accomodated by Kaufmann's theory [104], as well as other puzzling experimental findings from literature. From the theory's point of view, experiments, which have not observed peaks but kinks or discontinuities, are predicted to show peaks at the intersection region of the kinks and discontinuities. Potential reasons why literature did not observe such peaks could be because of technical temperature control reasons.

In particular, broad finite temperature steps of the data points combined with the sharp phase transitions make it harder to measure at the "sweet spot" temperature. Other reasons could be changes in environmental conditions, such as contamination or (micro environmental) pH-shifts, as proposed by literature [64]. Indeed, Fichtl *et al.* proposed a self-regulation of enzymes due to a change in H^+ at lipid monolayers, that a can lower the activity [97, 102]. Interestingly, Fichtl's prediction is a special case of the general principle from the quote presented above by Kimelberg and Papahadjopoulos [64].

As a final remark, the attachment of the enzyme to the membrane is simplified a binary state. This is a strong simplification of nature, where membrane affinity can be a continuous function of many physical quantities, such as: lipid-protein distance, electrostatic coupling of the membrane and the protein, and size of the protein. The attachment degree might enable the cell to fine-tune the response of the enzyme to a pulse propagating on the membrane in terms of sensitivity, intensity, saturation, and other characteristics. It might even be a dynamical process, requiring a sequence of pulses to move the system to the phase state.

Summarized the study of Kamenac *et al.* has revealed, that membrane associated enzyme activity is a function of temperature and therefore membrane phase state. To be more precise, this is true at least for ADAMTS13. To investigate the universality of this principle it is crucial to increase the variety of enzymes.

Comparison of ADAMTS13 and Acetylcholinesterase

A comparison the the two enzymes reveals, that acetylcholinesterase is fundamentally different from ADAMTS13, as figure 54b is qualitative different from figure 55a. The reason for the membrane selectivity of the enzyme remains a major future task and a key question to basic understanding of cell-cell communication. One major main reason for this might be the difference in turnover numbers, which vary by orders of magnitudes. Consequently to the short time constant of a turnover, as well as release of H^+ as a reaction product, the lipids become protonated, which changes the membrane phase state [102]. However, this is only plausible for lipids with an according pK_a value.

In detail, pK_a(PC) ≈ 1 [198], pK_a(PS) ≈ 5.5 [198, 248], therefore the pK_a values of the membranes are vastly different. Here, Fichtl's enzyme regulation model might play a role [97, 102, 106]: acetylcholinesterase produces protons in its catalytic activity and causes local acidification. If the H^+ production rate is higher than its removal via diffusion or reaction with the buffer, the local pH could change from pH=6.4 to pH=5.5. While this is reasonable [132, 249], suddenly, H^+ removal is possible by an alternative mechanism than pure diffusion. In detail, the protons will be absorbed by the membrane and are able to travel at the speed of sound [97] and dissociate elsewhere, where they can be buffered away.

In contrast, due to the low pK_a of 14:0 PC membrane, this additional H^+ removal mechanism can not be activated. As a consequence, the pH value drops further, until the enzyme activity is impeded by the low pH value, which is a well-known effect in classical biochemistry. This negative feedback will result in a steady state at an arbitrary lower activity than usual.

As the phase state can be significantly altered by protonation, biological consequences could be extensive. This is true especially for any membrane-mediated biological processes, such like domain formation, drug-liposome interactions, and membrane fusion [250].

At this point, I would like to generalize the mechanism of self regulation of enzymes. The generalized self regulation concept is based on the binding coefficient of enzymes being known to be a function of various quantities, such as lateral pressure. A critical threshold value exists e.g. for lateral pressure, which marks a transition of the enzyme being peripherically bound or transmembrane penetrating. Naturally, equilibrium is highly sensitive to the amphiphility of the enzyme. The transition of the membrane-association states as a function of lateral pressure has been shown in literature [144, 251].

For this membrane-association transition, a feedback might exist, where the product of the reaction shifts the equilibrium of the protein-membrane-association, leading to a conformational change of the enzyme and subsequent deactivation. A special case of this might be protons changing the intermolecular potential of the membrane due to different electrostatic forces - as proposed by Fichtl. A thorough study on acetylcholinesterase binding affinity as function of membrane phase state should be considered in future projects.

On the biological applications side, the presented data shows at least the plausibility of the trigger part in the trigger-detector-mechanism based on membrane associated enzymes. For the future, it would be intriguing to design an experiment to explicitly measure the detector potential. The hypothesis for the detector mechanism is that the phase transition temperature is a function of enzyme activity. However, several

studies in literature raise promising results. A similar behavior has been shown by Zhang *et al.*, who found a shift in melting temperature depending on the lipid bilayer thickness - modulated by a peptide [252]. The peptide Ac-K2-(LA)12-K2-amide has different conformations for different surrounding lipid chain lengths and is capable of shifting between 7.1 K and -2,4 K.

Melting Front Radius is a Function of Thermodynamic Quantities

Finally, I would like to address a refine the trigger-detector mechanism to real world biology. Part of the beauty of the thermodynamic nerve signalling models is based on thermodynamic specificity. Instead of requiring biochemical specificity by reaction cascades based on the lock and key principle, thermodynamic specificity requires particular combinations of thermodynamic quantities, as elaborated by Schneider [108]. In the following, I would like to add one more mechanism of robustness.

This concept picks up the model by Mouritsen and Bloom. In this model, the free energy of the system minimizes, if a thick transmembrane enzyme is surrounded by longer acyl-chain lipids or lipids in the gel state, as illustrated in figure 61. However, if no long-chain-lipids are available, but the free energy to elongate other surrounding lipids is small, this could resolve the mismatch, too. To be clear, it depends which mechanism, lipid rearrangement, or lipid phase transition is energetically favorable.

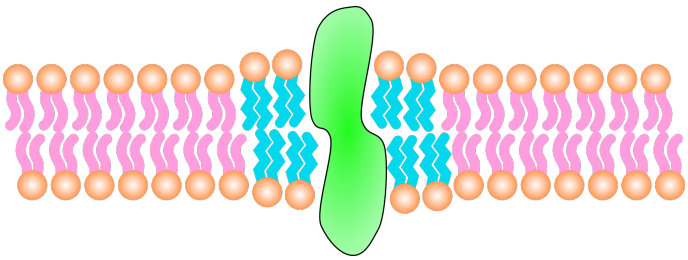

Figure 61: Melting front due to membrane-protein mismatch in the mattress model.

Such enzymes, which change their surrounding lipids phase state, have already been reported, such as bacteriorhodopsin [12]. Consequently, a spatial melting front exists as a stable circle-like form around the enzyme. To take this model further, a change in any intrinsic thermodynamic quantity, like pH or temperature, would change the radius of the melting front spatially. The radius would depend on chemical potential. This could be the microscopic picture of figure 62, where gel-like spots on an overall fluid membrane can be seen on a cell adhered to a coverslip. The *vice versa* could be valid for a thin transmembrane protein in a thick (gel-like) membrane.

This model would also resolve the contradiction, that recent studies brought up. On the one hand, phase transitions in cells are broad (FWHM $\approx$ 40 K) and at a

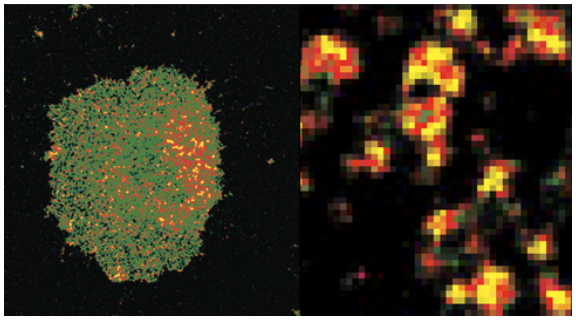

Figure 62: Generalized Polarization micrographs of mouse embryonic fibroblasts adhered to a coverslip. Adapted from [253].

constant temperature, the temperature equivalent distribution of cell membrane chain order is $\Delta T \approx 9\,\mathrm{K}$ [219]. On the other hand, phase transitions in cells have been found to be sharp [203]. By employing this model, the cell membrane would not melt at once, but locally shift the melting front radius, which can be sharp on the microscopic level, as well as broad on the macroscopic level.

7 Summary

Revisiting our hypothesis, the scope of this thesis is to consider phase transitions and their correlation with membrane involving processes and finally the implications of lipid membranes on biological processes. To meet the claim of generality and universality of this hypothesis, this thesis includes a large diversity of studies. The diversity reaches from fundamental studies to applied studies, even to a biomedical tool. The diversity further extends to vastly different areas in biology, ranging from transmembrane processes - such as permeabilization - to lateral, in-plane processes - such as enzymatic activity on membranes.

The results pick up on the findings of Parasassi *et al.* and use their phase transition-sensitive fluorescent dye Laurdan. Having Laurdan incorporated in the membrane, flow in microfluidic channels creates shear forces acting on the membrane over a temperature range. Indeed, the optical information of the membrane dye reveals a change in phase state. In detail, the shear forces decrease the chain order. However, the effect is most pronounced in the most sensitive point - at the phase transition temperature. This result could be qualitatively reproduced for another lipid type, which is a powerful reference.

On the quantitative side, 14:0 PC membranes display a shift in membrane phase transition temperature by $\frac{\partial T_\mathrm{m}}{\partial \dot{\gamma}}(24\,^\circ\mathrm{C}) \approx \frac{0.02\,\mathrm{K}}{1000\,\frac{1}{\mathrm{s}}}$, whereas 15:0 PC membranes appear more sensitive by $\frac{\partial T_\mathrm{m}}{\partial \dot{\gamma}}(33\,^\circ\mathrm{C}) \approx \frac{0.25\,\mathrm{K}}{1000\,\frac{1}{\mathrm{s}}}$. These results are highly interesting for therapeutic temperature-sensitive liposomes encapsulating drugs, as they are exposed to shear forces in blood flow. As the lipid composition has to be carefully adjusted to meet the phase transition temperature, the shear-mediated shift has to be accounted for for a precise control of membrane permeability and therefore the drug release.

The variety of vehicles for *in vivo* drug transportation are manifold. Besides liposomes, nanoparticles are a major player in this field. Yet, nanoparticle-membrane interactions have not been studied systematically as function of temperature and therefore phase state. The results of this study reveal that silica nanoparticle uptake in giant phosphocholine unilamellar vesicles is a complex function of the phase state. Peak uptake rates exist and do correlate with the phase transition. However, - contrary to expectations - the uptake peaks are shifted to $T = T_\mathrm{m} + 3\,\mathrm{K}$ relative to the phase transition temperature.

To elucidate this behavior, the model of Deserno *et al.* was applied. According to this model, three key parameters govern nanoparticle uptake - adhesion as the driving force, tension and bending as the impeding forces. While bending energy has been well-studied in literature, the adhesion as function of temperature has not.

A force spectroscopy study on the adhesion as function of phase state reveals the collapse of the adhesion in the phase transition region.

Diving deeper into the broad field of permeability, new *in vitro* cell permeabilization methods are highly desired. The groundwork for our new permeabilization method relies on fundamental experiments on passive uptake. Therefore, our study picks up the permeabilization experiments of Blicher *et al.* and combines them with shear forces from fluid flow. Unexpectedly, we observe all-or-nothing-like permeabilization behavior - entirely different from Blicher *et al.* - just by adding shear flow. All-or-nothing behavior is well-known from biology, like in triggering of action potentials. A possible connection of these results seem likely, as both are a membrane phenomenon. Further studies on this relation seem to be very fertile future projects.

The reason for the all-or-nothing-like behavior remains intriguing. Major lines of arguments are, firstly, that shear flow shifts phase transition temperature towards the experimental temperature and facilitates pore formation. The effect has been reported above, however, appears to be not predominant in this system. Secondly, pores could be created by mechanical disruption of the membrane. However, experiments using a different lipid type rules this explanation out. In the end, only a combination of a threshold shear force and proximity to the phase transition temperature could explain the all-or-nothing-like behavior, however, this remains another intriguing future project.

All the expertise in shearing, phase transitions and permeabilization is finally utilized to build a vector-free tool for permeabilization of suspended living cells. While doing so, several findings come our way. On the fundamental side, we find permeabilization to be a nonlinear function of shear rate.

On the applied side, the permeabilization of suspended HeLa cells is enhanced by more than one order of magnitude. To achieve this, surface acoustic waves are combined with a microfluidic channel to achieve an acoustofluidic cell trapping device. To trap the cells, surface acoustic waves couple into the fluid and generate vortices. These vortices are spatially and temporally fully controllable, which offers the opportunity to conduct a trapping protocol with various parameters.

To challenge the limits of this novel acoustofluidic *in vitro* cell permeabilization tool, we extend the size of the cargo from a fluorescent molecule (600 Da, Calcein), to a sugar (10,000 Da, FITC-Dextran), and finally to a protein (27,000 Da, eGFP). The acoustofluidic permeabilization tool succeeds in loading the cargo into the cells for all three categories to a great extent. It would be intriguing in future projects to add plasmids as potential cargo material and further test the limits of the novel tool.

To put the icing on the correlation of permeability and shear forces, I designed a new type of experiment. This new type of experiment has the power to visualize

the correlation as illustrative, and convincing, as it can possibly be. Therefore a shear treatment acts on adherent cells in a plate-plate viscosimeter. The powerful advantages of this experimental setup are manifold. Firstly, the viscosimeter enables a well-defined, continuous, linear shear profile - which captures the whole shear axis in one experiment. Secondly, the experimental setup is insensitive to artifacts lacking radial symmetry and insensitive to varying quality of cell passages - a leap forward for repeatability and robustness. Finally, adherent cells are immobile and allow for spatial information on the single cell level. Thanks to the spatial information, cell permeabilization is visible as a dark ring on the cell layer.

Secondly, a dark ring appears in the permeability fluorescence channel. After a careful analysis and normalization to the remaining, adherent cells, the finding persists. Adherent cell permeability is a non-linear function of shear rate, strongly supporting our correlation hypothesis. Latest studies and follow-up experiments have indeed confirmed this correlation.

As the final project, after covering the fields of fundamental biophysics, applied biophysics, and biomedical engineering, biochemistry remains as a major player in the field of biological sciences. Therefore, I pick up the findings of Fichtl *et al.* and measure the membrane phase transition acting on the enzyme activity. As a result, the membrane associated enzyme activity is a highly non-linear function of temperature and therefore phase state of the membrane. In detail, I observed Anti-Arrhenius behavior in the temperature interval above the phase transition temperature.

This result cannot be comprehended by the currently accepted induced fit theory. An alternative theory, which precisely predicts our findings, has been developed by Dr. Kaufmann. The consequences on the fundamental side are enormous, as lots of literature exists, where enzymatic activity has been measured without reference to the phase transition of the lipid membrane. More precisely, temperature steps are often too big, such that the phase transition could have been missed. This is amplified by using multilamellar vesicles with a significantly sharper phase transition of $\mathrm{FWHM}_{\mathrm{MLV}} \approx 0.1\,\mathrm{K}$, which could have resulted easily in missing activity measurements at the phase transition region.

To secure the experimental findings even further, additional experiments were designed and conducted to challenge the hypothesis. By exchanging the lipid to a longer acyl-chain lipid, the phase transition temperature changes without affecting the chemistry in any way. The results once again reveal a correlation of the maximum enzyme activity temperature and the membrane phase transition temperature.

In a final experiment, we do not measure enzyme activity as a function of temperature, but as a function of acyl-chain length. This allows for a simultaneous and

isothermal measurement, where the phase state is varied by the acyl-chain length of the lipids. Therefore, it is even possible to eliminate the lacking interface of freely dissolved enzymes, as now the reference is membrane associated enzyme. Once again, the results reveal significantly increased activity for the enzyme attached to the membrane at the phase transition.

The correlation of membrane-associated enzyme activity and membrane excess heat capacity supports the plausibility of a trigger and detection principle for the soliton nerve signalling theory.

8 Outlook

In this thesis, we have gained insights on the impact of phase transitions of membranes on cellular biological processes. We have seen the power of membranes at phase transitions due to highly non-linear behavior. Trans-membrane processes, such as endocytotic nanoparticle uptake and cell membrane permeabilization, as well as biochemical processes, such as enzymatic activity are extremely phase state sensitive. These results lead to two major conclusions for future studies.

The first major conclusion is on the general side. There is a demand for more optical spectroscopy on phase state-sensitive fluorescent dyes in artificial and cellular lipid membranes. Those promise a bright future, as they are associated with major advantages. The major advantages are the easy implementation, as dyes are inexpensive, easy to handle, allow for high-throughput of cells, and are commercially available and affordable equipment. The only disadvantage is the deviation from the natural membrane composition, as the fluorescent dye is incorporated into the membrane. However, this disadvantage can be easily circumvented by additionally using non-contaminating optical methods, such as Raman spectroscopy and infrared spectroscopy [34]. The following projects would greatly benefit from this method.

Firstly, in the nanoparticle-membrane adhesion experiments, it would be possible to simultaneously measure the lipid chain order and correlate the adhesion more inherently to the membrane phase state. However, these experiments would still have a bias for extremely low adhesion energies. This could be easily accommodated by keeping the retraction force constant and varying the temperature to test for a real cantilever jump-off.

Secondly, the acoustofluidic permeabilization tool could be improved by adding real-time chain order measurement at the vortices. This could reveal how the chaotic nature of the vortices influence the lipid chain order of the cells during treatment. I would expect a broad distribution of chain orders and fast temporal fluctuation of chain order. Furthermore, a controlled inflow of many cells at once, as well as applying a broader range of cargo sizes would enable careful analysis on cell stress and pore size by the permeabilization treatment - and therefore further improve permeabilization enhancement by parameter tuning.

Thirdly, the enzyme studies would greatly benefit from a simultaneous chain order measurement, especially, as Laurdan works well in artificial lipid membranes. However, the main experiments require studying many more combination of enzymes and lipids. The potential enzyme dependence, which findings in this thesis hints at, must be examined. A good starting point therefore is acetylcholinesterase at 14:0

PC and 12:0 PS membranes, as well as bacteriorhodopsin, due to its relevance in literature.

Finally, - and most intriguing to me - Laurdan-based chain order measurement would be of highest benefit in the plate-plate viscosimeter. While studying the detachment and permeability as function of shear rate and temperature, Laurdan could reveal, if the non-linearity is at $GP = 0$ and therefore at the phase transition. Furthermore, phase state measurements using Laurdan on cells, which were grown in various environments, could reveal highly valuable insights on current adaptation theories [254]. These environments could be growing the cells on a different temperature, pH, salt concentration, or even down to certain molecules like in the presence of ethanol.

The second major conclusion is the necessity for new reference experiments in future studies. During the studies of this thesis, I found profound evidence for the importance of phase transitions in biological systems, as published in several high-ranking journals. However, during discussions with parts of the community and in literature, the disregard and ignorance in parts of the community for this phenomenon became evident to me. This does not stop at the written and published level, such the following lecture notes (2018):

> "The impermeability of the lipid bilayer for charged molecules makes it a perfect electrical insulator." [137]

However, this has been proven wrong repetitively in literature since in 1973 [2, 139, 141]. Sadly, the verbal discussion took place on a non-factual level.

Therefore, control experiments on phase transitions of biological systems is commonly unknown and unchecked in literature. Such control experiments could include DSC experiments to check for first-order phase transitions or the addition of Laurdan to check for jumps in the GP when changing the environmental parameters. With the use of such control experiments, a clear line could be drawn between effects originating from molecular biochemical effects and fundamental ones originating from physics - especially thermodynamics.

9 Materials and Methods

The following materials and methods were used.

9.1 Artificial Lipid Membranes

Preparation of the Periphery

Work under the fume hood and use special gloves and safety goggles. Fill stock chloroform (Sigma-Aldrich, Taufkirchen, Germany) into two beakers with the labels pure and purer chloroform. The beakers height has to be sufficient (about 5 cm), so the cannula of the syringe can be immersed into the chloroform completely.

1. Aspirate as much pure chloroform as possible and empty the Hamilton® (Hamilton Bonaduz AG, Bonaduz, Swiss) syringe into a waste container.
2. Repeat five times in total.
3. Repeat step 1 five times with purer chloroform.
4. Clean glass vials by filling them with chloroform, vortexing, and discarding the solvent several times (about 2-3 times). Keep in mind, that when aiming for a certain lipid concentration, the cleaning chloroform has to fully evaporate.
5. Transfer desired lipid. Whenever immersing the syringe into a new lipid stock solution container do steps 1-3 prior to prevent contamination.
6. When finished, leave the syringed cleaned by following the steps 1-3.

Fabrication of the Lipid Cake

Use lipid stock solutions from Avanti (Avanti Polar Lipids, Birmingham, AL, United States of America) without further purification. Seal the lipid stock solution using the lid and additional Teflon sealing tape. For the sealing, cut an appropriate amount and wrap it tightly and clockwise around the glass vial-lid junction. The clockwise wrapping enhances sealing when the lid is tightened. This is important, as chloroform evaporates and the concentration of the lipid stock solution might rise, as well as water and other contaminants might intrude.

1. Take the lipids out of the freezer and wait for them to equilibrate to room temperature. Transfer the desired volume using an appropriate syringe into a cleaned glass vial.

2. Repeat step 1 for all desired lipids. Keep in mind to clean the syringe each time whenever the syringe gets contaminated or another lipid container is used. If the lipid mixture contains fluorescent dyes, minimize the exposure to light by using brown glass and wrapping aluminum foil around the glass vials at every step possible.

3. Once all desired lipids have been added, mix the lipids gently before drying out. Therefore, carefully rotate the glass vial gently while the lipids are still completely dissolved. This is critical for a homogeneous mixture.
If the lipids are used for electroformation or for film trough experiments, do not evaporate the solvent and stop at this point.

4. Evaporate the chloroform by a gentle stream of N_2 to obtain a dry lipid cake. The dry lipid cake still contains traces of chloroform, therefore place the glass vial in a desiccator under vacuum for several hours, preferably overnight.

If not stated otherwise use $m = 1\,\mathrm{mg}$ of total lipid mass.

Multilamellar Vesicles

1. Fabricate a lipid cake as described above.

2. Preheat the ultrasonic bath (Sonorex Super 10 P, BANDELIN electronic GmbH & Co. KG, Berlin, Germany) at least 10 K above phase transition temperature.

3. Hydrate the dry lipid cake by pipetting the desired aqueous solution to obtain the desired concentration. Usually, the aqueous solution is ultrapure water or buffer.

4. Seal the glass vial tightly with Teflon tape. Once the heat bath temperature has equilibrated. insert the glass vial into the heat bath.

5. Turn on the ultrasonic treatment at full power for $t = 30\,\mathrm{min}$.

6. After sonication, turn off the ultrasonic, but keep the temperature to allow for healing of the multilamellar vesicles from the ultrasonic stress ($t = 30\,\mathrm{min}$).

7. The multilamellar vesicles are now ready to use and typically appear milky and opalescent for the eye. Store in the fridge.

For further literature concerning fabrication techniques, the interested reader might refer to literature [255, 256].

When working with vesicles, subsequent characterization of the vesicles is recommended. Detailed, microscopic information could be obtained e.g. by using cryo transmission electron microscopy, macroscopic information can be obtained e.g. by using dynamic light scattering.

Small Unilamellar Vesicles

To fabricate small unilamellar vesicles, use the sonication technique, as described in literature [214]. Briefly, the steps are the following:

1. Fabricate multilamellar vesicles as described above.
2. Use a powerful sonicator (Sonoplus, BANDELIN electronic GmbH & Co. KG, Berlin, Germany) which has a vial holder.
3. Press the vial containing the suspension firmly into the holder.
4. Turn on the sonicator at: power $p = 65\,\%$, cycle time $t_{\mathrm{dutycycle}} = 50\,\%$, and total sonication time $t = 10\,\mathrm{min}$.

The small unilamellar vesicles can be stored in the fridge for several days, the interested reader might refer to a study on the storability of vesicles [257].

Large Unilamellar Vesicles

A common technique to fabricate large unilamellar vesicles is extrusion. Multiple commercially available devices exist, in this thesis, I use the Extruder Set from Avanti® Polar Lipids, Inc., which is similar to the one described in [258, 259]. The setup consists of a metal block, an extruder, and two appropriate Hamilton™ syringes.

1. Extruder setup preparation:
   a) Prepare the metal block by placing the metal block on top of a temperature regulated hot plate. Set the temperature to at least 10 K above the main phase transition temperature of the lipids.
   b) Clean the syringes and hard parts of the extruder using isopropyl alcohol and dry them thoroughly.
   c) Assemble the extruder by inserting the O-rings tightly into the grooves, then pre-wetting two filter supports and carefully placing into the center of the O-rings. Consequently place a polycarbonate filter (pore size 0.1 µm) carefully on top of one O-ring, and finally insert the Teflon parts into the

case and seal it tightly. Mount the extruder, as well as the syringes on the metal block and wait for all parts to equilibrate to temperature.

2. Fabricate multilamellar vesicles, as described above.

3. Preload the syringe with the same aqueous solution as used for lipid hydration and push the buffer into the extruder to fill dead volume inside the extruder and minimize loss.

4. Discard the buffer or ultrapure water remaining in the other syringe.

5. Load the multilamellar vesicle suspension inside one syringe and allow the multilamellar vesicle suspension to adjust to temperature.

6. Start extruding the vesicles by pushing the suspension gently from one syringe through the polycarbonate membrane of the extruder into the other syringe.

7. Push the suspension back into the first syringe.

8. Repeat the steps 7 and 8 at least 10 times for the sake of monodispersity of the large unilamellar vesicles.

9. End the extrusion by collecting the suspension from the syringe, which was not begun with.

10. Transfer the suspension into a fresh and clean glass vial and store it in the fridge. The vesicles can be stored several days.

For the enzyme kinetic experiments, use 13:0 PC, 14:0 PC or 15:0 PC and 1,2-dioleoyl-sn-glycero-3-[(N-(5-amino-1-carboxypentyl)iminodiacetic acid)succinyl] (nickel salt) (18:1 DGS-NTA (Ni)) and mix at a molar ratio of 98:2 in a glass vial. For these experiments, the final lipid concentration is $c_{\mathrm{L}} = 3\,\mathrm{mM}$.

Giant Unilamellar Vesicles

To fabricate giant unilamellar vesicles, use diluted lipids dissolved in chloroform as precursor material ($V = 125\,\mu\mathrm{L}$ 14:0 PC or 15:0 PC at 15 $\frac{\mathrm{mg}}{\mathrm{ml}}$ and $1\,\mu\mathrm{L}$ DiOC14 at 1 $\frac{\mathrm{mg}}{\mathrm{ml}}$). A common technique is electroformation. This protocol is slightly modified from the original publication by Angelova et al. [260].

The electroformation setup consists of a heat bath, a signal generator, and a chamber, which in turn consists of two electrodes and a spacer.

1. Clean the electrodes (FTO-coated glass slides, Sigma-Aldrich, Taufkirchen, Germany) and the spacer using isopropyl alcohol and dry them thoroughly using N_2.

2. Spread the lipid solution onto the coated side of the FTO-coated glass slides.

3. Immediately place the second FTO-coated glass slide on top, such that the coated sides are facing each other sandwiching the lipid solution. Once the lipid solution has evenly spread between the glass slides, which can be seen by the wetting edge, quickly pull them apart horizontally and let the chloroform evaporate.

4. To thoroughly extract the solvent, use a desiccator and apply vacuum for $t = 30$ min. Protect from light if fluorescent dye is used.

5. Assemble the formation chamber by clipping two slides together with a Teflon® spacer in between, where the coated sides face each other.

6. Fill the chamber with sucrose by using a syringe with a cannula, matching the holes in the Teflon spacer.

7. Use the lower hole for inserting the sucrose solution ($c = 150\,\mathrm{mOsM}$) and the upper hole for air removal. Avoid remaining air bubbles by tilting the chamber while carefully filling it.

8. Connect the assembled chamber to a signal generator.

9. Place the assembled and connected chamber into a heat bath at least 10 K above the lipids phase transition temperature and allow for equilibration.

10. Apply $U = 0.5\,\mathrm{V}$ peak-to-peak for $t = 15$ min at $f = 10\,\mathrm{Hz}$ at a rectangular shape.

11. Raise the voltage to $U = 2\,\mathrm{V}$ peak-to-peak for another $t = 2\,\mathrm{hours}$.

12. Extract the liquid using a pipette by sliding the FTO-coated glass slides carefully against each other until a slit opens.

13. Store the giant unilamellar vesicles in the fridge.

The interested reader might refer to literature for further optimized protocols [261, 262].

Supported Lipid Bilayer

A common technique to fabricate supported lipid bilayers is vesicle fusion, as described in literature [21, 212].

1. Fabricate small unilamellar vesicles as described previously.
2. Use a glass cover slip or freshly cleaved Mica (Muscovite Mica for AFM, Sigma-Aldrich, Taufkirchen, Germany).
3. If using glass cover slips, use a strong cleaning protocol, such as subsequent rinsing with various solvents, acids, bases, according to some protocols even at boiling temperatures and intense rinsing with ultrapure water, as described in literature [263, 264]. If using Mica, the cleaving replaces the cleaning of the surface. To cleave it, either use a scalpel, or exfoliating it using Scotch® Tape shortly before adding the vesicle suspension.
4. Add the small unilamellar vesicle suspension onto the substrate and let the suspension incubate in a heat bath at $T = T_m + 10\,K$ for several hours.
5. Rinse the cover slip with the bilayer excessively with aqueous solution to remove the unruptured excess vesicles. The supported lipid bilayer must not dry out and can be stored in the fridge. To check if the fabrication was successful, use FRAP [209] or continuous bleaching [265].

Note that during the incubation, the vesicles adsorb due to the hydrophilized surface and rupture, leaving a bilayer residue on the substrate, leading to a bilayer-residue-mosaic. The defects at the bilayer-residue edges heal over time by lipid relocation processes. However the rupture process only takes place if certain criteria are met, like critical surface coverage and stability of the vesicles, which is governed by the electrostatics of the system. The interested reader should refer to literature [266, 267] regarding the criteria and the kinetics of the supported lipid bilayer formation.

For the force spectroscopy experiments, use 14:0 PC and DiOC14 as the fluorescence dye. Hydrate the lipid cake by using $V = 1\,ml$ HEPES buffer containing NaCl ($c_{HEPES} = 15\,mM$, $c_{NaCl} = 75\,mM$). The fabrication of supported lipid bilayers was not always successful. For future experiments, I recommend two improvements. Firstly, Schönherr *et al.* [212] claim a critical rupture size of about 75 nm, therefore large unilamellar vesicles might be better suited than small unilamellar vesicles. Secondly, a cleaning protocol using a boiling solvent could produce better results. Try trichloroethylene as a vapor cleaning agent for organic residues in combination with a subsequent N_2-gun to blow off inorganic residues.

Supported Lipid Bilayer in a Black Microfluidic Channel

1. Fabricate a microfluidic channel, which will be described extensively in section 9.4.

2. Fabricate the desired small unilamellar vesicles suspension as described previously.

3. Flood the microfluidic channel with the small unilamellar vesicle suspension and seal the openings to prevent drying out.

4. Place the microfluidic channel in a heated chamber at $T = T_{\mathrm{m}} + 10\,\mathrm{K}$ and incubate over night.

5. Rinse thoroughly with aqueous solution, just as described previously for standard supported lipid bilayers.

While the supported lipid bilayer fabrication is similar, a peculiar type of microfluidic channel must be used, which is extensively described in literature [268]. In this publication, the authors add carbon-black pigments to the Polydimethylsiloxane, to prevent the auto-fluorescence of the Polydimethylsiloxane to interfere with the fluorescent dye emission signal of the supported lipid bilayer. In my experiments, I followed this ansatz, however used hand-filed charcoal instead of carbon-black pigments. This sufficiently absorbed the residual excitation signal and eliminated the Polydimethylsiloxane auto-fluorescence. The amount of charcoal which can be used is limited by substrate bonding, as charcoal impedes bonding proportionally to its fraction. As bonding strength is a function of forces acting on the microchannel, a precise charcoal concentration is obsolete and should be adjusted individually using a spectrometer. As a rough guide, no more than 25 wt% should be used.

Spectrometry on Multilamellar Vesicles in Shear Flow

1. Fabricate multilamellar vesicles using 14:0 PC and 15:0 PC, respectively. Use as fluorescent dyes DiOC14 (DiOC14:60012, Biotium, Fremont, CA, United States of America) and Laurdan (Laurdan:40227, Sigma-Aldrich, Taufkirchen, Germany) at a molar ratio of 5 mol%. Use ultrapure water as the aqueous solution.

2. Fabricate a black PDMS channel to minimize autofluorescence of the PDMS.

3. Set up the microfluidic periphery, consisting of the following:

a) Operate a standard upright microscope.

b) Place a heat bath below the black PDMS channel, such that the heat bath does not block the light path.

c) Connect the tubings to the channel.

d) Use an external, calibrated thermometer (PASPORT Quad Temperature Sensor, PASCO, Roseville, United States of America) to be certain about the exact temperature of the PDMS channel.

e) Load the multilamellar vesicles into a syringe and use a syringe pump (PHD 2000, Harvard Apparatus, Holliston, United States of America) to control the flow rate.

4. Conduct the spectrometry as follows:

a) Use a fluorescence microscope (Olympus BX51, Olympus, Tokyo, Japan) solely as an excitation light source.

b) Use a spectrometer (QE65000, Ocean Optics, Ostfildern, Germany) to measure the emission spectrum.

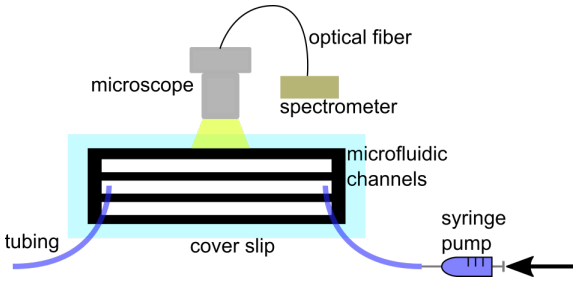

Figure 63: Experimental setup of the fluorescence emission spectroscopy of multilamellar vesicles under shear flow. Adapted from [215].

Generalized Polarization

A well-known quantity to quantify the fluidity of a membrane is the Generalized Polarisation (GP) [32, 269]. In detail, the characteristic emission maximum for the membrane ordered phase is at $\lambda = 460\,\text{nm}$ and at $\lambda = 490$ nm for the disordered phase. However, Generalized Polarization is a continuous quantity, defined by the intensity ratio of the two maximum wavelengths [32]:

$$GP = \frac{I_\text{B} - I_\text{R}}{I_\text{B} + I_\text{R}} \tag{43}$$

I_B and I_R are the emission intensities at $\lambda = 460\,\text{nm}$ (blue edge) and $\lambda = 490\,\text{nm}$ (red edge). Note that the GP is a dimensionless quantity ranging between $-1 < GP < 1$, where at -1 the membrane is completely fluid and completely ordered at 1.

To visualize and validate, we conduct calorimetric measurements and spectral measurements as function of temperature, as presented in figures 20b, 21a, and 21b. Clearly, the excess heat capacity exhibits a peak at $T_m = 24\,°\text{C}$, where the GP exhibits a quasi-step at $T = 24\,°\text{C}$. This step-like function reminds very much of a calorimetric measurement, where the y-axis is the heat Q and the x-axis is temperature T. As the heat capacity is defined as

$$c_p = \left(\frac{\mathrm{d}Q}{\mathrm{d}T}\right),$$

analogously, the derivative of the GP-value α can be identified as

$$\alpha = \left(\frac{\mathrm{d}GP}{\mathrm{d}T}\right).$$

It has the same shape at a structural phase transition, which is a peak, as the heat capacity.

From the technical perspective, the illumination source is critical. A mercury-vapor-based lamp as a UV-light source needs an excitation filter ($\lambda = 335\,\text{nm}–395\,\text{nm}$) to excite fluorescence in the vesicles. Do not use an emission filter, as the whole spectrum is of interest. To intensify the signal, a converging lens couples more light into the fiber going into the spectrometer. For slight quantitative differences to literature, note that any emission is also dependent on the excitation spectrum [32].

9.2 Vesicular Nanoparticle Uptake and Adhesion Forces

Nanoparticle uptake experiments consist of the vesicular system, the detection setup, and the evaluation method. The vesicular system requires a container where the nanoparticles and the vesicles interact.

Nanoparticle Uptake Setup

Giant unilamellar vesicles are a suitable model system due to their visibility under the fluorescence microscope (Axiovert 200M, Carl Zeiss Microscopy, Jena, Germany).

1. Fabricate giant unilamellar vesicles as described previously using 15:0 PC and 3,3'-ditetradecyloxacarbocyanine (Texas Red™ DHPE, Thermo Fisher Scientific Inc., United States of America) as the membrane dye. Use PBS buffer (pH = 7.0) containing either saccharose or glucose (D-(+)-glucose monohydrate,

Merck, Darmstadt, Germany). For all aqueous solutions, use ultrapure water (pure Aqua, Germany) with a specific resistance $\rho \leq 18\,\mathrm{M\Omega cm}$. Adjust osmolarity (Osmomat 030, Gonotec GmbH, Germany) to $c_\mathrm{n} = 150\,\mathrm{mM}$.

2. As a container, use a well plate (Nunc™ MicroWell™ 96-Well, flat, transparent, ThermoFisher Scientific Inc., Waltham, United States of America). A major advantage of well plates is the prevention of unspecific adhesion to the substrate.

3. Mount the well plate on the fluorescence microscope.

4. Dilute the giant unilamellar vesicles by adding $V = 2\,\mu\mathrm{l}$ into a well filled with $V = 70\,\mu\mathrm{l}$ consisting of [NaCl] = 56 mM, [Glucose] = 20 mM, [PBS] = 18 mM buffer and ultrapure water. Mix gently by aspiration and allow for a quick sedimentation due to a higher density of the encapsulated saccharose solution.

5. Control the temperature using a micro controller and a Peltier element. For the sake of robustness, measure and monitor the temperature in an equivalent adjacent well by a thermocouple. Preheat for $t = 30\,\mathrm{min}$ prior to each experiment to ensure an equilibrated temperature in the well plate.

6. Dilute the nanoparticles to a final surface area concentration of $c_\mathrm{A} = c(4\pi r^2) = 1\,\mathrm{m^2/l}$ (c number of particles per volume).

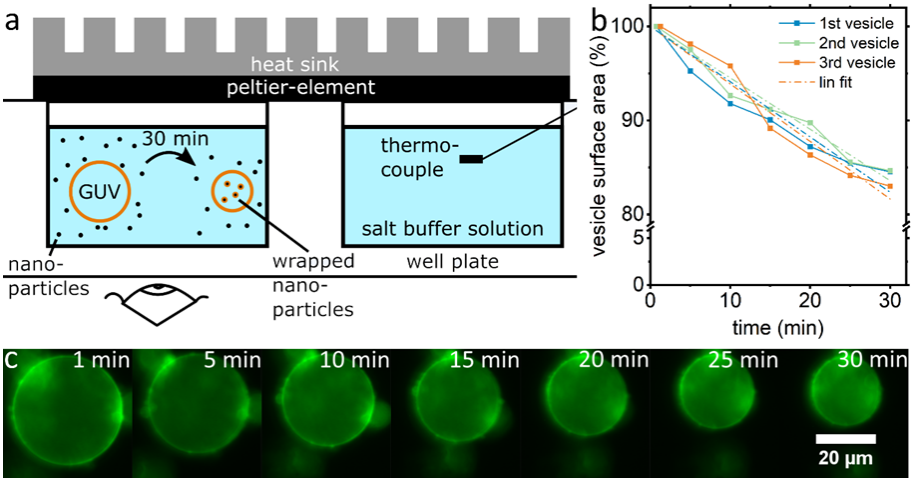

Figure 64: a) Schematic illustration of the measurement setup. b) Vesicle area as a function of time ($T = 34\,^\circ\mathrm{C}$). c) Fluorescent micrograph time series of a GUV after the addition of nanoparticles ($T = 37\,^\circ\mathrm{C}$). The vesicle clearly shrinks with ongoing time.

To start the experiment and quantification, the following steps are necessary:

1. Add the nanoparticles to start the uptake. While doing so, mix gently by pipette aspiration.

2. To quantify the uptake, take fluorescent micrographs to measure the vesicle surface area. Use distinct time steps of t_{step} = 5 min over an overall time period of t_{total} = 30 min, or t_{total} = 2 h, respectively. All chosen time scales are a compromise, balancing photo-bleaching of the fluorescent dye and micrograph quantity.

3. To evaluate the uptake, assume spherical isotropy to determine the surface area for each vesicle from a circular fit at every time step.

4. The shrinkage is function of time in-between a linear to exponential function - for the present nanoparticle size and surface area concentration [192]. Therefore, fit the data linearly, but take the parameter adjusted R^2 into account to monitor deviation from linearity.

Atomic Force Microscopy Setup

Measure the adhesion force between the membrane and the silica as function of temperature as follows:

1. Fabricate two supported lipid bilayers on mica following the protocol above. Use DMPC and 15:0 PC as lipids. For the sake of success rate in bilayer formation, add 5 mol% DOPC. Use 15 mM Hepes und 75 mM NaCl as buffer. Validate the quality qualitatively by continuous bleaching.

2. Insert the supported lipid bilayer into a BioCell™ (JPK BioAFM Business, Germany) to comfortably control the temperature.

3. Mount the BioCell™ on the optical microscope (ZEISS Axiovert 200M, Carl Zeiss Microscopy Deutschland GmbH, Germany).

4. Use MLCT-O10 cantilevers. Approach the cantilever and calibrate the setup characteristics by determining the spring constant k.

5. As the probing setup, take the MLCT-O10 cantilevers and glue a silica bead (⌀ = 7.38 µm, microParticles GmbH, Germany) to the cantilever following a JPK technical protocol [270]. Clean the silica-cantilever each time before inserting into the AFM in a plasma chamber.

6. Mount the atomic force microscope (JPK NanoWizard II, JPK BioAFM Business, Germany) and do the standard setup.

7. Determine the the sensitivity s and use the value for the spring constant from the prior measurement.

8. Set the temperature and wait for equilibration.

9. Set up a grid of 5 x 5 measurement points at 5 µm distance to prevent systematic errors due to local bilayer imperfections. Set up the approach at 2 µm/s at a force setpoint of $F = 20\,\mathrm{nN}$ and add a waiting time of one seconds to ensure relaxation of the adhesion process. Set up the retraction at 0.22 µm/s.

10. To identify the adhesion force, only use measurements with a clean adhesion peak.

Differential Scanning Calorimetry

A differential scanning calorimeter (DSC) is effectively an oven, which precisely measures temperature and power. More up-to-date devices regulate the power such that the heating rate is kept constant. The heating rate determines the operating mode, it could either be zero for an isotherm, or most commonly it could be a constant for a dynamic segment. Follow these steps to perform calorimetric measurements (MicroCal VP-DSC, MicroCal Inc., now Malvern Panalytical Ltd, United Kingdom):

1. Thoroughly clean both chambers by the following cleaning protocol.
   a) Clean an appropriate syringe to first extract all remaining reference fluids and discard into waste.
   b) Extract the remaining fluids from the sample chamber and discard into waste.
   c) Rinse the sample chamber with $V = 50\,\mathrm{ml}$ 1 vol.% Mucasol® (Schülke & Mayr GmbH, Norderstedt, Germany) in ultrapure water.
   d) Rinse the reference chamber with $V = 50\,\mathrm{ml}$ 1 vol.% Mucasol in ultrapure water.
   e) Rinse the sample chamber with $V = 50\,\mathrm{ml}$ ultrapure water.
   f) Rinse the reference chamber with $V = 50\,\mathrm{ml}$ ultrapure water.
   g) Clean an appropriate syringe to extract all remaining ultrapure water from the rinsing in both chambers and discard into waste.

2. Degas all fluids which are about to be measured in the DSC.

3. Clean an appropriate syringe to transfer the following materials.

4. Fill the reference chamber with the reference material with a small excess amount.

5. Fill the sample chamber with the sample material with a small excess amount.

6. Extract the excess by a standard syringe to ensure the same volume in both chambers. This could be done by using the top plane as a stop for the syringe, while the cannula has to at such length, that only a small - but constant - amount of liquid is extracted. The syringe needs to be clean and always extract the excess reference material first.

7. Close the lid and adjust the pressure to $p = 15\,\mathrm{psi}$ by the appropriate screw.

8. Setup the parameters in the software like number of up and down scans (6), heating rate ($\beta = 15\,\mathrm{K/h}$), and use the default values for data point frequency, filtering, and molarity.

Please note, that when an endothermic or an exothermic process of interest is taking place in the sample chamber, the heating rate deviates and has to be compensated by power regulation. If this is a reversible process (e.g. melting transition), it appears in every up and down scan. If this is an irreversible process (e.g. chemical reaction), it only appears during the the reaction time. Commonly, this results in the appearance of a peak in the first scan only. Accordingly, when studying reversible processes, it is good practice to do multiple up and down scans to get rid of irreversible processes.

Experimental Design and Baseline Subtraction

To evaluate a DSC measurement, data of power as function of time is converted into data of power as function of temperature. To obtain the excess heat capacity of the process, subtract the baseline. The baseline subtraction is often not trivial and requires thorough and careful thinking.

To study lipid melting transitions, a DSC measurement should fulfill various quality requirements.

1. Use a small heating rate (below 30 K per hour) to avoid heating inertia from limited heat conductivity of the device or sample. A higher heating rate will

overestimate the melting temperature and a higher cooling rate will underestimate the melting temperature. For excellent accuracy, use as low heating and cooling rates as possible and average over one up and down cycle.

2. The temperature should contain the peak or dip regime. Ideally, include a part of the constant or linear regime before and after the peak or dip - depending on the broadness of the melting peak - ±20 K around the transition. This enables a good estimation of the baseline.

In lipid membrane DSC measurements, pure lipid mixtures often display another phase, the ripple phase. Here, the main transition peak is accompanied by a smaller pretransition peak, which can not be separated from the main transition. Therefore, it is likely to assume that both transitions are continuous. In most cases the melting temperature is considered as the main peak temperature. However, some studies suggest to define the phase transition temperature where 50% of the enthalpy of both transitions has been reached. As the contribution of the pretransition is relatively small, this will cause a slight discrepancy towards lower temperatures and it would not change the results of this thesis, just slightly different numbers.

9.3 *In Vitro* Cells

Cell Culture Environment

To cultivate cells, use an incubator ($T = 37\,°C$, $c = 5\,\%$ CO_2), a biosafety bench, *in vitro* cells, and sterile consumables. The interested reader might refer to literature [271].

Working in a sterile environment includes extensive safety measures, such as:

- Wear a lab coat and gloves. Put sleeves inside the gloves, to prevent exposing skin inside the biosafety bench (HeraSafe KS, Thermo Electron Corporation, Waltham, MA, United States of America). Spray 70/30 (70 % Ethanol & 30 % distilled water) on Gloves each time before engaging the sterile environment from the non-sterile outside.

- Before operating inside the biosafety bench, turn on the ultraviolet light for $t = 30\,\text{min}$. To operate inside the biosafety bench, turn off UV light and turn on the airflow. Waiting $t = 30\,\text{s}$ for the the airflow to become laminar. After the waiting time, clean the biosafety bench using 70/30 and wait $t = 30\,\text{s}$ afterwards.

- Equipment entering into the biosafety bench needs to be cleaned thoroughly using 70/30. Sterile packaging must not be opened outside the biosafety bench. Prewarm all liquids which come into contact with the cells to 37 °C.

- Open containers only as long as necessary. Avoid operating over open containers or touching the inside of the container.
- Do not contaminate filters in pipettes or pipettes themselves.
- Clean the biosafety bench thoroughly after working using 70/30. After sealing the biosafety bench, turn on the UV light for $t = 30\,\text{min}$.

Cell Passaging

Find the cells (HeLa, ATCC® CCL-2™, Manassas, United States of America) in the incubator in a flask (Nunc™EasYFlask™25 cm^2, ThermoFisher Scientific Inc., Waltham, United States of America) at $c = 5\,\%$ CO_2, $c = 95\,\%$ humidity and $T = 37\,°\text{C}$.

1. Take the cells out and check the flask for pH changes (yellow indicates acidic environment or bacterial contamination, purple indicates fungus contamination) and confluence under the microscope.
2. Passage the cells at $\approx 70\,\%$ confluence using the following steps:
   a) Aspirate the cell medium using an appropriate sized serological pipette, therefore slightly tilt the cell flask to one bottom corner, place the pipette tip in the very corner, aspirate and discard the cell medium.
   b) Transfer 5 ml PBS ((D)PBS - solution (w/o Ca2+, w/o Mg2+), Bio&Sell GmbH, Nürnberg, Germany) into the cell flask and flush the bottom by repetitively aspirating and releasing the PBS (5 times), finally discard the PBS.
   c) Transfer a de-adhesion agent into the cell flask (1 mL Trypsin 0.025 % (Bio&Sell GmbH, Nürnberg, Germany) or Accutase® (Sigma Aldrich, St. Louis, MO, United States of America)).
   d) Transfer the cell flask into the incubator to allow for higher enzymatic activity of the enzymes in the de-adhesion agent. Visually check by tilting the cell flask into various directions and inspect the bottom: Once all white cell aggregates flow with the liquid and do not adhere at the bottom, stop the de-adhesion.
   e) Stop the de-adhesion by transfering the cell flask back into the bio-safety bench and add 4 ml of cell medium (10 % FBS (Fetal Bovine Serum, Sigma Aldrich, St. Louis, MO, United States of America), 1 % Pen-Strep solution, Bio&Sell GmbH, Nürnberg, Germany). Aspirate and release the solution as before.

f) Before transferring the desired proportion to a new cell flask, fill it with 5 ml cell medium prior to inserting the cells (commonly add $V = 500$ µL cell suspension to the $V = 5$ ml for a splitting of 1:10). To ensure even distribution of the cells, carefully agitate the cell flask.

g) Use the other $V = 4.5$ ml cell suspension for experiments or discard into waste. Dilute the cell suspension by adding medium or increase cell concentration by centrifuging and removal of the supernatant.

Freezing and Thawing of Cells

To freeze the cells, follow this protocol:

1. Passage the cells as described previously following the steps a)-g) with the remaining $V = 4.5$ ml cell suspension.
2. Transfer the remaining cell suspension into a centrifuge tube and centrifuge at $a = 100$ g until the cells have sedimented.
3. Carefully extract the supernatant until the cell aggregate remains with as little cell medium as possible.
4. Add $V = 1.5$ mL fridge-cold Biofreeze (Biofreeze Freezing Medium, Sigma Aldrich, St. Louis, MO, United States of America) and re-suspend the cells.
5. Transfer the cell suspension into a cryo tube (TPP™ Cryo Tubes, ThermoFisher Scientific Inc., Waltham, United States of America).
6. Store in the fridge for $t = 2$ h.
7. Transfer into the LN_2 dewar.

To unfreeze the cells, follow this protocol:

1. Prewarm cell medium in a heat bath at $T = 37\,°C$.
2. Prefill a centrifuge tube with $V = 5$ ml of cell medium and a cell flask with $V = 5$ ml cell medium.
3. Unfreeze the cryotube while holding it into the heat bath, while constantly inspecting the cryotube.
4. Immediately after being completely thawed, transfer the cell suspension into the prefilled centrifuge tube.

5. Centrifuge at $a = 100\,\mathrm{g}$. Discard the supernatant as much as possible to eliminate the BioFreeze (until $V \approx 0.2\,\mathrm{ml}$ supernatant is left).

6. Re-suspend the cells and transfer the concentrated cell suspension into the cell flask.

Cell Immobilization Protocol for Scanning Electron Microscopy

This protocol is a simplified version of Ramesan *et al.* [154]:

1. Incubate the cells overnight on a silicon wafer piece in cell medium to allow the cells to adhere to the substrate.

2. Fix the cells with $c = 2.5\,\%$ glutaraldehyd for $t = 60\,\mathrm{min}$ at room temperature and dehydrate in washing steps using $c = 0.1\,\mathrm{M}$ ethanol.

3. Dry the fixed cells overnight.

4. Load the sample in the scanning electron microscope.

9.4 Acoustofluidics

Acoustofluidics is a fusion of micro- to nano-scale acoustics and fluid mechanics. While this field by itself has many branches with various applications, I here focus on biomedical ones. Therefore, the acoustofluidic devices in this thesis consist of an interdigtial transducer (IDT) and a microfluidic channel.

Fabrication of Microfluidic Channel Masters

To fabricate microfluidic channel masters, clean room facilities, a photo resist, and photo-lithography are needed. The interested reader might refer to literature [272].

- Work in a flowbox (LOTUS Systems GmbH, Immendingen, Germany). Use a polished, unoxidated, appropriately sized silicon wafer (e.g. 3", MicroChemicals GmbH, Ulm, Germany).

- Apply a thorough cleaning procedure using various solvents in series as follows:
  - Immerse the silicon wafer into an acetone beaker and place the beaker in an ultrasonic bath for $t = 5\,\mathrm{min}$ at full power.

- Prepare another beaker with isopropyl alcohol and a waste beaker. To transfer the silicon wafer into the isopropyl alcohol beaker, apply a transfer procedure. The transfer procedure's only purpose is to keep the wafer wet while flushing away the prior solvent, as drying out allows for dust particles to adhere to the surface:
  * For transferring the wafer, use special wafer tweezers and hold the wafer at an edge not of interest.
  * Take out the wafer and immediately keep flushing the consequent solvent onto the wafer. The wafer must not dry out. Operate above the waste beaker.
  * When the prior solvent has been flushed off, immerse it into the beaker containing the next solvent, while still flushing.
  * Optionally, use further solvents like ethanol and water for the sake of cleanliness.
- Dry the substrate using N_2.
- Place the wafer onto the spin coater and lock the wafer in place by applying vacuum.
- Deposit the photoresist (SU8-50-100, micro resist technology, Berlin, Germany) onto the wafer (V≈ 1 ml per inch^2). See the manufacturer's data sheet for further information.
- Start the spin-coating process (DELTA 10 BM, SÜSS MicroTec Lithography GmbH, Garching, Germany).
- Soft-bake the coated wafer on a hot plate at $T = 65$ °C for few minutes (see MSDS). During soft-baking, photoresist solvent evaporates.
- Install the coated wafer into the mask aligner (Standard Mask Aligner MJB 3, SÜSS MicroTec Lithography GmbH, Garching, Germany), place the appropriate mask, and optionally choose a spectrum filter (i-line $\lambda = 365\,\text{nm}$).
- Expose the coated wafer to the UV light.
- post exposure bake the coated wafer, therefore place the wafer on a hot plate at $T = 95$ °C.
- Allow for cooling to room temperature.

– Develop the structure using an appropriate developer (mr-Dev 600, micro resist technology GmbH, Berlin, Germany). During development, gently shake the wafer forth and back to increase fresh developer supply.

– Stop the developing procedure by transferring the substrate into a beaker filled with ultrapure water.

– Rinse the wafer with isopropyl alcohol.

– Dry the wafer with N_2

– Hard bake at $T = 150\,°C$ for one hour.

For challenging structures, all processing steps might need improvement. Extensive discussions can be found in forums [273]. Easy to implement improvements are: higher substrate cleanliness, ramped and extended soft-baking periods ($t \approx 90\,\text{min}$), as well as hard-baking periods ($t \approx 90\,\text{min}$), and fragment exposure time into shorter intervals (e.g. $t = 15\,\text{s}$ and consequent $t = 45\,\text{s}$ cool-down waiting times).

Fabrication of Microfluidic Channels

To prepare a microfluidic channel for use, a microfluidic channel master is needed, Polydimethylsiloxane, as well as a substrate, a biopsy punching device and tubings [159].

- Prepare Polydimethylsiloxane by mixing the two components from the SYLGARD™ 184 Silicone Elastomer Kit (DOW Europe GmbH, Wiesbaden, Germany) in a 10:1 weight ratio.

- Mix thoroughly, until all streaks vanish and a homogeneous viscous fluid with air bubbles remains.

- Insert the master face-up into an appropriate sized plastic petri dish. For higher convenience, lay out aluminium foil on the inner surfaces of the petri dish and flatten the aluminium foil thoroughly. As the aluminium might not be perfectly even, levelling might be needed.

- Pour Polydimethylsiloxane carefully on top of the channel master, the total amount needed depends on the desired height of the microfluidic channel ($h \approx 1\,\text{cm}$).

- Place the petri dish into a levelled vacuum chamber and apply vacuum until all air bubbles have vanished.

- Insert the plastic petri dish into a levelled oven for at least four hours at $T = 70\,°\mathrm{C}$.
- Find the cured Polydimethylsiloxane as a transparent rubber on top of the microfluidic channel master.
- Use a scalpel to cut carefully and vertically through the Polydimethylsiloxane all the way down to the bottom of the microfluidic channel master. Do not apply too much pressure, as the master might crack.
- If aluminium foil has been layed out beneath the channel master and the PDMS, separate from the petri dish before cutting by prying it out or by breaking the plastic petri dish. Continue to cut around the structure of the master to finally take out the unbonded microfluidic channel.
- Before bonding, punch holes at the marked inlets and outlets using a biopsy punching device (PFM medical AG, Köln, Germany) at a size slightly smaller than the outer diameter of the tubing. Consider varying the sizes to adjust friction forces to use higher flow rate, so the tubings-inlet-interface does not leak (typically $\varnothing = 1.09\,\mathrm{mm}$ tube in a $\varnothing = 0.75\,\mathrm{mm}$ hole).
- For bonding, a clean substrate and microfluidic channels are crucial. Therefore, either clean both using isopropyl alcohol and blow dry thoroughly using N_2, or directly use the microfluidic channel after cutting it out from the master. In both cases, cover the surfaces on the microfluidic channel and on the substrate - the bonding interface - with Scotch tape to prevent adhesion of dust and dirt. Remove the Scotch tape as late as possible before exposing to plasma.
- To prepare the channel and substrate for bonding, use plasma (LabAsh 100E, Technics Plasma GmbH, Kirchheim, Germany, or see [274]) to hydrophilize the substrate and microfluidic channel.
- Immediately after plasma treatment, press the channel onto the substrate firmly and evenly for one minute.
- For ideal bonding, place the glass side of the bonded channel onto a hot plate at $T = 120\,°\mathrm{C}$ for $t = 2$ hours and cover with aluminium foil.

When using the channel for acoustofluidic purposes, do not bond the channel onto the substrate, but use a holder with screws to seal the system. Place the channel onto the substrate, so that the finger electrode structure precisely fits into the recess of the microfluidic channel.

Finally, use the microfluidic channels for microscopy purposes:

- Insert the tubing into the inlets and outlets and connect the other ends to syringes.
- Use an appropriate cannula outer diameter to firmly and carefully push the tubing onto the cannula.
- Load the syringe with the appropriate medium and connect the syringe to the cannula.
- For precise flow control, use flow pumps (Harvard PHD 2000, Instech Laboratories Inc., Plymouth Meeting, PA, United States of America). Clamp in the syringe into the flow pump and adjust the flow rate. Connect the outlet tubings to a (waste) container.
- Mount the microfluidic channel onto the microscope.

Surface Acoustic Wave Chip Preparation

Fabrication of surface acoustic chips is done in a two step process. In the first step, deposit a photoresist structure on a substrate material using photo-lithography similar to microfluidic channel master in 9.4. In the second step, the structure is metallized using physical vapor deposition and developed using solvents.

For the first step, follow the steps in 9.4 with the following alterations.

- Use two-side polished $LiNbO_3$ wafers (128° rot Y-Cut, $\lambda = 25$ µm, The Roditi International Co. Ltd., London, United Kingdom) at an appropriate size and mark the x-axis (highest acoustic propagation velocity) at a region of no interest using a diamond pen.
- Use the photoresist AZ® MiR™ 701 Photoresist cP (Microchemicals GmbH, Ulm, Germany) and use an appropriate developer (AZ® 726 MIF, Merck Performance Materials GmbH, Wiesbaden, Germany).
- Do not use wafer tweezers, but use regular tweezers and grab the substrate at the sides, not at the polished faces.
- Use the following parameters: softbaking $t = 1.5$ min & $T = 90$ °C, exposure $t = 15$ s, post exposure baking $t = 1$ min & $T = 110$ °C.

For the second step, follow the physical vapor deposition protocol:

- Clean the substrate by using plasma ($P = 200\,\mathrm{W}$ and $t = 20\,\mathrm{s}$ at $p = 500\,\mathrm{mTorr}$).
- Install the cleaned substrate in the physical vapor deposition device (ESTHER (Electronbeam-RF-Sputtering and Thermal Evaporation), Auto 500 Thin Film Coating System, BOC Edwards, Guildford, United Kingdom) and evacuate until $p < 10^{-5}\,\mathrm{mbar}$).
- Deposit three metal layers in the order Ti-Au-Ti (5 nm - 50 nm - 5 nm) at a rate of $1\,\frac{\text{Å}}{\mathrm{s}}$.
- Take the metallized substrate out and develop overnight in DMSO.
- If the development is incomplete, place the beaker with DMSO and the metallized substrate into a ultrasonic device and gradually and carefully increase power (starting at $\approx 40\,\%$) for some minutes. Too high ultrasonic power might damage the structure.
- Rinse DMSO off using ultrapure water.
- If the development is still incomplete, use Q-Tips to mechanically remove excessive metallized flakes.
- Rinse with isopropyl alcohol and dry using N_2.
- Eliminate eventual short cuts between the finger structures of the electrodes by applying a current of $U = 12\,\mathrm{V}$ DC voltage.

If needed, add a glass layer on top of the chip to protect the structure and even the surface.

- Rinse with isopropyl alcohol.
- Clean the chip further using plasma (LabAsh at $P = 800\,\mathrm{W}$ for $t = 5\,\mathrm{min}$).
- When installing the chips, cover a small region of the main electrodes at the edge of the chip with aluminium foil.
- Evacuate and deposit a layer of $d = 150\,\mathrm{nm}$ SiO at a rate of $1\,\frac{\text{Å}}{\mathrm{s}}$.

To increase accessibility, glue the chip into a circuit board and contact the electrodes using conductive silver. Connect the circuit board to a signal generator using RF-wiring.

For the acoustic traps, use tapered IDT (TIDT) with a continuous frequency range between $f = 79 - 83\,\mathrm{MHz}$. Check by using a vector network analyzer (Rohde & Schwarz ZVC 20KHz-8GHz Vector Network Analyser, Rohde & Schwarz, Germany). For employing three distinct traps, exclusively use three distinct frequencies $f_1 = 80.3$ MHz, $f_2 = 81.3$ MHz, and $f_3 = 82.3$ MHz. As a signal generator to control the TIDT, use a CellEvator (Advalytix, Munich, Germany) and contact with SMA-plugs on a circuit board and high frequency wiring. Use a customized LabView program (National Instruments, Austin, TX, United States of America) to enable the regulation of SAW-power P up to the required maximum of $P = 30$ dBm, as well as time-controlled frequency adjustment.

Acoustofluidic Setup

Note that Calcein is impermeable to the cell membrane by simple diffusion [275] at the used timescales. It is therefore suited as a model drug in these experiments and needs to be prepared as follows:

- Prepare a Calcein stock solution using DMSO and Calcein ($m_\mathrm{U} = 622.54\,\mathrm{Da}$) powder at a concentration of $c = 100\,\frac{\mathrm{mg}}{\mathrm{ml}}$. Dilute to $c = 0.2\,\frac{\mathrm{mg}}{\mathrm{ml}}$ using PBS before use.

- Prepare a solution of FITC-Dextran ($m_\mathrm{U} = 10\,\mathrm{kDa}$, Sigma-Aldrich Chemie GmbH, St. Louis, MI, United States of America) at a concentration of $c = 0.2\ \frac{\mathrm{mg}}{\mathrm{ml}}$.

- Prepare a solution of eGFP ($m_\mathrm{U} = 27\,\mathrm{kDa}$, produced by recombinant bacterial expression [276]) at a concentration of $c = 0.2\ \frac{\mathrm{mg}}{\mathrm{ml}}$. The interested reader might refer to [159, 160].

This setup is inspired by a previous study by our group [160]. Briefly, the setup is as follows.

- Press the Y-shaped microfluidic channel (cross section after the inlet $A = 100\,\mu\mathrm{m} * 100\,\mu\mathrm{m}$, cross section at the main channel $A = 200\,\mu\mathrm{m} * 100\,\mu\mathrm{m}$) on the chip (align TIDT and the recess under the microscope) with tubings and syringes attached as described in 9.4.

- Flush the tubings and the channel using 70/30, consequently flush excessively with cell medium to eliminate the alcohol.
- Load the two syringes with dye solution and cells respectively.
- Start the experiment by turning on the flow pumps and eventually the signal generator.
- Observe the propagation of the red cell suspension and the green Calcein in the inlet and consequently the outlet tube (inner diameter $\varnothing = 389\,\mu m$, Pro Liquid GmbH, Überlingen, Germany) of a length of $l = 9.3\,cm$.
- When all water has been pushed out of the outlet, switch the outlet from the waste to the well plate containing already $V = 200\,\mu l$ cell medium to collect the treated cells ($V = 100\,\mu l$).
- Finally, allow for a two-hour cell adhesion period to prevent the cells from detaching while exchanging the exterior dye-containing solution for dye-free cell medium.

Acoustofluidic Permeabilization

When the signal generator is turned off, the two fluids hardly mix in the channel. Mixing is limited by diffusion at the interface of the two liquids due to the laminar flow, as visualized in figure 65.

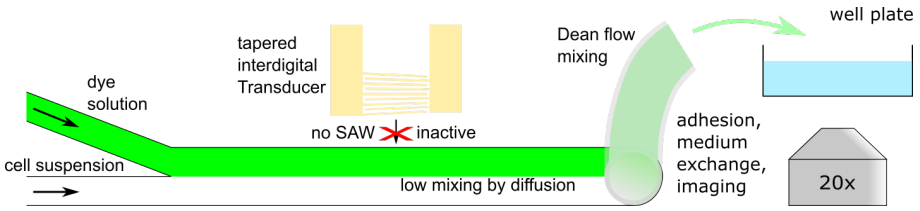

Figure 65: Microfluidic permeabilization setup and procedure. The dye solution and the cell suspension flow into the y-junction and hardly mix when in contact. The mixing is limited to diffusion at the interface due to laminar flow. At the outlet, the two liquids mix by Dean flow mixing, consequently, the cells are harvested for analysis. Adapted from [159].

When turning on the signal generator, surface acoustic waves are generated and propagate perpendicular to the flow direction. Once the surface acoustic waves reach the fluid ($x = 450\,\mu m$ from the Y-junction), energy is dissipated into the fluid, the wave becomes "leaky". In the chaotic advection of the fluid, the streamlines are

folded and therefore the fluids are mixed [161], as visualized in figure 66. This is when the cells are permeabilized and exposed to the dye. Furthermore, the cells are trapped here, as the folded streamlines form a pattern, two adjacent vortices at the intersection of the propagation path and the fluid flow path.

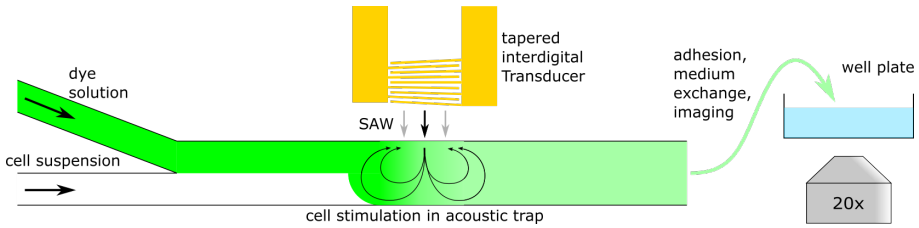

(a) Illustration of the acoustofluidic delivery setup. The dye solution and the cell suspension flow into the y-junction and hardly mix when in contact. At the active TIDT sites (gray and black arrows), SAW couple into the liquid and mix effectively by forming two vortices. The spatial position of the SAW changes by adjusting the RF frequency. The dye–cell suspension travels via tubing into a well plate. A two-hour adhesion period, dye-rinsing protocol, and fluorescence imaging follows.

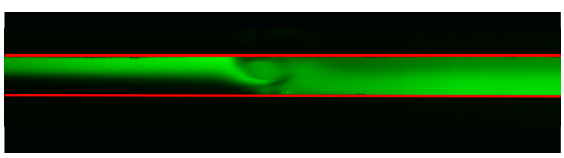

(b) Fluorescence image of Calcein in the channel. The fluorescent dye and cell suspension are mixed close to the TIDT site.

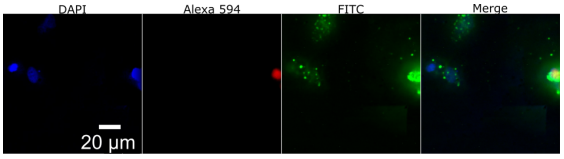

(c) Phase contrast image time series of HeLa cells trapped in SAW-induced vortices. The lines highlight the trajectories in the vortices.

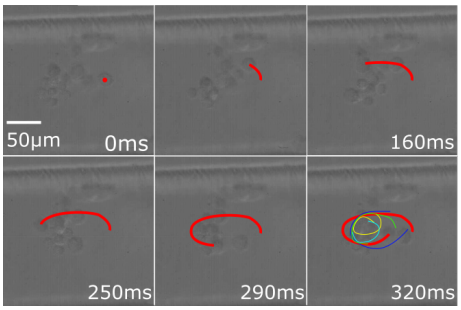

(d) Typical recorded images in the different fluorescent channels (DAPI/Alexa 594/FITC).

Figure 66: Acoustofluidic permeabilization setup and procedure. Adapted from [159].

The spatial location of the vortices shifts at distinct time intervals, which is triggered by changing the frequency of the signal generator. We applied three distinct frequencies (f = 80.3 – 81.3 – 82.3 MHz), each lasting $t_{\text{step}} = 3 * 20\,\text{s}$, resulting in a SAW cycle duration of $t_{\text{SAW}} = 1\,\text{min}$. This results in a pattern, that cells flow into the vortices from left to right and get trapped. As the cells flow in randomly, their dwell time at the active site ranges between $t_{\text{treatment}} =]0; 60\,\text{s}[$.

Once the cells have passed the active site and transition into the tubing, they remain permeable, and internalize the dye by diffusion, as shown in 5.2.1, until they are collected in a well plate for immobilization and fluorescence microscopy analysis. Once the last frequency is about to change back to the first, all cells are released from the trap. However, few cells are released stochastically from the trap at shorter time scales.

Data Acquisition and Processing

To acquire the data, stain the cells and take fluorescent micrographs as follows. To process the data, use a customized MATLAB (The MathWorks Inc., Natick, United States of America) script. The interested reader might refer to [226] for the complete MATLAB Script.

- Collect the cells from the experiment in a wellplate.
- Leave the wellplate in the incubator for $t = 2\,\text{h}$ to allow adhesion of the cells.
- Rinse the cells with cell medium to eliminate the remaining extracellular fluorescent dye.
- Stain the cells using Thermofisher ReadyProbes™ Cell Viability Imaging Kit Blue/Red (Thermo Fisher Scientific, Invitrogen, Waltham, United States of America) to stain the nuclei with Hoechst 33342 (blue) and dead cells with Propidium Iodide (red).
- To acquire fluorescent micrographs, use a fluorescence microscope (Axiovert 200M, Carl Zeiss Microscopy, Jena, Germany). In case of working with a mercury-vapor lamp, use corresponding excitation and emission filters:
  - $\lambda_{\text{ex,Hoechst33342}} = 365\,\text{nm}$
  - $\lambda_{\text{em,Hoechst33342}} = 440\,\text{nm}$
  - $\lambda_{\text{ex,Calcein}} = 485\,\text{nm}$
  - $\lambda_{\text{em,Calcein}} = 530\,\text{nm}$

- $\lambda_{\text{ex,PropidiumIodide}} = 560\,\text{nm}$
- $\lambda_{\text{em,PropidiumIodide}} = 610\,\text{nm}$

Acquire one fluorescent micrograph from every fluorescent channel, as well as a phase contrast micrograph. Finally, take a fluorescent micrograph in the Calcein channel from an empty area to subtract the systematic background.

- Run the MATLAB script. The functionality is as follows.
  - The cell nucleus is identified and spatially localized.
  - The nucleus is dilated by a factor of two to roughly account for the whole cell area.
  - The fluorescence intensity signal is evaluated. The outcome is a mean intensity per unit area.

This evaluation approximates the whole cell area as an dilatation of the nucleus by a factor of two. This remarks a conservative approximation and future experiments could improve this protocol by using a membrane staining, or by extracting the exact whole cell location from the phase contrast micrograph.

Particle Image Velocimetry

Characterize the flow pattern in the microchannel using particle image velocimetry (PIV). Use $\varnothing = 4{,}5\,\mu\text{m}$ large Polystyrene beads (Polybead™, Polysciences, Inc., United States of America) suspended in ultrapure water. The beads are pumped through the microchannel under the exact same conditions as the cells. Due to the laminar flow, they follow the streamlines. Record videos with a high-speed-camera (Photron UX, Photron Inc.) at a framerate of 1000 images per second. Analyze the video, use at least 300 frames with the MATLAB app PIVlab [231] to acquire the velocity distribution of the particles in the channel. Use this information to extract parameters like the shear rate. Here, the acoustofluidic parameters used were flow rate $Q = 80\ \frac{\mu\text{L}}{\text{h}}$and SAW input power $P = 28\,\text{dBm}$.

9.5 Enzyme Kinetics

The enzyme was kindly provided by Tobias Obser (Universitätsklinikum Hamburg-Eppendorf). Briefly, express the ADAMTS13 vector and insert a c-terminal 6xHis-Tag by in vitro mutagenesis using the QuikChange site directed mutagenesis kit (Stratagene) [277]. The transfection and expression was done as previously described [278]. The enzymes were used as follows.

- Store enzymes in LN_2 at their stock concentration.
- Once thawed, dilute to $c_{\mathrm{ADAMTS13}} = 10^{-11}\,\mathrm{M}$. Use it up as quickly as possible.

The only commercially available enzyme used was provided by the ACTIFLUOR™ ADAMTS13 Activity Assay kit. It was only used for complementary measurements for quantitative reference values.

Preparation of the ADAMTS13 Compositions

Use the commercially available assay ACTIFLUOR™ ADAMTS13 Activity Assay (LOXO GmbH, Dossenheim, Germany). This assay utilizes a synthetic minimal substrate, marked with a FRET fluorophore couple. The substrate from the assay is transformed into a stock solution as follows

- Dilute DMSO 1:4 with filtered deionized water to obtain a 25% DMSO solution.
- Reconstitute the substrate from the assay with $V = 300$ µL of the 25% DMSO solution.
- Wait $t = 5\,\mathrm{min}$ at room temperature.
- Mix gently.
- Aliquote $V = 6$ µL into tubes and freeze.
- Unfreeze only upon use.

Prepare the assay buffer as follows.

- Reconstitute the assay buffer with $V = 10$ mL of filtered deionized or distilled water.
- Wait for $t = 15\,\mathrm{min}$.
- Vortex briefly.
- Aliquote and freeze.

The interested reader might refer to the inventor of this assay [247].

Use two types of composition for the experiments, one for the sample, one for the reference. The sample composition consists of:

- buffer (assay buffer)

- large unilamellar vesicles (c_{Lipid} = 3 mM, 14:0 PC/15:0 PC : 18:1 DGS-NTA(Ni) in a 98:2 ratio)
- his-tagged ADAMTS13 enzyme ($c_{\text{ADAMTS13}} = 10^{-11}$ M)
- substrate (thaw and dilute 1:25 with assay buffer)

The reference composition consist of:

- buffer (assay buffer)
- buffer (the vesicles have been substituted with buffer)
- his-tagged ADAMTS13 enzyme ($c_{\text{ADAMTS13}} = 10^{-11}$ M)
- substrate (thaw and dilute 1:25 with assay buffer)

To prevent premature start of the reaction, separate the substrate from the rest and add to begin the reaction.

Continuous Kinetic Measurements

To obtain continuous fluorometric kinetics, use a plate reader (Tecan Infinite®F200 PRO, λ_{ex} = 485 nm,λ_{em} = 535 nm) and 96-well plates (Greiner, flat, black, Cat. No. 237105, ThermoFisher Scientific Inc., Waltham, MA, United States of America).

- Preheat the plate reader t = 30 min to the desired temperature, as well as the well plate before loading the well plate with the compositions.
- Load sample compositions and reference compositions into the wells.
- For further reference, fill one more well of the sample and reference composition respectively, where the enzyme has been substituted by buffer.
- Load the substrate into the wells below.
- To start the reaction, use a multipipette to transfer the substrate into the other wells.
- Start the measurement as soon as possible.
- To evaluate the activity, use a linear fit at the beginning of the reaction. Evaluate the time from t = 100 s until t = 1100 s of the kinetic measurement.

Fluorometric Endpoint Measurements

To obtain endpoint measurements, use a ®Mastercycler Gradient (Eppendorf SE, Hamburg, Germany) to control the temperature of the reaction. Use the following settings.

- Use the gradient mode to obtain a temperature gradient of ±10 K around T_m.
- Preheat the Thermocycler and the test tubes for $t = 30\,\mathrm{min}$.
- Use the small cavities in the brass block to fit in four rows à 12 PCR test tubes ($V = 0.2\,\mathrm{ml}$). One row consists of the sample composition, one row of the reference composition, and two rows of the substrate.
- Allow the temperature to equilibrate for another $t = 15\,\mathrm{min}$ before starting the reaction.
- Start the reaction by quickly pipetting six substrate well fillings at once into sample and reference tubes respectively for all wells.
- Measure the fluorescence results after $t = 30\,\mathrm{min}$ using a plate reader. Transfer volume of the PCR test tubes into a well plate and insert into the plate reader.
- Evaluate the slope of the kinetic measurement. To do so, determine the slope of the two data points at $I(t = 0\,\mathrm{s})$ and $I(t = 15\,\mathrm{min})$. As for the reactions in this thesis $I(t = 0\,\mathrm{s}) \approx 0$, an appropriate rate approximation is $\alpha = \frac{I(t=15\,\mathrm{min})}{15\,\mathrm{min}}$.

Colorimetric Endpoint Kinetic

Colorimetric endpoint kinetics are exclusively used for acetocholine esterases activity measurements. As the product is transparent, use 5,5-dithio-bis-(2-nitrobenzoic acid) (DTNB) to measure absorbance at $\lambda_\mathrm{max} = 412\,\mathrm{nm}$, also known as Ellman's reagent [244]. Absorbance is described by the Lambert-Beer law

$$A = \epsilon l c, \tag{44}$$

where A is the absorbance, ϵ is the molar attenuation coefficient ($\epsilon_\mathrm{DTNB} = 14{,}150\,\frac{1}{\mathrm{Mcm}}$ at $\lambda_\mathrm{max} = 412\,\mathrm{nm}$), l is the optical path length, and c is the concentration of the attenuating species. The following experimental peculiarities have to be considered:

- PBS was used as a buffer ($c = 50\,\mathrm{mM}$).

- In the cases of using 14:0 PC and 15:0 PC, no cage-lipid was used. The full $c = 3\,\mathrm{mM}$ lipids were either 14:0 PC or 15:0 PC respectively.
- Experiments using 12:0 PS were carried out at a pH = 6.4 by adjusting the PBS mono- and divalent solution ratios accordingly.
- The total enzyme acetocholine esterases in a well concentration was $c = 90\,\mathrm{nM}$.
- The total DTNB concentration was $c = 50\,\mathrm{nM}$.
- The total acetylthiocholine-iodine concentration was $c = 2\,\mathrm{mM}$.

Otherwise, follow the exact steps from the fluorometric endpoint kinetic in 9.5.

Note, that for all experiments using acetylcholinesterase, this enzyme has an intrinsic membrane anchor [102]. This anchor is specific to the acetylcholinesterase extracted from a pacific electric ray (*torpedo californica* [279]), which was kindly provided by Prof. Matthias Schneider, TU Dortmund, Germany and Prof. Silmann, Weizmann Institute, Israel.

Scanning Electron Microscopy

Scanning electron microscope images were taken with a ZEISS Merlin (Carl Zeiss Microscopy Deutschland GmbH, Germany), using a field emission cathode. Using a low landing energy of $U = 1\,\mathrm{kV}$ and a beam current of $I = 125\,\mathrm{pA}$, high-resolution topography images without beam damage could be achieved during image acquisition.

References

[1] Yuval Noah Harari. *Homo Deus*. Vintage, 2017. ISBN 9781784703936. doi:10.17104/9783406704024. URL https://www.beck-elibrary.de/index.php?doi=10.17104/9783406704024.

[2] Thomas Heimburg. *Thermal Biophysics of Membranes*. Wiley, jul 2007. ISBN 9783527611591. doi:10.1002/9783527611591. URL https://onlinelibrary.wiley.com/doi/book/10.1002/9783527611591.

[3] Karl Wilhelm Nägeli and Karl Eduard Cramer. *Pflanzenphysiologische Untersuchungen*. F. Schulthess, Zürich, 1855.

[4] W. Pfeffer. *Osmotische Untersuchungen. Studien zur Zellmechanik*. Leipzig Engelmann, 1877.

[5] Charles Ernest Overton. Über die osmotischen eigenschaften der lebenden pflanzen- und tierzelle. *Fäsi & Beer*, 1895.

[6] Irving Langmuir. THE CONSTITUTION AND FUNDAMENTAL PROPERTIES OF SOLIDS AND LIQUIDS. II. LIQUIDS. 1. *Journal of the American Chemical Society*, 39(9):1848–1906, sep 1917. ISSN 0002-7863. doi:10.1021/ja02254a006. URL https://pubs.acs.org/doi/abs/10.1021/ja02254a006.

[7] E. Gorter and F. Grendel. ON BIMOLECULAR LAYERS OF LIPOIDS ON THE CHROMOCYTES OF THE BLOOD. *Journal of Experimental Medicine*, 41(4):439–443, apr 1925. ISSN 1540-9538. doi:10.1084/jem.41.4.439. URL https://rupress.org/jem/article/41/4/439/26091/ON-BIMOLECULAR-LAYERS-OF-LIPOIDS-ON-THE.

[8] James Frederic Danielli and Hugh Davson. A contribution to the theory of permeability of thin films. *Journal of Cellular and Comparative Physiology*, 5(4):495–508, feb 1935. ISSN 0095-9898. doi:10.1002/jcp.1030050409. URL https://onlinelibrary.wiley.com/doi/10.1002/jcp.1030050409.

[9] J D ROBERTSON. The ultrastructure of cell membranes and their derivatives. *Biochemical Society symposium*, 16:3–43, 1959. ISSN 0067-8694. URL http://www.ncbi.nlm.nih.gov/pubmed/13651159.

[10] J. Lenard and S. J. Singer. PROTEIN CONFORMATION IN CELL MEMBRANE PREPARATIONS AS STUDIED BY OPTICAL ROTATORY DISPERSION AND CIRCULAR

DICHROISM. *Proceedings of the National Academy of Sciences*, 56 (6):1828–1835, dec 1966. ISSN 0027-8424. doi:10.1073/pnas.56.6.1828. URL http://www.pnas.org/cgi/doi/10.1073/pnas.56.6.1828.

[11] O.G. Mouritsen and M. Bloom. Mattress model of lipid-protein interactions in membranes. *Biophysical Journal*, 46(2): 141–153, aug 1984. ISSN 00063495. doi:10.1016/S0006-3495(84)84007-2. URL https://linkinghub.elsevier.com/retrieve/pii/S0006349584840072.

[12] Thad A. Harroun, William T. Heller, Thomas M. Weiss, Lin Yang, and Huey W. Huang. Experimental Evidence for Hydrophobic Matching and Membrane-Mediated Interactions in Lipid Bilayers Containing Gramicidin. *Biophysical Journal*, 76(2):937–945, feb 1999. ISSN 00063495. doi:10.1016/S0006-3495(99)77257-7. URL https://linkinghub.elsevier.com/retrieve/pii/S0006349599772577.

[13] Vitor H. Teixeira, Diogo Vila-Viçosa, António M. Baptista, and Miguel Machuqueiro. Protonation of DMPC in a Bilayer Environment Using a Linear Response Approximation. *Journal of Chemical Theory and Computation*, 10 (5):2176–2184, may 2014. ISSN 1549-9618. doi:10.1021/ct5000082. URL https://pubs.acs.org/doi/10.1021/ct5000082.

[14] Gregor Cevc, Anthony Watts, and Derek Marsh. Titration of the phase transition of phosphatidylserine bilayer membranes. Effects of pH, surface electrostatics, ion binding, and head-group hydration. *Biochemistry*, 20(17):4955–4965, aug 1981. ISSN 0006-2960. doi:10.1021/bi00520a023. URL http://pubs.acs.org/doi/abs/10.1021/bi00520a023.

[15] Robert B. Gennis. *Biomembranes*. Springer Advanced Texts in Chemistry. Springer New York, New York, NY, 1989. ISBN 978-1-4757-2067-9. doi:10.1007/978-1-4757-2065-5. URL http://link.springer.com/10.1007/978-1-4757-2065-5.

[16] E. Grell, E. Lewitzki, R. Schneider, G. Ilgenfritz, I. Grillo, and M. Von Raumer. Phase transitions in non-ionic detergent micelles. *Journal of Thermal Analysis and Calorimetry*, 68(2):469–478, 2002. ISSN 14182874. doi:10.1023/A:1016083501500.

[17] Thomas Heimburg. A Model for the Lipid Pretransition: Coupling of Ripple Formation with the Chain-Melting Transition. *Biophysical Journal*, 78 (3):1154–1165, mar 2000. ISSN 00063495. doi:10.1016/S0006-3495(00)76673-2. URL

http://dx.doi.org/10.1016/S0006-3495(00)76673-2http://linkinghub.elsevier.com/retrieve/pii/S0006349500766732.

[18] Yin Wang, Paraskevi Gkeka, Julian E. Fuchs, Klaus R. Liedl, and Zoe Cournia. DPPC-cholesterol phase diagram using coarse-grained Molecular Dynamics simulations. *Biochimica et Biophysica Acta - Biomembranes*, 1858(11):2846–2857, 2016. ISSN 18792642. doi:10.1016/j.bbamem.2016.08.005. URL http://dx.doi.org/10.1016/j.bbamem.2016.08.005.

[19] Michael D. Buschmann, Manuel J. Carrasco, Suman Alishetty, Mikell Paige, Mohamad Gabriel Alameh, and Drew Weissman. Nanomaterial delivery systems for mrna vaccines. *Vaccines*, 9(1):1–30, 2021. ISSN 2076393X. doi:10.3390/vaccines9010065.

[20] Evan A. Evans and Richard Skalak. *Mechanics and Thermodynamics of Biomembranes*. CRC Press, jan 2018. ISBN 9781351074339. doi:10.1201/9781351074339. URL https://www.taylorfrancis.com/books/9781351082785.

[21] C. Scomparin, S. Lecuyer, M. Ferreira, T. Charitat, and B. Tinland. Diffusion in supported lipid bilayers: Influence of substrate and preparation technique on the internal dynamics. *The European Physical Journal E*, 28(2):211–220, feb 2009. ISSN 1292-8941. doi:10.1140/epje/i2008-10407-3. URL http://link.springer.com/10.1140/epje/i2008-10407-3.

[22] Ernst Ising. Beitrag zur Theorie des Ferromagnetismus. *Zeitschrift für Physik*, 31(1):253–258, feb 1925. ISSN 0044-3328. doi:10.1007/BF02980577. URL http://link.springer.com/10.1007/BF02980577.

[23] V.P. Ivanova, I.M. Makarov, T.E. Schäffer, and T. Heimburg. Analyzing Heat Capacity Profiles of Peptide-Containing Membranes: Cluster Formation of Gramicidin A. *Biophysical Journal*, 84(4):2427–2439, apr 2003. ISSN 00063495. doi:10.1016/S0006-3495(03)75047-4. URL http://linkinghub.elsevier.com/retrieve/pii/S0006349503750474https://linkinghub.elsevier.com/retrieve/pii/S0006349503750474.

[24] Thomas Heimburg. Mechanical aspects of membrane thermodynamics. Estimation of the mechanical properties of lipid membranes close to the chain melting transition from calorimetry. *Biochimica et Biophysica Acta (BBA) - Biomembranes*, 1415(1):147–162, dec 1998. ISSN 00052736. doi:10.1016/S0005-2736(98)00189-8. URL https:

//linkinghub.elsevier.com/retrieve/pii/S0005273698001898.

[25] Marian Redón, José Manuel Guillamón, Albert Mas, and Nicolas Rozès. Effect of growth temperature on yeast lipid composition and alcoholic fermentation at low temperature. *European Food Research and Technology*, 232 (3):517–527, March 2011. ISSN 1438-2385. doi:10.1007/s00217-010-1415-3. URL https://doi.org/10.1007/s00217-010-1415-3.

[26] Toshio Sakamoto and Norio Murata. Regulation of the desaturation of fatty acids and its role in tolerance to cold and salt stress. *Current Opinion in Microbiology*, 5 (2):206–210, 2002. ISSN 1369-5274. doi:https://doi.org/10.1016/S1369-5274(02)00306-5. URL https://www.sciencedirect.com/science/article/pii/S1369527402003065.

[27] María Jesús Torija, Gemma Beltran, Maite Novo, Montse Poblet, José Manuel Guillamón, Albert Mas, and Nicolas Rozès. Effects of fermentation temperature and saccharomyces species on the cell fatty acid composition and presence of volatile compounds in wine. *International Journal of Food Microbiology*, 85(1): 127–136, 2003. ISSN 0168-1605. doi:https://doi.org/10.1016/S0168-1605(02)00506-8. URL https://www.sciencedirect.com/science/article/pii/S0168160502005068.

[28] M. Böttner, D. Ceh, U. Jacobs, and R. Winter. High Pressure Volumetric Measurements on Phospholipid Bilayers. *Zeitschrift für Physikalische Chemie*, 184(1-2):205–218, jan 1994. ISSN 2196-7156.

[29] Anne Charrier and F. Thibaudau. Main Phase Transitions in Supported Lipid Single-Bilayer. *Biophysical Journal*, 89(2):1094–1101, aug 2005. ISSN 00063495. doi:10.1529/biophysj.105.062463. URL http://dx.doi.org/10.1529/biophysj.105.062463https://linkinghub.elsevier.com/retrieve/pii/S0006349505727570.

[30] Andrea Alessandrini and Paolo Facci. Phase transitions in supported lipid bilayers studied by AFM. *Soft Matter*, 10(37): 7145–7164, 2014. ISSN 1744-683X. doi:10.1039/C4SM01104J. URL http://xlink.rsc.org/?DOI=C4SM01104J.

[31] C. Westerhausen, F.G. G. Strobl, R. Herrmann, A.T. T. Bauer, S.W. W. Schneider, A. Reller, A. Wixforth, and M.F. F. Schneider. Chemical and mechanical impact of silica nanoparticles on the phase transition behavior

of phospholipid membranes in theory and experiment. *Biophysical Journal*, 102(5):1032–1038, mar 2012. ISSN 00063495. doi:10.1016/j.bpj.2011.12.004. URL http://dx.doi.org/10.1016/j.bpj.2011.12.004https://linkinghub.elsevier.com/retrieve/pii/S0006349511053707.

[32] T. Parasassi, G. De Stasio, A. D'Ubaldo, and E. Gratton. Phase fluctuation in phospholipid membranes revealed by Laurdan fluorescence. *Biophysical Journal*, 57(6):1179–1186, jun 1990. ISSN 00063495. doi:10.1016/S0006-3495(90)82637-0. URL http://dx.doi.org/10.1016/S0006-3495(90)82637-0https://linkinghub.elsevier.com/retrieve/pii/S0006349590826370.

[33] H.H. Mantsch and R.N. McElhaney. Phospholipid phase transitions in model and biological membranes as studied by infrared spectroscopy. *Chemistry and Physics of Lipids*, 57(2-3):213–226, mar 1991. ISSN 00093084. doi:10.1016/0009-3084(91)90077-O. URL https://linkinghub.elsevier.com/retrieve/pii/000930849190077O.

[34] Paul Yager and Warner L. Peticolas. The kinetics of the main phase transition of aqueous dispersions of phospholipids induced by pressure jump and monitored by raman spectroscopy. *Biochimica et Biophysica Acta (BBA) - Biomembranes*, 688(3):775–785, jun 1982. ISSN 00052736. doi:10.1016/0005-2736(82)90291-7. URL https://linkinghub.elsevier.com/retrieve/pii/0005273682902917.

[35] C.W.M. Haest, A.J. Verkleij, J. De Gier, R. Scheek, P.H.J. Ververgaert, and L.L.M. Van Deenen. The effect of lipid phase transitions on the architecture of bacterial membranes. *Biochimica et Biophysica Acta (BBA) - Biomembranes*, 356(1):17–26, jul 1974. ISSN 00052736. doi:10.1016/0005-2736(74)90290-9. URL https://linkinghub.elsevier.com/retrieve/pii/0005273674902909.

[36] V. von Tscharner and H.M. McConnell. An alternative view of phospholipid phase behavior at the air-water interface. Microscope and film balance studies. *Biophysical Journal*, 36(2):409–419, nov 1981. ISSN 00063495. doi:10.1016/S0006-3495(81)84740-6. URL http://linkinghub.elsevier.com/retrieve/pii/S0006349581847406.

[37] J R Hazel. Influence of thermal acclimation on membrane lipid composition of rainbow trout liver. *American Journal of Physiology-Regulatory, Integrative and Comparative Physiology*, 236(1):R91–R101, jan 1979. ISSN 0363-6119.

doi:10.1152/ajpregu.1979.236.1.R91. URL http://www.ncbi.nlm.nih.gov/pubmed/434192http://www.physiology.org/doi/10.1152/ajpregu.1979.236.1.R91.

[38] J. C. Reinert and J. M. Steim. Calorimetric Detection of a Membrane-Lipid Phase Transition in Living Cells. *Science*, 168(3939):1580–1582, jun 1970. ISSN 0036-8075. doi:10.1126/science.168.3939.1580. URL https://www.sciencemag.org/lookup/doi/10.1126/science.168.3939.1580.

[39] J. M. Steim, M. E. Tourtellotte, J. C. Reinert, R. N. McElhaney, and R. L. Rader. CALORIMETRIC EVIDENCE FOR THE LIQUID-CRYSTALLINE STATE OF LIPIDS IN A BIOMEMBRANE. *Proceedings of the National Academy of Sciences*, 63(1):104–109, may 1969. ISSN 0027-8424. doi:10.1073/pnas.63.1.104. URL http://www.pnas.org/cgi/doi/10.1073/pnas.63.1.104.

[40] Esther I-Hsin Chow, S.Y. Chuang, and P.K. Tseng. Detection of a phase transition in red cell membranes using positronium as a probe. *Biochimica et Biophysica Acta (BBA) - Biomembranes*, 646(2):356–359, aug 1981. ISSN 00052736. doi:10.1016/0005-2736(81)90344-8. URL https://linkinghub.elsevier.com/retrieve/pii/0005273681903448.

[41] Haruto Nakayama, Toshio Mitsui, Masateru Nishihara, and Makoto Kito. Relation between growth temperature of E. coli and phase transition temperatures of its cytoplasmic and outer membranes. *Biochimica et Biophysica Acta (BBA) - Biomembranes*, 601:1–10, 1980. ISSN 00052736. doi:10.1016/0005-2736(80)90508-8. URL https://linkinghub.elsevier.com/retrieve/pii/0005273680905088.

[42] Miloš V. Beljanski, Pavle R Andjus, Andrija Hadži-Pavlović, Radivoje A. Srejić, and Dušan Vučelić. Differential scanning calorimetry of the plasma membrane-enriched fraction in Chara. *Plant Science*, 125(2):171–176, jun 1997. ISSN 01689452. doi:10.1016/S0168-9452(97)00077-0. URL https://linkinghub.elsevier.com/retrieve/pii/S0168945297000770.

[43] Kaushik Nag, Jesus Perez-Gil, Miguel L.F. Ruano, Lynn Anne D. Worthman, June Stewart, Cristina Casals, and Kevin M.W. Keough. Phase transitions in films of lung surfactant at the air-water interface. *Biophysical Journal*, 74(6):2983–2995, 1998. ISSN 00063495. doi:10.1016/S0006-3495(98)78005-1.

[44] Tea Mužić, Fatma Tounsi, Søren B. Madsen, Denis Pollakowski, Manfred Konrad, and Thomas Heimburg. Melting transitions in biomembranes. *Biochimica et Biophysica Acta (BBA) - Biomembranes*, 1861(11):183026, nov 2019. ISSN 00052736. doi:10.1016/j.bbamem.2019.07.014. URL https://linkinghub.elsevier.com/retrieve/pii/S0005273619301646.

[45] Kimiko Yamamoto and Joji Ando. Endothelial cell and model membranes respond to shear stress by rapidly decreasing the order of their lipid phases. *Journal of Cell Science*, 126(5):1227–1234, mar 2013. ISSN 0021-9533. doi:10.1242/jcs.119628. URL http://jcs.biologists.org/cgi/doi/10.1242/jcs.119628.

[46] Wolfgang Demtröder. *Experimentalphysik 1*. Springer, 1995. ISBN 9783540792949.

[47] K. H. de Haas, C. Blom, D. van den Ende, M. H. G. Duits, and J. Mellema. Deformation of giant lipid bilayer vesicles in shear flow. *Physical Review E*, 56(6):7132–7137, dec 1997. ISSN 1063-651X. doi:10.1103/PhysRevE.56.7132. URL https://link.aps.org/doi/10.1103/PhysRevE.56.7132.

[48] Rumiana Dimova, Karin A. Riske, Said Aranda, Natalya Bezlyepkina, Roland L. Knorr, and Reinhard Lipowsky. Giant vesicles in electric fields. *Soft Matter*, 3(7):817, 2007. ISSN 1744-683X. doi:10.1039/b703580b. URL http://xlink.rsc.org/?DOI=b703580b.

[49] Alfred Blume. A comparative study of the phase transitions of phospholipid bilayers and monolayers. *Biochimica et Biophysica Acta (BBA) - Biomembranes*, 557(1):32–44, oct 1979. ISSN 00052736. doi:10.1016/0005-2736(79)90087-7. URL https://linkinghub.elsevier.com/retrieve/pii/0005273679900877.

[50] J.H. Ipsen, O.G. Mouritsen, and M.J. Zuckermann. Theory of thermal anomalies in the specific heat of lipid bilayers containing cholesterol. *Biophysical Journal*, 56(4):661–667, oct 1989. ISSN 00063495. doi:10.1016/S0006-3495(89)82713-4. URL https://linkinghub.elsevier.com/retrieve/pii/S0006349589827134.

[51] Nicolas Färber, Jonas Reitler, Andrej Kamenac, and Christoph Westerhausen. Shear stress induced lipid order and permeability changes of giant unilamellar vesicles. *Biochimica et Biophysica Acta (BBA) - General Subjects*, 1866(10):130199, oct 2022. ISSN 03044165. doi:10.1016/j.bbagen.2022.130199.

URL https://linkinghub.elsevier.com/retrieve/pii/S0304416522001179.

[52] Peter K Robinson. Enzymes: principles and biotechnological applications. *Essays in biochemistry*, 59:1–41, 2015. ISSN 1744-1358. doi:10.1042/bse0590001. URL https://pubmed.ncbi.nlm.nih.gov/26504249. Publisher: Portland Press Limited.

[53] Anna Radzicka and Richard Wolfenden. Rates of Uncatalyzed Peptide Bond Hydrolysis in Neutral Solution and the Transition State Affinities of Proteases. *Journal of the American Chemical Society*, 118(26):6105–6109, January 1996. ISSN 0002-7863. doi:10.1021/ja954077c. URL https://doi.org/10.1021/ja954077c. Publisher: American Chemical Society.

[54] Robert Roskoski. Michaelis-Menten Kinetics. In *Reference Module in Biomedical Sciences*, pages 1–10. Elsevier, 2015. ISBN 978-0-12-801238-3. doi:https://doi.org/10.1016/B978-0-12-801238-3.05143-6. URL https://www.sciencedirect.com/science/article/pii/B9780128012383051436.

[55] R. John Ellis and Saskia M. van der Vies. Molecular Chaperones. *Annual Review of Biochemistry*, 60(1): 321–347, jun 1991. ISSN 0066-4154. doi:10.1146/annurev.bi.60.070191.001541. URL http://www.annualreviews.org/doi/10.1146/annurev.bi.60.070191.001541.

[56] Kenji Sasahara, Peter McPhie, and Allen P. Minton. Effect of Dextran on Protein Stability and Conformation Attributed to Macromolecular Crowding. *Journal of Molecular Biology*, 326(4):1227–1237, feb 2003. ISSN 00222836. doi:10.1016/S0022-2836(02)01443-2. URL https://linkinghub.elsevier.com/retrieve/pii/S0022283602014432.

[57] William C. Wimley and Stephen H. White. Experimentally determined hydrophobicity scale for proteins at membrane interfaces. *Nature Structural Biology*, 3(10):842–848, October 1996. ISSN 1545-9985. doi:10.1038/nsb1096-842. URL https://doi.org/10.1038/nsb1096-842.

[58] Enrico Di Stasio, Stefano Lancellotti, Flora Peyvandi, Roberta Palla, Pier Mannuccio Mannucci, and Raimondo De Cristofaro. Mechanistic studies on ADAMTS13 catalysis. *Biophysical journal*, 95 (5):2450–61, 2008. ISSN 1542-0086. doi:10.1529/biophysj.108.131532. URL http://www.ncbi.nlm.nih.gov/pubmed/18502798%5Cnhttp://www.pubmedcentral.nih.gov/

articlerender.fcgi?artid=PMC2517044.

[59] Heinrich Sandermann. Regulation of membrane enzymes by lipids. *Biochimica et Biophysica Acta (BBA) - Reviews on Biomembranes*, 515(3):209–237, sep 1978. ISSN 03044157. doi:10.1016/0304-4157(78)90015-1. URL http://www.sciencedirect.com/science/article/pii/0304415778900151http://linkinghub.elsevier.com/retrieve/pii/0304415778900151.

[60] E. Sackmann and R. Merkel. *Lehrbuch der Biophysik*. Wiley-VCH Verlag GmbH & Co. KGaA, 1. edition, 2010. ISBN 978-3527405350.

[61] S Manjula Jegasothy, Valentina Zabolotniaia, and Stephan Bielfeldt. Efficacy of a New Topical Nanohyaluronic Acid in Humans. *The Journal of clinical and aesthetic dermatology*, 7(3):27–9, mar 2014. ISSN 1941-2789. URL http://www.ncbi.nlm.nih.gov/pubmed/24688623http://www.pubmedcentral.nih.gov/articlerender.fcgi?artid=PMC3970829.

[62] Joy Hochstadt and Dennis Quinlan. The function and activity of certain membrane enzymes when localized on - and off - the membrane. *Journal of Cellular Physiology*, 89(4):839–852, dec 1976. ISSN 0021-9541. doi:10.1002/jcp.1040890452. URL http://doi.wiley.com/10.1002/jcp.1040890452.

[63] Harold K. Kimelberg and Demetrios Papahadjopoulos. Phospholipid requirements for (Na+ + K+)-ATPase activity: Head-group specificity and fatty acid fluidity. *BBA - Biomembranes*, 282(C):277–292, 1972. ISSN 00052736. doi:10.1016/0005-2736(72)90334-3.

[64] H Kimelberg and D Papahadjopoulos. Effects of phospholipid acyl chain fluidity, phase transitions, and cholesterol on (Na+ + K+)-stimulated adenosine triphosphatase. *The Journal of biological chemistry*, 249(4):1071–80, feb 1974. ISSN 0021-9258. URL http://www.ncbi.nlm.nih.gov/pubmed/4273517.

[65] P Palatini, F. Dabbeni-Sala, A Pitotti, A Bruni, and J.C. Mandersloot. Activation of (Na+ + K+)-dependent ATPase by lipid vesicles of negative phospholipids. *Biochimica et Biophysica Acta (BBA) - Biomembranes*, 466(1):1–9, apr 1977. ISSN 00052736. doi:10.1016/0005-2736(77)90203-6. URL http://linkinghub.elsevier.com/retrieve/pii/0005273677902036.

[66] C M Grisham and R. E. Barnett. Role of lipid-phase transitions in the

regulation of the (sodium + potassium ion)-dependent adenosinetriphosphatase. *Biochemistry*, 12 (14):2635–2637, jul 1973. ISSN 0006-2960. doi:10.1021/bi00738a013. URL http://pubs.acs.org/doi/abs/10.1021/bi00738a013.

[67] A. Boldyrev, E. Ruuge, I. Smirnova, and M. Tabak. Na,K-ATPase: The role of state of lipids and Mg ions in activity regulation. *FEBS Letters*, 80(2):303–307, 1977. ISSN 00145793. doi:10.1016/0014-5793(77)80463-8.

[68] T R Hesketh, G a Smith, M D Houslay, K a McGill, N. J. M. Birdsall, J C Metcalfe, and G B Warren. Annular lipids determine the ATPase activity of a calcium transport protein complexed with dipalmitoyllecithin. *Biochemistry*, 15(19): 4145–4151, sep 1976. ISSN 0006-2960. doi:10.1021/bi00664a002. URL http://pubs.acs.org/doi/abs/10.1021/bi00664a002.

[69] Giuseppe Inesi, Marshall Millman, and S. Eleter. Temperature-induced transitions of function and structure in sarcoplasmic reticulum membranes. *Journal of Molecular Biology*, 81(4):483–504, dec 1973. ISSN 00222836. doi:10.1016/0022-2836(73)90518-4. URL http://linkinghub.elsevier.com/retrieve/pii/0022283673905184.

[70] G B Warren, P a Toon, N J Birdsall, a G Lee, and J C Metcalfe. Reconstitution of a calcium pump using defined membrane components. *Proceedings of the National Academy of Sciences of the United States of America*, 71(3): 622–626, 1974. ISSN 0027-8424. doi:10.1073/pnas.71.3.622.

[71] C. Hidalgo, N. Ikemoto, and J. Gergely. Role of phospholipids in the calcium-dependent ATPase of the sarcoplasmic reticulum. Enzymatic and ESR studies with phospholipid-replaced membranes. *J. Biol. Chem.*, 251 (14):4224–4232, jul 1976. URL http://www.jbc.org/cgi/content/short/251/14/4224.

[72] H Sandermann. Reactivation of C 55 -isoprenoid alcohol phosphokinase apoprotein by synthetic lecithins. *FEBS Letters*, 21 (3):254–258, apr 1972. ISSN 00145793. doi:10.1016/0014-5793(72)80177-7. URL http://doi.wiley.com/10.1016/0014-5793%2872%2980177-7.

[73] J.A.F. A Op Den Kamp, M.Th. T Kauerz, and L.L.M. L van Deenen. Action of pancreatic phospholipase A2 on phosphatidylcholine bilayers in different physical states. *Biochimica et biophysica acta*, 406(2):169–77, oct 1975. ISSN 0006-3002.

doi:10.1016/0005-2736(75)90001-2. URL http://www.ncbi.nlm.nih.gov/pubmed/1191645https://linkinghub.elsevier.com/retrieve/pii/0005273675900012.

[74] A. Bruni, P.W.M. Van Dijck, and J. De Gier. The role of phospholipid acyl chains in the activation of mitochondrial ATPase complex. *Biochimica et Biophysica Acta (BBA) - Biomembranes*, 406(2):315–328, oct 1975. ISSN 00052736. doi:10.1016/0005-2736(75)90013-9.

[75] Jan C Wilschut, Joke Regts, Henk Westenberg, and Gerrit Scherphof. Action of phospholipases A2 on phosphatidylcholine bilayers. Effects of the phase transition, bilayer curvature and structural defects. *Biochimica et Biophysica Acta (BBA) - Biomembranes*, 508(2):185–196, apr 1978. ISSN 00052736. doi:10.1016/0005-2736(78)90324-3. URL http://linkinghub.elsevier.com/retrieve/pii/0005273678903243.

[76] Marty T Lehto and Frances J Sharom. PI-Specific Phospholipase C Cleavage of a Reconstituted GPI-Anchored Protein: Modulation by the Lipid Bilayer †. *Biochemistry*, 41(4):1398–1408, jan 2002. ISSN 0006-2960. doi:10.1021/bi011579w. URL http://pubs.acs.org/doi/abs/10.1021/bi011579w.

[77] Guy Beauregard and Basil D Roufogalis. The role of tightly bound phospholipid in the activity of erythrocyte acetylcholinesterase. *Biochemical and Biophysical Research Communications*, 77 (1):211–219, jul 1977. ISSN 0006291X. doi:10.1016/S0006-291X(77)80184-8. URL http://linkinghub.elsevier.com/retrieve/pii/S0006291X77801848.

[78] M. Nemat-Gorgani and E. Meisami. Use of Arrhenius plots of Na-K ATPase and acetylcholinesterase as a tool for studying changes in lipid-protein interactions in neuronal membranes during brain development. *Journal of Neurochemistry*, 32(3):1027–1032, 1979. ISSN 14714159. doi:10.1111/j.1471-4159.1979.tb04589.x.

[79] E. J. Frenkel, B. Roelofsen, U. Brodbeck, L. L. van Deenen, and P. Ott. Lipid-protein interactions in human erythrocyte-membrane acetylcholinesterase. Modulation of enzyme activity by lipids. *European journal of biochemistry / FEBS*, 109 (2):377–382, aug 1980. ISSN 0014-2956.

[80] P Overath and F Hill. Biogenesis of E. coli membrane: evidence for randomization of lipid phase. *Nature*, 1971. ISSN 00900028. doi:10.1038/newbio234264a0. URL http://www.nature.com/natur

e-newbio/journal/v234/n52/abs/newbio234264a0.html%5Cnpapers3://publication/uuid/466B96D2-E04D-4C9F-9A21-C8FDF9065B1A.

[81] J. Kumamoto, J. K. Raison, and J. M. Lyons. Temperature "breaks" in Arrhenius plots: A thermodynamic consequence of a phase change. *Journal of Theoretical Biology*, 31(1):47–51, apr 1971. ISSN 00225193. doi:10.1016/0022-5193(71)90120-2. URL http://linkinghub.elsevier.com/retrieve/pii/0022519371901202.

[82] John K Raison. The influence of temperature-induced phase changes on the kinetics of respiratory and other membrane-associated enzyme systems. *Journal of bioenergetics*, 4 (1):285–309, jan 1973. ISSN 0449-5705. URL http://www.ncbi.nlm.nih.gov/pubmed/4577759.

[83] M Mitranic, J.M. Sturgess, and M.A. Moscarello. The effect of temperature on the galactosyl- and sialyltransferase and on the ultrastructure of Golgi membranes. *Biochimica et Biophysica Acta (BBA) - Biomembranes*, 443 (2):190–197, aug 1976. ISSN 00052736. doi:10.1016/0005-2736(76)90502-2. URL http://linkinghub.elsevier.com/retrieve/pii/0005273676905022.

[84] G. Lenaz, A.M. Sechi, G. Parenti-Castelli, L. Landi, and E. Bertoli. Activation energies of different mitochondrial enzymes: Breaks in Arrhenius plots of membrane-bound enzymes occur at different temperatures. *Biochemical and Biophysical Research Communications*, 49(2):536–542, oct 1972. ISSN 0006291X. doi:10.1016/0006-291X(72)90444-5. URL http://linkinghub.elsevier.com/retrieve/pii/0006291X72904445.

[85] Vincent Massey, B. Curti, and H. Ganther. A Temperature-dependent Conformational Change in d-Amino Acid Oxidase and Its Effect on Catalysis. *J. Biol. Chem.*, 241(10):2347–2357, may 1966. URL http://www.jbc.org/cgi/content/long/241/10/2347.

[86] E. M. Merisko, G. K. Ojakian, and C. C. Widnell. The effects of phospholipids on the properties of hepatic 5'-nucleotidase. *Journal of Biological Chemistry*, 256(4):1983–1993, 1981. ISSN 00219258.

[87] Manfred Eigen and Gordon G. Hammes. *Elementary Steps in Enzyme Reactions (as Studied by Relaxation Spectrometry)*. nov 2006. doi:10.1002/9780470122709.ch1. URL http://doi.wiley.com/10.1002/9780470122709.ch1.

[88] Ramin Golestanian. Enhanced Diffusion of Enzymes that Cat-

alyze Exothermic Reactions. *Physical Review Letters*, 115(10): 108102, sep 2015. ISSN 0031-9007. doi:10.1103/PhysRevLett.115.108102. URL https://link.aps.org/doi/10.1103/PhysRevLett.115.108102.

[89] Xi Zhao, Henri Palacci, Vinita Yadav, Michelle M. Spiering, Michael K. Gilson, Peter J. Butler, Henry Hess, Stephen J. Benkovic, and Ayusman Sen. Substrate-driven chemotactic assembly in an enzyme cascade. *Nature Chemistry*, 10(3):311–317, mar 2018. ISSN 1755-4330. doi:10.1038/nchem.2905. URL http://dx.doi.org/10.1038/nchem.2905http://www.nature.com/articles/nchem.2905.

[90] Ah-Young Jee, Tsvi Tlusty, and Steve Granick. Master curve of boosted diffusion for 10 catalytic enzymes. *Proceedings of the National Academy of Sciences*, 117(47):29435–29441, nov 2020. ISSN 0027-8424. doi:10.1073/pnas.2019810117. URL http://www.pnas.org/lookup/doi/10.1073/pnas.2019810117.

[91] Efraim Racker and Peter C. Hinkle. Effect of temperature on the function of a proton pump. *The Journal of Membrane Biology*, 17(1):181–188, December 1974. ISSN 1432-1424. doi:10.1007/BF01870178. URL https://doi.org/10.1007/BF01870178.

[92] J I Korenbrot. Ion transport in membranes: Incorporation of biological ion-translocating proteins in model membrane systems. *Annual Review of Physiology*, 39(1):19–49, 1977. doi:10.1146/annurev.ph.39.030177.000315. URL https://doi.org/10.1146/annurev.ph.39.030177.000315. PMID: 139842.

[93] Nicolas Färber and Christoph Westerhausen. Broad lipid phase transitions in mammalian cell membranes measured by Laurdan fluorescence spectroscopy. *In Review - Scientific Reports*, 2021. doi:10.21203/rs.3.rs-515297/v1.

[94] R. Keegan, P.A. Wilce, E. Ruczkal-Pietrzak, and B.C. Shanley. Effect of ethanol on cholesterol and phospholipid composition of HeLa cells. *Biochemical and Biophysical Research Communications*, 114 (3):985–990, aug 1983. ISSN 0006291X. doi:10.1016/0006-291X(83)90657-5. URL https://linkinghub.elsevier.com/retrieve/pii/0006291X83906575.

[95] Martin P. Stewart, Robert Langer, and Klavs F. Jensen. Intracellular Delivery by Membrane Disruption: Mechanisms, Strategies, and Concepts. *Chemical*

Reviews, 118(16):7409–7531, aug 2018. ISSN 0009-2665. doi:10.1021/acs.chemrev.7b00678. URL https://pubs.acs.org/doi/10.1021/acs.chemrev.7b00678.

[96] H. G. Enoch, A. Catala, and P. Strittmatter. Mechanism of rat liver microsomal stearyl-CoA desaturase. Studies of the substrate specificity, enzyme-substrate interactions, and the function of lipid. *The Journal of biological chemistry*, 251(16):5095–5103, 1976. ISSN 00219258.

[97] Bernhard Fichtl, Shamit Shrivastava, and Matthias F Schneider. Protons at the speed of sound: Predicting specific biological signaling from physics. *Scientific Reports*, 6(February): 22874, 2016. ISSN 20452322. doi:10.1038/srep22874. URL http://dx.doi.org/10.1038/srep22874%5Cnhttp://10.1038/srep22874%5Cnhttp://www.nature.com/articles/srep22874#supplementary-information.

[98] D. Steppich, J. Griesbauer, T. Frommelt, W. Appelt, A. Wixforth, and M. F. Schneider. Thermomechanic-electrical coupling in phospholipid monolayers near the critical point. *Physical review. E, Statistical, nonlinear, and soft matter physics*, 81(6 Pt 1):061123, 2010. ISSN 1550-2376. doi:10.1103/PhysRevE.81.061123. URL http://www.ncbi.nlm.nih.gov/pubmed/20866394.

[99] Shamit Shrivastava and Matthias F. Schneider. Opto-Mechanical Coupling in Interfaces under Static and Propagative Conditions and Its Biological Implications. *PLoS ONE*, 8(7): e67524, jul 2013. ISSN 1932-6203. doi:10.1371/journal.pone.0067524. URL http://dx.plos.org/10.1371/journal.pone.0067524.

[100] Stefan Nuschele. *The Role of Interfaces in Enzyme Activity and Cell Adaptation*. PhD thesis, University of Augsburg, 2010.

[101] Søren S.L. Andersen, Andrew D. Jackson, and Thomas Heimburg. Towards a thermodynamic theory of nerve pulse propagation. *Progress in Neurobiology*, 88(2): 104–113, 2009. ISSN 03010082. doi:10.1016/j.pneurobio.2009.03.002.

[102] B. Fichtl, I. Silman, and M. F. Schneider. On the Physical Basis of Biological Signaling by Interface Pulses. *Langmuir*, 34(16): 4914–4919, 2018. ISSN 15205827. doi:10.1021/acs.langmuir.7b01613.

[103] Konrad Kaufmann. My Theory. *Anahit AB*, II:326, 2009.

[104] Matthias F. Schneider, Stefan Nuschele, Shamit Shrivastava,

Christian Fillafer, Bernhard Fichtl, Israel Silman, and Konrad Kaufmann. From Thermodynamic States to Biological Function by Einstein's Approach to Statistical Physics. *Biophysical Journal*, 102 (3):292a, jan 2012. ISSN 00063495. doi:10.1016/j.bpj.2011.11.1617. URL http://linkinghub.elsevier.com/retrieve/pii/S0006349511029651.

[105] Peter Grabitz, Vesselka P. Ivanova, and Thomas Heimburg. Relaxation Kinetics of Lipid Membranes and Its Relation to the Heat Capacity. *Biophysical Journal*, 82(1):299–309, jan 2002. ISSN 00063495. doi:10.1016/S0006-3495(02)75395-2. URL http://dx.doi.org/10.1016/S0006-3495(02)75395-2https://linkinghub.elsevier.com/retrieve/pii/S0006349502753952.

[106] B. Fichtl. *Integration der Biochemie in die Physik der Grenzfläche*. PhD thesis, University of Augsburg, 2016.

[107] A. Einstein. Theorie der Opaleszenz von homogenen Flüssigkeiten und Flüssigkeitsgemischen in der Nähe des kritischen Zustandes. *Annalen der Physik*, 338(16): 1275–1298, 1910. ISSN 00033804. doi:10.1002/andp.19103381612. URL http://doi.wiley.com/10.1002/andp.19103381612.

[108] Matthias F. Schneider. Living systems approached from physical principles. *Progress in Biophysics and Molecular Biology*, oct 2020. ISSN 00796107. doi:10.1016/j.pbiomolbio.2020.10.001. URL https://doi.org/10.1016/j.pbiomolbio.2020.10.001https://linkinghub.elsevier.com/retrieve/pii/S0079610720301000.

[109] A. Einstein. Über die von der molekularkinetischen Theorie der Wärme geforderte Bewegung von in ruhenden Flüssigkeiten suspendierten Teilchen. *Annalen der Physik*, 322(8): 549–560, 1905. ISSN 00033804. doi:10.1002/andp.19053220806. URL http://doi.wiley.com/10.1002/andp.19053220806.

[110] Alexander Kuklin, Dmitrii Zabelskii, Ivan Gordeliy, José Teixeira, Annie Brûlet, Vladimir Chupin, Vadim Cherezov, and Valentin Gordeliy. On the Origin of the Anomalous Behavior of Lipid Membrane Properties in the Vicinity of the Chain-Melting Phase Transition. *Scientific Reports*, 10(1):5749, April 2020. ISSN 2045-2322. doi:10.1038/s41598-020-62577-9. URL https://doi.org/10.1038/s41598-020-62577-9.

[111] R Kubo. The fluctuation-dissipation theorem. *Re-*

ports on Progress in Physics, 29(1):255–284, jan 1966. doi:10.1088/0034-4885/29/1/306. URL https://doi.org/10.1088/0034-4885/29/1/306.

[112] M. Schneider, S. Nuschele, S. Shrivastava, C. Fillafer, B. Fichtl, I. Silman, and K. Kaufmann. From Thermodynamic States to Biological Function by Einstein's Approach to Statistical Physics. *Biophysical Journal*, 102 (3):292a, jan 2012. ISSN 00063495. doi:10.1016/j.bpj.2011.11.1617. URL http://linkinghub.elsevier.com/retrieve/pii/S0006349511029651.

[113] W L Dean and C Tanford. Reactivation of lipid-depleted ca2+-atpase by a nonionic detergent. *Journal of Biological Chemistry*, 252(10): 3551–3553, 1977. ISSN 0021-9258. doi:https://doi.org/10.1016/S0021-9258(17)40426-1. URL https://www.sciencedirect.com/science/article/pii/S0021925817404261.

[114] Jörg Grandl, Sung Eun Kim, Valerie Uzzell, Badry Bursulaya, Matt Petrus, Michael Bandell, and Ardem Patapoutian. Temperature-induced opening of TRPV1 ion channel is stabilized by the pore domain. *Nature Neuroscience*, 13(6):708–714, jun 2010. ISSN 1097-6256. doi:10.1038/nn.2552. URL http://www.nature.com/articles/nn.2552.

[115] Ying Yin, Mengyu Wu, Lejla Zubcevic, William F. Borschel, Gabriel C. Lander, and Seok-Yong Lee. Structure of the cold- and menthol-sensing ion channel TRPM8. *Science*, 359(6372): 237–241, jan 2018. ISSN 0036-8075. doi:10.1126/science.aan4325. URL https://www.sciencemag.org/lookup/doi/10.1126/science.aan4325.

[116] S. G. Brohawn, J. del Marmol, and R. MacKinnon. Crystal Structure of the Human K2P TRAAK, a Lipid- and Mechano-Sensitive K+ Ion Channel. *Science*, 335(6067): 436–441, jan 2012. ISSN 0036-8075. doi:10.1126/science.1213808. URL https://www.sciencemag.org/lookup/doi/10.1126/science.1213808.

[117] M S Shearman, K Sekiguchi, and Y Nishizuka. Modulation of ion channel activity: a key function of the protein kinase c enzyme family. *Pharmacological Reviews*, 41 (2):211–237, 1989. ISSN 0031-6997. URL https://pharmrev.aspetjournals.org/content/41/2/211.

[118] Annette C. Dolphin, Paul A. Insel, Terrence F. Blaschke, and Urs A. Meyer. Introduction to the theme "ion channels and neuropharmacology: From the past

to the future". *Annual Review of Pharmacology and Toxicology*, 60 (1):1–6, 2020. doi:10.1146/annurev-pharmtox-082719-110050. URL https://doi.org/10.1146/annurev-pharmtox-082719-110050. PMID: 31914892.

[119] Kerstin Göpfrich, Chen-Yu Li, Iwona Mames, Satya Prathyusha Bhamidimarri, Maria Ricci, Jejoong Yoo, Adam Mames, Alexander Ohmann, Mathias Winterhalter, Eugen Stulz, Aleksei Aksimentiev, and Ulrich F. Keyser. Ion Channels Made from a Single Membrane-Spanning DNA Duplex. *Nano Letters*, 16(7):4665–4669, July 2016. ISSN 1530-6984. doi:10.1021/acs.nanolett.6b02039. URL https://doi.org/10.1021/acs.nanolett.6b02039. Publisher: American Chemical Society.

[120] A L HODGKIN and A F HUXLEY. A quantitative description of membrane current and its application to conduction and excitation in nerve. *The Journal of physiology*, 117(4):500–544, August 1952. ISSN 0022-3751. doi:10.1113/jphysiol.1952.sp004764. URL https://pubmed.ncbi.nlm.nih.gov/12991237.

[121] I. Tasaki and P. M. Byrne. Heat Production Associated with a Propagated Impulse in Bullfrog Myelinated Nerve Fibers. *The Japanese Journal of Physiology*, 42 (5):805–813, 1992. ISSN 0021-521X. doi:10.2170/jjphysiol.42.805. URL http://joi.jlc.jst.go.jp/JST.JSTAGE/jjphysiol/42.805?from=CrossRef.

[122] I. Tasaki and P.M. Byrne. Volume expansion of nonmyelinated nerve fibers during impulse conduction. *Biophysical Journal*, 57 (3):633–635, mar 1990. ISSN 00063495. doi:10.1016/S0006-3495(90)82580-7. URL https://linkinghub.elsevier.com/retrieve/pii/S0006349590825807.

[123] Jörg P. Kotthaus. A mechatronics view at nerve conduction, 2019.

[124] Y. Kobatake, I. Tasaki, and A. Watanabe. Phase transition in membrane with reference to nerve excitation. *Advances in biophysics*, 2:1–31, 1971. ISSN 0065-227X. URL http://www.ncbi.nlm.nih.gov/pubmed/4950262.

[125] B. Wunderlich, C. Leirer, A.-L. Idzko, U.F. Keyser, A. Wixforth, V.M. Myles, T. Heimburg, and M.F. Schneider. Phase-State Dependent Current Fluctuations in Pure Lipid Membranes. *Biophysical Journal*, 96(11):4592–4597, jun 2009. ISSN 00063495. doi:10.1016/j.bpj.2009.02.053. URL http://linkinghub.elsevier.com/retrieve/pii/S0006349509006638http:

//dx.doi.org/10.1016/j.bpj.2009.02.053https://linkinghub.elsevier.com/retrieve/pii/S0006349509006638.

[126] Christian Fillafer and Matthias F. Schneider. Temperature and excitable cells: Testable predictions from a thermodynamic perspective. *Communicative and Integrative Biology*, 6(6):1–5, 2013. ISSN 19420889. doi:10.4161/cib.26730.

[127] Simon Fabiunke, Christian Fillafer, Anne Paeger, and Matthias F. Schneider. Optical studies of membrane state during action potential propagation. *Progress in Biophysics and Molecular Biology*, 162:69–78, 2021. ISSN 0079-6107. doi:https://doi.org/10.1016/j.pbiomolbio.2020.11.001. URL https://www.sciencedirect.com/science/article/pii/S0079610720301218. On the Physics of Excitable Media. Waves in Soft and Living Matter, their Transmission at the Synapse and their Cooperation in the Brain.

[128] Andrej Kamenac, Tobias Obser, Achim Wixforth, and Matthias F Schneider. The activity of the intrinsically water - soluble enzyme ADAMTS13 correlates with the membrane state when bound to a phospholipid bilayer. *Scientific Reports*, pages 1–9, 2021. ISSN 2045-2322. doi:10.1038/s41598-021-04083-0. URL https://doi.org/10.1038/s41598-021-04083-0.

[129] J. Griesbauer, S. Bössinger, A. Wixforth, and M. F. Schneider. Propagation of 2D pressure pulses in lipid monolayers and its possible implications for biology. *Physical Review Letters*, 108 (19):1–5, 2012. ISSN 00319007. doi:10.1103/PhysRevLett.108.198103.

[130] M. I. Pérez-Camacho and J. C. Ruiz-Suárez. Propagation of a thermo-mechanical perturbation on a lipid membrane. *Soft Matter*, 13 (37):6555–6561, 2017. ISSN 1744-683X. doi:10.1039/C7SM00978J. URL http://dx.doi.org/10.1039/C7SM00978Jhttp://xlink.rsc.org/?DOI=C7SM00978J.

[131] M. Wurzel. A suggested mechanism for the action of choline esters on animal organs, inferred from a study of the effect of choline-,β-methylcholine-, and thiocholine-esters. *Experientia*, 15(11):430–433, nov 1959. ISSN 0014-4754. doi:10.1007/BF02157698. URL http://link.springer.com/10.1007/BF02157698.

[132] Christian Fillafer and Matthias F. Schneider. On the excitation of action potentials by protons and its potential implications for cholinergic transmission. *Protoplasma*, 253 (2):357–365, 2016. ISSN 0033183X. doi:10.1007/s00709-015-0815-4.

[133] Konrad Kaufmann. On the kinetics of acetylcholine at the synapse. *Naturwissenschaften*, 64 (7):371–376, jul 1977. ISSN 0028-1042. doi:10.1007/BF00368736. URL http://link.springer.com/10.1007/BF00368736.

[134] Michael R. Morrow, James H. Davis, Frances J. Sharom, and Mary P. Lamb. Studies on the interaction of human erythrocyte band 3 with membrane lipids using deuterium nuclear magnetic resonance and differential scanning calorimetry. *Biochimica et Biophysica Acta (BBA) - Biomembranes*, 858(1):13–20, jun 1986. ISSN 00052736. doi:10.1016/0005-2736(86)90286-5. URL https://linkinghub.elsevier.com/retrieve/pii/0005273686902865.

[135] Ernesto Freire, Tom Markello, Christopher Rigell, and Peter W. Holloway. Calorimetric and fluorescence characterization of interactions between cytochrome b5 and phosphatidylcholine bilayers. *Biochemistry*, 22(7):1675–1680, mar 1983. ISSN 0006-2960. doi:10.1021/bi00276a024. URL https://pubs.acs.org/doi/abs/10.1021/bi00276a024.

[136] Dmitri P. Kharakoz. Phase-Transition-Driven Synaptic Exocytosis: A Hypothesis and Its Physiological and Evolutionary Implications. *Bioscience Reports*, 21(6): 801–830, dec 2001. ISSN 0144-8463. doi:10.1023/A:1015588825142. URL https://portlandpress.com/bioscirep/article/21/6/801/54948/PhaseTransitionDriven-Synaptic-Exocytosis-A.

[137] Gerhard Gompper, Jan Dhont, Jens Elgeti, Christoph Fahlke, Dmitry Fedosov, Stephan Förster, Pavlik Lettings, and Andreas Offenhäusser. *Physics of Life*. ungszentrum Jülich GmbH, 2018. ISBN 978-3-95806-286-3. URL https://www.fz-juelich.de/pgi/EN/Leistungen/SchoolsAndCourses/SpringSchool/History/SpringSchool2018/Lecture-Notes/_node.html.

[138] Bertil Hille. *Ionic Channels of Excitable Membranes*. Sinauer Associates Inc., 3rd edition, 1991. ISBN 978-0878933235.

[139] D. Papahadjopoulos, K. Jacobson, S. Nir, and I. Isac. Phase transitions in phospholipid vesicles fluorescence polarization and permeability measurements concerning the effect of temperature and cholesterol. *Biochimica et Biophysica Acta (BBA) - Biomembranes*, 311(3): 330–348, 1973. ISSN 0005-2736. doi:https://doi.org/10.1016/0005-2736(73)90314-3. URL https://www.sciencedirect.com/science/article/pii/0005273673903143.

[140] J.F. Nagle and H.L. Scott. Lateral compressibility of lipid mono- and bilayers. Theory of membrane permeability. *Biochimica et Biophysica Acta (BBA) - Biomembranes*, 513(2):236–243, nov 1978. ISSN 00052736. doi:10.1016/0005-2736(78)90176-1. URL https://linkinghub.elsevier.com/retrieve/pii/0005273678901761.

[141] Andreas Blicher, Katarzyna Wodzinska, Matthias Fidorra, Mathias Winterhalter, and Thomas Heimburg. The Temperature Dependence of Lipid Membrane Permeability, its Quantized Nature, and the Influence of Anesthetics. *Biophysical Journal*, 96(11):4581–4591, jun 2009. ISSN 00063495. doi:10.1016/j.bpj.2009.01.062. URL http://dx.doi.org/10.1016/j.bpj.2009.01.062https://linkinghub.elsevier.com/retrieve/pii/S000634950900664X.

[142] Sergey A. Akimov, Pavel E. Volynsky, Timur R. Galimzyanov, Peter I. Kuzmin, Konstantin V. Pavlov, and Oleg V. Batishchev. Pore formation in lipid membrane II: Energy landscape under external stress. *Scientific Reports*, 7(1):12509, dec 2017. ISSN 2045-2322. doi:10.1038/s41598-017-12749-x. URL http://dx.doi.org/10.1038/s41598-017-12749-xhttp://www.nature.com/articles/s41598-017-12749-x.

[143] Sergey A. Akimov, Pavel E. Volynsky, Timur R. Galimzyanov, Peter I. Kuzmin, Konstantin V. Pavlov, and Oleg V. Batishchev. Pore formation in lipid membrane I: Continuous reversible trajectory from intact bilayer through hydrophobic defect to transversal pore. *Scientific Reports*, 7(1):12152, dec 2017. ISSN 2045-2322. doi:10.1038/s41598-017-12127-7. URL http://dx.doi.org/10.1038/s41598-017-12127-7http://www.nature.com/articles/s41598-017-12127-7.

[144] Vitaliy Oliynyk, Udo Kaatze, and Thomas Heimburg. Defect formation of lytic peptides in lipid membranes and their influence on the thermodynamic properties of the pore environment. *Biochimica et Biophysica Acta (BBA) - Biomembranes*, 1768(2):236–245, feb 2007. ISSN 00052736. doi:10.1016/j.bbamem.2006.10.007. URL https://linkinghub.elsevier.com/retrieve/pii/S0005273606003919.

[145] J. Gehl. Electroporation: theory and methods, perspectives for drug delivery, gene therapy and research. *Acta Physiologica Scandinavica*, 177(4):437–447, apr 2003. ISSN 00016772. doi:10.1046/j.1365-201X.2003.01093.x. URL http://doi.wiley.com/10.1046/j.1365-201X.2003.01093.x.

[146] Igor Vorobyov, Timothy E. Olson, Jung H. Kim, Roger E. Koeppe, Olaf S. Andersen, and Toby W. Allen. Ion-Induced Defect Permeation of Lipid Membranes. *Biophysical Journal*, 106(3):586–597, feb 2014. ISSN 00063495. doi:10.1016/j.bpj.2013.12.027. URL https://linkinghub.elsevier.com/retrieve/pii/S000634951305844X.

[147] Samir Mitragotri. Healing sound: the use of ultrasound in drug delivery and other therapeutic applications. *Nature Reviews Drug Discovery*, 4(3):255–260, mar 2005. ISSN 1474-1776. doi:10.1038/nrd1662. URL http://www.nature.com/articles/nrd1662.

[148] I. Lentacker, I. De Cock, R. Deckers, S.C. De Smedt, and C.T.W. Moonen. Understanding ultrasound induced sonoporation: Definitions and underlying mechanisms. *Advanced Drug Delivery Reviews*, 72:49–64, jun 2014. ISSN 0169409X. doi:10.1016/j.addr.2013.11.008. URL https://linkinghub.elsevier.com/retrieve/pii/S0169409X13002676.

[149] Soheyl Sheikh, Shambulingappa Pallagatti, B. Singh, Nidhi Puri, Ravinder Singh, and Aman Kalucha. Sonoporation, a redefined ultrasound modality as therapeutic aid: A review. *Journal of Clinical and Experimental Dentistry*, 3(3):e228–e234, 2011. ISSN 19895488. doi:10.4317/jced.3.e228. URL http://www.medicinaoral.com/odo/volumenes/v3i3/jcedv3i3p228.pdf.

[150] Sophie Mehier-Humbert, Thierry Bettinger, Feng Yan, and Richard H. Guy. Plasma membrane poration induced by ultrasound exposure: Implication for drug delivery. *Journal of Controlled Release*, 104(1):213–222, may 2005. ISSN 01683659. doi:10.1016/j.jconrel.2005.01.007. URL https://linkinghub.elsevier.com/retrieve/pii/S0168365905000313.

[151] Jason N. Belling, Liv K. Heidenreich, Zhenhua Tian, Alexandra M. Mendoza, Tzu-Ting Chiou, Yao Gong, Natalie Y. Chen, Thomas D. Young, Natcha Wattanatorn, Jae Hyeon Park, Leonardo Scarabelli, Naihao Chiang, Jack Takahashi, Stephen G. Young, Adam Z. Stieg, Satiro De Oliveira, Tony Jun Huang, Paul S. Weiss, and Steven J. Jonas. Acoustofluidic sonoporation for gene delivery to human hematopoietic stem and progenitor cells. *Proceedings of the National Academy of Sciences*, 117(20):10976–10982, may 2020. ISSN 0027-8424. doi:10.1073/pnas.1917125117. URL

http://www.pnas.org/lookup/doi/10.1073/pnas.1917125117.

[152] Itsuo Hanasaki, Jens H. Walther, Satoyuki Kawano, and Petros Koumoutsakos. Coarse-grained molecular dynamics simulations of shear-induced instabilities of lipid bilayer membranes in water. *Physical Review E*, 82(5): 051602, nov 2010. ISSN 1539-3755. doi:10.1103/PhysRevE.82.051602. URL https://link.aps.org/doi/10.1103/PhysRevE.82.051602.

[153] Daniel M. Hallow, Richard A. Seeger, Pavel P. Kamaev, Gustavo R. Prado, Michelle C. LaPlaca, and Mark R. Prausnitz. Shear-induced intracellular loading of cells with molecules by controlled microfluidics. *Biotechnology and Bioengineering*, 99(4):846–854, mar 2008. ISSN 00063592. doi:10.1002/bit.21651. URL https://linkinghub.elsevier.com/retrieve/pii/S0022202X15370834http://doi.wiley.com/10.1002/bit.21651.

[154] Shwathy Ramesan, Amgad R. Rezk, Chaitali Dekiwadia, Christina Cortez-Jugo, and Leslie Y. Yeo. Acoustically-mediated intracellular delivery. *Nanoscale*, 10(27): 13165–13178, 2018. ISSN 20403372. doi:10.1039/c8nr02898b.

[155] Shwathy Ramesan, Amgad R. Rezk, and Leslie Y. Yeo. High frequency acoustic permeabilisation of drugs through tissue for localised mucosal delivery. *Lab on a Chip*, 18 (21):3272–3284, 2018. ISSN 1473-0197. doi:10.1039/C8LC00355F. URL http://xlink.rsc.org/?DOI=C8LC00355F.

[156] Ryan P. Hodgson, Ming Tan, Leslie Yeo, and James Friend. Transmitting high power rf acoustic radiation via fluid couplants into superstrates for microfluidics. *Applied Physics Letters*, 94(2):024102, jan 2009. ISSN 0003-6951. doi:10.1063/1.3049128. URL http://aip.scitation.org/doi/10.1063/1.3049128.

[157] K. Sritharan, C. J. Strobl, M. F. Schneider, A. Wixforth, and Z. Guttenberg. Acoustic mixing at low Reynold's numbers. *Applied Physics Letters*, 88(5): 054102, jan 2006. ISSN 0003-6951. doi:10.1063/1.2171482. URL http://aip.scitation.org/doi/10.1063/1.2171482.

[158] A Wixforth. Acoustically Driven Programmable Microfluidics for Biological and Chemical Applications. *Journal of the Association for Laboratory Automation*, 11(6): 399–405, dec 2006. ISSN 15355535. doi:10.1016/j.jala.2006.08.001. URL http://jla.sagepub.com/lookup/doi/10.1016/j.jala.2006.08.001http:

//journals.sagepub.com/doi/10.1016/j.jala.2006.08.001.

[159] Andrej Kamenac, Felix L Schilberth, Ernst Wagner, Achim Wixforth, Ulrich Lächelt, and Christoph Westerhausen. Transient Permeabilization of Living Cells: Combining Shear Flow and Acoustofluidic Trapping for the Facilitated Uptake of Molecules. *Processes*, 9(6):913, may 2021. ISSN 2227-9717. doi:10.3390/pr9060913. URL https://www.mdpi.com/2227-9717/9/6/913.

[160] Christoph Westerhausen, Lukas Schnitzler, Dominik Wendel, Rafał Krzysztoń, Ulrich Lächelt, Ernst Wagner, Joachim Rädler, and Achim Wixforth. Controllable Acoustic Mixing of Fluids in Microchannels for the Fabrication of Therapeutic Nanoparticles. *Micromachines*, 7(9):150, sep 2016. ISSN 2072-666X. doi:10.3390/mi7090150. URL http://www.mdpi.com/2072-666X/7/9/150.

[161] Thomas Frommelt, Marcin Kostur, Melanie Wenzel-Schäfer, Peter Talkner, Peter Hänggi, and Achim Wixforth. Microfluidic mixing via acoustically driven chaotic advection. *Physical Review Letters*, 100(3):1–4, 2008. ISSN 00319007. doi:10.1103/PhysRevLett.100.034502.

[162] G. A. Jamieson and D. M. Robinson. *The Diversity of Membrane*. Butterworth-Heinemann, 1977. ISBN 9780408707237. doi:10.1016/C2013-0-04223-5. URL https://linkinghub.elsevier.com/retrieve/pii/C20130042235.

[163] James C. Weaver and Yu.A. Chizmadzhev. Theory of electroporation: A review. *Bioelectrochemistry and Bioenergetics*, 41(2):135–160, dec 1996. ISSN 03024598. doi:10.1016/S0302-4598(96)05062-3. URL https://linkinghub.elsevier.com/retrieve/pii/S0302459896050623.

[164] J.C. Weaver. Electroporation of cells and tissues. *IEEE Transactions on Plasma Science*, 28 (1):24–33, 2000. ISSN 00933813. doi:10.1109/27.842820. URL http://ieeexplore.ieee.org/document/842820/.

[165] Boris Rubinsky. Irreversible Electroporation in Medicine. *Technology in Cancer Research & Treatment*, 6(4): 255–259, aug 2007. ISSN 1533-0346. doi:10.1177/153303460700600401. URL http://journals.sagepub.com/doi/10.1177/153303460700600401.

[166] Hester J. Scheffer, Karin Nielsen, Marcus C. de Jong, Aukje A.J.M. van Tilborg, Jenny M. Vieveen, Arthur (R.A.) Bouwman, Sybren Meijer, Cornelis van Kuijk, Petrousjka (M.P.) van den Tol, and

Martijn R. Meijerink. Irreversible Electroporation for Nonthermal Tumor Ablation in the Clinical Setting: A Systematic Review of Safety and Efficacy. *Journal of Vascular and Interventional Radiology*, 25(7): 997–1011, jul 2014. ISSN 10510443. doi:10.1016/j.jvir.2014.01.028. URL https://linkinghub.elsevier.com/retrieve/pii/S1051044314001018.

[167] Sascha Buchegger, Caroline Vogel, Rudolf Herrmann, Bernd Stritzker, Achim Wixforth, and Christoph Westerhausen. Antibacterial metal ion release from diamond-like carbon modified surfaces for novel multifunctional implant materials. *Journal of Materials Research*, 31(17):2571–2577, sep 2016. ISSN 0884-2914. doi:10.1557/jmr.2016.275. URL https://www.cambridge.org/core/product/identifier/S0884291416002752/type/journal_article.

[168] Sascha Buchegger, Natascha Schuster, Bernd Stritzker, Achim Wixforth, and Christoph Westerhausen. Multilayer diamond-like amorphous carbon coatings produced by ion irradiation of polymer films. *Surface and Coatings Technology*, 327: 42–47, oct 2017. ISSN 02578972. doi:10.1016/j.surfcoat.2017.08.010.

[169] S. Buchegger, A. Kamenac, S. Fuchs, R. Herrmann, P. Houdek, C. Gorzelanny, A. Obermeier, S. Heller, R. Burgkart, B. Stritzker, A. Wixforth, and C. Westerhausen. Smart antimicrobial efficacy employing pH-sensitive ZnO-doped diamond-like carbon coatings. *Scientific Reports*, 9(1), 2019. ISSN 20452322. doi:10.1038/s41598-019-53521-7.

[170] Romy Ettlinger, Marthe Sönksen, Monika Graf, Natalia Moreno, Dmytro Denysenko, Dirk Volkmer, Kornelius Kerl, and Hana Bunzen. Metal–organic framework nanoparticles for arsenic trioxide drug delivery. *Journal of Materials Chemistry B*, 6(40): 6481–6489, 2018. ISSN 2050-750X. doi:10.1039/C8TB01899E. URL http://xlink.rsc.org/?DOI=C8TB01899E.

[171] Romy Ettlinger, Natalia Moreno, Dirk Volkmer, Kornelius Kerl, and Hana Bunzen. Zeolitic Imidazolate Framework-8 as pH-Sensitive Nanocarrier for “Arsenic Trioxide” Drug Delivery. *Chemistry – A European Journal*, 25(57):13189–13196, oct 2019. ISSN 0947-6539. doi:10.1002/chem.201902599. URL https://onlinelibrary.wiley.com/doi/abs/10.1002/chem.201902599.

[172] Mauro Ferrari. Cancer nanotechnology: opportunities and challenges. *Nature Reviews Cancer*, 5(3):161–171, mar 2005. ISSN 1474-175X. doi:10.1038/nrc1566. URL http://www.nature.com/articles/nrc1566.

[173] Omid C. Farokhzad and Robert Langer. Impact of Nanotechnology on Drug Delivery. *ACS Nano*, 3(1):16–20, jan 2009. ISSN 1936-0851. doi:10.1021/nn900002m. URL https://pubs.acs.org/doi/10.1021/nn900002m.

[174] Aaron C. Anselmo and Samir Mitragotri. Nanoparticles in the clinic: An update. *Bioengineering & Translational Medicine*, 1(1): 10–29, mar 2016. ISSN 2380-6761. doi:10.1002/btm2.10143. URL https://onlinelibrary.wiley.com/doi/abs/10.1002/btm2.10143https://onlinelibrary.wiley.com/doi/10.1002/btm2.10003.

[175] Mohammad J. Hajipour, Katharina M. Fromm, Ali Akbar Ashkarran, Dorleta Jimenez de Aberasturi, Idoia Ruiz de Larramendi, Teofilo Rojo, Vahid Serpooshan, Wolfgang J. Parak, and Morteza Mahmoudi. Antibacterial properties of nanoparticles. *Trends in Biotechnology*, 30(10): 499–511, oct 2012. ISSN 01677799. doi:10.1016/j.tibtech.2012.06.004. URL https://linkinghub.elsevier.com/retrieve/pii/S0167779912000959.

[176] Kristina Riehemann, Stefan W. Schneider, Thomas A. Luger, Biana Godin, Mauro Ferrari, and Harald Fuchs. Nanomedicine-Challenge and Perspectives. *Angewandte Chemie International Edition*, 48(5):872–897, jan 2009. ISSN 14337851. doi:10.1002/anie.200802585. URL http://doi.wiley.com/10.1002/anie.200802585.

[177] Robby A. Petros and Joseph M. DeSimone. Strategies in the design of nanoparticles for therapeutic applications. *Nature Reviews Drug Discovery*, 9(8): 615–627, aug 2010. ISSN 1474-1776. doi:10.1038/nrd2591. URL http://www.nature.com/articles/nrd2591.

[178] Wenbin Lin. Introduction: Nanoparticles in Medicine. *Chemical Reviews*, 115(19):10407–10409, oct 2015. ISSN 0009-2665. doi:10.1021/acs.chemrev.5b00534. URL https://pubs.acs.org/doi/10.1021/acs.chemrev.5b00534.

[179] David Julian McClements and Hang Xiao. Is nano safe in foods? Establishing the factors impacting the gastrointestinal fate and toxicity of organic and

inorganic food-grade nanoparticles. *npj Science of Food*, 1(1): 6, dec 2017. ISSN 2396-8370. doi:10.1038/s41538-017-0005-1. URL http://dx.doi.org/10.1038/s41538-017-0005-1http://www.nature.com/articles/s41538-017-0005-1.

[180] Ken Donaldson, Lang Tran, Luis Albert Jimenez, Rodger Duffin, David E. Newby, Nicholas Mills, William MacNee, and Vicki Stone. Combustion-derived nanoparticles: A review of their toxicology following inhalation exposure. *Particle and Fibre Toxicology*, 2:1–14, 2005. ISSN 17438977. doi:10.1186/1743-8977-2-10.

[181] R. Merget, T. Bauer, H. Küpper, S. Philippou, H. Bauer, R. Breitstadt, and T. Bruening. Health hazards due to the inhalation of amorphous silica. *Archives of Toxicology*, 75(11-12): 625–634, jan 2002. ISSN 0340-5761. doi:10.1007/s002040100266. URL http://link.springer.com/10.1007/s002040100266.

[182] Alexander T. Bauer, Elwira A. Strozyk, Christian Gorzelanny, Christoph Westerhausen, Anna Desch, Matthias F. Schneider, and Stefan W. Schneider. Cytotoxicity of silica nanoparticles through exocytosis of von Willebrand factor and necrotic cell death in primary human endothelial cells. *Biomaterials*, 32(33):8385–8393, 2011. ISSN 01429612. doi:10.1016/j.biomaterials.2011.07.078. URL http://dx.doi.org/10.1016/j.biomaterials.2011.07.078.

[183] Kohei Yamashita, Yasuo Yoshioka, Kazuma Higashisaka, Kazuya Mimura, Yuki Morishita, Masatoshi Nozaki, Tokuyuki Yoshida, Toshinobu Ogura, Hiromi Nabeshi, Kazuya Nagano, Yasuhiro Abe, Haruhiko Kamada, Youko Monobe, Takayoshi Imazawa, Hisae Aoshima, Kiyoshi Shishido, Yuichi Kawai, Tadanori Mayumi, Shin Ichi Tsunoda, Norio Itoh, Tomoaki Yoshikawa, Itaru Yanagihara, Shigeru Saito, and Yasuo Tsutsumi. Silica and titanium dioxide nanoparticles cause pregnancy complications in mice. *Nature Nanotechnology*, 6 (5):321–328, 2011. ISSN 17483395. doi:10.1038/nnano.2011.41.

[184] Qiaoya Lin, Parinaz Fathi, and Xiaoyuan Chen. Nanoparticle delivery in vivo: A fresh look from intravital imaging. *EBioMedicine*, 59:102958, 2020. ISSN 2352-3964. doi:https://doi.org/10.1016/j.ebiom.2020.102958. URL https://www.sciencedirect.com/science/article/pii/S2352396420303340.

[185] Shuhua Zhao, Xinli Lin, Long Zhang, Lei Sun, Jun Li, Wensheng Yang, and Zhiwei Sun. The in vivo investigation of fe3o4-nanoparticles acute toxicity in mice. *Biomedical Engineering: Applications, Basis and Communications*, 24(03):229–235, 2012. doi:10.4015/S1016237212500056. URL https://doi.org/10.4015/S1016237212500056.

[186] Joao Paulo Mattos Almeida, Allen L Chen, Aaron Foster, and Rebekah Drezek. In vivo biodistribution of nanoparticles. *Nanomedicine*, 6(5):815–835, jul 2011. ISSN 1743-5889. doi:10.2217/nnm.11.79. URL https://www.futuremedicine.com/doi/10.2217/nnm.11.79.

[187] Marco P. Monopoli, Dorota Walczyk, Abigail Campbell, Giuliano Elia, Iseult Lynch, Francesca Baldelli Bombelli, and Kenneth A. Dawson. Physical-Chemical Aspects of Protein Corona: Relevance to in Vitro and in Vivo Biological Impacts of Nanoparticles. *Journal of the American Chemical Society*, 133(8):2525–2534, mar 2011. ISSN 0002-7863. doi:10.1021/ja107583h. URL https://pubs.acs.org/doi/10.1021/ja107583h.

[188] Christian Kirchner, Tim Liedl, Stefan Kudera, Teresa Pellegrino, Almudena Muñoz Javier, Hermann E. Gaub, Sonja Stölzle, N. Fertig, and Wolfgang J. Parak. Cytotoxicity of Colloidal CdSe and CdSe/ZnS Nanoparticles. *Nano Letters*, 5(2):331–338, feb 2005. ISSN 1530-6984. doi:10.1021/nl047996m. URL https://pubs.acs.org/doi/10.1021/nl047996m.

[189] Anna Lesniak, Anna Salvati, Maria J. Santos-Martinez, Marek W. Radomski, Kenneth A. Dawson, and Christoffer Åberg. Nanoparticle Adhesion to the Cell Membrane and Its Effect on Nanoparticle Uptake Efficiency. *Journal of the American Chemical Society*, 135(4):1438–1444, jan 2013. ISSN 0002-7863. doi:10.1021/ja309812z. URL https://pubs.acs.org/doi/10.1021/ja309812z.

[190] Hagar I. Labouta, Nasimeh Asgarian, Kristina Rinker, and David T. Cramb. Meta-Analysis of Nanoparticle Cytotoxicity via Data-Mining the Literature. *ACS Nano*, 13(2):acsnano.8b07562, jan 2019. ISSN 1936-0851. doi:10.1021/acsnano.8b07562. URL https://pubs.acs.org/doi/10.1021/acsnano.8b07562.

[191] Florian G. Strobl, Florian Seitz, Christoph Westerhausen, Armin Reller, Adriano A. Torrano, Christoph Bräuchle, Achim Wixforth, and Matthias F. Schneider.

Intake of silica nanoparticles by giant lipid vesicles: influence of particle size and thermodynamic membrane state. *Beilstein Journal of Nanotechnology*, 5(1):2468–2478, dec 2014. ISSN 2190-4286. doi:10.3762/bjnano.5.256. URL http://www.beilstein-journals.org/bjnano/content/5/1/256.

[192] F G Strobl, D M Czubak, A Wixforth, and C Westerhausen. Ion controlled passive nanoparticle uptake in lipid vesicles in theory and experiment. *Journal of Physics D: Applied Physics*, 52(29):294001, jul 2019. ISSN 0022-3727. doi:10.1088/1361-6463/ab1994. URL https://iopscience.iop.org/article/10.1088/1361-6463/ab1994.

[193] Bin Zheng, Hanjie Wang, Huizhuo Pan, Chao Liang, Wanying Ji, Li Zhao, Hongbin Chen, Xiaoqun Gong, Xiaoli Wu, and Jin Chang. Near-Infrared Light Triggered Upconversion Optogenetic Nanosystem for Cancer Therapy. *ACS Nano*, 11(12):11898–11907, dec 2017. ISSN 1936-0851. doi:10.1021/acsnano.7b06395. URL https://pubs.acs.org/doi/10.1021/acsnano.7b06395.

[194] Markus Deserno. Elastic deformation of a fluid membrane upon colloid binding. *Physical Review E*, 69(3):031903, mar 2004. ISSN 1539-3755. doi:10.1103/PhysRevE.69.031903. URL https://link.aps.org/doi/10.1103/PhysRevE.69.031903.

[195] Doncho V. Zhelev and David Needham. Tension-stabilized pores in giant vesicles: determination of pore size and pore line tension. *Biochimica et Biophysica Acta (BBA) - Biomembranes*, 1147(1):89–104, apr 1993. ISSN 00052736. doi:10.1016/0005-2736(93)90319-U. URL https://linkinghub.elsevier.com/retrieve/pii/000527369390319U.

[196] Markus Deserno and William M. Gelbart. Adhesion and Wrapping in Colloid-Vesicle Complexes. *The Journal of Physical Chemistry B*, 106(21):5543–5552, may 2002. ISSN 1520-6106. doi:10.1021/jp0138476. URL https://pubs.acs.org/doi/10.1021/jp0138476.

[197] W. Helfrich. Elastic Properties of Lipid Bilayers: Theory and Possible Experiments. *Zeitschrift für Naturforschung C*, 28(11-12):693–703, dec 1973. ISSN 1865-7125. doi:10.1515/znc-1973-11-1209. URL https://www.degruyter.com/document/doi/10.1515/znc-1973-11-1209/html.

[198] Derek Marsh. *Handbook of Lipid Bilayers*. CRC Press, feb 2013. ISBN 9780429193125. doi:10.1201/b11712. URL

https://www.taylorfrancis.com/books/9781420088335.

[199] L. Fernandez-Puente, I. Bivas, M. D. Mitov, and P. Méléard. Temperature and Chain Length Effects on Bending Elasticity of Phosphatidylcholine Bilayers. *Europhysics Letters (EPL)*, 28 (3):181–186, oct 1994. ISSN 0295-5075. doi:10.1209/0295-5075/28/3/005. URL https://iopscience.iop.org/article/10.1209/0295-5075/28/3/005.

[200] Philippe Méléard, Claire Gerbeaud, Tanja Pott, Laurent Fernandez-Puente, Isak Bivas, M.D. Mitov, Jean Dufourcq, and Pierre Bothorel. Bending elasticities of model membranes: influences of temperature and sterol content. *Biophysical Journal*, 72(6):2616–2629, jun 1997. ISSN 00063495. doi:10.1016/S0006-3495(97)78905-7. URL https://linkinghub.elsevier.com/retrieve/pii/S0006349597789057.

[201] Chau-hwang Lee, Wan-chen Lin, and Jyhpyng Wang. All-optical measurements of the bending rigidity of lipid-vesicle membranes across structural phase transitions. *Physical Review E*, 64(2): 020901, jul 2001. ISSN 1063-651X. doi:10.1103/PhysRevE.64.020901. URL https://link.aps.org/doi/10.1103/PhysRevE.64.020901.

[202] Gabriel Popescu, Takahiro Ikeda, Keisuke Goda, Catherine A. Best-Popescu, Michael Laposata, Suliana Manley, Ramachandra R. Dasari, Kamran Badizadegan, and Michael S. Feld. Optical Measurement of Cell Membrane Tension. *Physical Review Letters*, 97(21): 218101, nov 2006. ISSN 0031-9007. doi:10.1103/PhysRevLett.97.218101. URL https://link.aps.org/doi/10.1103/PhysRevLett.97.218101.

[203] Carina S. Fedosejevs and Matthias F. Schneider. Sharp, localized phase transitions in single neuronal cells. *Proceedings of the National Academy of Sciences of the United States of America*, 119 (8):1–6, 2022. ISSN 10916490. doi:10.1073/pnas.2117521119.

[204] C. R. Safinya, E. B. Sirota, D. Roux, and G. S. Smith. Universality in interacting membranes: The effect of cosurfactants on the interfacial rigidity. *Physical Review Letters*, 62(10):1134–1137, mar 1989. ISSN 0031-9007. doi:10.1103/PhysRevLett.62.1134. URL https://link.aps.org/doi/10.1103/PhysRevLett.62.1134.

[205] Igal Szleifer, Diego Kramer, Avinoam Ben-Shaul, William M. Gelbart, and S. A. Safran. Molecular theory of curvature elasticity in surfactant films. *The*

Journal of Chemical Physics, 92 (11):6800–6817, jun 1990. ISSN 0021-9606. doi:10.1063/1.458267. URL http://aip.scitation.org/doi/10.1063/1.458267.

[206] Evan Evans and Ron Kwok. Mechanical calorimetry of large dimyristoylphosphatidylcholine vesicles in the phase transition region. *Biochemistry*, 21(20):4874–4879, sep 1982. ISSN 0006-2960. doi:10.1021/bi00263a007. URL https://pubs.acs.org/doi/abs/10.1021/bi00263a007.

[207] E. Evans and W. Rawicz. Entropy-driven tension and bending elasticity in condensed-fluid membranes. *Physical Review Letters*, 64(17):2094–2097, apr 1990. ISSN 0031-9007. doi:10.1103/PhysRevLett.64.2094. URL http://www.ncbi.nlm.nih.gov/pubmed/9962131https://link.aps.org/doi/10.1103/PhysRevLett.64.2094.

[208] Dong Chen and Maria M. Santore. Large effect of membrane tension on the fluid–solid phase transitions of two-component phosphatidylcholine vesicles. *Proceedings of the National Academy of Sciences*, 111(1):179–184, jan 2014. ISSN 0027-8424. doi:10.1073/pnas.1314993111. URL http://www.pnas.org/lookup/doi/10.1073/pnas.1314993111.

[209] Travers H. Anderson, Younjin Min, Kim L. Weirich, Hongbo Zeng, Deborah Fygenson, and Jacob N. Israelachvili. Formation of Supported Bilayers on Silica Substrates. *Langmuir*, 25 (12):6997–7005, jun 2009. ISSN 0743-7463. doi:10.1021/la900181c. URL https://pubs.acs.org/doi/10.1021/la900181c.

[210] Jacob N Israelachvili. *Intermolecular and surface forces*. Academic press, 2011.

[211] R. Hogg, T. W. Healy, and D. W. Fuerstenau. Mutual coagulation of colloidal dispersions. *Trans. Faraday Soc.*, 62:1638–1651, 1966. doi:10.1039/TF9666201638. URL http://dx.doi.org/10.1039/TF9666201638.

[212] Holger Schönherr, Joseph M. Johnson, Peter Lenz, Curtis W. Frank, and Steven G. Boxer. Vesicle Adsorption and Lipid Bilayer Formation on Glass Studied by Atomic Force Microscopy. *Langmuir*, 20 (26):11600–11606, dec 2004. ISSN 0743-7463. doi:10.1021/la049302v. URL https://pubs.acs.org/doi/10.1021/la049302v.

[213] Aleksey Vishnyakov, Ting Li, and Alexander V. Neimark. Adhesion of Phospholipid Bilayers to Hydroxylated Silica: Existence of Nanometer-Thick Water Interlayers. *Langmuir*, 33(45):13148–13156,

nov 2017. ISSN 0743-7463. doi:10.1021/acs.langmuir.7b03582. URL https://pubs.acs.org/doi/10.1021/acs.langmuir.7b03582.

[214] Christoph G. Wittmann, Andrej Kamenac, Florian G. Strobl, Dietmar Czubak, Achim Wixforth, and Christoph Westerhausen. Ionic Strength and the Supporting Material Strongly Influence the Adhesion of Silica to Supported Lipid Bilayers. *Advanced Biosystems*, 2(8): 1800087, aug 2018. ISSN 23667478. doi:10.1002/adbi.201800087. URL http://doi.wiley.com/10.1002/adbi.201800087.

[215] Jacob David Brunner. *Messung des Phasenzustands von Lipidmembranen mittels Fluoreszenzmikroskopie*. Bachelors thesis, University of Augsburg, 2019.

[216] Nicolas Färber. *Permeabilität und Phasenzustand von Zellmembranen unter Scherfluss*. Masters thesis, University of Augsburg, 2019.

[217] Christoph Greb. Fluorescent Dyes, 2012. URL https://www.leica-microsystems.com/science-lab/fluorescent-dyes/.

[218] Margaret N. Holme, Illya A. Fedotenko, Daniel Abegg, Jasmin Althaus, Lucille Babel, France Favarger, Renate Reiter, Radu Tanasescu, Pierre-Léonard Zaffalon, André Ziegler, Bert Müller, Till Saxer, and Andreas Zumbuehl. Shear-stress sensitive lenticular vesicles for targeted drug delivery. *Nature Nanotechnology*, 7(8):536–543, aug 2012. ISSN 1748-3387. doi:10.1038/nnano.2012.84. URL http://www.nature.com/articles/nnano.2012.84.

[219] Nicolas Färber, Jonas Reitler, Julian Schäfer, and Christoph Westerhausen. Transport Across Cell Membranes is Modulated by Lipid Order. *Advanced Biology*, page 2200282, jan 2023. ISSN 2701-0198. doi:10.1002/adbi.202200282. URL https://www.researchsquare.com/article/rs-1297077/v1https://onlinelibrary.wiley.com/doi/10.1002/adbi.202200282.

[220] Andrej Kamenac, Manuel Sirch, Simon Neidinger, and Christoph Westerhausen. Phase-State Dependent Silica Nanoparticle Uptake of Giant Unilamellar Vesicles. February under revision. doi:10.21203/rs.3.rs-754056/v1. URL https://www.researchsquare.com/article/rs-754056/v1. ISSN: 2693-5015 Type: article.

[221] Yareni A. Ayala, Ramin Omidvar, Winfried Römer, and Alexander Rohrbach. Thermal fluctuations of the lipid membrane determine particle uptake into Giant Unilamellar Vesicles. *Nature Communications*,

14(1):65, jan 2023. ISSN 2041-1723. doi:10.1038/s41467-022-35302-5. URL https://www.nature.com/articles/s41467-022-35302-5.

[222] K. H. de Haas, C. Blom, D. van den Ende, M. H. G. Duits, B. Haveman, and J. Mellema. Rheological Behavior of a Dispersion of Small Lipid Bilayer Vesicles. *Langmuir*, 13(25):6658–6668, dec 1997. ISSN 0743-7463. doi:10.1021/la970564p. URL https://pubs.acs.org/doi/10.1021/la970564p.

[223] Christoph Naumann, Thomas Brumm, and Thomas M. Bayerl. Phase transition behavior of single phosphatidylcholine bilayers on a solid spherical support studied by DSC, NMR and FT-IR. *Biophysical Journal*, 63 (5):1314–1319, nov 1992. ISSN 00063495. doi:10.1016/S0006-3495(92)81708-3. URL http://dx.doi.org/10.1016/S0006-3495(92)81708-3https://linkinghub.elsevier.com/retrieve/pii/S0006349592817083.

[224] N. Bibissidis, K. Betlem, G. Cordoyiannis, F. Prista-von Bonhorst, J. Goole, J. Raval, M. Daniel, W. Góźdź, A. Iglič, and P. Losada-Pérez. Correlation between adhesion strength and phase behaviour in solid-supported lipid membranes. *Journal of Molecular Liquids*, 320: 114492, dec 2020. ISSN 01677322. doi:10.1016/j.molliq.2020.114492. URL https://linkinghub.elsevier.com/retrieve/pii/S0167732220349035.

[225] Katharina Biechele. *Membrane State and Permeability under Influence of Thermodynamic Forces*. Masters thesis, Albert Ludwig University of Freiburg, 2020.

[226] Felix Ludwig Schilberth. *Entwicklung mikrofluidischer Methoden zur induzierten Wirkstoffaufnahme in lebende Zellen*. Masters thesis, University of Augsburg, 2018.

[227] Thomas M. Geislinger and Thomas Franke. Hydrodynamic lift of vesicles and red blood cells in flow — from Fåhræus & Lindqvist to microfluidic cell sorting. *Advances in Colloid and Interface Science*, 208: 161–176, jun 2014. ISSN 00018686. doi:10.1016/j.cis.2014.03.002. URL http://linkinghub.elsevier.com/retrieve/pii/S000186861400102Xhttps://linkinghub.elsevier.com/retrieve/pii/S000186861400102X.

[228] M. S.F. Clarke and P. L. McNeil. Syringe loading introduces macromolecules into living mammalian cell cytosol. *Journal of cell science*, 102 (Pt 3(3):533–41, jul 1992. ISSN 0021-9533. URL http://www.ncbi.nlm.nih.gov/pubmed/1506433.

[229] William Reginald Dean. Fluid motion in a curved channel. *Proceedings of the Royal Society of London. Series A, Containing Papers of a Mathematical and Physical Character*, 121(787): 402–420, nov 1928. ISSN 0950-1207. doi:10.1098/rspa.1928.0205. URL https://royalsocietypublishing.org/doi/10.1098/rspa.1928.0205.

[230] Armon Sharei, Janet Zoldan, Andrea Adamo, Woo Young Sim, Nahyun Cho, Emily Jackson, Shirley Mao, Sabine Schneider, M.-J. Han, Abigail Lytton-Jean, Pamela A. Basto, Siddharth Jhunjhunwala, Jungmin Lee, Daniel A. Heller, Jeon Woong Kang, George C. Hartoularos, K.-S. Kim, Daniel G. Anderson, Robert Langer, and Klavs F. Jensen. A vector-free microfluidic platform for intracellular delivery. *Proceedings of the National Academy of Sciences*, 110(6):2082–2087, feb 2013. ISSN 0027-8424. doi:10.1073/pnas.1218705110. URL http://www.pnas.org/cgi/doi/10.1073/pnas.1218705110.

[231] William Thielicke and Eize J. Stamhuis. PIVlab – Towards User-friendly, Affordable and Accurate Digital Particle Image Velocimetry in MATLAB. *Journal of Open Research Software*, 2, oct 2014. ISSN 2049-9647. doi:10.5334/jors.bl. URL http://openresearchsoftware.metajnl.com/articles/10.5334/jors.bl/.

[232] Peter Debye and Erich Hückel. Zur Theorie der Elektrolyte. I. Gefrierpunktserniedrigung und verwandte Erscheinungen. *Physikalische Zeitschrift*, 24(185):305, 1923.

[233] Evan Evans, Volkmar Heinrich, Florian Ludwig, and Wieslawa Rawicz. Dynamic Tension Spectroscopy and Strength of Biomembranes. *Biophysical Journal*, 85(4):2342–2350, oct 2003. ISSN 00063495. doi:10.1016/S0006-3495(03)74658-X. URL https://linkinghub.elsevier.com/retrieve/pii/S000634950374658X.

[234] Yukihiro Tamba, Hirotaka Ariyama, Victor Levadny, and Masahito Yamazaki. Kinetic Pathway of Antimicrobial Peptide Magainin 2-Induced Pore Formation in Lipid Membranes. *The Journal of Physical Chemistry B*, 114(37): 12018–12026, sep 2010. ISSN 1520-6106. doi:10.1021/jp104527y. URL https://pubs.acs.org/doi/10.1021/jp104527y.

[235] O. Liarzi and B. L. Epel. Development of a quantitative tool for measuring changes in the coefficient of conductivity of plasmodesmata induced by developmental, biotic, and abiotic signals. *Protoplasma*, 225(1-2):

67–76, apr 2005. ISSN 0033-183X. doi:10.1007/s00709-004-0079-x. URL http://link.springer.com/10.1007/s00709-004-0079-x.

[236] J.C. Bischof, J. Padanilam, W.H. Holmes, R.M. Ezzell, R.C. Lee, R.G. Tompkins, M.L. Yarmush, and M. Toner. Dynamics of cell membrane permeability changes at supraphysiological temperatures. *Biophysical Journal*, 68 (6):2608–2614, jun 1995. ISSN 00063495. doi:10.1016/S0006-3495(95)80445-5. URL https://linkinghub.elsevier.com/retrieve/pii/S0006349595804455.

[237] Huaying Chen, Zhihang Yu, Siwei Bai, Huaxiu Lu, Dong Xu, Chang Chen, Di Liu, and Yonggang Zhu. Microfluidic models of physiological or pathological flow shear stress for cell biology, disease modeling and drug development. *TrAC Trends in Analytical Chemistry*, 117: 186–199, aug 2019. ISSN 01659936. doi:10.1016/j.trac.2019.06.023. URL https://linkinghub.elsevier.com/retrieve/pii/S0165993619301943.

[238] Theodore G. Papaioannou, Emmanouil N. Karatzis, Manolis Vavuranakis, John P. Lekakis, and Christodoulos Stefanadis. Assessment of vascular wall shear stress and implications for atherosclerotic disease. *International Journal of Cardiology*, 113 (1):12–18, oct 2006. ISSN 01675273. doi:10.1016/j.ijcard.2006.03.035. URL https://linkinghub.elsevier.com/retrieve/pii/S0167527306004335.

[239] S. Weinbaum, S.C. Cowin, and Yu Zeng. A model for the excitation of osteocytes by mechanical loading-induced bone fluid shear stresses. *Journal of Biomechanics*, 27(3):339–360, mar 1994. ISSN 00219290. doi:10.1016/0021-9290(94)90010-8. URL https://linkinghub.elsevier.com/retrieve/pii/0021929094900108.

[240] Damien Maggiorani, Romain Dissard, Marcy Belloy, Jean-Sébastien Saulnier-Blache, Audrey Casemayou, Laure Ducasse, Sandra Grès, Julie Bellière, Cécile Caubet, Jean-Loup Bascands, Joost P. Schanstra, and Bénédicte Buffin-Meyer. Shear Stress-Induced Alteration of Epithelial Organization in Human Renal Tubular Cells. *PLOS ONE*, 10(7): e0131416, jul 2015. ISSN 1932-6203. doi:10.1371/journal.pone.0131416. URL https://dx.plos.org/10.1371/journal.pone.0131416.

[241] Jongwon Kim and Ramana M. Pidaparti. Computational Analysis of Lung and Isolated Airway Bifurcations under Mechanical Ventilation and Normal Breathing. *Fluids*, 6

(11):388, oct 2021. ISSN 2311-5521. doi:10.3390/fluids6110388. URL https://www.mdpi.com/2311-5521/6/11/388.

[242] Sarah Stolberg and Kara E. McCloskey. Can shear stress direct stem cell fate? *Biotechnology Progress*, 25(1):10–19, jan 2009. ISSN 87567938. doi:10.1002/btpr.124. URL https://onlinelibrary.wiley.com/doi/10.1002/btpr.124.

[243] A. M. Jötten, S. Angermann, M. E. M. Stamp, D. Breyer, F. G. Strobl, A. Wixforth, and C. Westerhausen. Correlation of in vitro cell adhesion, local shear flow and cell density. *RSC Advances*, 9 (1):543–551, 2019. ISSN 2046-2069. doi:10.1039/C8RA07416J. URL http://xlink.rsc.org/?DOI=C8RA07416J.

[244] G. L. Ellman, K. D. Courtney, V. Andres, and R. M. Featherstone. A new and rapid colorimetric determination of acetylcholinesterase activity. *Biochemical Pharmacology*, 7(2):88–95, 1961. ISSN 00062952. doi:10.1016/0006-2952(61)90145-9.

[245] Andrej Kamenac. *Korrelation von Phasenübergängen und Aktivität membrangebundener Enzyme*. Masters thesis, University of Augsburg, 2016.

[246] Lin Zhang, Heather L. Lawson, Vallathucherry C. Harish, Jason D. Huff, Mary Ann Knovich, and John Owen. Creation of a recombinant peptide substrate for fluorescence resonance energy transfer-based protease assays. *Analytical Biochemistry*, 358(2):298–300, 2006. ISSN 00032697. doi:10.1016/j.ab.2006.06.022.

[247] Koichi Kokame, Yuko Nobe, Yoshihiro Kokubo, Akira Okayama, and Toshiyuki Miyata. FRETS-VWF73, a first fluorogenic substrate for ADAMTS13 assay. *British Journal of Haematology*, 129(1):93–100, 2005. ISSN 00071048. doi:10.1111/j.1365-2141.2005.05420.x.

[248] Yong Xie, Yanan Jiang, and Dor Ben-Amotz. Detection of amino acid and peptide phosphate protonation using Raman spectroscopy. *Analytical Biochemistry*, 343(2): 223–230, August 2005. ISSN 0003-2697. doi:10.1016/j.ab.2005.05.038. URL https://www.sciencedirect.com/science/article/pii/S0003269705004124.

[249] H. I. Silman and Arthur Karlin. Effect of local pH changes caused by substrate hydrolysis on the activity of membrane-bound acetylcholinesterase. *Biochem.*, 58:1664–1668, 1967. ISSN 00278424.

[250] Yong Zhou and Robert M. Raphael. Solution pH Alters Mechanical and Electrical Properties of Phosphatidylcholine Membranes: Relation between Interfacial Electrostatics, Intramembrane Potential, and Bending Elasticity. *Biophysical Journal*, 92(7):2451–2462, apr 2007. ISSN 00063495. doi:10.1529/biophysj.106.096362. URL https://linkinghub.elsevier.com/retrieve/pii/S0006349507710500.

[251] Robert O. Fox and Frederic M. Richards. A voltage-gated ion channel model inferred from the crystal structure of alamethicin at 1.5-Å resolution. *Nature*, 300 (5890):325–330, nov 1982. ISSN 0028-0836. doi:10.1038/300325a0. URL http://www.nature.com/articles/300325a0.

[252] Yuan-Peng Zhang, Ruthven N. A. H. Lewis, Robert S. Hodges, and Ronald N. McElhaney. Peptide Models of Helical Hydrophobic Transmembrane Segments of Membrane Proteins. 2. Differential Scanning Calorimetric and FTIR Spectroscopic Studies of the Interaction of Ac-K2-(LA)12-K2-amide with Phosphatidylcholine Bilayers. *Biochemistry*, 34(7): 2362–2371, feb 1995. ISSN 0006-2960. doi:10.1021/bi00007a032. URL https://pubs.acs.org/doi/abs/10.1021/bi00007a032.

[253] Katharina Gaus, Soazig Le Lay, Nagaraj Balasubramanian, and Martin A. Schwartz. Integrin-mediated adhesion regulates membrane order. *Journal of Cell Biology*, 174 (5):725–734, 2006. ISSN 00219525. doi:10.1083/jcb.200603034.

[254] J R Hazel. Thermal adaptation in biological membranes: Is homeoviscous adaptation the explanation? *Annual Review of Physiology*, 57(1):19–42, 1995. doi:10.1146/annurev.ph.57.030195.000315. URL https://doi.org/10.1146/annurev.ph.57.030195.000315. PMID: 7778864.

[255] F Szoka and D Papahadjopoulos. Comparative Properties and Methods of Preparation of Lipid Vesicles (Liposomes). *Annual Review of Biophysics and Bioengineering*, 9(1): 467–508, jun 1980. ISSN 0084-6589. doi:10.1146/annurev.bb.09.060180.002343. URL http://www.pnas.org/cgi/doi/10.1073/pnas.73.11.3862http://www.annualreviews.org/doi/abs/10.1146/annurev.bb.09.060180.002343.

[256] D D Lasic. The mechanism of vesicle formation. *Biochemical Journal*, 256(1):1–11, nov 1988. ISSN 0264-6021. doi:10.1042/bj2560001. URL http://biochemj.org/lookup/doi/10.1042/bj2560001.

[257] Sushma Savarala, Selver Ahmed, Marc A. Ilies, and Stephanie L.

Wunder. Formation and Colloidal Stability of DMPC Supported Lipid Bilayers on SiO 2 Nanobeads. *Langmuir*, 26(14): 12081–12088, jul 2010. ISSN 0743-7463. doi:10.1021/la101304v. URL https://pubs.acs.org/doi/10.1021/la101304v.

[258] Nathan J. Alves, William Cusick, Jared F. Stefanick, Jonathan D. Ashley, Michael W. Handlogten, and Basar Bilgicer. Functionalized liposome purification via liposome extruder purification (lep). *Analyst*, 138:4746–4751, 2013. doi:10.1039/C3AN00680H. URL http://dx.doi.org/10.1039/C3AN00680H.

[259] Robert C. MacDonald, Ruby I. MacDonald, Bert Ph.M. Menco, Keizo Takeshita, Nanda K. Subbarao, and Lan-rong Hu. Small-volume extrusion apparatus for preparation of large, unilamellar vesicles. *Biochimica et Biophysica Acta (BBA) - Biomembranes*, 1061(2):297–303, jan 1991. ISSN 00052736. doi:10.1016/0005-2736(91)90295-J. URL https://linkinghub.elsevier.com/retrieve/pii/000527369190295J.

[260] M. I. Angelova, S. Soléau, Ph. Méléard, F. Faucon, and P. Bothorel. Preparation of giant vesicles by external AC electric fields. Kinetics and applications. In *Trends in Colloid and Interface Science VI*, volume 89, pages 127–131. Steinkopff, Darmstadt, 1992. doi:10.1007/BFb0116295. URL http://link.springer.com/10.1007/BFb0116295.

[261] Marie Breton, Mooud Amirkavei, and Lluis M. Mir. Optimization of the Electroformation of Giant Unilamellar Vesicles (GUVs) with Unsaturated Phospholipids. *The Journal of Membrane Biology*, 248(5):827–835, oct 2015. ISSN 0022-2631. doi:10.1007/s00232-015-9828-3. URL http://link.springer.com/10.1007/s00232-015-9828-3.

[262] L.-Ruth Montes, Alicia Alonso, Felix M. Goñi, and Luis A. Bagatolli. Giant Unilamellar Vesicles Electroformed from Native Membranes and Organic Lipid Mixtures under Physiological Conditions. *Biophysical Journal*, 93(10):3548–3554, nov 2007. ISSN 00063495. doi:10.1529/biophysj.107.116228. URL https://linkinghub.elsevier.com/retrieve/pii/S0006349507716065.

[263] L.K. Tamm and H.M. McConnell. Supported phospholipid bilayers. *Biophysical Journal*, 47(1):105–113, jan 1985. ISSN 00063495. doi:10.1016/S0006-3495(85)83882-0. URL http://www.ncbi.nlm.nih.gov/pubmed/3978184http:

//www.pubmedcentral.nih.gov/articlerender.fcgi?artid=PMC1435076http://linkinghub.elsevier.com/retrieve/pii/S0006349585838820https://linkinghub.elsevier.com/retrieve/pii/S0006349585838820http://dx.doi.org/.

[264] Edwin Kalb, Sammy Frey, and Lukas K. Tamm. Formation of supported planar bilayers by fusion of vesicles to supported phospholipid monolayers. *Biochimica et Biophysica Acta (BBA) - Biomembranes*, 1103(2):307–316, jan 1992. ISSN 00052736. doi:10.1016/0005-2736(92)90101-Q. URL https://linkinghub.elsevier.com/retrieve/pii/000527369290101Q.

[265] Azusa Oshima, Hiroshi Nakashima, and Koji Sumitomo. Evaluation of Lateral Diffusion of Lipids in Continuous Membranes between Freestanding and Supported Areas by Fluorescence Recovery after Photobleaching. *Langmuir*, 35(36):11725–11734, sep 2019. ISSN 0743-7463. doi:10.1021/acs.langmuir.9b01595. URL https://pubs.acs.org/doi/10.1021/acs.langmuir.9b01595.

[266] Ralf P. Richter, Rémi Bérat, and Alain R. Brisson. Formation of Solid-Supported Lipid Bilayers: An Integrated View. *Langmuir*, 22 (8):3497–3505, apr 2006. ISSN 0743-7463. doi:10.1021/la052687c. URL https://pubs.acs.org/doi/10.1021/la052687c.

[267] Tania Kjellerup Lind, Marité Cárdenas, and Hanna Pauliina Wacklin. Formation of Supported Lipid Bilayers by Vesicle Fusion: Effect of Deposition Temperature. *Langmuir*, 30(25):7259–7263, jul 2014. ISSN 0743-7463. doi:10.1021/la500897x. URL https://pubs.acs.org/doi/10.1021/la500897x.

[268] Lukas Galla, Dominik Greif, Jan Regtmeier, and Dario Anselmetti. Microfluidic carbon-blackened polydimethylsiloxane device with reduced ultra violet background fluorescence for simultaneous two-color ultra violet/visible-laser induced fluorescence detection in single cell analysis. *Biomicrofluidics*, 6(1):014104, mar 2012. ISSN 1932-1058. doi:10.1063/1.3675608. URL http://aip.scitation.org/doi/10.1063/1.3675608.

[269] T. Parasassi, G. De Stasio, G. Ravagnan, R.M. Rusch, and E. Gratton. Quantitation of lipid phases in phospholipid vesicles by the generalized polarization of Laurdan fluorescence. *Biophysical Journal*, 60(1):179–189, jul 1991. ISSN 00063495. doi:10.1016/S0006-3495(91)82041-0. URL http://dx.doi.org/10.1016/

S0006-3495(91)82041-0https://linkinghub.elsevier.com/retrieve/pii/S0006349591820410.

[270] Jaime Agudo-Canalejo and Reinhard Lipowsky. Critical particle sizes for the engulfment of nanoparticles by membranes and vesicles with bilayer asymmetry. *ACS Nano*, 9(4):3704–3720, 2015. ISSN 1936086X. doi:10.1021/acsnano.5b01285.

[271] Charis-P. Segeritz and Ludovic Vallier. Cell Culture. In *Basic Science Methods for Clinical Researchers*, pages 151–172. Elsevier, 2017. doi:10.1016/B978-0-12-803077-6.00009-6. URL https://linkinghub.elsevier.com/retrieve/pii/B9780128030776000096.

[272] Younan Xia and George M. Whitesides. SOFT LITHOGRAPHY. *Annual Review of Materials Science*, 28(1):153–184, aug 1998. ISSN 0084-6600. doi:10.1146/annurev.matsci.28.1.153. URL http://www.annualreviews.org/doi/10.1146/annurev.matsci.28.1.153.

[273] F. Chollet. SU-8: Thick Photo-Resist for MEMS, 1991. URL https://memscyclopedia.org/su8.html.

[274] Kathryn Haubert, Tracy Drier, and David Beebe. PDMS bonding by means of a portable, low-cost corona system. *Lab on a Chip*, 6(12):1548, 2006. ISSN 1473-0197. doi:10.1039/b610567j. URL http://xlink.rsc.org/?DOI=b610567j.

[275] Bernhard Illes, Patrick Hirschle, Sabine Barnert, Valentina Cauda, Stefan Wuttke, and Hanna Engelke. Exosome-Coated Metal–Organic Framework Nanoparticles: An Efficient Drug Delivery Platform. *Chemistry of Materials*, 29(19):8042–8046, oct 2017. ISSN 0897-4756. doi:10.1021/acs.chemmater.7b02358. URL https://pubs.acs.org/doi/10.1021/acs.chemmater.7b02358.

[276] Kevin Maier and Ernst Wagner. Acid-Labile Traceless Click Linker for Protein Transduction. *Journal of the American Chemical Society*, 134(24):10169–10173, jun 2012. ISSN 0002-7863. doi:10.1021/ja302705v. URL https://pubs.acs.org/doi/10.1021/ja302705v.

[277] Wolf Achim Hassenpflug, Ulrich Budde, Tobias Obser, Dorothea Angerhaus, Elke Drewke, Sonja Schneppenheim, and Reinhard Schneppenheim. Impact of mutations in the von Willebrand factor A2 domain on ADAMTS13-dependent proteolysis. *Blood*, 107(6):2339–2345, mar 2006. ISSN

0006-4971. doi:10.1182/blood-2005-04-1758.

[278] Wolf Achim Hassenpflug, Tobias Obser, Julia Bode, Florian Oyen, Ulrich Budde, Sonja Schneppenheim, Reinhard Schneppenheim, and Maria Alexandra Brehm. Genetic and Functional Characterization of ADAMTS13 Variants in a Patient Cohort with Upshaw-Schulman Syndrome Investigated in Germany. *Thrombosis and Haemostasis*, 118(4):709–722, apr 2018. ISSN 03406245. doi:10.1055/s-0038-1637749. URL `http://www.thieme-connect.de/DOI/DOI?10.1055/s-0038-1637749`.

[279] A. H. Futerman, R. M. Fiorini, E. Roth, M. G. Low, and I. Silman. Physicochemical behaviour and structural characteristics of membrane-bound acetylcholinesterase from Torpedo electric organ. Effect of phosphatidylinositol-specific phospholipase C. *The Biochemical journal*, 226(2):369–77, mar 1985. ISSN 0264-6021. URL `http://www.ncbi.nlm.nih.gov/pubmed/2986594http://www.pubmedcentral.nih.gov/articlerender.fcgi?artid=PMC1144721`.

Danksagung

- Prof. Dr. Christoph Westerhausen - Danke für das einzigartige Mentoring. Danke für Unterstützung in alle Richtungen, egal ob Stipendien, wissenschaftliche Netzwerke, oder exotische Konferenzen. Danke für das Möglichmachen von Allem und danke für all die gefeierten Erfolge. Danke für die vielen bpm zu besonderen Anlässen. Danke für dein Vertrauen. Und auch in Zukunft wird gelten: Chris keine Schande machen!

- Prof. Dr. Matthias Schneider - Danke für das Zweitgutachten. Danke für Abende am Lagerfeuer in Maßbach, voller Musik und Diskussionen.

- Prof. Dr. Achim Wixforth - Danke, dass du ein Gönner bist. Danke, dass du mich in allem nach besten Kräften unterstützt hast. Danke, dass du dein Gitarrensolo nachholen wirst.

- Meine Freunde & Kollegen am Lehrstuhl:
  - Maximilian Gnedel - Danke, dass du mein Trauzeuge bist.
  - Anna Jötten - Danke für deine Leidenschaft bei Gesellschaftsspielen.
  - Maximilian Sonner - Danke für dein brillantes Aktienwissen.
  - Lukas Schnitzler - Danke für die zahlreichen Fußballtrainings.
  - Sebastian Pentz - Danke für die Goldschmiede-Saga.
  - Jonas Reitler - Danke für das einmalige 1:0 und den Institutscup-Pokal.
  - Sascha Buchegger - Danke für die eloquente Balletlehrerin.
  - Emeline Nysten - Danke für dein Lachen bei chubby bunny.
  - Matthias Weiß - Danke für das Aufrechterhalten von After-Work-Events.
  - Manuel Brugger - Danke, dass wir Chris keine Schande gemacht haben.
  - Kathrin Baumgartner - Danke für die tolle Zeit in Jülich.
  - Sven Fuchs - Danke für den Sieg in Mario Kart N64 gegen EP IV.
  - Jochen Taiber - Danke für deine Gefasstheit beim Schafkopfen.
  - Sophie Mauritz - Danke für den Ruhm des EP I am gesamten Institut.
  - Patrick Kudella - Danke für das Poster in unserem Büro.
  - Marie-Theres Mayer - Danke für die verstopften Atemwege beim Lehrstuhlseminar.

  - Joshua Winkeljann - Danke für dein versiertes Bausparvertragswissen.
  - Felix Schilberth - Danke für laue Sommerabende am Institut.
  - Nicolas Färber - Danke für deine Expertise zu Arbeitssicherheit.
  - Manuel Sirch - Danke für deine kulinarische Bildung in kakaohaltigen Erfrischungsgetränken.
  - Simon Neidinger - Danke für den diabolischen Tassenstreich.
  - Katharina Biechele - Danke, dass du Einstände, Ausstände und Geburtstage ernst genommen hast.
  - Johannes Heyn - Danke für Freakonomics.
  - Jacob Brunner - Danke für die kreativen Ramschvariationen.
  - Dominik Schildmann - Danke für die Zeit an der PIII.
  - Maximilian Metzner - Danke für das geniale Burgerrezept.
- Team Technik: Olga Ustinov, Andreas Spörhase und Sidonie Lieber - Danke, ohne euch ginge gar nichts.
- Joachim Herz Stiftung - Danke für die Förderung und danke für diese schier unglaubliche Community.
- Nanosystems Initiative Munich - Danke für das Funding und die Zeit im Student Board.
- Center for NanoScience - Danke für das klasse Netzwerk und die genialen Events.
- Meine Familie:
  - Corinna Kamenac - Danke, dass du ein Fré Bâgé bist. Danke, dass du das alles möglich gemacht hast.
  - Salomé Kamenac - Danke, dass du auch eine Doktorarbeit schreiben willst.
  - Nathan Kamenac - Danke, dass du gerade nichts schreiben willst und mit allem einverstanden bist.
  - Biljana Kamenac - Danke fürs Erinnern.